ÖAW
Austrian Academy of Sciences

IBN
INSTITUTE OF BIOPHYSICS AND NANOSYSTEMS RESEARCH

ANNUAL REPORT 2010

Fractal Perception of Change

AUSTRIAN SAXS BEAMLINE AT elettra

Austrian Small Angle X-ray Scattering (SAXS) Beamline at ELETTRA

Annual Report 2010

- Compiled by Sigrid Bernstorff
- Cover layout by Michael Rappolt

Table of Contents

Preface

Peter Laggner
Director
Institute of Biophysics and Nanosystems Research
Austrian Academy of Sciences

These are stormy times, also for the research community in Europe. When you read this, the economic reality – one of the stronger factors in life – might have changed to an extent that would dictate a different tune.

Nevertheless, this report on yet another year of extremely fruitful activity at the Austrian SAXS-station at Elettra is a good source for optimism. The quality and number of published results continues to increase despite stagnation or even decreasing financial resources at the funding institutions and in the individual institutes of our users. This is a strong signal for the fact that the use of our SAXS beamline is a potent factor towards success in the individual research plans. With the combined efforts of all parties concerned, our ranking remains in the top group of the Champions League of synchrotron SAXS worldwide which is not a minor achievement considering the financial limitations.

Nanomaterial research and structural biophysics are again dominating. The focus on technology and life science is stronger than ever before. In addition, the methodological progress, e.g. in high-throughput techniques, microfluidics, gas-phase SAXS and deep X-ray lithography is quite remarkable. These are important assets in the pursuit of attracting a wider user community for synchrotron SAXS.

Thus, we are well prepared to weather any storms ahead. “In the fields of observation, chance favors only the prepared mind” (Louis Pasteur). Not just in the fields of observation, I would add.

As always, I want to thank our partners and users most cordially for their contributions to our successful operation.

Alfonso Franciosi
Chief Executive Officer
Sincrotrone Trieste S.C.p.A.

We are very pleased to have the opportunity to write this preface to the 2010 Annual Report of the SAXS Beamline of the Austrian Academy of Sciences. The notable scientific production of the SAXS Beamline with a renewed emphasis on nanomaterials research and structural biophysics, and the recent upgrades in areas such as high-throughput techniques and microfluidics, show how the Beamline is attracting a wider user community and yielding a continued high demand. All of these make the SAXS Beamline an example of what a successful scientific partnership can achieve

Despite the challenging financial situation that is seriously affecting scientific reesearch worldwide, here in Trieste we were able to exploit the enhanced capabilities of Elettra while developing of the new free-electron laser (FEL) source FERMI@Elettra. The Elettra third-generation light source has become one of the few synchrotron radiation sources in the world that operate in top-up mode, and the one and only machine in the world that was not designed for top-up, but has been successfully converted to operate in top-up mode. Elettra routinely operates in top-up mode at both 2.0 and 2.4 GeV, and the users are benefitting from the higher stability and the increased average brightness of the source. The uptime was 96-97% and the mean time between failures was 140 hours, with a record-breaking uninterrupted top-up stint for users of 195 hours. The major project of realignment of the storage ring has been completed, as has the hardware for the beam-based alignment, increasing the reliability and ease of operation of the machine.

The upgrade of the Elettra beamlines to take full advantage of the new source characteristics continues. For example, a new, redesigned undulator for the SuperESCA/ESCAmicroscopy beamlines was successfully installed, substantially increasing the high-energy beamline

performance. A new, high-performance x-ray detector was installed at the XRD1 beamline, together with an in-house developed, versatile sample changer holding 50 samples.

The FERMI@Elettra project has the objective to provide ultraviolet and soft x-ray radiation of unprecedented brilliance in ultrashort and synchronizable pulses for spectroscopy, microscopy, and diffraction applications. The uniqueness of such a project when compared to other FEL projects in the United States (LCLS), Germany (FLASH and XFEL) and JAPAN (SCSS), consists in the use, since its conception, of a *seeding* scheme, that is of a laser optical signal for obtaining the initial stimulated emission by the electron bunches. This allows for a far better control on the intensity and lineshape of the output FEL pulses as compared to machines that use the alternate self-amplified spontaneous emission (SASE) method, where the random nature of the spontaneous emission process yields large variation in pulse intensity and lineshape.

FERMI@Elettra has been planned as an incremental facility, starting with a FEL-1 laser based on a first series of insertion devices of original design and construction and operating between 100 and 20 nanometers, followed by a second, FEL-2 laser. which has been designed to reach few nanometers in the fundamental emission and 1 nm (1248 eV) in the third harmonic. The FEL-1 line, consisting of a planar undulator (the modulator) and six APPLE-II undulators (the radiators) was completed in November 2010. The wavelength of the FEL radiation can be varied thanks to the variable undulator gap, down to 10 mm. Furthermore, the use of APPLE II undulators allows control of the FEL polarization that can be varied from linear to circular. Few weeks after completing the installation of FEL-1, on December 13, 2010 first evidence of coherent emission in the 60 to 20 nm range was obtained.

The benefit of using external seeding in terms of spectral bandwidth and photon energy stability was evident since the very first days of FEL operation, when spectral measurements showed that the pulse bandwidth was close to the Fourier limit. At 43 nm the measured photon flux currently exceeds 10^{13} photons per pulse. Similar flux intensities have been measured at 52 nm and at 32.5 nm. At the lower wavelength limit of FEL-1, 20 nm, the photon flux achieved to date is larger than 10^{12} photons per pulse. Once FEL operation is optimized, its stability over a few hours is truly remarkable: the central wavelength jitter is below 10^{-4}, the spectral bandwidth stability is below the 3% level and the intensity jitter is about 10%.

While commissioning of FEL-1 continues, four beamlines are being completed - Diffraction and Projection Imaging (DIPROI), TIMEX and TIMER within the Elastic and Inelastic Scattering (EIS) program, Low Density Matter (LDM) - in the new experimental hall. Some twenty-seven new international partner institutions are involved in the upgrade of Elettra and in the development and use of the new FERMI@Elettra source. A call for proposals for user beamtime will be published by the end of 2011 with beamtime assignments to external users expected to begin in the second half of 2012. Installation of the FEL-2 undulators will start at the end of 2011. The FEL-2 line runs parallel to the FEL-1 line at a distance of 1 meter. An HGHG double cascade scheme is adopted for FEL-2, thus there is a first stage with one modulator and two radiators followed by a second stage with one modulator and six radiators. The first harmonic wavelength for FEL-2 will range from 20 nm to 4 nm. Commissioning of FEL-2 is expected to start in the first half of 2012.

On the institutional side, on November 30, 2010, the Italian Government and the Government of the Friuli Venezia Giulia Region signed a Memorandum of Understanding in which they agreed to jointly support the "internationalization" of Sincrotrone Trieste, i.e., the evolution of Sincrotrone Trieste toward a European Research Intrastructure Consortium. The follow-up was uncommony swift. The research ministers of Austria, Croatia, the Czech Republic, Italy, Poland, Romania, Serbia, and Slovenia have all signed a Memorandum of Understanding expressing their intention to establish a Central European Research Infrastructure Consortium (CERIC) that will include Elettra and FERMI as core facilities. A Trieste Declaration of the Science and Technology Ministers of the Central European Initiative in the same direction was signed on October 19, 2011. The next few months will be devoted to develop the CERIC governing scheme and reinforcing and expanding our network of partners in Italy and Europe. Our long-standing relation with the Austrian Academy of Sciences will play a major role.

We take this opportunity to thank our Austrian partners for their professionalism and steady dedication over the years. We at Elettra look forward to expanding the scope and depth of our collaboration and exploring together the frontiers that the new upgraded Elettra and FERMI will open for all of us.

The SAXS Group

HEAD OF PROJECT: Peter Laggner [1)]

e-mail: peter.laggner@oeaw.ac.at

SCIENTISTS: Heinz Amenitsch [1), 3)]

e-mail: amenitsch@elettra.trieste.it

Sigrid Bernstorff [2)]

e-mail: bernstorff@elettra.trieste.it

Michael Rappolt [1), 3)]

e-mail: michael.rappolt@elettra.trieste.it

POST DOCS: Fernando Cacho [1), 3)]

e-mail: fernando.cacho@elettra.trieste.it

Dražan Jozić [2)] (from 1.10.2010)

e-mail: drazan.jozic@elettra.trieste.it

Karin Jungnikl [1, 3)] (until 31.10.2010)

e-mail: karin.jungnikl@elettra.trieste.it

Benedetta Marmiroli [1, 3)]

e-mail: benedetta.marmiroli@elettra.trieste.it

SCIENTIFIC ASSISTANT: Barbara Sartori [1, 3)]

e-mail: barbara.sartori@elettra.trieste.it

TECHNICIAN: Christian Morello [2)]

e-mail: christian.morello@elettra.trieste.it

1) Institute for Biophysics and Nanosystems Research, Austrian Academy of Sciences, Schmiedlstraße 6, 8042 Graz, Austria.
Tel 0043-316-4120 302
Fax 0043-316-4120 390

2) Sincrotrone Trieste, Strada Statale 14, km 163.5, 34012 Basovizza (TS), Italy.
Tel 0039-040-375 81
Fax 0039-040-938 0902

3) Institute for Biophysics and Nanosystems Research, Austrian Academy of Sciences
c/o Sincrotrone Trieste

The SAXS-Beamline in General

Small Angle X-ray Scattering has become a well known standard method to study the structure of various objects in the spatial range from 1 to 1000 Å, and therefore instruments capable to perform such experiments are installed at most of the synchrotron research centers. The high-flux SAXS beamline at ELETTRA is mainly intended for time-resolved studies on fast structural transitions in the sub-millisecond time region in solutions and partly ordered systems with a SAXS-resolution of 10 to 1400 Å in real-space.
The photon source is the 57-pole wiggler whose beam is shared and used simultaneously with a Macromolecular Crystallography beamline. The wiggler delivers a very intense radiation between 4 and 25 keV of which the SAXS-Beamline accepts 3 discrete energies, namely 5.4, 8 and 16 keV. The beamline optics consists of a flat double crystal monochromator and a double focusing toroidal mirror.
A versatile SAXS experimental station has been set-up, and an additional wide-angle X-ray scattering (WAXS) detector monitors simultaneously diffraction patterns in the range from 1 to 9 Å. The sample station is mounted move-able onto an optical table for optimising the sample detector distance with respect to SAXS resolution and sample size.
Besides the foreseen sample surrounding the users have the possibility to install their own specialised sample equipment. In the design phase, besides technical boundary conditions, user friendliness and reliability have been considered as important criteria.
The optimisation of the beamline with respect to high-flux and consequently high flux density, allows to perform the following experiments:

- Low Contrast Solution Scattering
- Grazing Incidence Scattering and Surface Diffraction
- Micro-Spot Scanning
- X-ray Fluorescence Analysis
- Time-Resolved Studies ≥ 11 μs
- Simultaneously Performed Small- and Wide-Angle Measurements (SWAXS) on:
    - Gels
    - Liquid Crystals
    - (Bio) Polymers
    - Amorphous Materials
    - Muscles

Furthermore, using 5.4 and 16 keV energies, the beamline is widely applicable also to very thin, e.g. single muscle fibers, and optically thick (high Z) specimen, as often used in e.g., material science and solid state physics.

THE INSERTION DEVICE

The wiggler for the SAXS beamline consists of three 1.5 m long segments, each having 19 poles. The device can work with a minimum gap of 20 mm, which corresponds to K=20 at 2 GeV. The main parameters of the wiggler are:

- Critical Energy 4.1 keV
- Radiation Power 8.6 kW
- Flux 3.5×10^{14} ph/s/mrad/0.1%BW (at 400 mA)

The wiggler radiation cone has a horizontal width of 9 mrad. From this the SAXS-beamline accepts vertically 0.3 mrad, and horizontally +/-0.5 mrad at a 1.25 mrad off-axis position. The resulting source size for 8 keV photons is 3.9 x 0.26 mm^2 (horiz. x vert.).

THE OPTICS

The optics common with the diffraction beamline consists of:

- C-Filter and Beryllium window assembly to reduce the power load on the first optical elements by a factor of 2 and to separate the beamline vacuum from the storage ring.
- Beam defining slit chamber which allows to define the SAXS beam on three sides before the monochromator in order to reduce the straylight in the downstream beamline sections.

The SAXS beamline optics consists of:

- A double-crystal monochromator consisting of four individual chambers, in which three interchangeable asymmetric Si(111) crystal pairs are used to select one of three fixed energies. Each of the crystal pairs is optimised for the corresponding energy to accomplish a grazing angle of 2°. The energy resolution $\Delta E/E$ of the monochromator is in the range of 0.7 - 2.5 10^{-3}.
- A baffle chamber after the monochromator is used as an adjustable straylight fenditure.
- A segmented toroidal mirror focuses the light in horizontal and vertical direction with a 1/2.5 magnification onto the SAXS-detector.
- An aperture slit reduces the straylight after the monochromator and the toroidal mirror.
- A guard slit defines the illuminated region around the focal spot. The spot size on the detector is 1.6 mm horizontally and 0.6 mm vertically. The calculated flux at the sample is in the order of 10^{13} ph/s at 400 mA. For a maximum sample size of 5.4 x 1.8 mm^2 correspondingly a flux density of 10^{12} ph/s/mm^2 has been calculated.

SAMPLE STAGE

The multipurpose sample stage allows to perform fast time-resolved relaxation studies based on temperature- or pressure-jumps as well as stopped flow experiments. Shear jump relaxation experiments are planned. Specifically, T-jumps can be induced by an infra-red light pulse (2 ms) from an Erbium-Glass laser, raising the temperature about 20 °C in an aqueous sample volume of 10 µl. A hydrostatic pressure cell with a maximal accessible angular range of 30° for simultaneous SAXS and WAXS measurements is available. P-jumps are realised by switching fast valves between a low and a high pressure reservoir, increasing or decreasing the hydrostatic pressure in the range from 1 bar to 2.5 kbar within a few ms. A Differential Scanning Calorimeter (DSC) allows for DSC-scans simultaneously to SWAXS measurements. In an overview, the following sample manipulations are possible (further details, see pages 25 and 29-36):

- Temperature Manipulations: Ramps, Jumps and Gradient Scans
- Pressure Manipulation: Scan and Jumps
- Stopped Flow Experiments
- SWAXS Measurements Applying Mechanical Stress
- Calorimetric measurements

Scientific Applications	Low Contrast Solution Scattering, Grazing Incidence Surface Diffraction, Micro-Spot Scanning, X-ray Fluorescence Analysis, Time-Resolved Studies ≥ 11 μs and Simultaneously Performed Small- and Wide-Angle Measurements (SWAXS) on: Gels Liquid Crystals (Bio) Polymers Amorphous Materials Muscles
Source characteristics	Wiggler (NdFeB Hybrid): Period 140 mm No. full poles 57 Gap 20 mm B_{max} 1.607 T Critical Energy ε_c 4.27 keV Power (9 mrad) 8.6 kW Effective source size FWHM 3.9 x 0.26 mm^2(h x v)
Optics	Optical elements: *Double crystal monochromator*: Si (111) asym. cut, water cooled. *Mirror*: two–segment,toroidal, Pt coated. Distance from source: 18.4 m 26.5 m Acceptance 1 mrad/0.3 mrad (h x v) Energy (3 selectable) 5.4, 8, 16 keV (0.77, 1.54, 2.3 Å) Energy resolution ΔE/E 0.7-2.5 x 10^{-3} Focal spot size FWHM 1.2 x 0.6 mm^2 (h x v) Spot at Sample FWHM 5.4 x 1.8 mm^2(h x v) Flux at sample 7.5 x 10^{12} ph s^{-1}(2 GeV, 300 mA, 8 keV)
Experimental apparatus	Resolution in real space: 10-1400 Å (small-angle), 1- 9 Å (wide-angle) Sample stage: temperature manipulations: ramps, jumps and gradient scans, pressure manipulation: scan and jumps, stop flow experiments, SWAXS measurements applying mechanical stress, SWAXS measurements applying magnetic fields. In-line calorimetric measurements simultaneously with SWAXS. Detectors: 1D gas-filled detectors for simultaneous small- and wide-angle (Gabriel type), 2D CCD (Photonic Science) and Mar300 Image Plate for small-angle, Vantec-1D (Bruker AXS), Pilatus 2D detector.
Experiment control	Beamline control: Program-units written in LabView for Windows 1 D detector control: PC-card and software from Hecus X-ray Systems GmbH, Graz. 2 D detector control: Software from corresponding detector system.

CURRENT STATUS

The beamline has been built by the Institute for Biophysics and Nanosystems Research (IBN), Austrian Academy of Science in collaboration with staff members from Sincrotrone Trieste, and is in user operation since September 1996. The set-up of the beamline started at the beginning of January 1995 with the installation of the support structure. Until the end of 1995, the 8 keV single energy system had been realised. The upgrade to the full three energy system was finished in spring 1998. Time resolved experiments require fast X-ray detectors and data acquisition hard- and software. Depending on the desired resolution in time and in reciprocal space, on isotropic or anisotropic scattering of the sample, one-dimensional position sensitive (delay-line type) or two-dimensional CCD detectors are employed.

In August 2002 our new chemistry and X-ray laboratory went into operation. The chemistry unit serves mainly for sample preparation and analysis for both, in house research and external user groups, whereas the X-ray laboratory allows on-site testing of samples before moving on to the SR beamline (see page 37).

In May 2008 we extended about 3 m also our experimental hutch. It is now possible to increase the sample to detector distance and therefore improve our minimum SAXS resolution or maximise the flux density at sample position for certain experiments.

In conclusion, due to wide versatility of the beamline and the highly flexible sample stage, there are nearly no limits for the realisation of an experiment, and you are welcome by our team to propose any interesting and highlighting investigation for the benefit of material and life sciences.

Application for Beamtime at ELETTRA

1. Beamtime Policy at SAXS beamline

According to the agreement from March 2001 regarding the co-operation between the Austrian Academy of Sciences and Sincrotrone Trieste, at the Austrian SAXS-beamline the available beamtime of about 5000 hours/year is distributed as follows:

- 35% for Austrian Users, type: "CRG" (Collaborating Research Group)
- 35% for Users of Sincrotrone Trieste (General Users (GU))
- 30% is reserved for beamline maintenance and in-house research

In both user beamtime contingents also any industrial, proprietary and confidential research can be performed according to the "General User Policy" of Sincrotrone Trieste.

To apply for CRG and GU user beamtime proposals must be submitted according to the rules of Sincrotrone Trieste. The international review committee at ELETTRA will rank the proposals according to their scientific merit assessment. Based on this decision beamtime will be allocated according to the specific quotes for the beamtimes (CRG/GU) either for the following semester ("normal application") or for the next two years ("long term application"). However, at the moment no more than a maximum of 10% of the beamtime will be assigned to "long term" projects.

2. How to apply for beamtime

There are two deadlines each year for proposals, namely August 31st and February 28th. Accepted proposals will receive beamtime either in the then following first or second half year period, respectively. The Application Form must be completed on-line according to the following instructions.

ELETTRA USERS OFFICE
Strada Statale 14 - km 163.5
34012 Basovizza (Trieste), ITALY
Tel: +39 040 375 8628 / 8538- fax: + 39 040 375 8565
e-mail: useroffice@elettra.trieste.it

INSTRUCTIONS GIVEN BY THE USERS OFFICE
(see also http://www.elettra.trieste.it/UserOffice/)

1. Read carefully the General Guidelines.

2. Connect to the Virtual Unified Office: https://vuo.elettra.trieste.it/pls/vuo/guest.startup using your favorite browser with JavaScript enabled.

3. Select the Virtual Unified Office link.

4. When prompted, insert your ID and password. If you are a new user fill in the registration form with your data and choose your institution with the search button; in case your institution does not appear in the list, please contact useroffice@elettra.trieste.it giving all the details about it. When registered, you will receive an acknowledgment with your ID and password. You can change your password, if you wish. In case you forget your password, please don't register again but contact useroffice@elettra.trieste.it. At any moment you can select the help button and view more detailed instructions. By inserting your ID and password you will be able to continue.

5. Select the proposals button in the User functions group.

6. Select add and fill in on-line the proposal form. Please, type your proposal in English. Repeat this procedure for each proposal you intend to submit.

7. In case of continuation proposal: a) attach the experimental report of previous measurements; b) give your previous proposal number.

8. When finished, submit the proposal electronically, selecting the save button.

9. Print the proposal form together with each related safety form.

10. Sign the safety form(s).

11. Mail all signed safety form(s) as printed copy to the Users Office.

NOTE:

For technical questions related to proposals submission or other practical issues, contact useroffice@elettra.trieste.it

For scientific questions related to the possibility of performing a given experiment, contact bernstorff@elettra.trieste.it or amenitsch@elettra.trieste.it

Users and institutes performing experiments in 2010

Australia

Commonwealth Scientific and Industrial Research Organisation (CSIRO), Division of Materials Science & Engineering, Clayton South MDC, Victoria

FALCARO Paolo

Austria

Austrian Academy of Science, Institute of Biophysics and Nanosystems Research, Graz

AMENITSCH Heinz
BOULGAROPOULOS Beate
CACHO-NERIN Fernando
JUNGNIKL Karin
LAGGNER Peter
MARMIROLI Benedetta
PABST Georg
RAPPOLT Michael
SARTORI Barbara
WEISER Paul

Graz University of Technology, Institute for Chemistry and Technology of Organic Materials, Graz

NOVAK J.

Graz University of Technology, Institute for Chemistry and Technology of Materials, and Christian Doppler Laboratory for Nanocomposite Solar Cells, Graz

EDLER Michael
FISCHEREDER Achim
RATH Thomas
SCHENK A.
TRIMMEL Gregor

University of Vienna, Faculty of Physics, Dep. Physics of Nanostructured Materials

KERBER Michael B.
POLT Gerald
SCHAFLER Erhard
ZEHETBAUER Michael J.

Croatia

Institute of Physics, Zagreb

KREGAR Z.
KRSTULOVIĆ N.
MILAT Ognjen
MILOŠEVIĆ S.
SALAMON Krešimir

"Ruđer Bošković" Institute, Zagreb

BOGDANOVIĆ-RADOVIĆ I.
BOZICEVIĆ Iva
BULJAN Maya
DESNICA Uroš
DJERDJ Igor
DUBčEK Pavo
ETLINGER Božidar
GAJOVIĆ Andreja
GRACIN, Davor
JANICKI V.
JAKSIC, Milko
JERČINOVIČ Marko
JURAIĆ Krunoslav
KARLUŠIĆ M.
PIVAC Branko
RADIĆ Nikola
TURKOVIC Aleksandra

Czech Republic

Academy of Sciences of the Czech Republic, Institute of Macromolecular Chemistry, Prague

BALDRIAN Josef

Charles University, Faculty of Mathematics and Physics, Prague

HOLY Vaclav
VALEŠ Vaclav

Masaryk University, Faculty of Science, Department of Condensed Matter Physics, Brno

BERNATOVA S.
BURŠÍK J.
CAHA Ondrej
MEDUNA Mojmir
MIKULÍK Petr
RŮŽIČKA Jiri
SVOBODA M.

University of Pardubice, Department of Physics, Pardubice, and Academy of Sciences of the Czech Republic, Institute of Macro-molecular Chemistry, Prague

STEINHART Milos

Denmark

University of Copenhagen, Faculty of Pharmaceutical Sciences, Department of Pharmaceutics and Analytical Chemistry, Copenhagen

YAGHMUR Anan

Finland

University of Helsinki, Faculty of Pharmacy, Centre for Drug Research

SCHMITT Mechthild
URTTI Arto
YAMADA K.

France

Institut National Polytechnique de Lorraine, Laboratoire d'énergétique et de mécanique théorique et appliquée, Vandoeuvre-lès-Nancy

ANDRE S.

SOLEIL Synchrotron, SWING Beamline, Gif-sur-Yvette

PEREZ J.

Université de Paris-sud, Faculté de Pharmacie, UMR CNRS, Chatênay-Malabry

BOURGAUX Claudie
LEPELTIER Elise
VACHON Jean-Jacques

Université Pierre et Marie Curie, Laboratoire Chimie de la Matière Condensée, Paris

GROSSO David

Université d' Orleans, Centre de Recherche sur la Matiére Divisée

SINTUREL Christophe
VAYER Marylène

University of Strasbourg, Institute of Solid and Fluid Mechanics, Strasbourg

REMOND Y.

Germany

Helmholtz Zentrum Dresden-Rossendorf, Dresden

GRENZER J.
MUECKLICH A.

Max-Planck-Institute for Coal Research, Mülheim / Ruhr

NITZ J.
SCHMIDT Wolfgang

Technische Universität Braunschweig, Institut für Pharmazeutische Technologie, Braunschweig

BUNJES Heike
JOSEPH Sonja

University of Bremen, Institute of Solid State Physics

SPECKMANN Moritz
ZARGHAM Ardalan

India

Saha Institute of Nuclear Physics, Surface Physics Division, Kolkata
CHATTERJEE P.
HAZRA S.

UGC-DAE-CSR, University Campus, Indore
GUPTA Ajay
KUMAR Dileep

School of Physics, Devi Ahilya University, Indore
PANDIT Pallavi

Italy

Associazione CIVEN, Nano Fabrication Facility, Venice
COSTACURTA Stefano

CNR, Istituto di Chimica e Tecnologia dei Polimeri, Pozzuoli
DURACCIO Donatella
PEZZUTO Marilena
SILVESTRE Clara

CNR - ISMN, Bologna
GRECO Pierpaolo

C.N.R. - IMM, Bologna
LISCIO Fabiola
MILITA Silvia

CNR - Institute of Material Structure, Monterotondo, Rome
MARI Alessandra
SUBER Lorenza

CNR - Institute of Crystallography, Monterotondo, Rome
CAMPI Gaetano
PIFFERI Augusto

CNR, Istituto di Cristallografia, Sezione di Trieste
ARRIGHETTI Gianmichele
BARBA Luisa

IOM - CNR National Laboratorio, TASC, Trieste
GRENCI Gianluca
TORMEN Massimo

Maxun s.r.l., Trieste
ANTONIOLLI Francesca
RADIVO Andrea

Sincrotrone Trieste, Trieste
BERNSTORFF Sigrid
JOZIĆ Dražan
MORELLO Christian

SISSA-ELETTRA NanoInnovation Lab, SISSA-ISAS, Trieste
CASALIS Loredana
SCOLES Giacinto

SISSA-ISAS (International School of Advanced Studies), Laboratory of Prion Biology, Neurobiology Sector, Basovizza/Trieste
BENETTI Federico

S.I.S.S.A.-I.S.A.S. Unit, Italian Institute of Technology, Trieste
LEGNAME Giuseppe

University of Camerino, Department of Bioscience and Biotechnology
AMICI Augusto
MARCHINI Cristina
MONTANI Maura

Università di Padova, Dip. di Biologia, Padova
BELTRAMINI Mariano
BUBACCO L.
TESSARI I.

Università Politecnica delle Marche, Depart. Science of Life and Environment, Ancona
BALDASSARRI Enrico
MARIANI Paolo
ORTORE Maria Grazia
SPINOZZI Francesco

University of Rome "La Sapienza", Department of Molecular Medicine
CARACCIOLO Giulio
POZZI Daniela

Università di Sassari, Laboratorio di Scienza dei Materiali e Nanotecnologie, CR-INSTM, D.A.P., Alghero
INNOCENZI Plinio
MALFATTI Luca
MARONGIU Daniela

University of Trieste, Center of Excellence for Nanostructured Materials (CENMAT), INSTM and Department of Pharmaceutical Sciences, Trieste
Da ROS Tatiana
PRATO Maurizio
TOMA Francesca Maria

University of Trieste, Department of Materials and Natural Resources

COZZARINI Luca
LUGHI Vanni

Università di Udine, Dipartimento di Scienze degli Alimenti

CALLIGARIS Sonia
DA PIEVE Sara
NICOLI M.C.

Luxembourg

Centre de Recherche Public Henri Tudor, Advanced Materials and Structures Department, Esch-sur-Alzette

ADDIEGO F.
RUCH D
TONNIAZZO V.

Portugal

Universidade do Minho, Centro de Física, Braga

GOMES Maria.J.M.
LEVICHEV Sergey
MARTÍN-SÁNCHEZ J.
PINTO Sara R. C.
ROLO Anabela G.
VIEIRA Eliana M. F.

Slovenia

Josef Stefan Institute, Ljubljana

ČEH M.
CORDOYIANNIS G.
DRAŽIĆ G.
JESENEK D.

Josef Stefan Institute, and Jozef Stefan International Postgraduate School Ljubljana

LAHAJNAR Gojmir

Josef Stefan Institute, Ljubljana, and University of Maribor, Faculty of Natural Sciences and Mathematics, Maribor

KRALJ Samo
ZIDANSEK Alexander

National Institute of Chemistry, Ljubljana

PODBRSCEK Peter

National Institute of Chemistry, and Center of Excellence for Polymer Materials and Technologies, Ljubljana

BITENC Mark
CRNJAK OREL Zoric

University of Ljubljana, Faculty of Computer and Information Science

OREL Bojan

Spain

Universitat Autonoma de Barcelona, Faculty of Medicine, Biophysics Unit, Bellaterra, Barcelona

TEIXEIRA Cilâine Verônica

United Kingdom

Keele University, Department of Physics, Keele

FULLER Watson
ARUMUGAM Mahendrasingam
WRIGHT Anthony

University of Huddersfield, School of Applied Sciences

BELTON Daniel
LAITY Peter

University of Reading, Polymer Science Centre, Whiteknights, Reading

DAVIS Fred J.
MITCHELL Geoffrey R.
OLLEY Robert H.

List of Performed Experiments

2010 (first half year)

Proposal	Proposer	Institution	Country	Title	Research Field
20095008	TURKOVIC Aleksandra	Ruder Bošković Insitute, Zagreb	Croatia	Study of polymer electrolyte for Zn rechargeable nano-structured Galvanic Cells via combined in-situ SAXS/DSC/WAXD measurements	Materials Science
20095009	BULJAN Maja	Ruder Bošković Insitute, Zagreb	Croatia	Ordering of QDs in amorphous matrices by ion-beam irradiation	Materials Science
20095025	HOLY Vaclav	Charles University, Prague	Czech Republic	Grazing-incidence diffuse scattering from ferro-magnetic MnAs precipitates in GaAs	Materials Science
20095029	JUNGNIKL Karin	AAS, IBN, Graz	Austria	In-situ study of the co-assembly of surfactant micelles and silica precursor during hydrolysis and ageing of precursor solutions	Materials Science
20095072	NAGY Gergely	Institut Laue-Langevin	France	Structural parameters and flexibility of the multilame-llar thylakoid membranes	Life Sciences
20095085	SCHAFLER Erhard	Uni. Vienna, Inst. for Material Physics	Austria	Existence and kinetics of dislocation generation in semicrystalline gamma phase isotactic polypropylene (gamma-iPP) by in-situ WAXS and SAXS deformation	Materials Science
20095122	CALLIGARIS Sonia	Uni. Udine, Dip. di Scienze degli alimenti	Italy	Study on the physical structure of self-assembly structures formed by monoglycerides for food application by using synchrotron XRD analysis	Life Sciences
20095129	SINTUREL Christophe	Uni. Orleans, Dep. Matiére Divisée	France	GISAXS study of the self organisation of polystyrene-b-polylactide in thin films upon solvent exposure	Chemisty
20095155	JAKSIC Milko	Ruder Bošković Insitute, Zagreb	Croatia	Morphology of ion tracks in SrTiO3, SiO2 and (Ge+SiO2)/SiO2 multilayer	Materials Science
20095160	BALDRIAN Josef	Czech Academy of Sciences, Inst. of Macromole-cular Chemi-stry, Prague	Czech Republic	Kinetics of intercalation and de-intercalation induced by secondary crystallization and melting in PEO-b-PPO-b-PEO/organoclay nanocompo-sites	Materials Science
20095161	MARMIROLI Benedetta	Austrian Academy of Sciences (AAS), Institute of Biophysics and Nanosystems Research (IBN), Graz	Austria	Sub millisecond time-resolved SAXS studies of calcium carbonate formation in presence of additives	Materials Science
20095175	CAMPI Gaetano	C.N.R. - Istituto di Cristallografia, Monterotondo / Rome	Italy	Liquid crystal template for silver nanoparticle superstructures	Chemisty
20095214	MITCHELL Geoffrey	Uni. Reading, Dept. of Physics	United Kingdom	Defining crystal morphology using self-assembling additives	Materials Science

20095283	CIASCA Gabriele	Uni. Rome "La Sapienza", Dep. of Physics	Italy	Shape variations of ferritin as a function of the aluminium and iron content	CIASCA Gabriele
20095327	BIANCONI Antonio	Uni. Rome "La Sapienza", Dep. of Physics	Italy	Tau polymerization in to PHF in the presence of methylene blue	Materials Science
20095368	LUGHI Vanni	Uni. Trieste, Dep. of Materials and Applied Chemistry	Italy	Characterization of 3D close-packed semiconductor nanocrystal assemblies and of multiphase nanostructured materials by means of static and time-resolved SWAXS	Materials Science
20095395	ARUMUGAM Mahendrasin-gam	Uni Keele, Dept. of Physics	UK	Investigation of the blooming in chocolate using time resolved SAXS/WAXS techniques	Life Sciences
20095430	ZIDANSEK Aleksander	Institute Jozef Stefan, Ljubljana	Slovenia	SAXS study of ferrofluid-liquid crystals mixtures	Materials Science
20095465	SCHMIDT Thomas Jr.	Uni. Bremen, Inst. for Solid State Physics	Germany	Ordering of Pt nanoparticles on functionalized self-assembled monolayers	Materials Science
20095470	SCHMIDT Wolfgang	Max Planck Institute for Coal research, Muehlheim / Ruhr	Germany	Cryogenic Argon adsorption and room temperature vapor adsorption on CMK-5 type carbon investigated by in-situ SAXS	Materials Science
Inhouse Research	YAMADA Kazuhito	AAS, IBN & Uni. Helsinki, Viikki Drug Discovery & Development Technology Center	Austria & Finland	Characterization of a new ocular drug delivery system with SAXS	Life Sciences
Inhouse Research	DUBCEK Pavo	Sincrotrone & Ruder Bošković Insitute, Zagreb	Italy & Croatia	Structural study of pulsed laser deposited GaAs	Materials Science
Inhouse Research	JUNGNIKL Karin	AAS, IBN, Graz	Austria	The initial stages of mesophase formation in silica aerosol particles during evaporation induced self assembly (EISA)	Materials Science
Inhouse Research	RADIC Nikola	Sincrotrone & Ruder Bošković Insitute, Zagreb	Italy & Croatia	GISAXS and XRR characterization of the W/C multilayers	Materials Science

2010 (second half year)

Proposal	Proposer	Institution	Country	Title	Research Field
20095344	GUPTA Ajay	Inter Uni. Consortium for DAE Facilities, University Campus, Indore	India	Interface effects in structural transformation and melting of Langmuir-Blodgett films using depth resolved in-plane diffraction measurements	Materials Science
20100039	CARACCIOLO Giulio	Uni. Roma "La Sapienza", Dip. di Chimica	Italy	Nanostructure of a Novel Multicomponent Envelope-type Nanoparticle System (MENS) for Gene Delivery	Life Sciences
20100057	TURKOVIC Aleksandra	Ruder Bošković Insitute, Zagreb	Croatia	Study of Polymer Electrolyte for Zn Rechargeable Nanostructured Galvanic Cells via Combined in Situ SAXS/DSC/WAXD Measurements	Materials Science

20100075	ADDIEGO Frederic	Research Center "Henri Tudor", Dep. of Advanced Materials & Structures, Esch-sur-Alzette	Luxembourg	Cavitation kinetic of semi-crystalline polymers revealed by time-resolved small-angle x-ray scattering	Materials Science
20100087	BELTON Daniel	Uni. Huddersfield, School of Applied Sciences	United Kingdom	SAXS Studies of Novel Internally Supported Liposomes	Life Sciences
20100094	RADIC Nikola	Ruder Bošković Insitute, Zagreb	Croatia	GISAXS and XRR characterization of the W/C multilayers	Materials Science
20100168	SCHMITT Mechthild	Uni. Helsinki, Viikki Drug Discovery and Development Technology Center, Helsinki	Finland	In situ SAXS characterization of injectable ocular drug delivery systems	Life Sciences
20100193	HAZRA Satyajit	Saha Institute of Nuclear Physics, Surface Physics Division, Kolkata	India	Substrate effects on the formation of CTAB-silica mesostructured films	Materials Science
20100196	BOURGAUX Claudie	C.N.R.S. - Uni. Paris Sud	France	Interaction of a new anticancer prodrug with lipid model membranes	Life Sciences
20100237	MARMIROLI Benedetta	AAA, IBN, Graz	Austria	Sub millisecond time-resolved SAXS studies of calcium carbonate formation in presence of additives	Materials Science
20100238	AMENITSCH Heinz	AAA, IBN, Graz	Austria	In situ formation of hierarchical structures in mesoporous materials by the aerosol route	Materials Science
20100262	PIVAC Branko	Ruder Bošković Insitute, Zagreb	Croatia	Si quantum dots production in silicon nitride/Si and silicon nitride/Ge multilayers: process characterization and optimization	Materials Science
20100271	BULJAN Maja	Ruder Bošković Insitute, Zagreb	Croatia	Influence of ion type on properties of quantum dot lattices formed by ion beam irradiation	Materials Science
20100290	MEDUNA Mojmir	Masaryk Univ., Dep. Condensed Matter Physics, Brno	Czech Republic	Study of oxygen precipitation in Czochralski silicon annealed by Tabula Rasa using SAXS	Materials Science
20100354	MARIANI Paolo	Univ. Politecnica delle Marche, Sez.Scienze Fisiche, Ancona	Italy	Pressure effects on amyloid fibrils and oligomers of alpha-synuclein: a SAXS investigation on their dissociation and reversible nature	Life Sciences
20100409	TRIMMEL Gregor	Techn. Uni. Graz - Inst. for Chem. and Technology of Organic Materials	Austria	Investigation on the self assembly and thermal conversion processes to mesoporous metal sulfide layers for photovoltaic applications - A time resolved GISWAXS study	Materials Science
20100410	GOMES Maria	Uni. Minho, Physics Dep.	Portugal	GID and GISAXS investigations of flash memory structures based on semiconductor nanocrystals	Materials Science
20100417	PABST Georg	AAA, IBN, Graz	Austria	In Situ Study of Sphingomyelinase Activity in Plasmamembrane Mimetics	Life Sciences
20100436	GRACIN Davor	Ruder Bošković Insitute, Zagreb	Croatia	Origins of quantum confinement effects in thin film solar cells materials - extension of previous experiments	Materials Science
20100458	DURACCIO Donatella	CNR di Pozzuoli, Inst. of Chemistry & Polymer Technology	Italy	Shear-Induced Isothermal Crystallization of Isotactic Polypropylene (iPP) based Nanocomposites with Montmorillonite (MMT)	Materials Science

Inhouse Research	MILITA Silvia	C.N.R. , Inst. IMM, Bologna	Italy	In-situ study of amyloid peptide self-assembly process in micro-confined environments	Life Sciences
Inhouse Research	AMENITSCH Heinz & BUCAK Seyda	AAA, IBN, Graz &Yeditepe Uni., Dep. of Chemical Engineering	Austria &Turkey	Peptide Nanotube Dissolution Kinetics	Life Sciences
Inhouse Research	RAPPOLT Michael & FEHR Sonja	AAA, IBN, Graz & Inst. für Pharmazeutische Technologie - Techn. Uni. Braunschweig	Austria & Germany	Studies on the mechanism delaying the polymorphic transition of solid triglyceride drug carrier nanoparticles	Life Sciences
Inhouse Research	AMENITSCH Heinz & TEIXEIRA Cilaine Veronica	AAA, IBN, Graz & Uni. Barcelona, Dep. of Medicine, Biophysics Unit	Austria & Spain	Study of saponins micellar behaviour and their interaction with membranes; as a way to understand their imunological and/or toxic effects mechanism	Life Sciences
Inhouse Research	AMENITSCH Heinz & DA ROS Tatiana	AAA, IBN, Graz & Uni. Trieste, Dip. di Scienze Farmaceutiche	Austria & Italy	From SAXS to cellular uptake: CNT interactions with lipids	Life Sciences

User Statistics

1. Number of submitted proposals and assigned shifts from 1995 until December 2011

The Austrian SAXS-beamline at ELETTRA opened to users in September 1996. Since then many experiments have been performed related to the fields of life science, materials science, physics, biophysics, chemistry, medical science, technology and instrumentation.

The assignment of beamtime at this beamline is done separately for the group of "General Users" (GU) and the "Collaborating Research Group" (CRG), i.e., the Austrian users. Beamtime was assigned to the proposals of each group in the order of the rating received by the Scientific Committee, and up to the maximum number of shifts available to each group according to the contract between "The Austrian Academy of Sciences" and the "Sincrotrone Trieste". Until December 1997 up to 30 % of the beamtime was given to CRG, up to 55 % to GU, and 15% was reserved for maintenance purposes. From January 98 to June 2001 the quota for beamtime was up to 35 % for CRG, up to 50 % for GU, and again 15% reserved for maintenance purposes. From July 2001 on the two contingents for user proposals from CRG and GU receive up to 35% of the beamtime each. The remaining 30 % of beamtime are used for inhouse research projects as well as for maintenance purposes.

Figure 1 gives an overview of the numbers of received proposals, the numbers of requested and assigned shifts, as well as the percentage between assigned and requested shifts during the last years. As can be seen in Fig.1, the request for beamtime at the SAXS-beamline increased strongly until the first half year of 1999. Then, probably due to the high rejection rates, the number of submitted proposals decreased somewhat during 2001, which resulted in a better ratio of accepted / rejected proposals. This oscillating behaviour of beamtime request can also be seen for the period 2002 – 2011 where after higher numbers of submitted proposals slightly reduced request periods follow. The numbers for the second semester of 2007 and first of 2008 reflect also that, due to the long shut-down from 1.10.2007 to 3.03.2008 (for the new booster-electron-injector installation) less proposals were submitted, and less beamtime was available.

In 2010, in total 67 proposals (8 from CRG, and 59 from GU) were submitted. From these 21 GU proposals were submitted by "new" usergroups, i.e. groups which so far had never beamtime at the SAXS beamline. From these, 10 GU proposals were accepted by the review committee.

Figure 1 (Next page). The statistical information about the beamtime periods since end of 1995 are given for the groups "CRG", and "GU" separately, as well as for both together ("Total"). Shown are, for all beamtime periods (from top to bottom):
● Number of received proposals, ● Number of requested shifts,
● Number of assigned shifts, and ● Relation between assigned and requested shifts

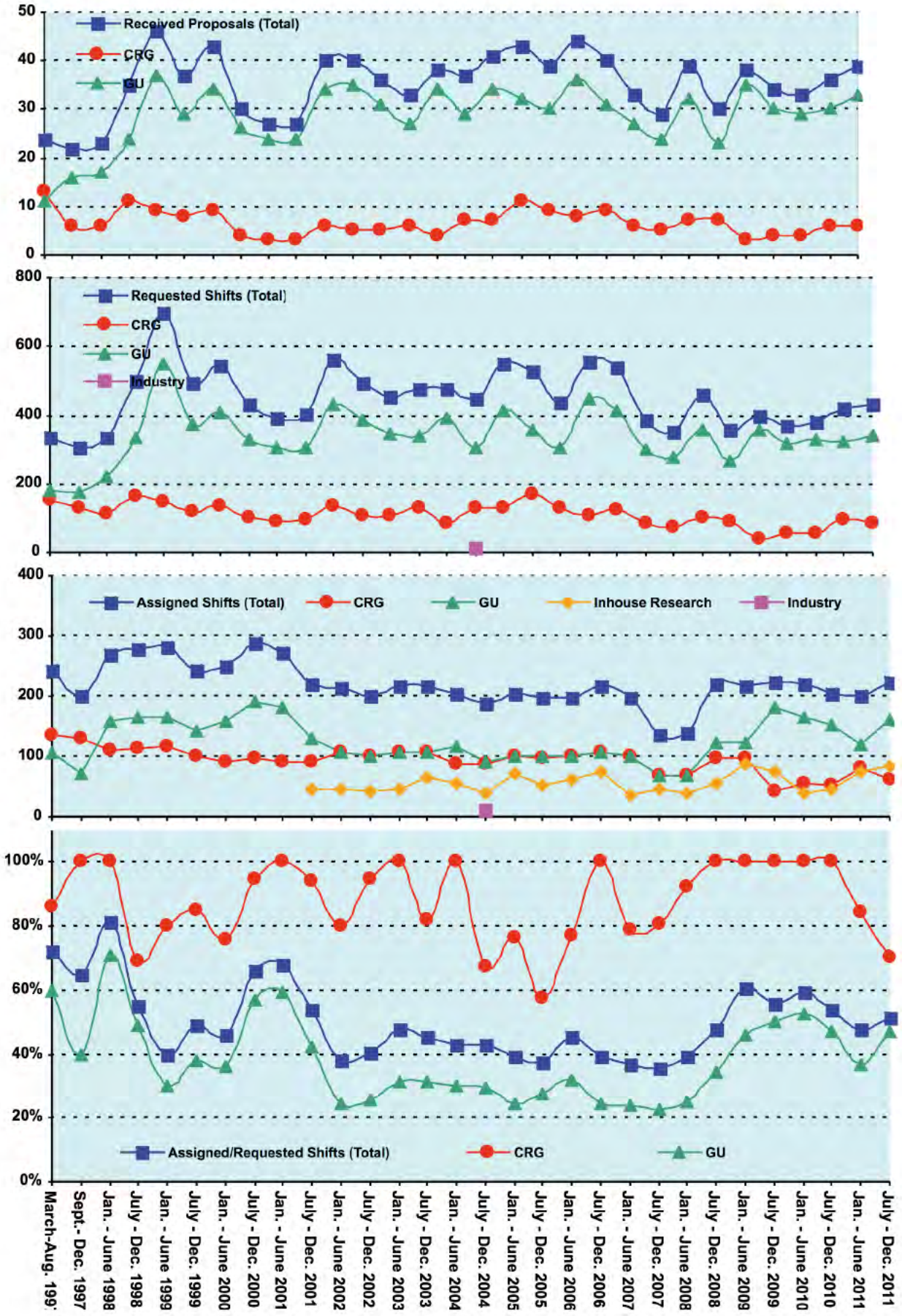
Received Proposals (Total)
CRG
GU
Requested Shifts (Total)
CRG
GU
Industry
Assigned Shifts (Total)
CRG
GU
Inhouse Research
Industry
Assigned/Requested Shifts (Total)
CRG
GU
March-Aug. 199
Sept.- Dec. 1997
Jan. - June 1998
July - Dec. 1998
Jan. - June 1999
July - Dec. 1999
Jan. - June 2000
July - Dec. 2000
Jan. - June 2001
July - Dec. 2001
Jan. - June 2002
July - Dec. 2002
Jan. - June 2003
July - Dec. 2003
Jan. - June 2004
July - Dec. 2004
Jan. - June 2005
July - Dec. 2005
Jan. - June 2006
July - Dec. 2006
Jan. - June 2007
July - Dec. 2007
Jan. - June 2008
July - Dec. 2008
Jan. - June 2009
July - Dec. 2009
Jan. - June 2010
July - Dec. 2010
Jan. - June 2011
July - Dec. 2011

2. Provenience of users

During 2010, 158 users from 59 institutes in 15 countries have performed experiments at the SAXS beamline. In Fig. 2 are shown both the provenience of these users, and of their respective institutes. Each user or institute was counted only once, even though many users performed experiments in both beamtime periods of 2010.

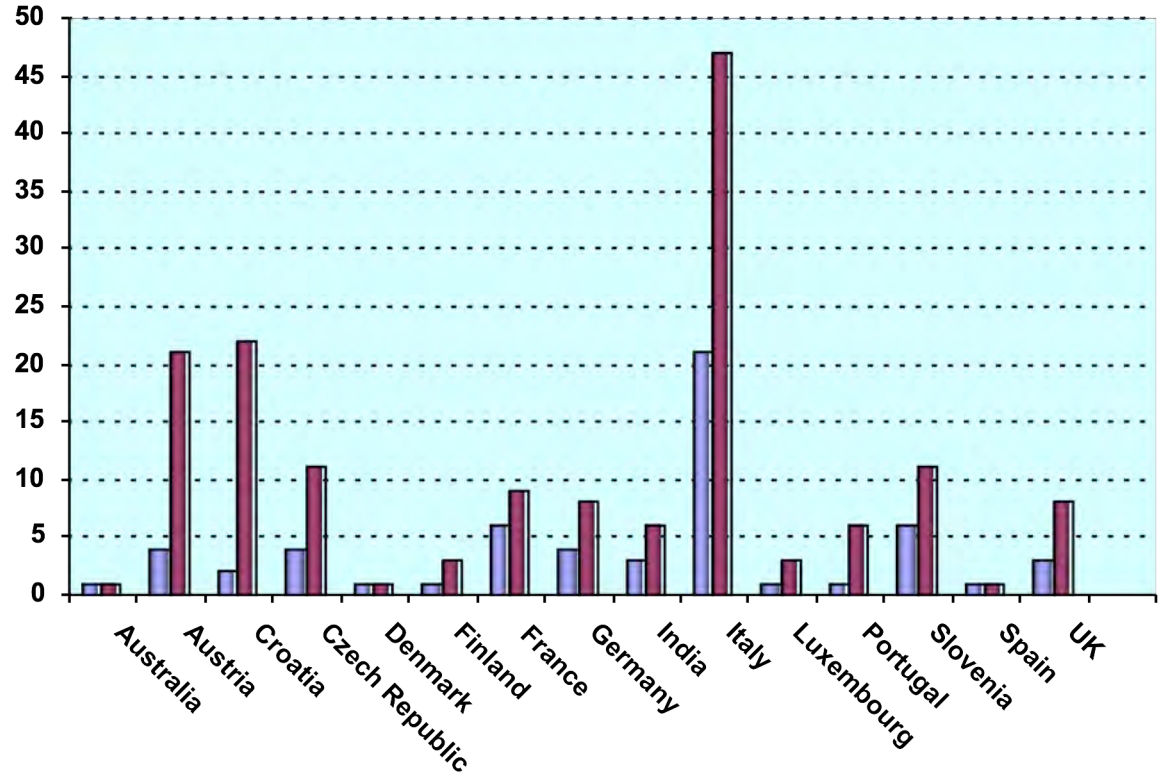

Figure 2. Nationality of the Austrian SAXS beamline users in the year 2010. The number of users (red) and the corresponding number of institutes (blue) are shown for each country.

3. Documentation of experimental results

As could be expected, with the start of user-operation at the SAXS-beamline the number of contributions to conferences started to increase strongly. With a delay of one year - the average time needed for paper publications - also the number of publications increased accordingly, as can be seen in Fig. 3.

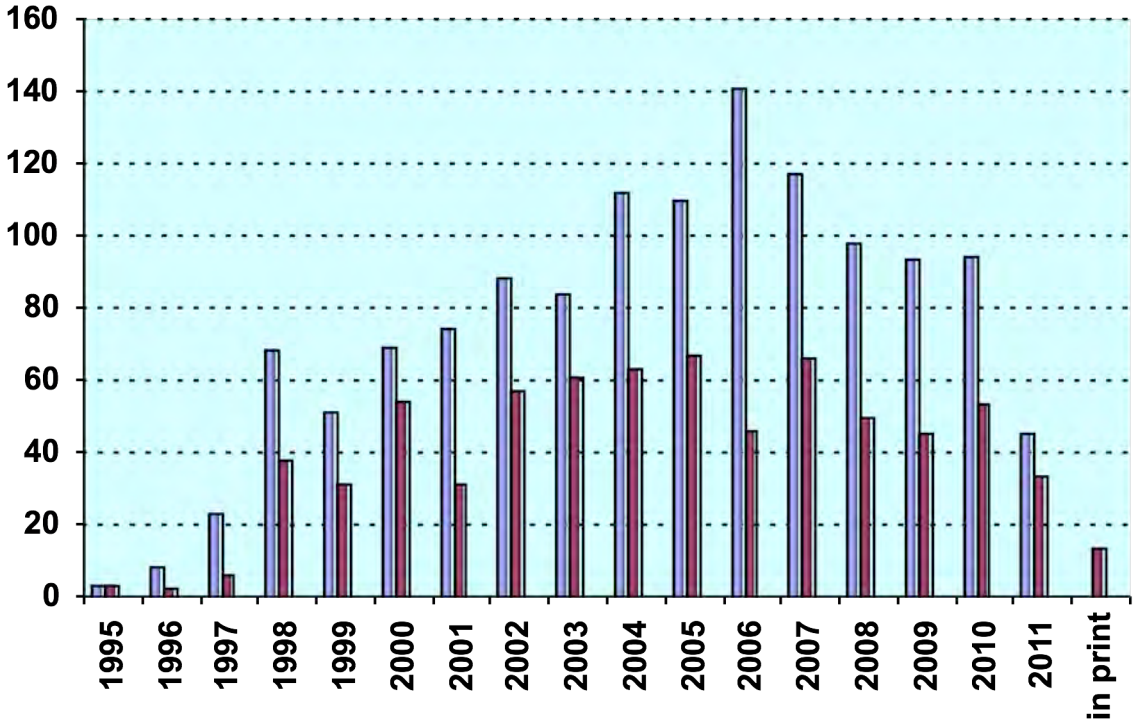

Figure 3. Number of conference contributions (blue) and of refereed paper publications (red) for the years 1995-2010. Also contributions, which have been published until June 2011 as well as those in print at that time are included.

In addition, from 1995 until June 2011, the following documentations based on instrumentation of the SAXS-beamline, or on data taken with it, have been produced:

Technical Reports on Instrumentation: 5
Contributions to Elettra Newsletters: 15
Contributions to Elettra Highlights: 35
Habil Thesis: 4
PhD Thesis: 89
Master Thesis: 43

Experimental Possibilities at the SAXS-beamline

1. NEW DEVELOPMENTS

Paste-Sample Holder

A new holder for gel- and paste-like samples with high viscosity has been designed (Fig. 1A). Samples are placed in a long hole within 1 mm thick steel plates which are closed in front and back with 25 µm thick mica windows by attaching them with a thin film of Baysilone-Paste (Bayer, Leverkusen, Germany). Finally, the sample plates are fixed between the sample holder body and cover piece by two screws (Fig. 1B). Leak tightness has been proved until 95 °C. The main advantages of the new cell are (i) easy and quick mounting of the sample, and (ii) the possibility to now assemble multiple samples in advance in the sample holder plates indepently of the sample holder in use.

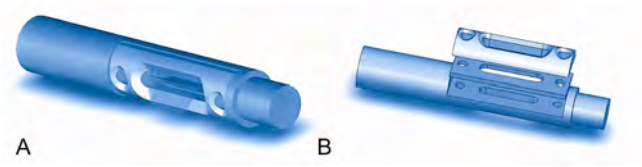

Figure 1. A: Assembled paste-sample holder. **B:** Exploded view drawing of the sample holder. From bottom to top the sample holder body, sample holder plate and the cover piece for closing are shown.

2. ACCESSIBLE SAXS AND WAXS RANGES

Simultaneous SAXS- and WAXS-measurements can be performed using a linear sensitive gas detector (Gabriel type, windows size 8 x 100 mm, active length 86.1 mm with a resolution of 0.135 mm/channel) for the WAXS-range, and either a second linear Gabriel type detector (windows size 10 x 150 mm, active length 134 mm with a resolution of 0.159 mm/channel), or the 2D CCD-system for the SAXS-range. A specially designed vacuum chamber (SWAXS-nose, see Annual Report of 1996/97, p. 32) allows to use both scattering areas below (for SAXS) and above (for WAXS) the direct beam, respectively.

Depending on the photon energy maximum SAXS resolutions of 2000 Å (5.4 keV), 1400 Å (8 keV) or 630 Å (16 keV) are available. The available possible WAXS-ranges are summarised in Table 1. The overall length of the SWAXS-nose in the horizontal direction, measured from the sample position, is 512 mm and the fixed sample to WAXS-detector distance is 324 mm. At the shortest SAXS camera-length an overlap in the d-spacings covered by the SAXS- and WAXS-detectors, respectively, is possible: then, the common regime lies around 9 Å.

Range	**2θ [deg]**	**d-spacing (Å)**		
		8 keV	5.4 keV	16 keV
1	9.4	*9.40*	14.03	4.27
	27.6	*3.23*	4.82	1.47
2	27.4	3.25	4.86	1.48
	45.6	1.99	2.97	0.90
3	45.4	2.00	2.98	0.91
	63.6	1.46	2.18	0.66
4	63.4	1.47	2.19	0.67
	81.6	1.18	1.76	0.54

Table 1. Possible d-spacing ranges in the WAXS-regime at the SAXS-beamline at ELETTRA. Since the WAXS-detector can be mounted at four different fixed positions on the SWAXS-nose (range 1-4), with the three possible energy choices (5.4, 8 and 16 keV) this results in 12 different d-spacing regimes. In italic the most common choice (8 keV, range 1) is highlighted. This range is suited for experiments, e.g., on lipid-systems and (bio)polymers.

3. CALIBRATION OF THE S-AXIS AND FLAT FIELD CORRECTION

At the SAXS beamline various standards are used for the angular (s-scale) calibration of the different detectors:

- Rat tail tendon for the SAXS detector - high resolution (rtt*.dat)
- Silver behenate for the SAXS detector – medium and low resolution (agbeh*.dat)
- Para-bromo benzoic acid for the WAXS detector – WAXS range 1 and 2 (pbromo*.dat)
- Combination of Cu, Al foils and Si powder for the WAXS detector – WAXS range 2 and higher

In Figure 1 a typical diffraction pattern of rat tail tendon is shown, depicting the diffraction orders (from the first to the 14th order) measured with a "high" resolution set-up (2.3 m) and the delay-line gas detector. The d-spacing is assumed to be 650 Å, but this value can vary depending on humidity up to 3%. Thus, the rat tail tendon is often used only to determine the position of the direct beam (zero order), while the absolute calibration is performed using the diffraction pattern of Silver behenate powder. Fig. 2 depicts a diffraction pattern of Silver behenate measured with "medium" resolution set-up (1.0 m) from the first to the 4th order (repeat spacing 58.4 Å) [1].

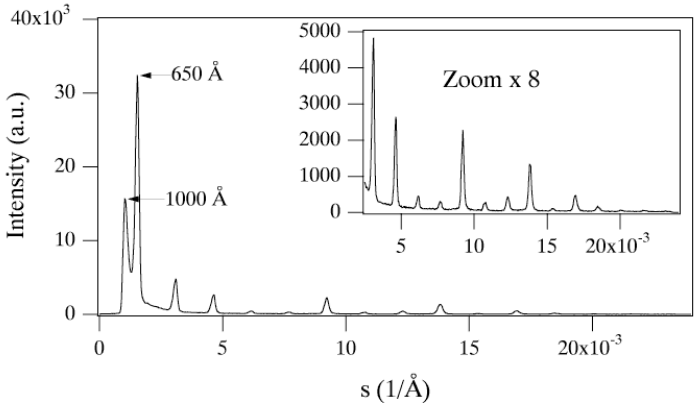

Figure 1. SAXS diffraction pattern of the collagen structure of rat tail tendon fibre at a distance of 2.3 m

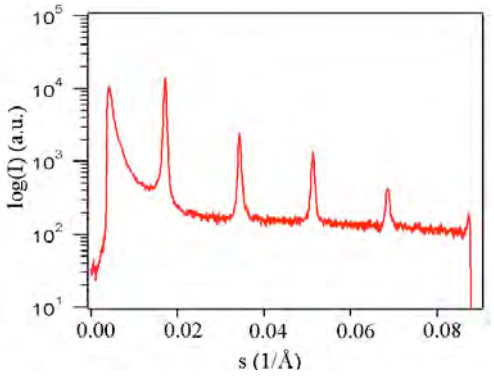

Figure 2. SAXS diffraction pattern of Ag behenate powder at a distance of 1.0 m

In Figure 3 a typical WAXS pattern of p-bromo benzoic acid is shown. The diffraction peaks are indexed according to the values given in Table 2, taken from [2].

d-spacing/Å	rel. intensity	d-spacing/Å	rel. intensity
14.72	18000	4.25	490
7.36	1200	3.96	2380
6.02	330	3.84	10300
5.67	980	3.74	26530
5.21	6550	3.68	1740
4.72	26000	3.47	760

Table 2. d-spacings and relative intensities of p-bromo benzoic acid according to [2].

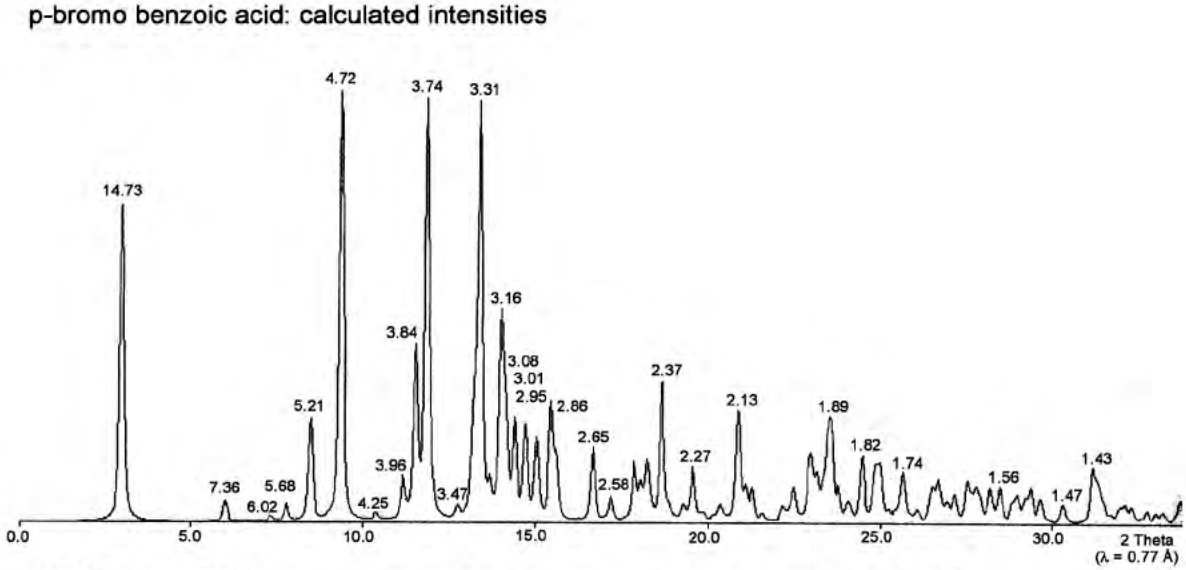

Figure 3. Calculated diffraction pattern of p-bromo benzoic acid. d-spacings are given in Å.

The s-scale for both, the SAXS and the WAXS range, can be obtained by linear regression, i.e., the linear relation between the known s-values of the calibrant versus the measured peak positions has to be found.

A further correction is regarding the flat field response (efficiency) of the detectors. For this correction, the fluorescence light of various foils are used to illuminate the detectors rather homogeneously:

At 8 keV: iron foil (100 µm thick), fluorescence energy: 6.4 keV K_α, 7.1 keV K_β (effic*.dat)
At 16 keV: copper foil (> 100 µm thick), fluorescence energy: 8.028 keV $K_{\alpha 2}$, 8.048 keV $K_{\alpha 1}$, 8.905 keV K_β (effic*.dat)

The measured scattering pattern are corrected for the detector efficiency simply by dividing them by the fluorescence pattern. Note: The average of the detector efficiency data should be set to unity and a small threshold should be applied to avoid any division by zero.

[1] T.N. Blanton et. al., Powder Diffraction 10, (1995), 91
[2] K. Ohura, S. Kashino, M. Haisa, J. Bull. Chem. Soc. Jpn. 45, (1972), 2651

4. AVAILABLE SAMPLE MANIPULATIONS STAGES

1. General

Usually the sample is mounted onto the sample alignment stage which allows the user to place the sample into the beam with a precision of 5µm (resolution: 1µm). In Fig. 5 the ranges for vertical and horizontal alignment as well as the maximum dimensions of the sample holders are given. The maximum weight on the sample stage is limited to 10 kg. In case the envelope dimensions of a sophisticated sample station provided by the users are slightly larger than those given in Fig. 5, the user can ask the beamline responsible for a check up of his space requirements. If it does not fit at all to these specifications, user equipment can also be mounted directly onto the optical table, which allows much larger spatial dimensions.

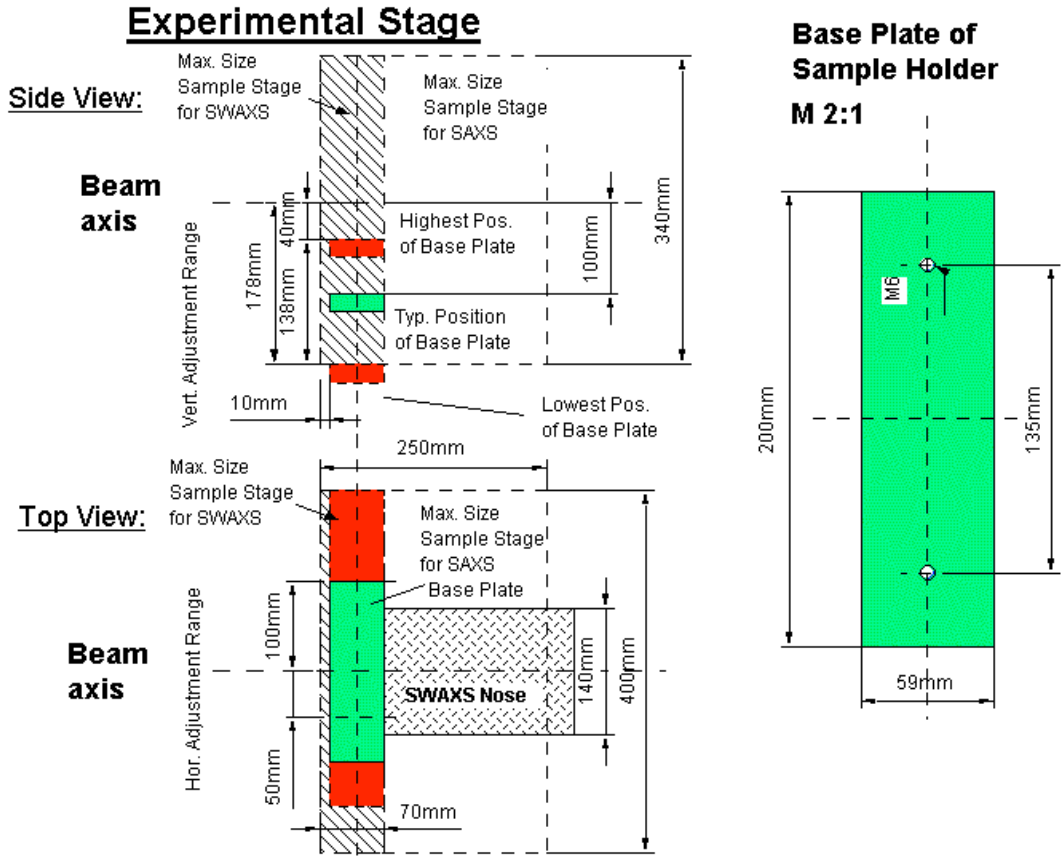

Figure 5. Maximum dimensions and alignment range of the sample holder to be mounted via a base-plate onto the standard alignment stage (left), and dimensions of the base-plate (right).

2. Sample Holders

As standard equipment for liquid samples Paar capillaries (diameter: 1 and 2 mm) are used thermostated with the KPR (Peltier heating/cooling) sample holders (Anton Paar, Graz, Austria). For use in these sample holders flow through capillaries and Gel holders are standard equipment. Temperature scans can be performed with KPR (-30-70 °C). Typically the precision and the stability of this systems is 0.1 °C. Additionally thermostats for temperature control or cooling proposes can be used at the beamline (-40 - 200 °C). Helium and Nitrogen gas bottles are available at the beamline, for other gases please contact the beamline responsible.

Multiple-sample holders can be mounted onto the standard sample manipulator. At present holders are available for measuring in automatic mode up to 30 solid samples at ambient temperature or up to 4 liquid or gel samples in the temperature range 0 – 95 °C.

3. Online Exhaust System

At the experimental station is available a custom-built fume cover and chemical exhaust system for toxic gases. Thus it is possible to e.g. study in-situ chemical reactions, during which toxic gases might develop.

4. Stopped Flow Apparatus

A commercial stopped flow apparatus (manufactured by Bio-Logic, Paris, France), especially designed for Synchrotron Radiation SAXS investigations of conformation changes of proteins, nucleic acids and macromolecules, is available. The instrument consists of a 4-syringe cell with 3 mixer modules manufactured by Bio-Logic. Each syringe is driven independently from the others by an individual stepping-motor, which allows a high versatility of the mixing sequence (flow-rate, flow duration, sequential mixing). For example, injection sequences using one or up to 4 syringes, unequal filling of syringes, variable mixing ratio, reaction intermediate ageing in three- or four-syringe mode etc.. The solution flow can be entirely software-controlled via stepping motors, and can stop in a fraction of a millisecond.

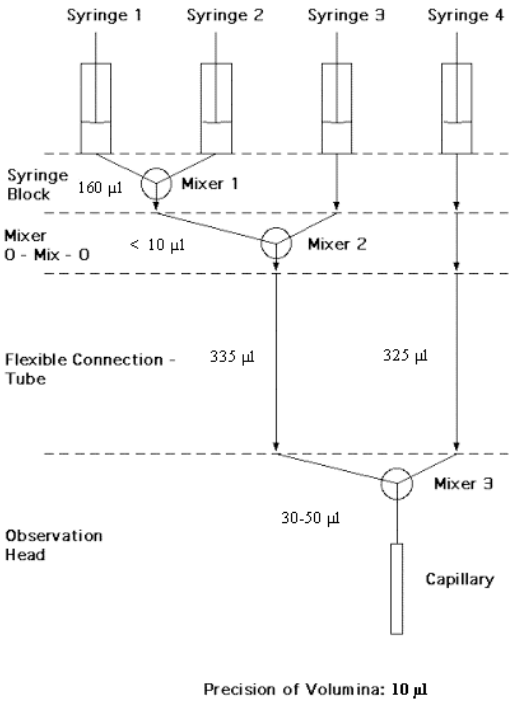

The software allows the set-up of the shot volumes of each of the 4 syringes in a certain time interval. Up to 20 mixing protocols can be programmed. Additionally macros for the repeated execution of individual frames can be defined. Furthermore, the input and output trigger accessible for user operation can be programmed. In the usual operation modus the start of rapid mixing sequence is triggered from our X-ray data-acquisition system (input trigger).

After the liquids have been rapidly mixed, they are filled within few ms into a 1 mm quartz capillary - situated in the X-ray beam- , which is thermostated with a water bath. Depending on the diffraction power of the sample time resolutions of up to 10 ms can be obtained.

Figure 6. Sketch of the stop flow system.

The main parameter of the system are:

- Thermostated quartz capillary (1 mm)
- Temperature stability 0.1 °C
- Total sample used per mixing cycle (shot volume): 100 µl
- Maximum 2θ angle of 45°
- Total Volume 8 ml
- Dead volume 550 µl
- Flow rate: 0.045 – 6 ml/s
- Duration of flow 1 ms to 9999 ms/Phase
- Dead time: 1 ms
- Reservoir volume: 10 ml each

Further information can be found at the webpage: http://www.bio-logic.fr/

5. Grazing Incidence Small Angle X-ray Scattering

Grazing incidence studies on solid samples, thin film samples or Langmuir-Blodget-films can be performed using a specially designed sample holder, which can be rotated around 2 axes transversal to the beam. Furthermore the sample can be aligned by translating it in both directions transversal to the beam. The precisions are 0.001 deg for the rotations and 5 µm for the translations. Usually the system is set to reflect the beam in the vertical direction. According to the required protocol and the actual assembly of the rotation stages ω, θ, 2θ and φ scans can be performed.

6. Temperature Gradient Cell

A temperature gradient cell for X-ray scattering investigations on the thermal behaviour of soft matter manybody-systems, such as in gels, dispersions and solutions, has been developed. Depending on the adjustment of the temperature gradient in the sample, on the focus size of the X-ray beam and on the translational scanning precision an averaged thermal resolution of a few thousands of a degree can be achieved.

7. Flow-through Cell

The flow through cell works in a simple manner: Special quartz capillaries (Glas Technik & Konstruktion, Schönwalde/Berlin) of 1.5 mm diameter and wide openings of about 3 mm at each end, can be inserted into the standard Anton Paar sample holder, which allows various temperature treatments (T-range 25-300 or –30-70 °C, respectively). Thin tubes are connected directly to the capillary ends and a constanst flow is achieved by a peristaltic pump.

8. IR-Laser T-Jump System for Time-Resolved X-ray Scattering on Aqueous Solutions and Dispersions

The Erbium-Glass Laser available at the SAXS-beamline (Dr. Rapp Optoelektronik, Hamburg, Germany) delivers a maximum of 4 J per 2ms pulse with a wavelength of 1.54 μm onto the sample. The laser-beam is guided by one prism onto the sample, which is filled in a glass capillary (1 or 2 mm in diameter) and Peltier or electronically thermostated in a metal sample holder (A. Paar, Graz, Austria). With a laser spotsize of maximal 7 mm in diameter a sample-volume of maximal 5.5 μl or 22 μl, respectively, is exposed to the laser-radiation. In a water-solutions/dispersions with an absorption coefficient of A = 6.5 cm^{-1} T-jumps up to 20°C are possible.

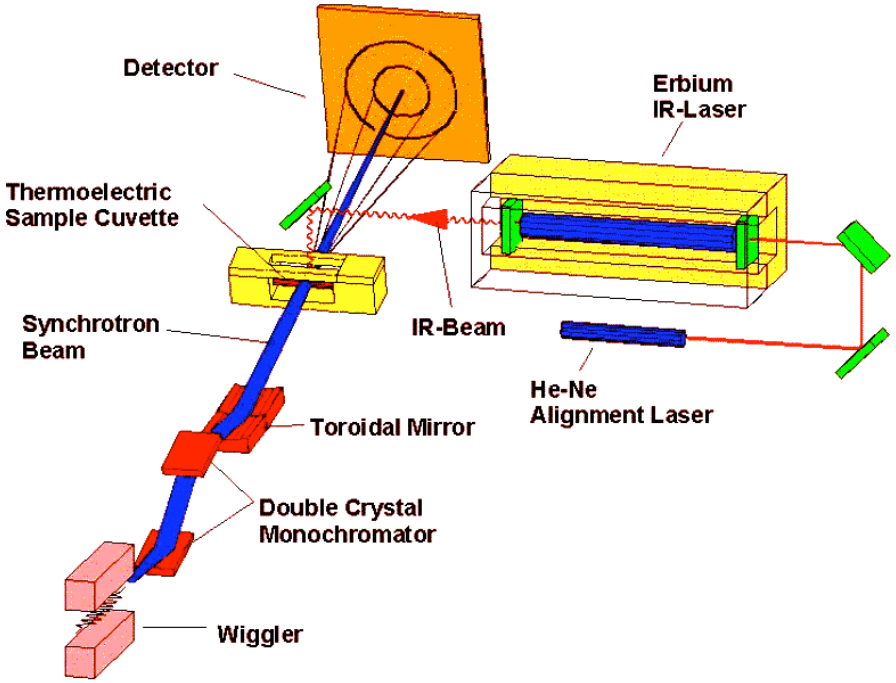

Figure 7. Sketch of the T-jump set-up.

9. High Pressure Cell System

SWAXS measurements of samples under pressure can be performed from 1 to 2500 bar, from 0 to 80 °C in the scattering angle region up to 30 degrees, both in the static or time-resolved mode, e.g. p-jump or p-scan, with a time-resolution down to the ms range. Precise pressure scans of any speed within a broad range (e.g. ca. 1.0 bar/s - 50 bar/s in the case of water as pressurising medium, and a typical sample volume) can be performed. Alternatively, dynamic processes can be studied in pressure-jump relaxation experiments with jump amplitudes up to 2.5 kbar/10ms in both directions (pressurising and depressurising jumps).
In most applications diamond windows of 0.75 mm thickness (each) are used. The transmission of one pair (entrance and exit window) is 0.1 at 8 keV, i.e. lower than 0.3, the value for the originally used 1.5 mm thick Be-windows. However the loss in intensity is more than compensated for by the considerably lower background scattering of diamond thus leading to higher q-resolution in the experiments.
The sample thickness can be 0.6-4.0 mm, with a volume of approximately 0.5-3 mm^3 completely irradiated by pin-hole collimated (< 1.0 mm diameter) X-rays.

The pressure cell system is flexible and can be built according to the needs of the particular experiment. Normally, a liquid (water, ethanol or octanol) is used as pressurising medium. But in principle, also gaseous media can be employed as well. N_2 has been successfully tested, and measurements in supercritical CO_2 became frequent.
Beside bulk measurements on samples in transmission set-up, also grazing incidence experiments using silicon wafer with highly aligned samples on its surface inserted in the high-pressure cell have been carried out successfully.

10. Oxford Cryostream Cooler

The Cryostream cooler creates a cold environment only a few millimeters from the nozzle position. The temperature and the flow of the nitrogen gas stream is controlled and regulated by a Programmable Temperatur Controller based on an 'in stream' heater and a thermo-sensor before it passes out over the sample.

The system has been especially developed for X-ray crystallography to perform diffraction experiments on e.g. shock frozen bio-crystals. However, the programmable temperature controller allows further implication for SAXS-experiments, e.g., rapid temperature drops in solvents. The design of the Cryostream Cooler facilitates:

- Nitrogen stream temperatures from -190 to 100 °C
- Stability of 0.1 °C,
- Refill without any disturbance of the temperature at the sample
- Temperature ramps can easily be carried out remotely controlled with scan rates up 6 °C/min
- Individual temperature protocols can be cycled
- T-jumps in both directions can be performed by rapid transfer of the sample in a pre-cooled or -heated capillary using an fast syringe driver reaching a minimum temperature of -80 °C. Here, typical scan rates are about 15 °C/sec with a total process time in the order of 10 sec.

Further information can be found at the webpage: http://www.oxfordcryosystems.co.uk/

11. In-line Differential Scanning Calorimeter (DSC)

The in-line micro-calorimeter built by the group of Michel Ollivon (CNRS, Paris, France) allows to take simultaneously time-resolved synchrotron X-ray Diffraction as a function of the Temperature (XRDT) and high sensitivity DSC from the same same sample.
The microcalorimetry and XRDT scans can be performed at any heating rate comprised between 0.1 and 10 °C/min with a 0.01 °C temperature resolution in the range -30/+130 °C. However, maximum cooling rates are T dependent and 10°C/min rates cannot be sustained below 30°C since cooling efficiency is a temperature dependent process. Microcalorimetry scans can be recorded independently, and also simultaniously, of X-ray patterns. The microcalorimeter head can also be used as a temperature controlled sample-holder for X-ray measurements while not recording a microcalorimetry signal. Isothermal microcalorimetry is also possible when a time dependent thermal event such as meta-stable state relaxation or self-evolving reaction, is expected. The sample capillaries have a diameter of 1.5 mm and are filled over a length of 10 mm.

12. Tension Cell

Together with the external user group Schulze-Bauer/Holzapfel the research team constructed a general-purpose tension cell. This particular cell was designed for *in-situ* tensile testing with the particular feature that the sample could be completely immersed in a solvent (e.g. physiological solution), which is of particular interest for the blood vessel or collagen fiber testing. The sample container can be attached to a thermal bath to control the temperature in the range from 5 to 95 ºC. A screw with an appropriate opening for the passage of the X-ray beam can adjust the optical thickness of the sample container continuously and optimize the set-up for different sample geometries.
The fully remote controlled system allows to control not only the fiber extension from 0 to 50 mm, but also it records simultaneously the force signal in the range from 0 to 25 N and as an option the optically determined Video extensometer signal to measure the transversal contraction of the sample.

13. Larger experimental hutch

After the prolungation of the experimental hutch by about 3m we have now the possibility to e.g. permanently install a diffractometer (roll on/roll off), or a micro focus set-up, which delivers focal spot sizes down to 10 μm and thus will allow for micro spot scanning SWAXS experiments with a new X-Y scanning stage.
On the other hand we can increase the sample to detector distance and therefore improve our minimum SAXS resolution or maximise the flux density at the sample position for certain experiments. Nevertheless this prolongation of the experimental hutch will ensure the sustainable development of the beamline also in the future by giving us the opportunity to realize new optical concepts, e.g. new mirrors, Fresnel or refractive lenses.

5. AVAILABLE DETECTORS

1. 2D Image Plate

The Mar300 Image Plate detector with a circular active area of 300mm in diameter is the largest-area detector available to users of the beamline, with a spatial resolution (pixel size) of 150μm. This detector has two modes of operation (180mm or 300mm), depending on the desired active area, which result in image sizes of 1200x1200 and 2000x2000, respectively. They are stored in the mar image format (16 bit for compactness, with higher precision extensions for values out of range), and can be processed and converted using the Fit2D program [1]. Typical applications are those that need a large Q-range with high dynamic range (typical values of 10^5), i.e. solution scattering from proteins and nanoparticles, temperature-step scans, slow processes like nanoparticle formation, mesophase formation, etc. The exposure time for the Image Plate is given in seconds, with typical values between 1 and 60. Readout time depends on the chosen active area (for 180mm mode, about 130 seconds; for 300mm mode, about 210 seconds), and therefore it is not suitable for samples where high time resolution is needed. Exposure information, number of images in the series and other information is automatically written to a summary file after each image.
So far the detector cannot be triggered by an external trigger input. Controlling an additional (external) device or experiment can only be done by hardware wiring of the TTL shutter signal.

2. 2D Pilatus 100K Detector System

The Pilatus 100K detector system (http://www.dectris.com/sites/pilatus100k.html) operates in "single photon counting" mode and is based on the CMOS hybrid pixel technology: the X-rays are directly transformed into electric charge, and processed in the CMOS readout chips. This new design has no dark current or readout noise, a high dynamic range of 1000000 (20 bits), a read-out time of less than 3 ms, a framing rate of over 200 images/s and an excellent point spread function of < 1 pixel.

3. 2D CCD-Camera System

The CCD has a 115 mm diameter input phosphor screen coupled by means of a fiber optic to the image intensifier, which itself is coupled with an additional taper to the CCD (charged coupled device). The spatial resolution of a pixel is 79 μm. The number of pixels is 1024 x 1024 and they can be pinned down to 2 x 2 and 4 x 4. The dynamic range of the CCD is 12 bit. The dark current of the CCD is in the order of 100 ADU (off-set) and the readout noise (read out speed: 10 MHz) is in the order of 6 ADU. (The CCD is cooled by multistage Peltier element for reducing the dark noise.) The intensifier gain is adjustable between 200 and 20000 photons full dynamic range. Typical readout times and exposure times are 150 ms and 100 ms, respectively. The readout times can be reduced down to 100 ms by using the pinning mode of the CCD. Between the frames additional wait times can be programmed e.g. for reducing the radiation damage in the sample or to extend the time for measuring long time processes. For the external control a TTL trigger signal is provided (active low, when the CCD is accumulating an image), which is used to control the electromagnetic fast shutter of the beamline on one hand. On the other hand this signal can be used also to trigger processes as requested by the user.

The CCD is controlled by Image Pro+, which also includes some simple data treatment capabilities:

- flat fielding/background corrections
- enhanced filters and FFT
- calibration utilities (spatial and intensity)
- segmentation and thresholding
- arithmetic logic operations
- various measurements, like surface, intensity, counts, profiles
- advanced macro management

The data are stored in 12 bit – TIFF format and can be directly processed with FIT2D [1]

[1] A.P. Hammersley, "Fit2D: an introduction and overview", ESRF Internal Report, ESRF97HA02T, 1997
[2] http://www.esrf.eu/computing/scientific/FIT2D/

4. 1D Vantec Detector

The one-dimensional high count rate capable Vantec-1 Detector from BrukerAXS Inc. has an active area of 50 x 16 mm and reaches a spatial resolution of about 50 µm, which is smaller than the resolution obtained by the presently used Gabriel Type Gas detectors. Moreover its new gas amplification principle based on the Microgap technology [1] allows much higher count rates compared to the old system. Now the main limitation is the data acquisition system with its maximum integral count rate of about 1 MHz. In the present data acquisition system HCI (Hecus X-ray Systems, Graz, Austria) the detector has the following performance:

- Minimal time resolution: 11 µs
- Maximum No. of frames: 512 (depending on the no. of channels)
- Maximum integral count rate: 1 MHz

5. 1D Gabriel-type Detector System

Two Gabriel-type detectors are available, which have an active area of 100 x 8 mm and 150 x 8 mm, respectively. Both have 1024 pixels, and thus the corresponding spatial resolution is about 135 microns and 175 microns, respectlively. They can be used simultaneously, and are run with the data acquisition system HCI (Hecus X-ray Systems, Graz, Austria). This detector system has the following performance:

- Minimal time resolution: 11 microsec
- Maximum No. of frames: 512
- Maximum integral count rate: 40 kHz

6. OFFLINE SITE LABORATORIES

In August 2002 our new chemistry and X-ray laboratory went into operation. The 70 m^2 big laboratory is divided in two parts, in which the bigger share of 43 m^2 is occupied by the chemistry lab. This unit serves mainly for sample preparation and analysis for both, in house research and external SAXS user groups. In the X-ray laboratory the set-up of a SWAX camera for simultaneous small and wide angle scattering has been completed (Hecus X-ray Systems, Graz, Austria: www.hecus.at), which allows on-site testing of samples before moving on to the SR beamline. The chemistry lab is meanwhile equipped with:

- micro centrifuge (max. 13200 rpm; model 5415D from Eppendorf , Hamburg, Germany)
- Chemical fume hood, equipped with a carbon filter for general organic solvents (model GS8000 from Strola, Italy)
- vacuum drying oven (min. pressure 1 mbar; max. T: 200 °C, precision +/- 0.4°C; Binder WTB, Tuttlingen. Germany)
- balance (min.-max.: 0.001 - 220g; model 770 from Kern & Sohn, Balingen, Germany)
- Magnetic stirrer with heating plate and thermometer, temp max 260°C
- vortex for microtubes (model MR 3001 and REAX; both from Heidolph, Schwabach, Germany)
- two water baths :
  - Unistat CC, freely programmable in the range from -30 to 100°C (Huber, Offenburg, Germany);
  - Lauda M3, available for heating only (Lauda-Könighofen, Germany)
- ultrasonic bath with water heater (VWR International, Milano, Italy)
- Ultrasonic processor equipped with a 3 mm probe (Sonics VCX130, SY-LAB Geräte GmbH, Germany)
- HPLC pump, Pharmacia LKB; working range, 0,01-9,99 ml/min, 0,1-40MPa
- HPLC pump, Gilson 307; working range, 0,01- 5 ml/min, 0,1-60MPa
- three syringe pumps, low pressure; flow rate range, 1µl/hr – 2120 ml/hr
- four syringe pumps, high pressure: P max ~ 60 bar
- three high pressure infusion modules: P max ~ 690 bar

Further, four working benches (one with a water sink), two fridges (+ 4°C) and a separate freezer (- 20 °C), standard glassware, syringes and needles of different sizes, µ-pipettes (p10 - p100 - p200 - p1000), as well as some standard chemical reagents (e.g., chloroform, ethanol, methanol); deionized water (milli-RO and ultrapure milli-Q water) is available.

Figure 4. View of the Chemistry laboratory (left) and X-Ray laboratory (right).

User Contributions

Material Science

CAVITATION KINETIC OF SEMI-CRYSTALLINE POLYMERS REVEALED BY TIME-RESOLVED SMALL-ANGLE X-RAY SCATTERING

F. Addiego[1], S. Patlazhan[2], S. André[3], D. Ruch[1], V. Tonniazzo[1], Y. Rémond[4], and S. Bernstorff[5]

1.) Centre de Recherche Public Henri Tudor, Advanced Materials and Structures Department, 66 Rue de Luxembourg, Esch-sur-Alzette, Luxembourg
2.) Semenov Institute of Chemical Physics of Russian Academy of Sciences, 4 Kosygin Street, Moscow, 119991 Russian Federation
3.) Institut National Polytechnique de Lorraine, Laboratoire d'énergétique et de mécanique théorique et appliquée, 2 Avenue de la Forêt de Haye, 54504 Vandoeuvre-lès-Nancy, France
4.) University of Strasbourg, Institute of Solid and Fluid Mechanics, 2 Rue Boussingault, F-67000 Strasbourg, France
5.) Sincrotrone Trieste, Strada Statale 14, in AREA Science Park, 34149 Basovizza / Trieste, Italy

The main originality of this work was the investigation of cavitation mechanisms occurring in semi-crystalline polymers during complex loading programs (cyclic tension / compression, tension + compression + relaxation…). Indeed, using synchrotron radiation facilities, cavitation mechanisms in such materials were only studied during monotonous tensile loading [1,2]. In this work, we performed complex loading programs by means of a specific micro-tensile/compressive stage (Kammrath equipment), while cavitation mechanisms were investigated in real-time using the SAXS beamline of the Elettra synchrotron. We studied five polyethylene grades: HDPE-1 (Mw = 55,000 g/mol), HDPE-2 (Mw = 105,000 g/mol), UHMWPE (Mw = 5.000.000 g/mol), recycled HDPE-2, and recycled HDPE - 2 / vegetal fibers composite. We performed 37 mechanical tests and recorded 12,000 SAXS patterns by means of a Dectris 100K Pilatus 2D detector configured to provide scattering information in the range 40-800 angstroms.

A typical result is shown in Figure 1. In this example, HDPE-2 is deformed in tension until a viscoplastic deformation level of 7.5 % (stage A-C), then it was compressed until the stress level of -16.3 MPa (stage C-E). At the undeformed state (A), one notes the presence of a scattering ring resulting from the scattering of crystalline lamellae. The ring intensity is homogeneous demonstrating no preferential orientation at the undeformed state. When the yield point is reached (B), the formation of scattering lobs can be seen near the beam stop. This phenomenon is linked to the formation of cavities oriented perpendicular to the tensile direction. With increasing tensile deformation level up to 7.5 %, the scattering intensity of the cavities drastically increases and becomes much higher than the scattering intensity of the lamellae. As a result, the scattering intensity of the lamellae cannot be seen on SAXS pattern after image treatment. During the compressive stage (C-E), one first notes a weak but significant recovery of the cavities until the stress reaches 0 MPa. Indeed, the scattering intensity on SAXS pattern slightly decreases (C-D). When the stress becomes negative (D-E), the recovery of cavities seems to be more marked. At the higher compression level (E), the cavities are almost totally recovered, residual cavities are however present. We also observed that the cavitation kinetics are markedly influenced by the molecular weight (the higher the molecular weight, the lower the cavitation) and by the presence of vegetal fibers (cavitation is due to fiber / matrix dedonding instead of matrix cavitation as in neat materials).

All the results are currently under examination and will probably lead to at least two scientific papers in high-impact journals. It is anticipated that the scattering signal will be carefully analyzed in terms of shape and structure factors and that a volume variation of the material will be calculated from the scattering intensity of the cavities [2]. This experimental volume variation will be compared to our theoretical prediction of volume variation of semi-crystalline polymers [3,4]. Note that first results of the present work were presented at an international Conference devoted to material science [4].

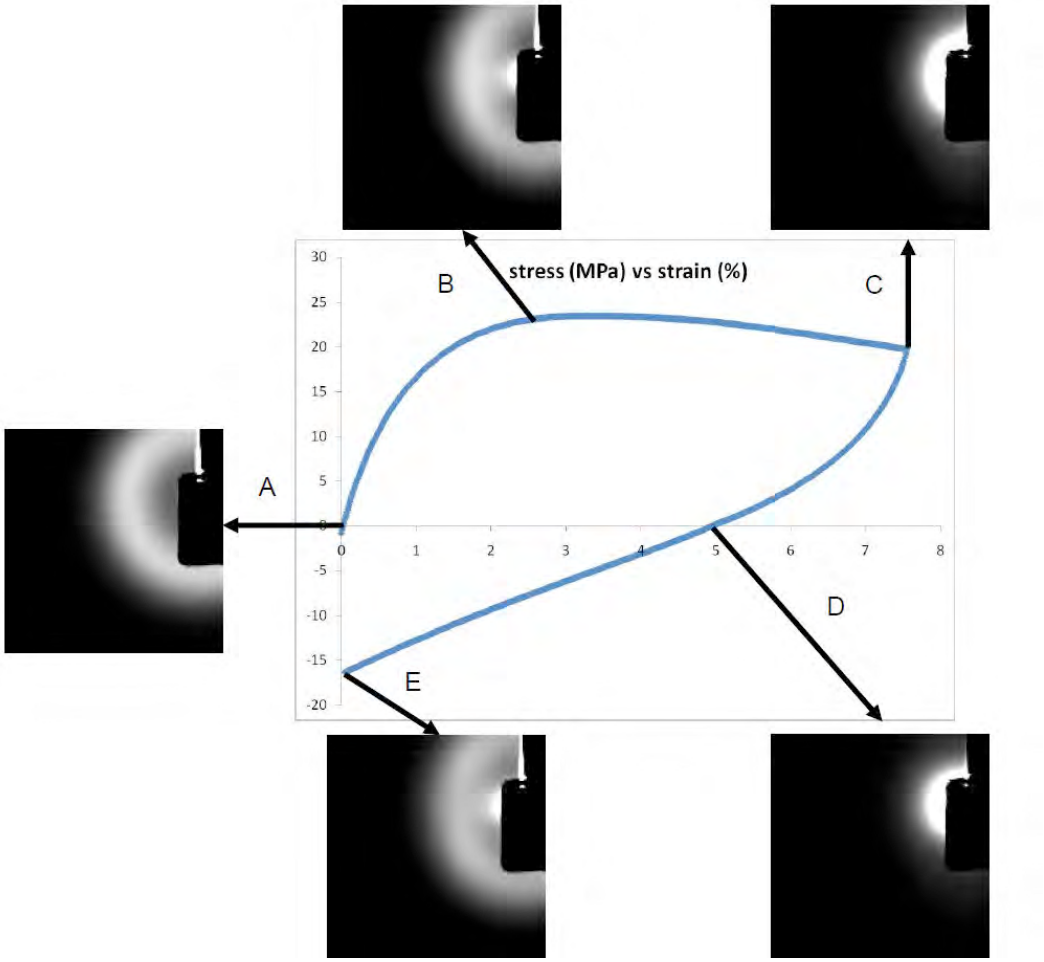

Figure 1. Typical stress – strain curve of HDPE-2 (reference LyonDellBasell GD7255) including a tensile stage (A to C) and a compression stage (C to E) with SAXS patterns recorded in real-time displaying cavitation kinetic (room temperature, 5 µm/s); note that tensile direction is horizontal on SAXS patterns

References:

[1] M.F. Butler, A.M. Donald, and A.J. Ryan; Time resolved simultaneous small- and wide-angle X-ray scattering during polyethylene deformation. II. Cold drawing of linear polyethylene; Polymer, **39**, 39-52 (1998)

[2] S. Humbert, O. Lame, J.M. Chenal, C. Rochas, and G. Vigier; New Insight on Initiation of Cavitation in Semicrystalline Polymers: In-Situ SAXS Measurements; Macromolecules; **43**, 7212-7221 (2010)

[3] S. Patlazhan, K. Hizoum, and Y. Remond; Stress-Strain Behavior of High-Density Polyethylene below the Yield Point : Effect of Unloading Rate; Polym. Sci. Ser. A; **50**; 507-513 (2008)

SELF-ASSEMBLY OF QUANTUM DOTS IN AMORPHOUS SYSTEMS

M. Buljan[1], U.V. Desnica[1], I. Bogdanović-Radović[1], M. Karlušić1, N. Radić[1], S. Bernstorff[2] and V. Holý[3]

1.) Ruđer Bošković Institute, Bijenička cesta 54, Zagreb, Croatia
2.) Sincrotrone Trieste, SS 14 km163,5, 34012 Basovizza, Italy
3.) Charles University in Prague, Ke Karlovu 5, 121 16Prague, Czech Republic

The investigation of semiconductor quantum dots (QDs) formation and ordering is very important due to the very interesting properties of QD-containing materials and the large range of possible applications. Especially interesting are quantum dots formed by ion-beam assisted self-assembly ion amorphous wide-bandgap matrices. It is well known that such systems have a narrower distribution of sizes and mutual distances of QDs. Therefore materials containing self-assembled QDs have many possible applications in different nanotechnology fields.

We have demonstrated recently two efficient methods for the production of ordered QD arrays [1,2]. The first method (self-assembling growth type) is based on temperature driven nucleation and surface morphology effects that occur during the film growth. The second method (ion-beam assisted self-assembly) consists in the interaction of an ion beam with a multilayer causing a regularly ordering of the QDs along lines in the irradiation direction.

We have used the GISAXS technique to make a comparative analysis of the structural properties of quantum dot lattices formed by the two production methods mentioned above in $(Ge+SiO_2)/SiO_2$ multilayer systems. For that purpose, films containing twenty $(Ge+SiO_2)/SiO_2$ periods were deposited onto fused quartz substrates. For the self-assembling growth, the films were deposited at 500 ^oC, while for ion beam assisted self assembly the deposition was done at room temperature. After the deposition the film deposited at RT was irradiated by 3MeV O^{3+} ions. Both films were annealed at 800 ^oC for 1 h in vacuum.

The structural analysis of the films was performed by combination of the transmission electron microscopy (TEM) and grazing incidence small angle X-ray scattering (GISAXS) methods. A TEM image of the film produced by self-assembled growth and the corresponding GISAXS image are shown in Figs.1 (a) and (b) respectively. Bragg spots due to correlation in the positions of the quantum dots are visible in the GISAXS map. We performed a numerical analysis of the measured GISAXS data using the procedure described in Ref. [1]. The simulated GISAXS map is shown in Fig. 1(c). An analogue procedure was performed for the ion-beam irradiated film. The ordering along the irradiation direction is nicely visible in the Fourier transform of the TEM image shown in Fig. 1(d), and in the GISAXS map of the film (Fig. 1(e), where a tilted Bragg sheet appears.

The size distributions of the Ge quantum dots formed in the films are shown in Fig. 2(a). For the calculation of the size distributions we have used the parameters obtained from the fitting of the GISAXS data. The widths of the distributions are approximately the same, while slightly larger quantum dots were found in the irradiated film. The size obtained for that film is expectably larger due to a slightly larger Ge content in that film. The optical properties of the films are shown in Fig. 2(b). From the figure is evident that the absorbance curve for the film obtained by self-assembling growth starts from larger energies. That result is in accordance with the size-dependence quantum confinement effect which predicts a larger band gap for smaller QDs.

In summary, we have compared the structural and optical properties of $(Ge+SiO_2)/SiO_2$ multilayer films prepared by two different techniques. We have shown that both methods result in relatively narrow size distributions, but the mean QD size is different due to the different Ge content in the films after deposition at different temperatures. The optical properties of the film are different indicating a large influence of the QD size on it via

quantum confinement effects. More details about the mentioned properties are given in Ref. [3].

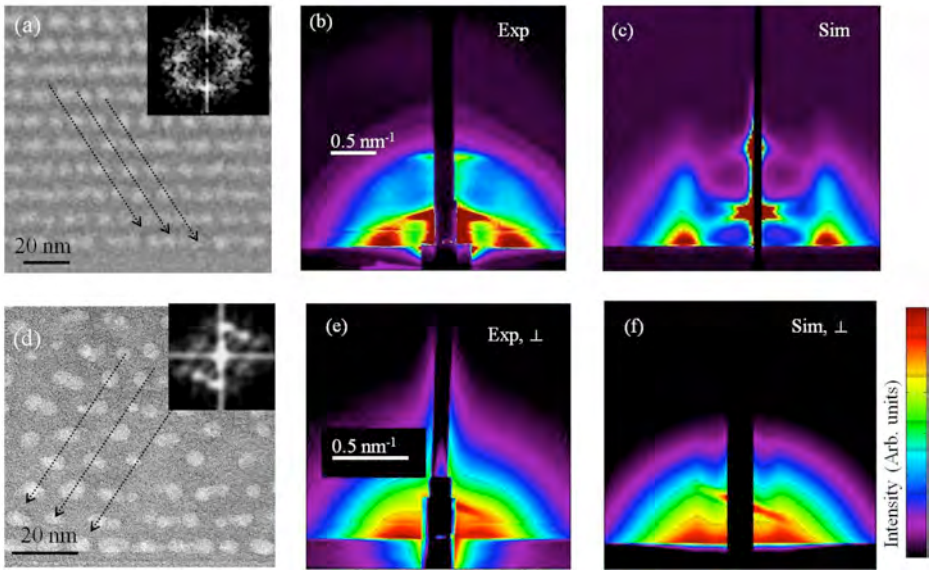

Figure 1. (a) TEM image of the film produced by self-assembling growth. (b), (c) GISAXS maps of the film produced by self-assembling growth and corresponding simulation respectively. (d) TEM image of the film produced by ion-beam irradiation of amorphous multilayer (e), (f) The corresponding GISAXS map and its simulation respectively. The ordering direction is indicated by arrows.

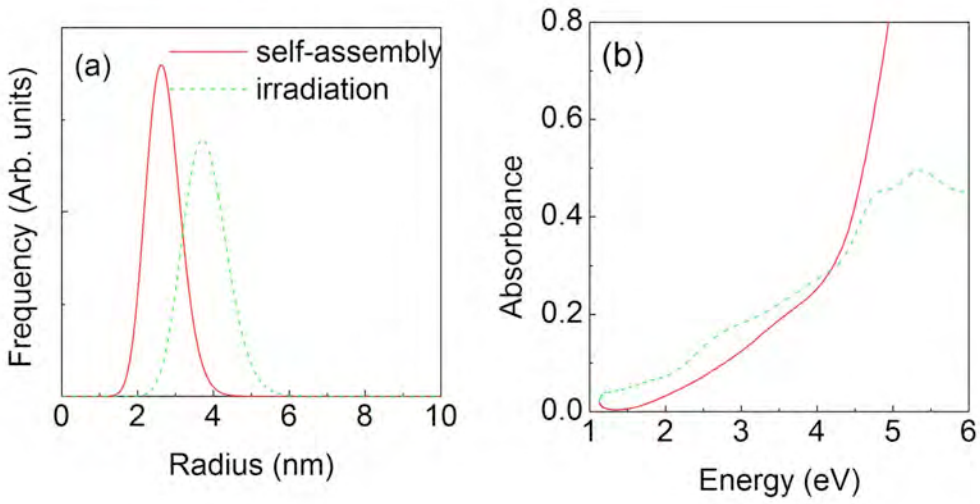

Figure 2. (a) Size distributions of the Ge quantum dots formed in $(Ge+SiO_2)/SiO_2$ multilayers by self-assembled growth and by ion beam irradiation. (b) Absorption spectra of the films prepared by self-assembled growth and by ion beam irradiation in the UV/VIS range.

References:

[1] M. Buljan, U.V. Desnica, G. Dražić, M. Ivanda, N. Radić, P. Dubček, K. Salamon, S. Bernstorff, V. Holý; Phys. Rev. B **79**, 035310 (2009)

[2] M. Buljan, I. Bogdanović-Radović, M. Karlušić, U.V. Desnica, G. Dražić, N. Radić, P. Dubček, K. Salamon, S. Bernstorff, V. Holý. Appl. Phys. Lett. 95,063104, (2009)

[3] M. Buljan, U.V. Desnica, I. Bogdanović-Radović, N. Radić, M. Ivanda, G. Dražić, Bernstorff, T V. Holý, Vacuum , in press (2011)

THE INFLUENCE OF RIPPLED SUBSTRATES ON THE SELF-ASSEMBLY OF QUANTUM DOTS

M. Buljan[1], N. Radić, J. Grenzer[2], A. Mucklich[2], S. Bernstorff[3] and V. Holý[4]

1.) Ruđer Bošković Institute, Bijenička cesta 54, 10000 Zagreb, Croatia
2.) Helmholtz Zentrum Dresden-Rossendorf, 01328 Dresden, Germany
3.) Sincrotrone Trieste, SS 14 km163,5, 34012 Basovizza, Italy
4.) Charles University in Prague, Ke Karlovu 5, 121 16 Prague, Czech Republic

Semiconductor quantum dots (QDs) embedded in a wide band gap amorphous matrix such as Ge dots in amorphous SiO_2 have attracted a lot of attention recently because of their interesting properties and prospective application in photonics and photovoltaic devices. In our previous paper [1], we improved the periodicity of the dot positions by growing $(Ge+SiO_2)/SiO_2$ multilayers by magnetron sputtering. However, in these previous studies, the multilayers were deposited on a flat Si or glass substrate. Consequently, only a short-range ordering of the QDs could be achieved so that the ordered QD arrays appeared in small randomly oriented domains, each ordered domain consisting of only few QDs. During the last year we have demonstrated for the first time with a deposition of an amorphous multilayer on a periodically corrugated—rippled substrate, that the corrugation periodicity overcomes the above mentioned problem. In particular, we observed the formation of a three-dimensional (3D) QD lattice, where the arrangement of the QDs within the layers follows very well the substrate geometry. The inner structure of the quantum dots formed by this method can be easily controlled and tuned from amorphous to crystalline by the annealing procedure.
For that purpose, films containing five, ten and twenty $(Ge+SiO_2)/SiO_2$ periods were deposited onto periodically corrugated (rippled) and on flat Si(111) substrates. The deposition was performed simultaneously on both types of substrates by magnetron sputtering. Figure 1 shows an AFM picture of a corrugated surface, which was used as a substrate for the multilayer deposition and the basic idea of the experiment. From the Fourier transformation (FT) of the picture (inset of Fig. 1a) we determined the corrugation period of ripples to be (19 ±2) nm.

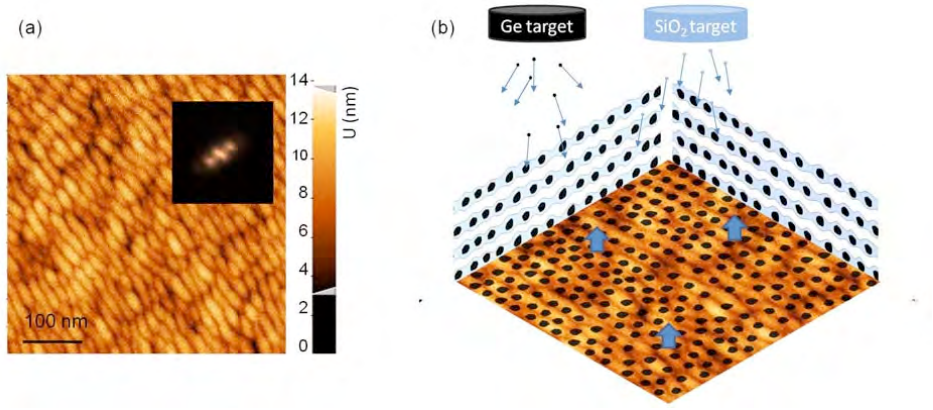

Figure 1. (a) The atomic-force microscopy picture of a rippled Si surface along with its Fourier transformation (in the inset). (b) Schematic drawing of the magnetron sputtering deposition process of a multilayer on the rippled surface. The growth direction is indicated by wide arrows.

The structural analysis of the films was performed by combination of the transmission electron microscopy (TEM) and grazing incidence small angle X-ray scattering (GISAXS) methods. The TEM micrograph of the multilayer containing 20 periods, taken in the direction perpendicular to the ripples direction is shown in the left side of Fig. 2. From the TEM image follows that the QDs form in the valleys between the ripples, so they follow the substrate morphology. The correlation of the dot positions at different interfaces (indicated by dashed

lines in Fig. 2) is visible in the whole depicted sample area showing that the dots form a large three-dimensional QD lattice. This effect is especially well visible in the FT of the TEM image where asymmetrically arranged distinct spots are visible. The FT of the TEM cross-section made in direction parallel to the ripples (see Ref. [2]) also shows distinct spots that are arranged symmetrically. Such correlation properties, which are different for different cross-section directions, indicate that indeed the QDs are ordered within one large domain, while for the case of deposition on the flat substrate, ordered regions appear only in small randomly oriented.

The regularity of the quantum dots positions is nicely visible in the GISAXS maps of the films, shown in right side of Fig. 2. The GISAXS data shown there have been obtained at the synchrotron Elettra, Trieste, SAXS beamline, using a photon energy of 8 keV, and two-dimensional photon detectors. The GISAXS map of the rippled substrate (indicated by SUBSTRATE in Fig. 2) prior to deposition shows only two lateral streaks originating from the periodicity of the ripples. After the deposition of a 5 bi-layer film a beautiful GISAXS intensity distribution (indicated by 5 PERIODS) is obtained showing that the formed QDs follow the morphology of the rippled substrate in their arrangement. Increasing the number of deposited layers to ten (indicated by 10 PERIODS in Fig. 2), the lateral features in the GISAXS images become slightly broader, showing a small increase in the QD position disorder with increasing layer number. We have performed a numerical analysis and fitted the 2D GISAXS maps obtained for different azimuthal directions of the probing beam and for films deposited on flat and rippled substrates (details are given in Ref [2]). From such analysis becomes visible that a rippled substrate improves the ordering of QDs and causes a narrowing of the size distribution of the QD array with respect to the one obtained for the case of a flat substrate.

Such QD array was used for the investigation of charge trapping properties of Ge QDs in SiO2 matrix [3], and there we have shown the important relation between charge trapping by Ge QDs or by surface / interface traps and annealing treatment of the films.

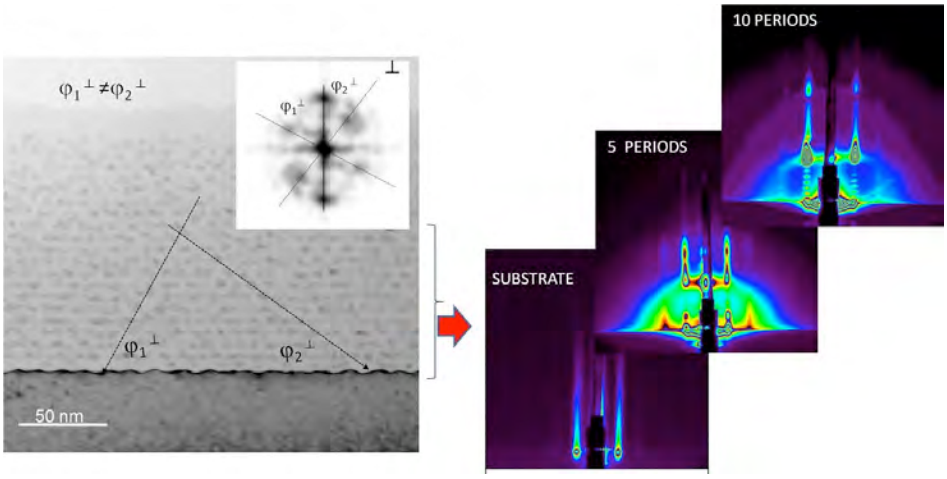

Figure 2. Transmission electron micrograph of the cross-section of a $(Ge+SiO_2)/SiO_2$ multilayer deposited on a rippled Si substrate taken in the direction across the ripples. The arrows indicate the correlations in the positions of the dots. The GISAXS maps were measured on the rippled substrate prior the deposition,and on multilayers containing 5 and 10 periods in the direction perpendicular to the ripples.

References:

[1] M. Buljan, U.V. Desnica, G. Dražić, M. Ivanda, N. Radić, P. Dubček, K. Salamon, S. Bernstorff, V. Holý; Phys. Rev. B **79**, 035310 (2009)

[2] M. Buljan, J. Grenzer, A. Keller, N. Radić, V. Valeš, S. Bernstorff, T. Cornelius, H. T. Metzger, V. Holý, Phys. Rev. B **82**, 125316 (2010)

[3] M. Buljan, J. Grenzer, V. Holý, N. Radić, T. Mišić-Radić, S. Levichev, , S. Bernstorff, B. Pivac, I. Capan; Appl. Phys. Lett. 97, 163117 (2010)

STUDY OF OXYGEN PRECIPITATION IN CZOCHRALSKI SILICON ANNEALED BY TABULA RASA USING SAXS

O. Caha[1], M. Meduňa[1], S. Bernatová[1], J. Růžička[1], P. Mikulík[1], J. Buršík[1], M. Svoboda[1], and S. Bernstorff[2]

1.) Masaryk University, Faculty of Science, Department of Condensed Matter Physics, Kotlářská 2, CZ-6113 Brno, Czech Republic
2.) Sincrotrone Trieste, SS 14 km 163.5, 34012 Basovizza (TS), Italy

We have studied a series of Si samples annealed using various temperature processes. The pieces cut from Si wafers were annealed at different nucleation temperatures (500 °C, 550 °C and 600 °C) and further at 800 °C and 1000 °C for various periods. Some of the samples were exposed to high temperature preanneal process called Tabula Rasa at 1150 °C for 3 minutes in order to eliminate the growth history of the ingot. We aimed to characterize the morphology of oxygen precipitates by SAXS and to determine the impact of high temperature preanneal on the precipitate growth.

Originally low boron doped 111 Si wafers 2 mm thick were cut and then annealed. From some samples stripes 10 x 2 mm^2 with a surface 220 were splitted. The samples had to be polished down to thickness between 0.1 and 0.2 mm since the transmission of Si at the used 8keV is quite low. Because of the potentially low signal, duplicates of the same samples were also enriched by copper in order to enhance the contrast between the SiO_2 clusters and Si matrix. The rough surface of the samples did not allow the measurement in reflection GISAXS geometry because the diffuse surface scattering in this setup dominates in the measured signal. The SAXS intensity maps were collected by the MAR image plate available at the beamline.

Since all the samples measured in this experiment were also investigated by infrared transmission spectroscopy and few of them also by SANS at ILL in Grenoble, typically two kinds of precipitate shapes were expected in the annealed samples. The more round sphere-like ones occupy a larger volume and they are smaller than the plate-like precipitates which volume ratio is much smaller. The plate-like precipitates have to be represented by streaks in the SAXS images.

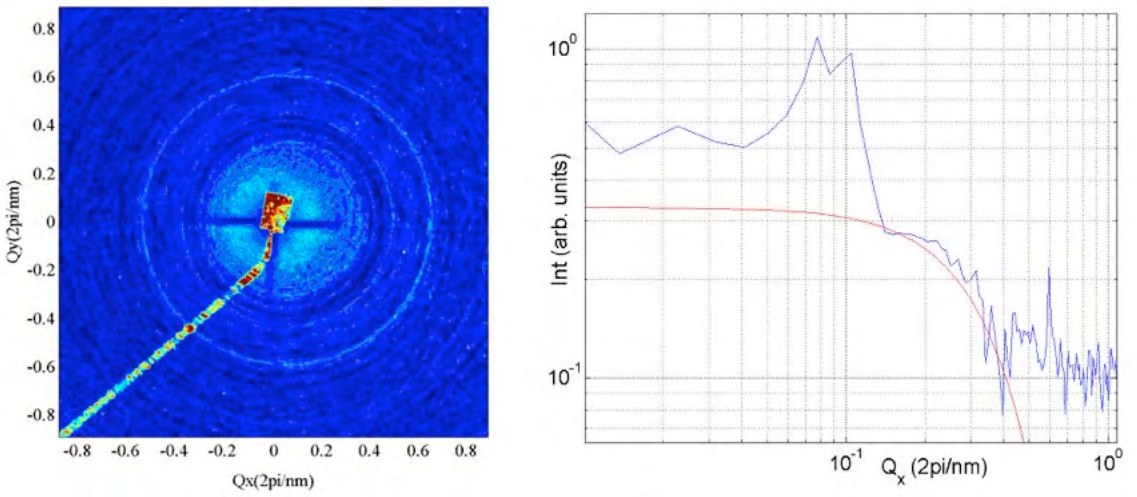

Figure 1. Scattering from a Si 111 wafer annealed at 600 °C/8h + 800 °C/4h + 1000 °C/16h and thinned down to 0.16 mm. The left panel shows the central part of the SAXS image and the right panel shows the loglog plot with the Guinier aproximation curve representing 6 nm clusters.

In this SAXS experiment, we have detected a very weak scattering from precipitates which seems to be more isotropic than anisotropic (see an example image in Figure 1). Due to the limited camera length, we could see scattering from clusters not larger than 10 nm. Typically the diameter of possible detected clusters varies from 5 nm to 10 nm. These clusters can represent a rest of the oxygen clusters after nucleation or voids created in Si wafer during the cooling process.
In some of the collected images streaks at various orientations were also detected, but the analysis did not confirm that they are originating from the plate-like clusters. Figure 2 presents an example of scattered intensity on a sample showing a streak where the defects in Si were decorated by Cu atoms. Similar images were obtained in samples without Cu atoms inside wafers. Isotropic scattering was detected in most of the measurement.
Since the scattered intensity is very low, the analysis of the data requires detailed mathematical processing and analysis. The effect of various temperature treatment is difficult to distinguish in this data due to low contrast between Si an SiO_2 and thus low scattered signal.

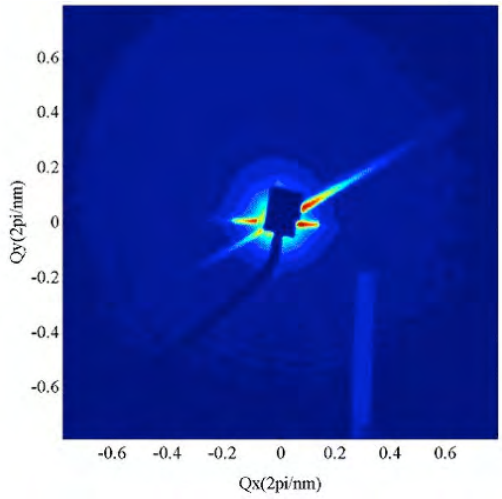

Figure 2. Scattering from a Si 220 wafer annealed at 600 °C/8h + 800 °C/4h + 1000 °C/24h, thinned down to 0.16 mm and decorated by Cu atoms in order to enhance the contrast of the clusters.

References:

[1] O. Caha, M. Meduňa, S. Bernatová, J. Růžička, P. Mikulík, J. Buršík, M. Svoboda, and S. Bernstorff, Extended abstract of SILICON 2010 conference: ISBN:978-80-254-7361-0

SUBSTRATE AND DRYING INDUCED CHANGE IN THE SHAPE OF MICELLES INSIDE CTAB-SILICA MESOSTRUCTURED FILMS

P. Chatterjee[1], S. Hazra[1] and H. Amenitsch[2]

1.) Surface Physics Division, Saha Institute of Nuclear Physics, 1/AF Bidhannagar, Kolkata 700064, India
2.) Institute of Biophysics and Nanosystem Research, Austrian Academy of Sciences, Schmiedlstrasse 6, 8042 Graz, Austria

Surfactant-templated mesostructured silica materials, discovered by Mobil researchers in 1992 [1], are the subject of intense research due to their potential applications as membranes, low dielectric-constant insulators (so-called low κ-materials), sensors, optoelectronic devices, etc. [2-4] In many applications, such materials often are required in the form of thin films, which can be grown by a procedure called evaporation-induced self-assembly (EISA) [2]. In the thin film form, film-substrate interaction and the subsequent drying with time can play an important role in controlling the structure of the film. The adsorption of surfactant molecules on solid surfaces in aqueous solutions suggests the strong role of the substrate surface condition, apart from concentration of the surfactant, in structure formation through different attachments [5]. The substrate surface condition can be modified through termination of the surface with OH or H groups, which essentially modifies the surface free energy or polar-nonpolar (hydrophilic-hydrophobic) or electrostatic nature of the surface [6-8]. However, not much work has been carried out to understand the role of such substrate surface conditions on the initial attachment of silica coated surfactant molecules, which can not only control the initial mesostructure [9] but also the final mesostructure of the film through subsequent drying. Moreover, understanding the role of alcohol on those structures and their control is very important, as it is known that alcohol can act as cosolvent or cosurfactant and can modify the mesostructure, accordingly [10].

In order to understand those issues, mesostructured films (by selecting fixed ratio of surfactant and silica) were prepared after adding different amounts of alcohol before spin coating on OH- and H-terminated Si substrates and were then characterized using complementary the x-ray reflectivity (XR) [8,11,12] and grazing incidence small angle x-ray scattering (GISAXS) [13,14] techniques. XR measurements were performed on a versatile x-ray diffractometer setup (D8 Discover, Bruker AXS at Saha Institute) [8] as a function of time (the first measurement of each sample was carried out 15 hours after the preparation) to see the effect of drying in the structure of the film. GISAXS measurements of the dried films were performed using a synchrotron source (SAXS beam line at Elettra) at an energy of 8 keV [15]. The scattered beam was detected using a 30 cm diameter (2000×2000 pixels) image plate detector (mar300, Marresearch GmbH), by placing it at about 90 cm downstream of the sample. For data collection, α was kept slightly greater (0.5-0.6°) than the critical angle α_c of the sample. The direct beam was stopped and the specular reflected beam was attenuated to avoid saturation of the detector.

A centered rectangular (*c*2*mm* space group) structure (Figure 1) is observed in dried films on both the substrates showing a clear deviation from a perfect 2D-hexagonal (*p*6*m*) structure. Such deviation (Figure 2) is directly related to the change in the shape of the micelles with or without silica coating layer inside the film. With time the silica materials try to squeeze due to drying, which can be expressed exponentially with a critical drying time of about 1 day. However, such squeezing is only allowed along the out-of-plane direction and not along the in-plane direction due to the attachment of the film on the substrate. Asymmetric squeezing makes the structure compressed and also creates stress. The latter deteriorates the ordering of the film. The compression depends on the silica wall thickness; the larger the thickness the larger is the compression. The silica wall thickness again depends on the amount of excess

alcohol. More we add the excess alcohol less is the thickness and hence the compression, which is clearly observed in the structure of the film. Excess alcohol not only acts as cosolvent as mentioned before, but also acts as cosurfactant. According to the latter, the size of the micelles increases exponentially in the measurement domain with a critical amount of excess alcohol of 15 cc. The analysis of the XR data measured in different time intervals and the GISAXS data measured on the dried films suggest that during deposition, cylindrically shaped micelles are circular on hydrophilic OH-Si substrates to form a perfect 2D-hexagonal structure (with $r_l/r_s \approx 1$), while elliptically on hydrophobic H-Si substrates to form compressed 2D-hexagonal structure (with $r_l/r_s \approx 1.1$). Such difference in shape is related to the different attachment of the film on the substrate, namely silica on OH-Si substrate and hemicylindrical micelles on H-Si substrate. For the dried films, maximum and minimum deformed structures (i.e. $r_l/r_s \approx 1.62$ and 1.35) are observed for the thick film on OH-Si substrate and for the thin film on H-Si substrate, respectively. However, considering the shape of the micelles, the maximum and minimum deformed shapes are predicted for the thick film on H-Si substrate and for the thin film on OH-Si substrate, respectively. Combining the initial shape and the effect of compression with time, which are related to the nature of the substrate and the amount of excess alcohol, respectively, final structures of the dried films along with the shape of the micelles are formed, which are of immense importance for their proper use as template and other applications.

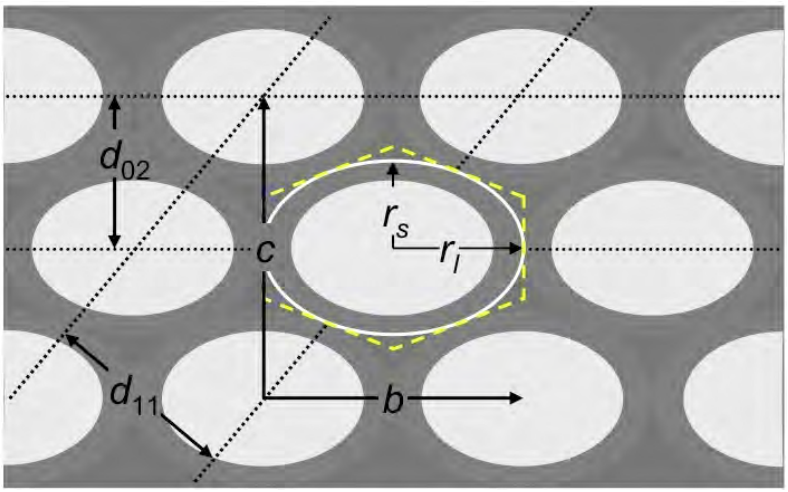

Figure 1. Schematic of a compressed 2D-hexagonal i.e. centered rectangular (*c*2*mm*) mesostructure with unit cell parameters (*b* and *c*), lattice spacing (d_{02} and d_{11}), Wigner-Seitz cell (yellow dashed lines) and corresponding ellipse (white curve) with semi-major (r_l) and semi-minor (r_s) axis.

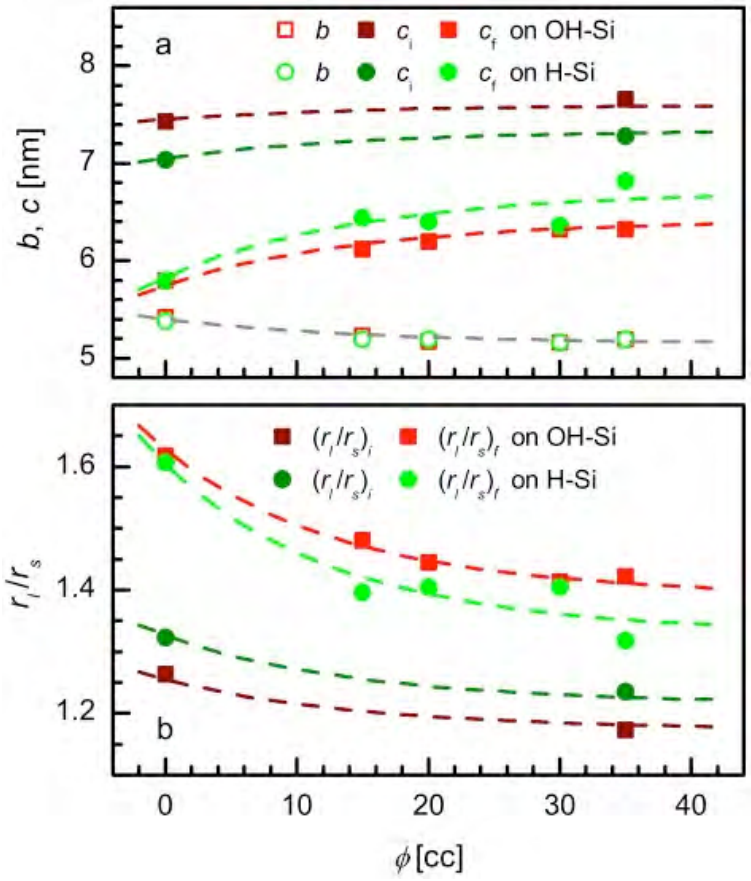

Figure 2. Influence of excess alcohol (ϕ) on (a) the in-plane (b) and out-of-plane (c) unit cell parameters of the compressed 2D-hexagonal structure and (b) the ratio of semi-major and semi-minor axis (r_l/r_s) of elliptical shaped micelles including silica coating layer for the films of different thickness on hydrophilic and hydrophobic Si substrates. Subscripts i and f represent parameters corresponding to the initial and final time of the measurements, respectively.

References:

[1] J. S. Beck et al.; J. Am. Chem. Soc. **114**, 10834 (1992)
[2] C. J. Brinker, Y. Lu and A. Sellinger, Adv. Mater. **11**, 579 (1999)
[3] S. Besson et al.; J. Mater. Chem. **13**, 404 (2003)
[4] L. Nicole et al.; J. Mater. Chem. **15**, 3598 (2005)
[5] M. J. Rosen; Surfactants and Interfacial Phenomena (John Wiley, NJ, 2004)
[6] H. F. Okorn-Schmidt; IBM J. Res. Dev. **43**, 351 (1999)
[7] X. G. Zhang; Electrochemistry of Silicon and its Oxide (Kluwer Academic, New York, 2004)
[8] J. K. Bal, S. Kundu and S. Hazra; Phys. Rev. B **81**, 045404 (2010)
[9] H. Yang et al.; J. Mater. Chem. **7**, 1285 (1997)
[10] D. A. Doshi et al; J. Phys. Chem. B, **107**, 7683 (2003)
[11] I. K. Robinson and D. J. Tweet; Rep. Prog. Phys. **55**, 599 (1992)
[12] X-Ray and Neutron Reflectivity: Principles and Applications; Eds. J. Daillant and A. Gibaud (Springer, Paris, 1999)
[13] A. Naudon and D. Babonneau; Z. Metallkd. **88**, 596 (1997)
[14] S. Hazra et al.; Physica B **283**, 97 (2000)
[15] H. Amenitsch et al.; Rev. Sci. Instrum. **5**, 506 (1998)

SAXS STUDY OF LIQUID CRYSTALS

G. Cordoyiannis[1], D. Jesenek[1], S. Kralj[1,2], G. Lahajnar[1,3], A. Zidanšek[1,2,3] and H. Amenitsch[4]

1.) J. Stefan Institute, Jamova 39, 1000 Ljubljana, Slovenia
2.) Department of Physics, Faculty of Natural Sciences and Mathematics, University of Maribor, Koroška 160, 2000 Maribor
3.) Jožef Stefan International Postgraduate School, Jamova 39, 1000 Ljubljana, Slovenia
4.) Institute of Biophysics and Nanosystems Research, Austrian Academy of Sciences, Schmiedlstr. 6, A-8012 Graz, Austria

For the study of the isotropic to Smectic-A (I-SmA) phase transition of liquid crystal 12CB four samples have been measured, the pure 12CB and three mixtures of it with controlled-pore glass (CPG) matrices. The average pore diameter was 15.1, 11.5 and 7.5 nm, respectively. Pure CPG samples have been additionally checked in order to confirm the (expected) narrow-size distribution of the pore size.

These measurements have systematically explored the structural and phase transition behavior of the system in the smallest possible CPG sizes, approaching the size of liquid crystal molecular length. Contrary to larger pore diameters, where a constant dilation of the smectic layers was observed [1], here a rather peculiar behavior has been noticed. The smectic layer thickness for 15.1 nm pores is similar to larger CPGs, for 11.5 nm it shows an abrupt increase and, finally, for the 7.5 nm CPG it drops to the bulk-like value. The results obtained by SAXS are combined with high-resolution calorimetric data acquired at Jožef Stefan Institute (Ljubljana, Slovenia). The calorimetric data are in accordance with SAXS, confirming the anomalous behavior for the 11.5 nm pore CPGs (Figure 1). The SAXS experiments have revealed substantial information concerning the dimensional crossover and scaling behavior of CPG-confined liquid crystals and a manuscript is currently under preparation [2]. The interpretation of results will allow to probe the relative strength of various mechanisms such us finite-size effects, elasticity, surface wetting etc. Our preliminary analysis has shown that different mechanisms are important in different pore-size regimes.

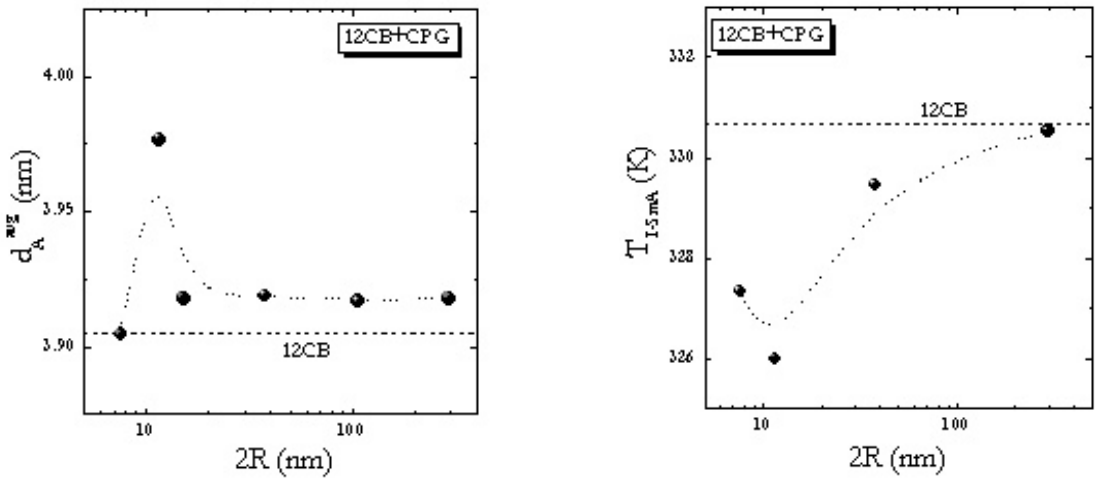

Figure 1. The anomalous behavior in the smectic layer thickness (left) and in transition temperature (right), as revealed by SAXS and high-resolution calorimetry.

Two samples have also been measured for the study of the Smectic-A to chiral Smectic-C (SmA-SmC*) phase transition, the pure SCE9 and one mixture with close-to-spherical magnetic nanoparticles (diameter of ~ 20 nm) of 14 % weight. Measurements were conducted

at several temperatures in the vicinity of the SmA-SmC* phase transition in order to obtain the evolution of the (smectic) order parameter and probe possible pre-transitional effects (e.g. tilt induced above the transition temperature).

By exploiting the unique small-angle capabilities of Austrian SAXS Beam Line, the size distribution of nanoparticles could be clearly seen (Figure 2). No pre-transitional effects have been observed in the SmA phase, contrary to other kinds of nanoparticles mixed with chiral liquid crystals [3].

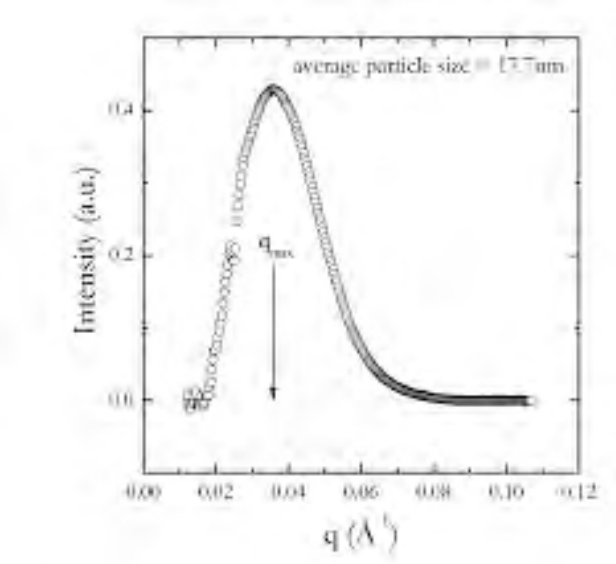

Figure 2. The magnetic nanoparticles narrow size distribution as revealed by SAXS.

References:

[1] G. Cordoyiannis, A. Zidanšek, G. Lahajnar, Z. Kutnjak, H. Amenitsch, G. Nounesis, S. Kralj, Influence of confinement in controlled-pore glass on the layer spacing of smectic-A liquid crystals, Phys. Rev. E 79: 051703 (2009)

[2] S. Kralj et al., in preparation (2011)

[3] G. Cordoyiannis, S. Kralj, G. Nounesis, Z. Kutnjak, and S. Žumer, Pretransitional effects near the smectic-A–smectic-C* phase transition of hydrophilic and hydrophobic aerosil networks dispersed in ferroelectric liquid crystals, Phys. Rev. E 75: 021702 (2007)

WORKING GAS PRESSURE AS A TOOL TO CONTROL THE STRUCTURE OF GaAs DURING PULSED LASER DEPOSITION

P. Dubček[1], B. Pivac[1], S. Milošević[2], N. Krstulović[2], Z. Kregar[2], S. Bernstorff[3]

1.) R. Boskovic Institute, Bijenicka 54, Zagreb, Croatia
2.) Institute for Physics, Bijenicka 46, Zagreb, Croatia
3.) Sincrotrone Trieste, SS 14, km 163.5, Basovizza (TS), Italy

Pulsed laser deposition (PLD) is an alternative, simple and convenient method for producing thin films of various types of materials among which also nanoscaled materials. In such materials the quantum confinement becomes a dominant effect and it significantly modifies the properties of such materials. PLD using very short pulses are particularly interesting for deposition of complex multi-element films, preserving the stoichiometry of the parent materials.

Here we report on the investigation of the influence of different working gas and working gas pressure on femtosecond PLD GaAs. For this purpose, two series of samples, using Ar and He working gas, have been prepared under pressures of 0.01, 0.1, 1 and 10 mbars, while the number of pulses was 1000. For these, the GISAXS intensity distributions are shown in Fig. 1. The top and bottom row correspond to Ar and He working gas, respectively. The pressure is increasing from left to right. Only the left side of each of the GISAXS images represents the measured data, while the right side is the result of the simulation of the measured values.

For the two lower pressures, the GISAXS data almost resemble those obtained for lower puls number, suggesting that the film thickness/nature is similar. Indeed, we have been able to simulate the data successfully using a cylindrical particle shape in our model.

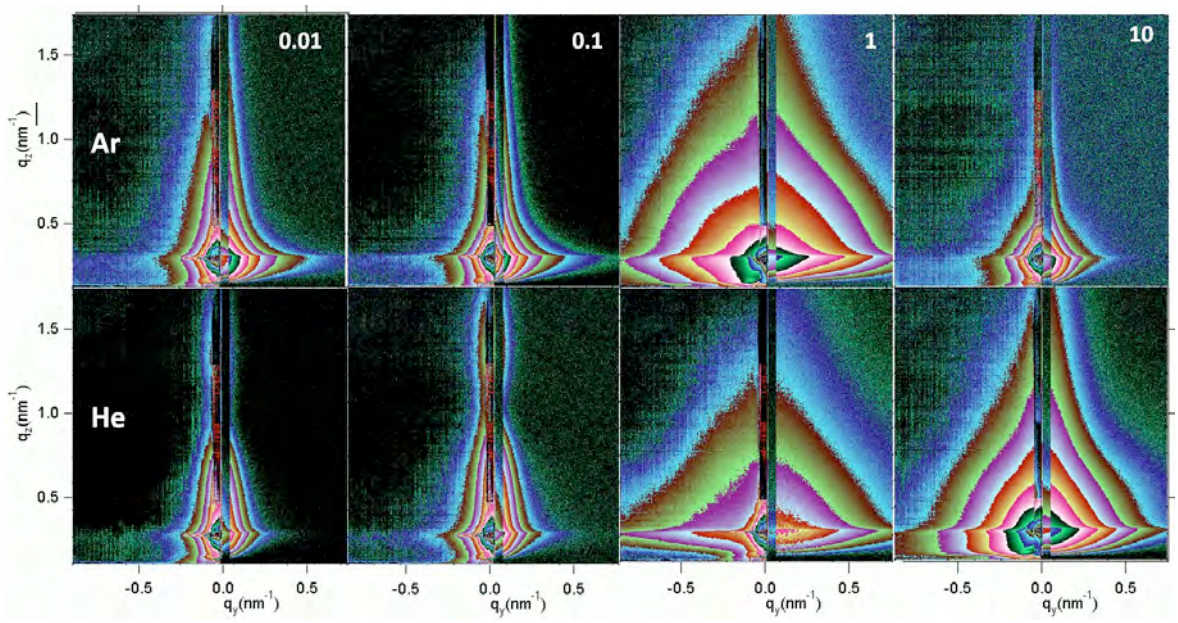

Figure 1. GISAXS intensities for Ar and He assisted PLD of GaAs for different working gas pressure, i.e. 0.01, 0.1, 1 and 10 mbar. The left side of each of the images is the color coded measured intensity, while the right side is the calculated intensity.

The difference between the two working gasses is minimal for the lowest pressure, (0.01mbar), and it should diminish completely with a further pressure reduction. On the other side, for the higher pressure, the GISAXS signal is more spread over the detector angular range, indicating smaller particle sizes. However, this does not hold for the at 10mbar Ar deposited sample, where the particle sizes are again larger. The overall trend for He deposited

samples seems a smoother function of the pressure. Also for the two lower pressure values, the GISAXS signal exhibits oscillations in vertical direction, a clear indication of particle height uniformity over the sample surface. In-plain particle to particle correlation was not included in the fitting function since no depletion of the central part of intensity has been observed.

Apparently, at low working gas pressure, a rather homogeneous, well defined film was formed. Actually, what we have seen by GISAXS are details of the inner film structure and columnar growth. This can be approximated by cylinders rather easily. The particle height is a good measure of the film thickness. As the gas pressure is increased, growth of particles of diverse size is favored, since the energy of the atoms deposited from the plasma is reduced. In this way, atoms are sticking to the surface very close to the place of arrival, and, since the rearrangement is lower, a less compact film is formed.

Generally, a low working gas pressure results in a relatively compact film with a wide variation of the size of the columnar structures in the film, and it is well modeled by log-normal size distribution of cylinders, but the use of higher pressure results in an increased roughness, and more spherical particles, and it is better modeled by hemispherical structures that follow the log-normal size distribution again. Our results suggest that He compared to Ar is a more promising working gas for a better and smoother control of the GaAs nanoparticles growth by nanosecond PLD. As a general rule, using He results in narrower size distributions that are produced for the diverse pulse numbers and working gas pressures. This is most obvious from the formed particle height distribution under pressures lower than 1 mbar. Results of the fitting are summarized and displayed in fig. 2.

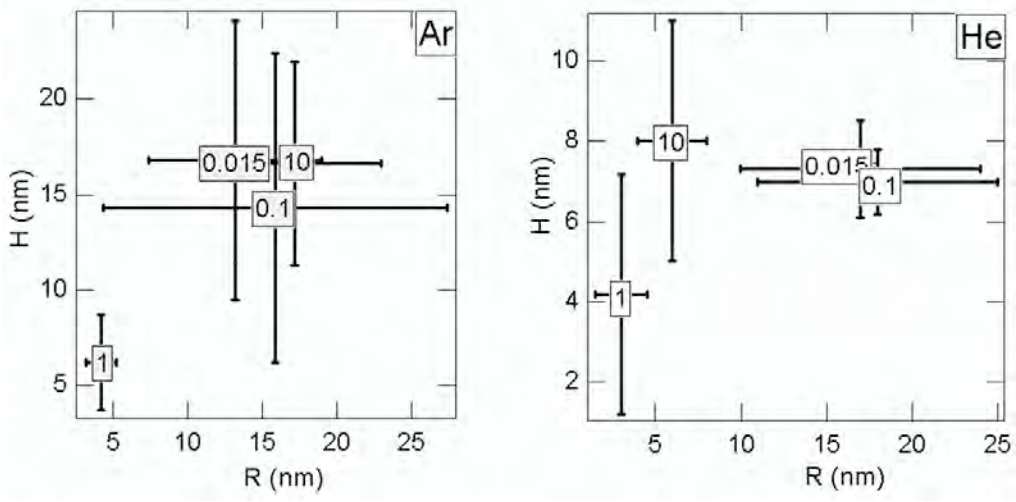

Figure 2. Results of log normal size distribution simulations of the experimental data vs. working gas pressure, for Ar and He assisted deposition left and right, respectively. Height vs. radius is plotted. The size ranges resembling error bars are actually the size distribution widths. The numbers on the graphs indicate the gas pressure in mbar.

GERMANIUM NITRIDE QUANTUM DOTS FORMATION IN SILICON DIOXIDE MATRIX

P. Dubcek[1], B. Pivac[1], N. Radic[1] and S. Bernstorff[2]

1.) R. Boskovic Institute, Bijenicka 54, Zagreb, Croatia
2.) Sincrotrone Trieste, SS 14, km 163.5, Basovizza (TS), Italy

Recently, silicon and germanium nanocrystals embedded in a silicon dioxide matrix have been widely studied for their luminescence and charge retention properties for integration as optoelectronic and microelectronic devices in complementary metal-oxide semiconductor technology. The strict control of the size, shape, passivation and density of the formed nanocrystals is mandatory.

Here we report a case study of GeN formation in post annealed multilayers. Samples were produced by magnetron spattering of nominally 3 nm thick SiO_2 / SiO_2+Ge bilayers, that were repeated 20 times. 10% of N_2 was added to Ar working gas in order to facilitate nitride formation. Substrates were held at room temperature or at 500ºC.

GISAXS results are shown in figure 1. Due to the periodicity of the structure, a Bragg peak appears at $q_z \sim 2.2$ nm^{-1}. From the Bragg peak displacement we can conclude that some chemical transition is induced by annealing: for the sample deposited at room temperature the multilayer d-spacing was reduced from 3.6 nm to 3.1 nm, while this reduction is from 3.0 nm to 2.8 nm in the case of 500ºC substrate temperature. Nitride formation in the latter case is taking place already during the deposition, hence the d-spacing reduction is less pronounced.

Nitrogen introduced into bilayers at room temperature causes a poor contrast in the bilayer, and the Bragg peak is barely visible in scattering from an as deposited sample prior to annealing. Furthermore, the diffusion of deposited atoms during annealing is also hindered, therefore the bilayer contrast is still weak, and the overall scattering pattern is barely altered (left side of figure 1.). It appears that nitrogen introduced into the deposition procedure at room temperature is non favoring for particle formation. However, the average interface roughness between the layers appears to be smoother at lower deposition temperature, according to the shape of the SAXS scattering. We ascribe this to the missing particle formation.

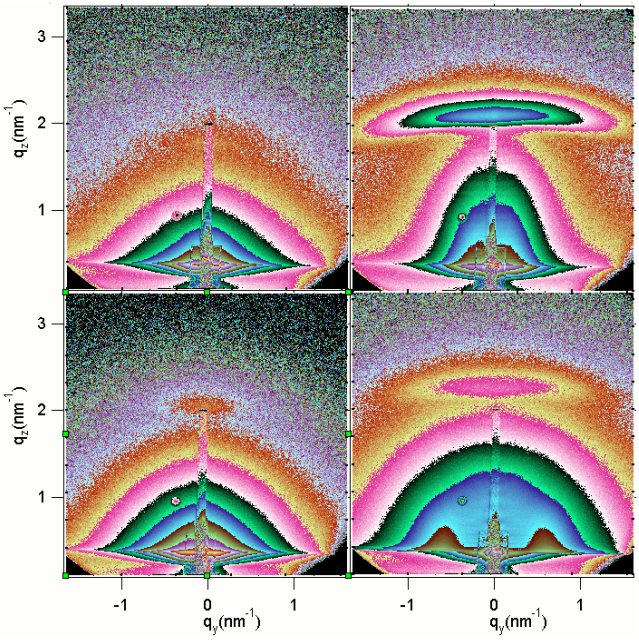

Figure 1. GISAXS scattering pattern of SiO_2 / SiO_2+Ge multilayers deposited at room temperature and 500ºC, left and right column, respectively. The bottom row corresponds to samples which where post annealed at 800ºC.

On contrary, higher temperature deposition results in a good contrast within the bilayer (stronger Bragg peaks) and, after annealing, a rather strong scattering from quantum dots, that are fairly ordered within the layer, which is evident from the side maxima at $q_y \sim 0.7$ nm^{-1}. It appears that the increased freedom of deposited atom movement on the hot surface during the deposition and thus contribution of kinetic energy of the deposition favors both nitride and particle formation.

Numerical fitting to elliptical particles reveals that they are 3.5 nm in diameter, both in horizontal and vertical direction, and that the average particle to particle distance within the layer is 10.5 nm. These numbers suggest that the particles grew too big in vertical direction (their diameter roughly equals the thickness of the bilayer) and also the interparticle distance within the layer is slightly too large for proper selfassembly both in horizontal and vertical direction.

Further investigation should reveal the chemical composition of the quantum dots as well as the level of crystallization as a function of both deposition and annealing temperature. Also, further study of the influence of the deposition parameters is under way in order to gain better control of both sizes and self assembly of the produced nanoparticles.

AMORPHOUS-NANO-CRYSTAL SILICO FILMS AS A SOLAR CELLS MATERIAL

D. Gracin[1], K. Juraić,[1] A. Gajović[1], I. Djerdj[1], S. Bernstorff[2], D. Jozic[2] and M. Čeh[3]

1.) Ruđer Bošković Institute, Bijenička 54, 10000 Zagreb, Croatia
2.) Sincrotrone Trieste, SS 14 km 163.5, 34012 Basovizza (TS), Italy
3.) Jožef Stefan Institute, Jamova 39, 1000 Ljubljana, Slovenia

Nano-crystalline (nC) thin films are a promising candidate for producing high efficiency solar cells. These expectations are based on using quantum confinement effects connected with nano-meter sized objects in the form of ordered 3D domains, called also nano-crystals. One of the proposed concepts for high-efficient cells is using several active materials with various optical gaps in a multi-layer structure where solar cells are stacked one on top of the other. In this experiment we show how multi-layer multi-gap solar cell can be designed with only one type of material using the fact that the variation in the optical gap can be achieved by changing the size of the nano-crystals [1-3].

The first step in this effort is the formation of thin films with a homogeneous size distribution of the nano-crystals in particularly across the depth of the film. For this purpose we used the common Plasma Enhanced Chemical Vapor Deposition technique (PECVD) and the deposition conditions described earlier [4, 5]. The nano-structure was examined by using various methods.

The samples were first analyzed by Raman spectroscopy in order to estimate the crystal to amorphous fraction and the average size of the nano-crystals. Typical spectra are plotted in Fig.1 for two nC-amorphous samples and for a mono-crystalline sample in the frequency range of the transversal optical (TO) phonon vibration. Obviously, the TO peak positions of the nC crystals are shifted relative to the position in mono-crystalline silicon. Assuming that this shift is a consequence of only the quantum confinement effects, the size of the crystals can be estimated according to the relation

$$D_{RAMAN} = 2\pi\left(2.24 / \Delta\omega\right)^{1/2}$$

where $\Delta\omega$ is the peak shift of the TO mode in nC-Si towards lower wave numbers with respect to the peak of μc-Si (521 cm^{-1}). For the plotted samples, the calculated values using above formula were 2 nm and 5 nm for sample A and B respectively.

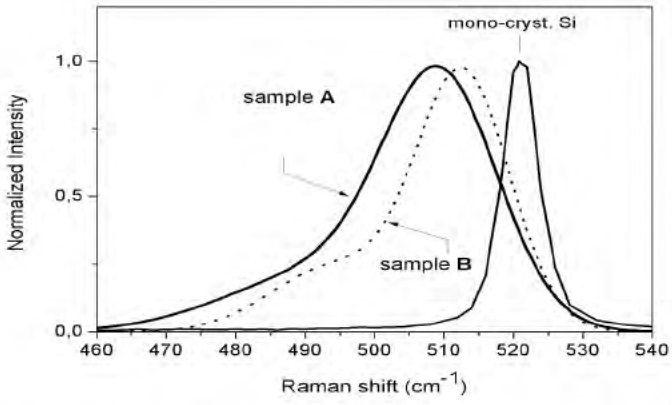

Figure 1. Raman spectra for two nano-crystalline-amorphous thin films with different average nano-crystal sizes ($d_A \approx$ 2 nm, $d_B \approx$ 5 nm) and of mono-crystalline Si (plotted for comparison)

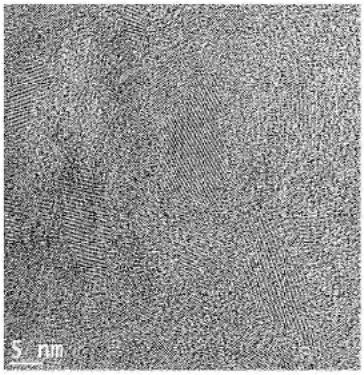

Figure 2. HRTEM micrograph

The selected samples were also examined by HRTEM. The micrographs confirm that the studied samples contain isolated nano-sized ordered domains with sizes similar to those estimated by Raman spectroscopy. One example is plotted in Fig.2.

GISAXS and GIWAXS were used for the determination of the in depth homogeneity of the deposited layers. The measurements were performed using the X-ray beam energy of 8 keV (corresponding to the wavelength λ= 0.154 nm). The grazing angle of incidence, φi, was step scanned between the critical angle φc and $\varphi c + 0.20^0$ in order to examine the in-depth distribution of the "particles" in the deposited films [6]. The GISAXS patterns for all the applied angles and all the examined samples in this series had a similar shape indicating a homogeneous structure throughout the sample depth. Typical results for sample A are plotted in Fig.3.

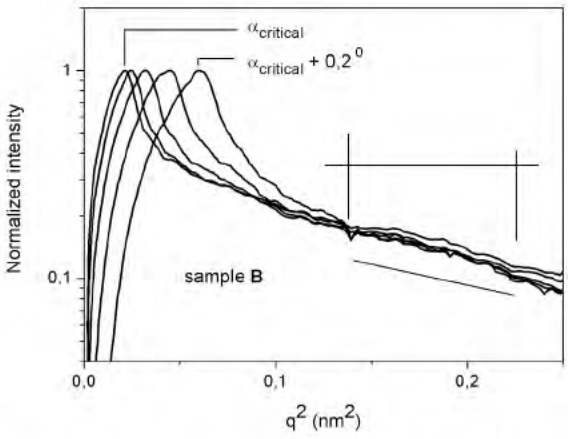

Figure 3. Normalized SAXS intensity of the scattered beam as a function of the wave vector $q=4\pi \sin\Theta/\lambda$

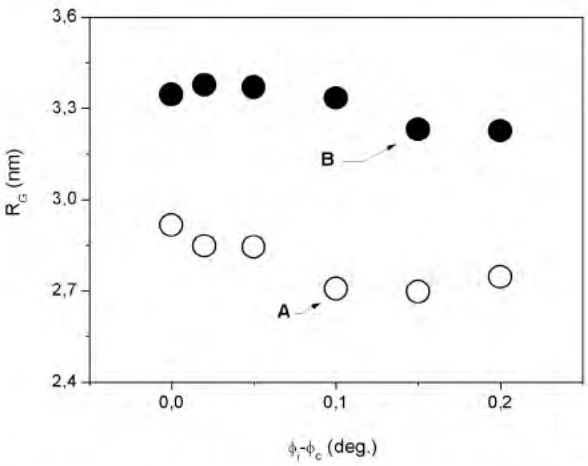

Figure 4. The radius of gyration as a function of the difference between the critical and the actual grazing incidence angle; the marks "A" and "B" correspond to the samples from Fig.1.

The radii of gyration, R_G, were estimated from horizontal cross sections taken from the 2D GISAXS patterns, using a simple Guinier approximation [7, 8] in the range where the approximation is valid (assigned in Fig.3). The results for 2 characteristic samples are plotted in Fig. 4 as a function of the difference between the actual angle and the critical angle, $\varphi i - \varphi c$. The zero value corresponds to the sample surface while the value 0.20 provides information across the entire layer depth. The plotted results confirm the homogeneity of the samples. The R_G values are proportional to the particles sizes and are larger for sample B than for sample A, which is consistent with the crystal sizes obtained by Raman spectroscopy. However, assuming spherical particles, the particles sizes calculated from GISAXS are somewhat larger than those obtained by Raman.

The GIWAXS spectra showed characteristic peaks of Si crystals (Fig. 5) that were analyzed using the Scherrer expression for line broadening:

$$(\varepsilon_{obs} - \varepsilon_{instr}) = \frac{K\lambda}{D_V \cos\theta}$$

where ε is the peak width calculated by fitting the peaks to the Voigt profile and the D_V average crystal size. The in that way calculated values are very similar to the R_G values

obtained from GISAXS which indicates that the objects seen by Raman, HRTEM, GISAXS and GIWAXS are the same, e.g. Si nano-crystals embedded in an amorphous Si matrix.
A possible application of the studied a-nC-Si:H layers as active part in multilayer solar cells was tested by integrating them in a typical p-i-n solar cell structure. The typical spectral response expressed as quantum efficiency QE (the ratio between generated current and incident photon flux) is shown in Fig. 6 and compared with the spectral response of amorphous and micro-crystalline cells. Obviously, if using all three forms of thin silicon films in one multilayer cell structure, a much larger part of the solar spectrum can be covered than in the case of cells with only a single form of Si, resulting thus in a higher energy conversion efficiency.
The "blue shift" of the maximum of the QE in nano-crystalline solar cells compared to amorphous and microcrystalline cells was ascribed to the quantum size effects associated with nano-crystals identified by the applied methods [10].

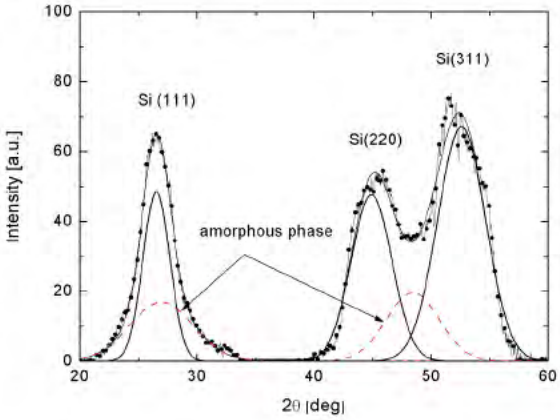

Figure 5. GIWAXS shows characteristic peaks of Si crystals

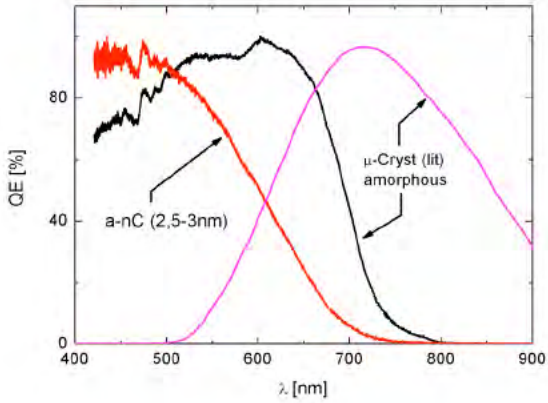

Figure 6. The quantum efficiency of solar cells with amorphous (black line), micro-crystalline (magenta) and amorphous – nano-crystalline (red) material as active part

References

[1] T.J. Bukovski and J.H. Simmons, Crit. Rev. Solid State Mat. Sci. 27 (2002) 119
[2] M.C. Beard, K.P. Knutsen, P. Yu, J.M. Luther, Q.Song, WK. Metzger, R.J. Ellingson and A.J. Nozik, NanoLett. 7 (2007) 2506
[3] D.L. Williamson, Mater. Res. Soc. Symp. Proc. 377 (1995) 251
[4] D. Gracin, S. Bernstorff, P. Dubček, A. Gajović and K. Juraić, J. Appl. Crystallogr. 40 (2007) s373
[5] D. Gracin, S. Bernstorff, P. Dubček, A. Gajović and K.Juraić, Thin Solid Films 515 (2007) 5615
[6] K. Juraić, D. Gracin, B. Šantić, D. Meljanac, N. Zorić, A. Gajović, P. Dubček, S. Bernstorff, M. Čeh, Nucl. Instr. and Meth. B 158 (2010) 259
[7] E. Edelberg, S. Bergh, R. Naone, M. Hall and E.S. Aydil, J. Appl. Phys. 81 (1997) 2410
[8] O. Glatter and O. Kratky, Small Angle X-Ray Scattering, Academic Press, London, 1982, 272.
[9] J.K. Williamson, W.H. Hall, Acta Metall., 1 (1953) 22
[10] D. Gracin, A. Gajović, K. Juraić, M. Čeh, Z. Remeš, A. Poruba, M. Vaneček, J. Non-Cryst. Solids, 354 (2008) 2286

STRUCTURE OF FE_2O_3/TIO_2 NANOCRYSTALS IN SILICA MATRIX

V. Holý[1], M. Buljan[2], V. Janicki[2], V. Valeš[1] and S. Bernstorff[3]

1.) Charles University in Prague, Ke Karlovu 5, 121 16Prague, Czech Republic
2.) Ruđer Bošković Institute, Bijenička cesta 54, Zagreb, Croatia
3.) Sincrotrone Trieste, SS 14 km163,5, 34012 Basovizza, Italy

We have investigated the structure of (Fe_2O_3+SiO_2) / (TiO_2+SiO_2) /SiO_2 multilayers and its change during post growth annealing. The multilayers have been deposited by electron-beam evaporation on Si substrates by room temperature. We have grown an extensive series of samples differing in the thickness d of the Fe_2O_3+SiO_2 and TiO_2+SiO_2 layers keeping constant the thickness of the SiO_2 layers of 10 nm.

After the deposition, the samples have been annealed at various temperatures from 300 to 700°C in air or forming Gas (4% H_2 in Ar). The structure of the nanocrystals has been studied by grazing-incidence small-angle x-ray scattering (GISAXS) at the SAXS beamline at ELETTRA, using the photon energy of 8 keV. The scattered radiation was detected by a MAR image plate placed in the distance of about 1.5 m behind the sample. An evacuated flight tube was used between the sample and detector in order to suppress the scattering of x-rays in the air.

Examples of the GISAXS intensity maps are in Fig1. 1 a,c, showing the maps of sample with d = 2 nm annealed at 700°C (sample A - panel a) and 900°C (sample B – panel c). We have compared the measured data with simulations, panels (b) and (d) in Fig. 1 display the simulated intensity distributions. In the simulations we assume that in a given multilayer period, the nanoparticles create a disordered two-dimensional array with mean basis vectors $\boldsymbol{a}_{1,2}$. The disorder in the particle positions obeys a two-dimensional short-range order model [1]; their random lateral displacements $\boldsymbol{U}_L$ (see Fig. 2) are characterized by the root-mean square (rms) deviation σ_L. The relative positions of the nanoparticles in subsequent periods are described by the third mean basis vector $\boldsymbol{a}_3$ and the random mutual lateral displacements $\boldsymbol{U}_V$ have the rms deviation σ_V. Therefore, the parameter σ_L describes the degree of ordering of lateral particle positions, while σ_V characterizes the degree of the "inheritance" of the lateral positions in successive periods. Since only a short-range ordering of the particles is assumed, the azimuthal orientation of the triplets of the basis vectors $\boldsymbol{a}_{1,2,3}$ was assumed random. Then, only the lengths of the in-plane basis vectors $a_L \equiv |\boldsymbol{a}_1| = |\boldsymbol{a}_2|$ and the vertical component $a_V \equiv a_{3z} = D$ can be reliably determined (D is the multilayer period). The particles are assumed uniaxial ellipsoids with mean horizontal and vertical radii $R_{L,V}$. In the simulations we took into account a statistical distribution of the particle sizes; however the simulation results appeared rather insensitive to the rms dispersion of the sizes. The simulation program includes also x-ray refraction and absorption effects in the SiO_2 matrix by using the DWBA method (see [2] for details).

From the comparison of the measured and simulated data we were able to find the most probable values of the model parameters shown in table 1. We have also measured standard x-ray diffraction curves; we have found no diffraction peaks in sample A but the diffraction curve of sample B exhibited distinct peaks of rutile TiO_2 and hematite a-Fe_2O_3 phases. Using the standard Williamson-Hall procedure we estimated the radii of the rutile and hematite nanoparticles (see Tab. 1).

sample	d	T (°C)	gas	x-ray diffraction		GISAXS					
				R_{TiO2}	R_{Fe2O3}	R_L	R_V	a_L	a_V	σ_L	σ_V
A	2.0	700	FG			3.5 ± 1.0	1.5 ± 1.0	8 ± 3	12.5 ± 0.5	2 ± 1	4 ± 1
B	2.0	900	air	3.2 ± 1.0	2.7 ± 1.0	5.0 ± 0.5	3.0 ± 0.5	16 ± 5	11.5 ± 0.5	5 ± 1	10 ± 1

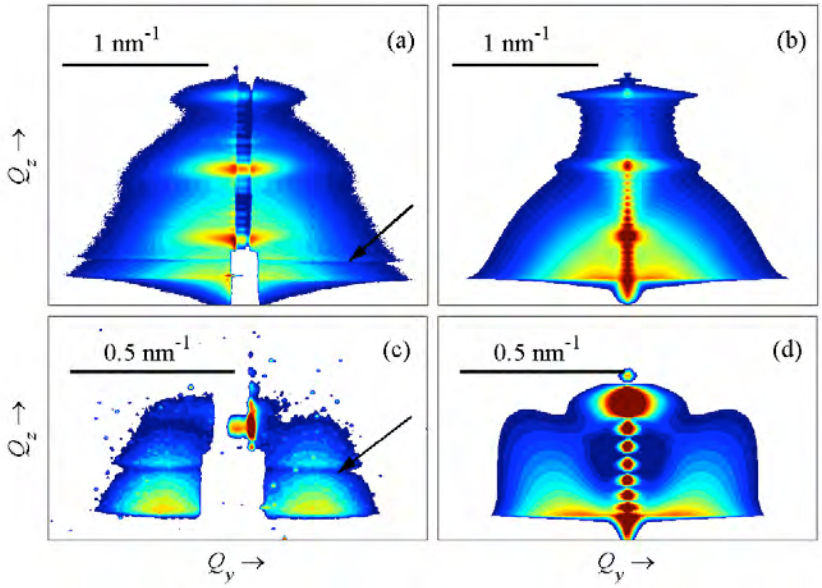

Figure 1. Measured (a,c) and simulated (b,d) GISAXS intensity maps of samples A (a,b) and B (c,d). The step of the intensity contours is $10^{0.3}$ and $10^{0.1}$ for panels (a,b) and (c,d). Narrow horizontal streaks observed in experimental data and denoted by arrows are caused by multiple scattering effects and they are not taken into account in the simulations.

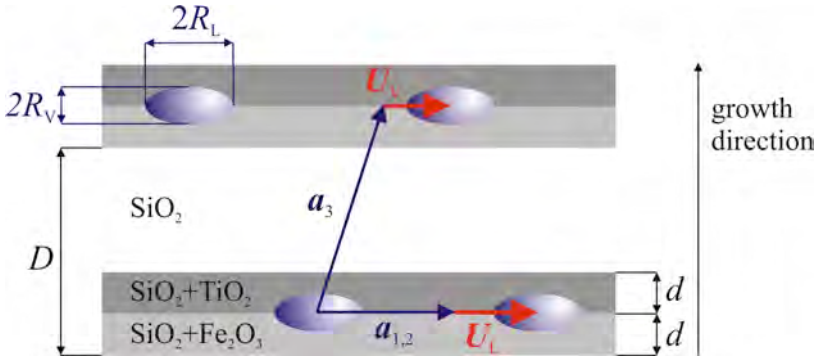

Figure 2. Sketch of the sample geometry; $\boldsymbol{a}_{1,2,3}$ denote the mean basis vectors of the disordered three-dimensional array of the nanoparticles, $\boldsymbol{U}_{L,V}$ are the random displacements of the nanoparticles from their mean positions.

References:

[1] M. Buljan, J. Grenzer, V. Holý, N. Radić, T. Mišić-Radić, S. Levichev, S. Bernstorff, B. Pivac, and I. Capan, Appl. Phys. Lett. **97**, 163117 (2010)
[2] G. Renaud, R. Lazzari, and F. Leroy, Surf. Sci. Reports 64, 255 (2009)

AEROSOL FLOW REACTOR WITH CONTROLLED TEMPERATURE GRADIENT FOR *IN SITU* GAS-PHASE X-RAY EXPERIMENTS

K. Jungnikl, M. Rappolt, I. Shyjumon, B. Sartori, P. Laggner and H. Amenitsch

Institute of Biophysics and Nanosystems Research, Austrian Academy of Sciences, Schmiedlstr. 6, Graz, Austria

This new experiment consists of an *in situ* set-up for the evaporation induced self-assembly (EISA) of mesoporous materials [1] in the gas phase. Previous studies have been performed at the end of the heating stage [2,3] and have shown that the lattice constant of the hexagonal phase of mesoporous silica depends strongly on the conditions of sample preparation (in situ, in situ deposited or collected powder) [4]. In order to study the self-assembly process directly during the heating process, a window less two stage furnace was constructed, which can be continuously be scanned with the X-ray beam [5]. The main components and a picture of the set-up at the electron storage ring ELETTRA is shown in Fig. 1. The aerosol flow is guided through a cooling and afterwards through heating stage placed as close as possible together in order to introduce a high temperature gradient (Fig. 1,insert).
As test reaction aerosols were produced from solutions of the surfactant CTAB and EtOH as well as CTAB/EtOH/H_2O.

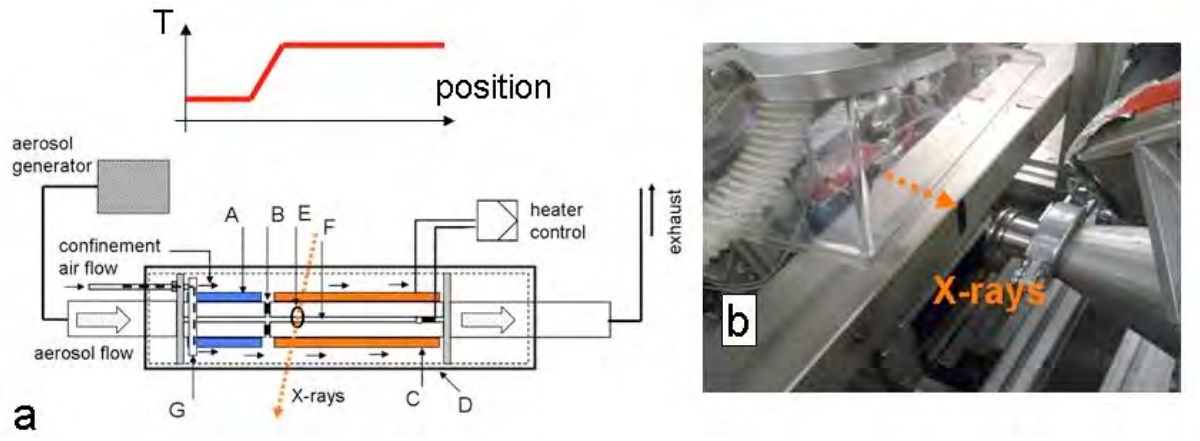

Figure 1. (a) Schematic drawing of the working principle of the flow reactor (adapted from reference [5]. A: Cooled part of the dryer, B: insulating separation, C: heated part. The position of D: confinement shell and E: window is fixed, the inner dryer tube with F: axial slit is moved inside by a motor stage to change the measurement position within the aerosol flow path. A PT100 is mounted at the end of the F: slit to control the heating according to the maximum aerosol temperature. G: Ring-shaped outlet for confinement air into the shell. Insert indicates the change of temperature along the position of the furnace (b) Aerosol dryer mounted at the SAXS beamline at ELETTRA

Fig. 2a shows SAXS measurements of aerosol of CTAB/EtOH solution during spray drying. A clear increase of peak height was observed in the measurements during initial mesostructure formation and subsequent drying caused by the crystallization of CTAB from a highly concentrated, ethanol solution. The maximum observed at q ~ 2.1 nm^{-1} corresponds to a lattice-spacing of ~ 3 nm that is larger than the length of the stretched CTAB tailgroup of ~ 2.2 nm, possibly relating to a strongly tilted surfactant bilayer. The observed slight changes of peak position (Fig. 2b) is explained such as: Initial evaporation of the interlamellar ethanol results in a slight decrease of lattice-spacing, subsequent evaporation of ethanol intercalated in the surfactant layer results in a slight increase of the characteristic repeat distance at the final drying stage. The opposite behavior of the H2O containing solution can be explained by a steric effect of H2O-molecules associated with the surfactant headgroups during initially

faster evaporation of ethanol, before water finally evaporates with a time-delay at the final stage.

The purpose of these first measurements was to show the feasibility of following the mesophase formation in the gas-phase with the presented set-up. The results show a potential for characterizing also chemically more complex systems that might show interesting behavior in 3D-confinement.

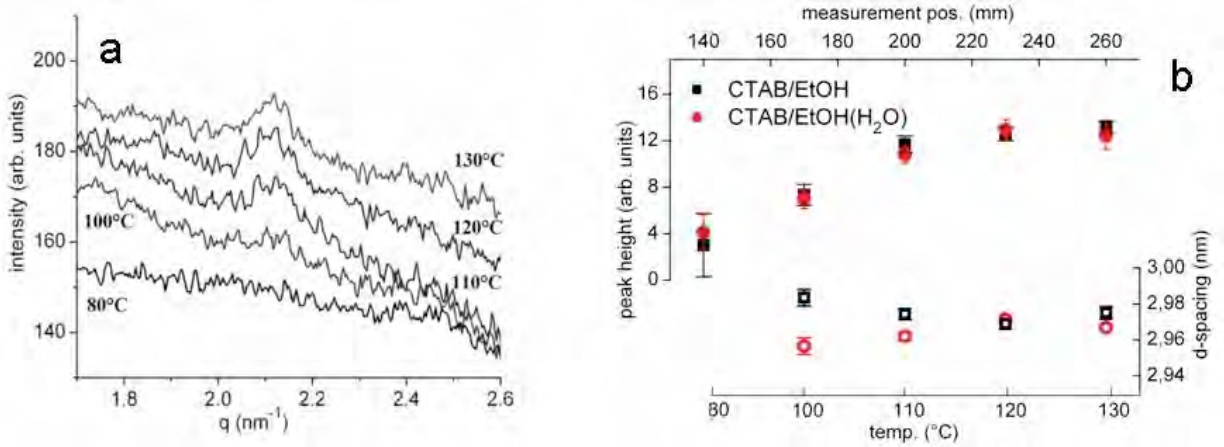

Figure 2. (a) SAXS patterns of aerosol of CTAB/EtOH solution during drying at the maximum set temperature of 150°C. The curves are offset for better visibility (b) Peak height (full circles/squares) and *d* spacing (open circles/squares) during drying of CTAB/EtOH and CTAB/EtOH/(H2O) solutions.

References:

[1] C. J. Brinker, Y. Lu, A. Sellinger and H. Fan; Evaporation-induced self-assembly: Nanostructures made easy; Adv.Mater **11**, 579 - 585 (1999)

[2] C. Boissiere, D. Grosso, H. Amenitsch, A. Gibaud, A. Coupe N. Baccile and C. Sanchez; First in-situ SAXS studies of the mesostructuration of spherical silica and titania particles during spray-drying process; Chemical Communications **9**, 2798 - 2799 (2003)

[3] I. Shyjumon, M. Rappolt, B. Sartori, H. Amenitsch and P. Laggner; Novel in situ setup to study the formation of nanoparticles in the gas phase by small angle x-ray scattering; Review of Scientific Instruments **79**, 043905 (2008)

[4] I. Shyjumon, M. Rappolt, B. Sartori, F. Cacho-Nerin, G. Grenci, P. Laggner and H. Amenitsch; Mesostructured Silica Aerosol Particles: Comparison of Gas-Phase and Powder Deposit X-ray Diffraction Data; Langmuir **27**, 5542 - 5548 (2011)

[5] K. Jungnikl, M. Rappolt, I. Shyjumon, B. Sartori, P. Laggner and H. Amenitsch; Aerosol Flow Reactor with Controlled Temperature Gradient for In Situ Gas-Phase X-Ray Experiments-Measurements of Evaporation-Induced Self-Assembly (EISA) in Aerosols; Aerosol Science and Technology **45**, 805 - 810 (2011)

CHARACTERIZATION OF LIQUID JET INSTABILITY AT THE NANOSCALE USING SAXS

B. Marmiroli[1], F. Cacho-Nerin[1], B. Sartori[1], G. Grenci[2], J. Perez[3], P. Laggner[1], M. Tormen[2], and H. Amenitsch[1]

1.) Institute of Biophysics and Nanosystem Research, Austrian Academy of Sciences, Schmiedlstraße 6, Graz, Austria
2.) IOM-CNR at Elettra Synchrotron, S.S. 14 km 163.5, Trieste, Italy
3.) SWING Beamline, SOLEIL Synchrotron, L'Orme des Merisiers Saint-Aubin - BP 48 91192 Gif-sur-Yvette, France

Spray and liquid jets are widely used in industrial aplications, i.e. propulsion, diesel engine technology, manufacturing, ink-jet printing, thanks to the effects deriving from their complex multiphase flows [1]. Moreover, the recent industrial and scientific development of microfluidic systems has raised great interest in understanding the flows in small spatial dimensions [2]. Such interest has been further promoted by the development of free electron lasers and the consequent need to develop new, high throughput techniques to characterize biological macromolecules. The breakup of a liquid jet from a microscopic nozzle offers a nearly ideal technique for generating microdroplet streams [3]. Many theoretical studies have been dedicated to understand the dynamics and the instabilities of liquid jets both at the micro and the macroscale [4]. More recently, simulations have been conducted to describe their behavior, but from the experimental point of view, there is a lack of techniques that can give support to the theoretical predictions. In fact, existing measurement techniques are mainly based on light scattering and suffer from absorption, reflection and multiple scattering due to the existence of a huge number of droplets and complex air-liquid interface morphology when the jet is breaking up. A step towards quantitative measurement of jet parameters has been recently made by Wang et al., who reported a method based on ultrafast synchrotron X-ray full field phase contrast imaging to reveal instantaneous velocity and internal structure of optically dense sprays [5]. However, there is still a great need for accurate experimental measurement as input for further theoretical study.

We have found that synchrotron SAXS can give fundamental quantitative information to investigate transient phenomenon dynamics of liquid jets. The time dependent morphology of the jet and its subsequent breakup can be detected. We have therefore explored jets of different diameters (250μm-20μm), nozzle geometry, flow rates and also various solvents. We measured the signal of the liquid jet at increasing distance, therefore at increasing time, from the nozzle exit. We performed a scanning SAXS imaging with a step of 20 μm. The alignment of the jet to the beam was guaranteed with a precision of more than 10 μm using a cameras system [6], the transmission, and the WAXS signal. Both HPLC tubes and microfluidic devices [7] were used to produce the jet.

We determined the time of instability onset and the evolution of the dimension of the droplets forming on the jet surface. These data will contribute to the design of devices and systems with improved and predictable performance, i.e. in the field of material synthesis and characterization.

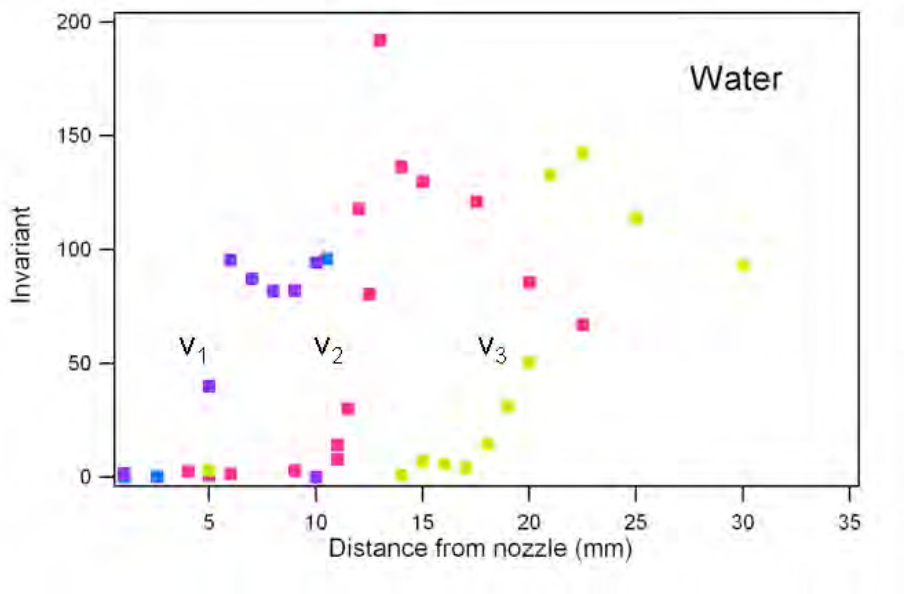

Figure 1. Invariant in function of distance from the nozzle of a water jet of diameter 100 μm for three jet speeds. The onset of the jet instability can be seen as a sharp increase in the invariant value. The higher the jet speed the higher the distance from the nozzle of the onset of the instability.

Acknowledgements:

We would like to thank M. Rappolt for useful discussion, C. Morello and A. Allemandi for the precious technical support.

References:

[1] R. D. Reitz, F. V. Bracco, The enciclopedia of fluid mechanics, Gulf publisher, New Jersey,**3**, 223-249 (1986)
[2] T. M. Squires, S. R. Quake, Microfluidics: Fluid physics at the nanoliter scale, Rev Mod. Phys, **77**, 977 (2005)
[3] U. Weierstall et al, Droplet streams for serial crystallography of proteins, Exp Fluids, **44**, 675 (2008)
[4] J. Eggers, E. Villermauc, Physics of liquid jets , Rep. Prog. Phys., **71**, 036601 (2008)
[5] Y. Wang et al, Ultrafast X-ray study of dense-liquid-jet flow dynamics using structure-tracking velocimetry, Nature Physics, **4**, 305 (2008)
[6] B. Marmiroli et al, Experimental set-up for time resolved small angle x-ray scattering studies of nanoparticles formation using a free –jet micromixer, Nucl. Inst.Meth. in Phys. Research B., **268**, 329 (2010)
[7] B. Marmiroli et al, Free jet micromixer to study fast chemical reactions by small angle X-ra Scattering, Lab Chip, **9**, 2063 (2009)

INTERFACE EFFECTS IN MELTING OF LANGMUIR-BLODGETT FILMS USING DEPTH RESOLVED IN-PLANE DIFFRACTION MEASUREMENTS

P. Pandit[1], A. Gupta[2], D. Kumar[2] and S. Bernstorff[3]

1.) School of Physics, Devi Ahilya University, Indore 452017, India
2.) UGC-DAE-CSR, University Campus, Khandwa Road, Indore 452017, India
3.) Sincrotrone Trieste, SS 14, Km 163.5, I-34049 Basovizza, Trieste, Italy

The effect of interfaces on melting of thin films of soft condensed matter has been a topic of great current interest. The melting behaviour of thin films can get affected significantly because of variation in interface free energy. The objective of the present experiment is to study the effect of sandwiching of Cadmium Arachidate (CdA) Langmuir-Blodgett (LB) multilayer between two metallic films, on its melting behaviour. Three different multilayers were prepared with the structure: Si substrate/ Ni (70 nm) / CdA (13 monolayer)/ X, where X stands for i) 2nm Ni layer (film designated as CdA_Ni); ii) 10nm Al layer (film designated as CdA_Al), or iii) no top layer (film designated as CdA).

The metallic layers form an x-ray waveguide structure. The X-ray standing wave technique was used to do depth resolved in plane diffraction measurements, so as to elucidate any difference in the melting behaviour of the interfacial region of the film from that of the bulk. X-rays of 8 KeV were used for simultaneous measurement of reflectivity (using a 1D detector) and in-plane diffraction (using a 2D Pilatus detector) at the SAXS beam line of the Elettra synchrotron. A miniature boron nitride furnace was used for controlled heating of the sample kept in a protective atmosphere of nitrogen gas.

Typical in plane x-ray diffraction pattern of the LB film consists of two peaks at q_{xy} = 15.6 and 16,8 nm^{-1} corresponding to the (01+ $1\bar{1}$) and (10) reflections, which is in conformity with earlier studies [1]. Fig. 1 shows the variations in the intensity of the (01+ $1\bar{1}$) peak as a function of the angle of incident of x-rays in case of the sample CdA_Al. One can see that the incidence angle dependence of the intensity exhibits two clear peaks at angles $\alpha_1 = 0.195^0$ and $\alpha_2 = 0.245^0$, which represent resonance enhancement of the x-ray intensity inside the wave guide corresponding to the TE_0 and TE_1 modes respectively. The inset of Fig. 1 shows the simulated field distribution inside the LB film for the above two angles. One can see that diffraction measurements done at the TE_0 excitation would provide information about the structural changes in the centre of the film, while at the TE_1 excitation the information would be weighted towards the two interfaces.

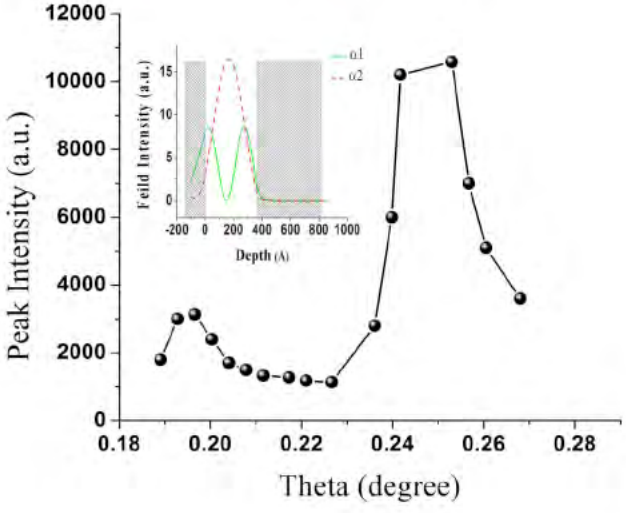

Figure 1. The variations in the intensity of the (01+ $1\bar{1}$) peak as a function of the grazing angle of incident of x-rays in the sample CdA_Al. The inset shows the simulated field distribution inside the LB film for angles of incidence corresponding to the TE_0 and TE_1 modes

Two sets of temperature dependent in-plane XRD measurements were done with the angle of incidence kept equal to α_1 and α_2 respectively. Fig. 2 gives some representative in-plane XRD patterns of the film CdA_Al as a function of temperature taken at angle of incidence α_2. One can see that with increasing temperature both peaks shift to lower angles due to thermal expansion. However the peak corresponds to the $(01+ 1\bar{1})$ reflection, shifts at a faster rate and finally merges with the first peak. The distortion of the lattice from a regular hexagon can be quantified in terms of the parameter $\Delta\gamma = 60^0 - \gamma$, with $\gamma = \cos^{-1}(q_2/2q_1)$, where q_1 and q_2 are the position of (10) and $(01+ 1\bar{1})$ peaks respectively [1]. Fig 3 gives the variation at $\Delta\gamma$ with temperature at the two angles α_1 and α_2. One can see that around the temperature of 350K, $\Delta\gamma$ rapidly drops down, indicating the decrease in distortion. This behavior is very similar to that observed in case of the film without top Al layer.

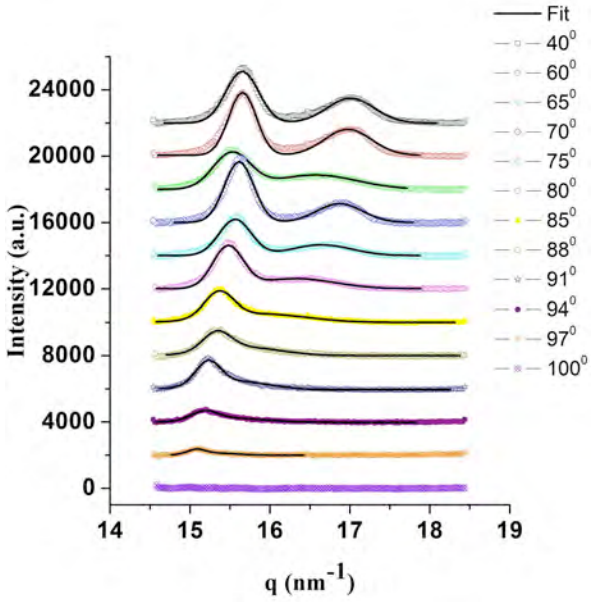

Figure 2. The in plane XRD of the film CdA_Al as a function of temperature taken at the grazing angle of incidence α_2

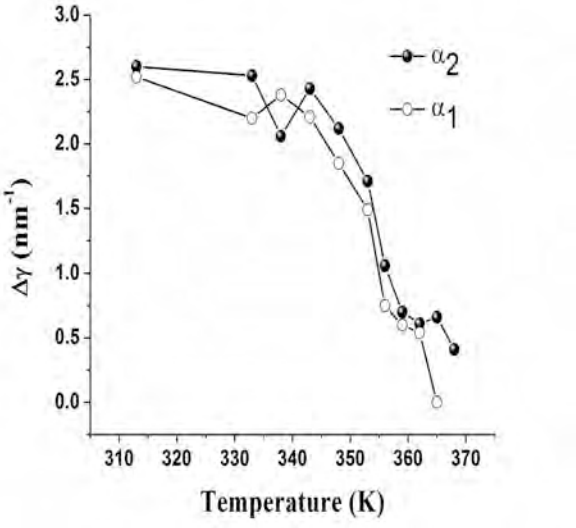

Figure 3. The variation of $\Delta\gamma$ with temperature for XRD taken at the two angles α_1 and α_2

Fig 4a gives the temperature dependent width of diffraction peaks at two angles of incidence. For comparison the widths of the two peaks for the sample without top Al layer are shown in Fig 4b. The peak width is related to the size of the coherent domains. In sample CdA_Al, from the observed widths at room temperature, the domain size comes out to be 29.1 nm^{-1} along (10) direction and 6.6 nm^{-1} along (01) direction. From Fig 4 one can see that the dominant effect of the top Al layer is seen in the temperature dependence of the peak width. In the sample CdA, the width of the $(01+ 1\bar{1})$ peak corresponding to α_1 and α_2 exhibit very different behaviour. The $(01+ 1\bar{1})$ peak corresponding to angle α_1 exhibits strong broadening beyond a temperature of 353K, as compared to the peak corresponding to angle α_2. This behaviour is in agreement with earlier studies [1] and has been interpreted in terms the formation of an intermediate smectic phase with having ordering only along the (10) direction. Further, one may note that the surface region melts at a temperature of 97^0 while the bulk melts at 100^0C, i.e., at a temperature 3^0 higher than the surface. In contrast to the results on sample CdA, in the sample CdA_Al no excessive broadening of the $(01+ 1\bar{1})$ peak is observed. Thus in this sample the melting behaviour of the surface is very similar to that of the bulk. However even in this sample the melting temperature of the interfacial region is 3^0

below that of the bulk. Studies were also done on sample CdA_Ni. The results on this sample qualitatively agree with those of the sample CdA_Al.

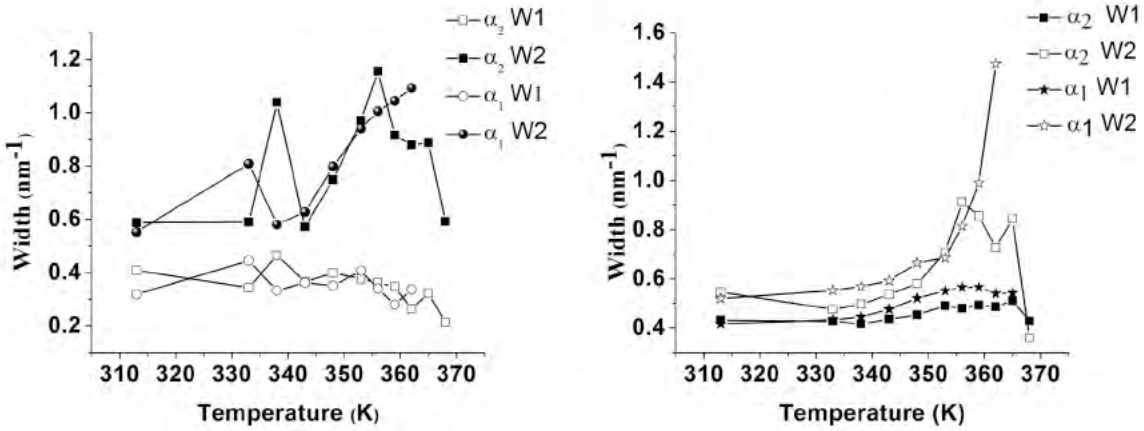

Figure 4. The width of x-ray diffraction peaks taken at the angles of incidence α_1 and α_2. W1 and W2 are the widths of the (10) and (01+ 1$\bar{1}$) peaks respectively. Figure (a) corresponds to sample CdA_Al, while Figure (b) corresponds to the sample CdA

Following conclusions can be drawn from these studies: 1) In the samples both with and without top metallic layer the melting temperature of the surface/interface region is 3^0 below that of the bulk. This difference in the melting temperature can be attributed to the difference in the free energies at the surface/interface and the bulk. 2) The top metal layer (Al or Ni) does not have any significant effect on the melting temperature of the bulk as well as surface/interface and also on the transition temperature to the hexaticlike phase. 3) However, the melting behaviour of the surface gets strongly modified because of the top surface layer. In case of a free surface the melting takes place via an intermediate smectic phase, while the presence of a top metallic layer suppresses this intermediate phase.

References:

[1] A. Gupta, P. Rajput, S. Bernstorff, H. Amenitsch; Low-Dimensionality Effects in the Melting of the Langmuir-Blodgett Multilayer, Langmuir 24, 7793-7796 (2008)

[2] H. D. Sikes, D. K.Schwartz; Two-Dimensional Melting of an Anisotropic Crystal Observed at the Molecular Level, Science 278, 1604 (1997)

SELF-ASSEMBLY OF GE QUANTUM DOTS AND VOIDS IN AN ALUMINA FILM

S. R. C. Pinto[1], M. Buljan[2], A. G. Rolo[1], J. Martín-Sánchez[1], S. Bernstorff[3] and M. J. M. Gomes[1]

1.) Centro de Física, Universidade do Minho, 4710-057 Braga, Portugal
2.) Rudjer Boskovic Institute, Bijenicka 54, 10000 Zagreb, Croatia,
3.) Sincrotrone Trieste, SS 14, km 163.5, Basovizza (TS), Italy

The production of regularly ordered lattices of quantum dots (QDs) or voids is of great interest for many relevant technological applications. However, the knowledge about the production of regularly ordered structures in amorphous matrices is very limited. We demonstrate a self-assembled growth of a three-dimensional well ordered Ge QD lattice, in a single 500 nm-thick layer, during magnetron RF-sputtering deposition of a $Ge+Al_2O_3$ mixture at an elevated substrate temperature [1]. A well ordered three-dimensional body centered tetragonal QD lattice within the whole deposited volume is obtained. The parameters of the lattice can be tuned by changing the deposition parameters. The observed self-assembly of QDs is explained by diffusion mediated nucleation and surface morphology effects, and it is simulated by a kinetic Monte Carlo model. Surprisingly, during subsequent thermal treatment of those films the germanium atoms were lost from the film by out diffusion, and ordered void lattices were formed replicating the ordered Ge QDs structure present before the annealing [2]. The formed QDs or voids are very small in size (less than 4.0 nm), have a narrow size distribution and a very dense packing density, which are excellent features for applications in nanotechnology.

Results

I – As-grown ordered Ge NCs samples

The results of the structure investigations of the films are presented in Fig 1 (taken from [1]).

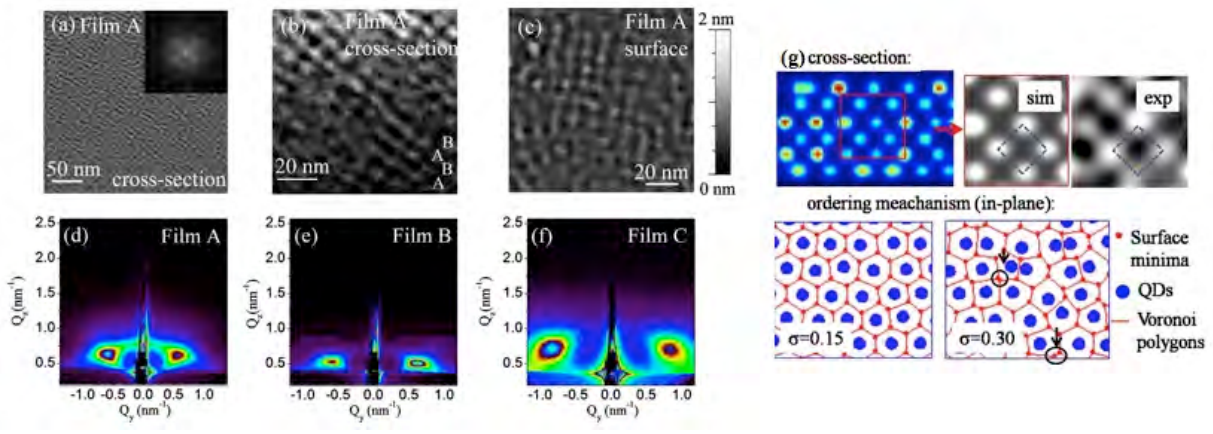

Figure 1. Structure of 3 films which were grown under different conditions: (a) Transmission electron microscopy (TEM) cross section image. The inset shows the corresponding Fourier Transform (FT); (b) TEM cross section with a better resolution, showing an ABAB type of QD ordering. (c) Atomic force microscopy (AFM) image of a film surface showing square like in-plane ordering of QDs. (d–f) Grazing incidence small angle X-ray scattering (GISAXS) maps of films A–C. Strong Bragg spots confirm the formation of well ordered 3D arrays of NCs. All maps demonstrate the same type of NC arrangement, but with different positions in reciprocal space. So, the NCs lattice and NC size are very sensitive with respect to the deposition conditions. Using a model of growth [3] and Monte-Carlo Simulation we observed the growth of a BCT-like QD lattice (g), the NC layer stacking sequence is ABAB. This regularity is improved with the number of deposited layers

II – Formation of ordered voids lattices after annealing

After the deposition, the film was annealed in air (pressure 10^{-2} mbar) at 800 ºC for 1h. Figure 2 (taken from [2]) presents the main structural properties of the films after annealing.

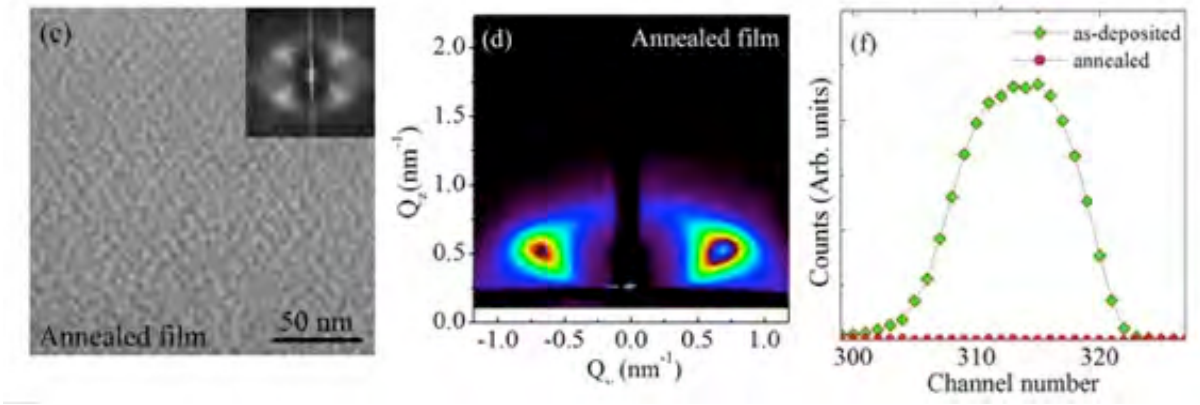

Figure 2. (c) TEM cross section image and (d) GISAXS map showing that after annealing the objects present a similar arrangement type as the as-grown samples, (f) The RBS results show the loss of Ge during the annealing treatments.

A detailed elemental analysis of the films performed by the EDXS method, XRD and Raman measurements is shown in fig 3 (adapted from [2]).

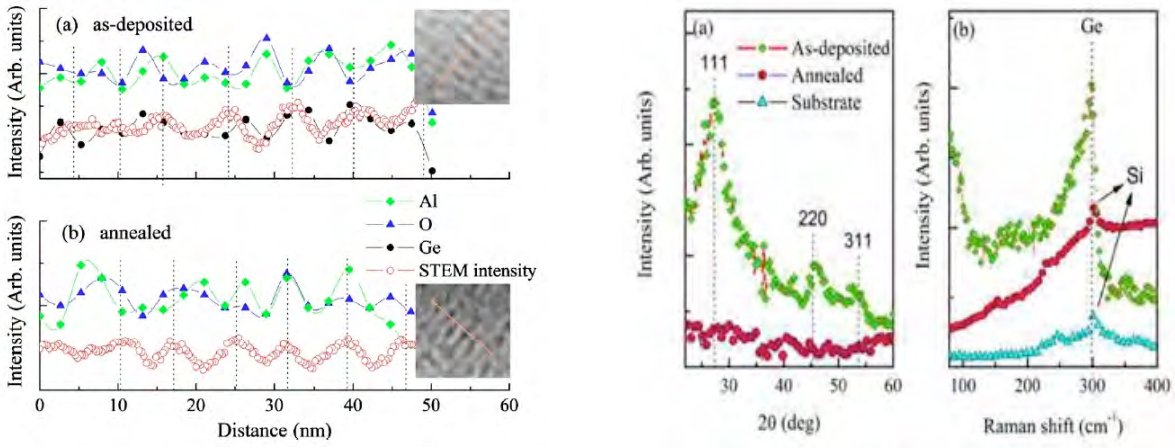

Figure 3. EDXS results show that the ratio O:Al does not change significantly after the annealing. No evidence for any other crystalline phases except the Si substrate is visible in the XRD and Raman spectra which is in excellent agreement with the conclusion that a void lattice has been formed in an amorphous alumina matrix.

Conclusions:

In this report we show the formation of large and well ordered 3D BCT lattices of Ge NCs in amorphous alumina matrix, supported by a kinetic Monte-Carlo simulation, and the dependence of the lattice parameters on the depositions conditions. We observed that the regularity of the NCs positions in alumina improves with the increase of the layer thickness. After annealing, 3D well ordered nanovoids lattice in a thin amorphous alumina film is obtained. The resulting voids have sizes of a few nanometers and show a narrow size distribution. Also the voids sizes can be controlled by the deposition parameters.

References

[1] M. Buljan, et al., Phys. Rev. B 82 (2010) 235407
[2] S. R. C. Pinto, et al., Appl. Phys. Let. 97 (2010)
[3] M. Buljan, et al., Phys. Rev. B 79 (2009) 035310

EXISTENCE AND KINETICS OF DISLOCATION GENERATION IN SEMICRYSTALLINE GAMMA PHASE ISOTACTIC POLYPROPYLENE (GAMMA-IPP) BY IN-SITU WAXS AND SAXS DEFORMATION

G. Polt[1], F. Spieckermann[1], H. Wilhelm[1], M.B. Kerber[1], E. Schafler[1], M. Zehetbauer[1] and S. Bernstorff [2]

1.) Physics of Nanostructured Materials, Faculty of Physics, University of Vienna, A-1090 Vienna
2.) Sincrotrone Trieste, Basovizza, Italy

In-situ WAXS and SAXS measurements during plastic deformation were successfully performed on γ – iPP samples. Since strong relaxation effects can be observed in polymers during unloading, which results in considerable differences between the loaded and the unloaded state, it is necessary to use an in-situ setup for the experiment. The recorded profiles were evaluated by means of Multi Reflection X-ray Profile Analysis (MXPA) [1].
Earlier investigations on α – crystallized isotactic polypropylene (α – iPP) [2] and poly(3-hydroxybutyrate) (PHB) [3] proved the functional efficiency of this method, furthermore it was shown that there are no dislocation generation mechanisms activated in PHB (although the initial dislocation density is higher than in α – iPP for example). Present measurements with high γ – phase concentration indicate a similar behaviour in dislocation density development with increasing strain as PHB does.
Figure 1a shows the dislocation density development with increasing strain of a sample containing 87% of γ – phase and of pure α – iPP. The significant deviation in the evolution of the dislocation density is based on a different deformation mechanism. In the case of α – iPP the main deformation mechanism is the crystallographic slip within the crystalline lamellae which is accompanied by a dislocation generating process leading to an increase of the dislocation density. Since the chains in γ – iPP are aligned in a non – parallel way the main slip mechanism in polymers, the chain slip, is prohibited. Therefore, the critical resolved shear stress (CRSS) which is necessary to activate a slip system seems to be too high so that no mobile dislocations are generated resulting in an interlamellar shear of the amorphous layers as the primary deformation mechanism. As a consequence the dislocation density slightly increases at the beginning of deformation and stays relatively constant at higher strains.
The CSD – size of the α and γ – phase of iPP is shown in Figure 1b. Since the CSD – size represents the smallest coherently scattering domain size in a crystal, it can be related to the lamellae thickness in polymers. The thicker lamellae in the case of the γ - phase may be caused by the long crystallization time of 4 to 6 hours. However, a decrease of the CSD – size with increasing strain could be observed for the α and γ – phase of iPP.

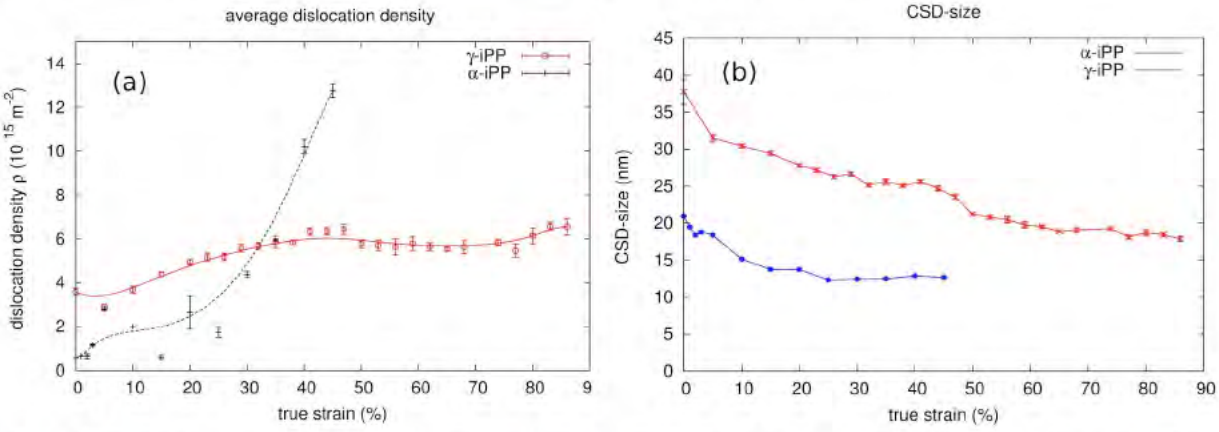

Figure 1. (a) Comparison of the dislocation density development of α- and γ-iPP (b) Evolution of the lamellae thickness with increasing strain of α- and γ-iPP

The behaviour of the dislocation density and CSD - size as a function of the applied strain of the γ – sample can be explained in terms of misfit dislocations. A single crystal can be imagined as an aggregate of crystalline blocks with small differences in the relative orientation against each other. If the misorientation between two blocks exceeds an angle of ~1.5°, the two parts are interpreted as individual coherently scattering domains by the MWPA – method. It is expected that misfit dislocations are located within the boundaries of the crystalline blocks. If deformation occurs the crystalline blocks start to fragment as a result of a bending of the lamellae and/or due to the formation of shear bands resulting in a decrease of the CSD – size (Figure 2). The associated increase of the area between these blocks leads to a simultaneous multiplication of misfit dislocations which are located within the block boundaries and in further consequence to a slight increase of the dislocation density within the first 40% of deformation.

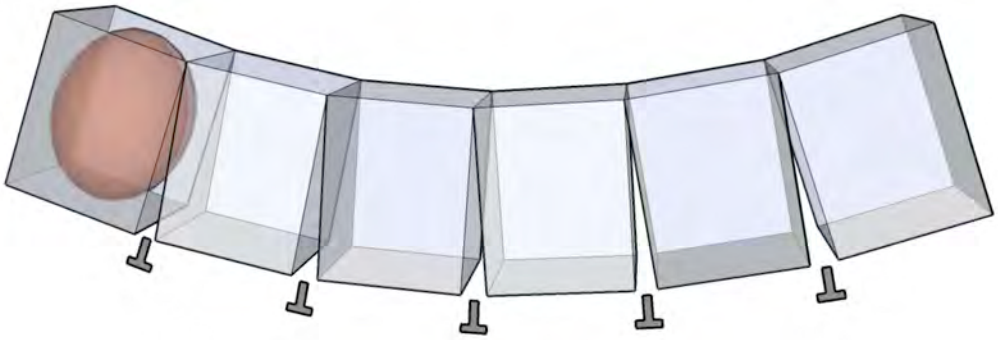

Figure 2. The deformation induced fragmentation of the lamella leads to a decrease in the CSD-size

References:

[1] T. Ungár, J. Gubicza, G. Ribárik & A. Borbély; Crystallite size distribution and dislocation structure determined by diffraction profile analysis: principles and practical application to cubic and hexagonal crystals; J. App. Cryst. **34**, 298-310 (2001)

[2] H. Wilhelm, A. Paris, E. Schafler, S. Bernstorff, J. Bonarski, T. Ungar & M. Zehetbauer; Evidence of dislocations in melt-crystallised and plastically deformed polypropylene; Mater.Sci.Eng. A 387–389 (2004)

[3] F. Spieckermann, H. Wilhelm, E. Schafler, M. Kerber, S. Bernstorff and M. Zehetbauer; Plasticity and X-ray Line Profile Analysis of the Semicrystalline Polymer Poly(3-hydroxybutyrate); Journal of Physics: Conference Series, 240, 012146 (2010)

NANOSCALE MULTILAYERS AS OPTICAL ELEMENTS FOR THE X-RAY OPTICS

N. Radić[1], K. Salamon[2], P. Dubček[1], O. Milat[2], M. Jerčinović[1], G. Dražić[3], S. Bernstorff[4]

[1]Rudjer Bošković Institute, Bijenička 54, Zagreb, Croatia
[2]Institute of Physics, Bijenička 46, Zagreb, Croatia
[3]Josef Stefan Institute, Jamova 30, Ljubljana, Slovenia
[4]Sincrotrone Trieste, Basovizza, Italy

Synthetic multilayer mirrors made up of alternating layers of highly reflective and highly transmissive materials have important uses such as for X-ray spectroscopy etc. In particular, a demand for mirrors in the short-wavelength region arose from the development of ever smaller electronic components by using a photolithographic process. Here, the resolution is limited by the wavelength of light. Hard X-ray applications require a high efficiency multilayer interference structure with a small period, imposing strong demands on the quality of the constituent layers. From the viewpoint of both technology and optical properties, the tungsten/carbon combination is one of the best for X-ray radiation. Both these elements exhibit different phases, which allows for a further parameters variation.

Several series of W/C multilayers have been prepared by sequential magnetron deposition onto various substrates - glass, silica, alumina and mono-Si. Besides geometrical parameters - carbon layer thickness, tungsten layer thickness and total number of bilayers - three processing parameters have been used to control the phase composition of either the carbon or tungsten layers: the substrate temperature (RT-750 °C) for the carbon phase, the working gas pressure (2-20 mtorr) and the discharge power (20-40 W) for the tungsten phases (ά/β) ratio.

The morphology of the surface and multilayer interfaces – a decisive multilayer property for the role of X-ray mirrors - have been determined by two global (XRR, GISAXS) and two local methods (TEM, AFM). It was found that a higher ($\geq$ 200°C) substrate temperature is detrimental for the carbon layer surface smoothness, so the examined multilayers have been deposited onto substrates at nominally room temperature.

Grazing Incident Small Angle X-ray Scattering (GISAXS) measurements were performed at the ELETTRA synchrotron radiation source, Trieste (Italy), at the SAXS beamline, using the X-ray beam energy of 8 keV. A 2-dim Mar300 Image plate detector with spatial resolution of 0.15mm and 16 bit dynamic range was used for the scattered X-rays detection. The grazing incident angle was 0.1º above the critical angle (corresponding to about 100 nm X-ray penetration depth). The tungsten phases (ά/β) ratio has been monitored by simultaneous WAXS measurement, taken in the angle range of 30-50º, with an 1D gas filled Gabriel type detector.

Specular reflectivity (XRR) yields information about the sample structure only in the direction perpendicular to the surface. 2D GISAXS experiments allow for the determination of lateral structure parameters, e.g. the correlation length or static structure parameters of (buried) interfaces and the dependence of the vertical correlation length on the lateral characteristic length [1,2]. The scattered diffuse intensity is concentrated in the so-called Bragg sheets, which means that the roughness is mostly correlated among different interfaces. A comprehensive set of C/W multilayers have been examined by the GISAXS method. An example of the obtained results is given in Fig. 1.

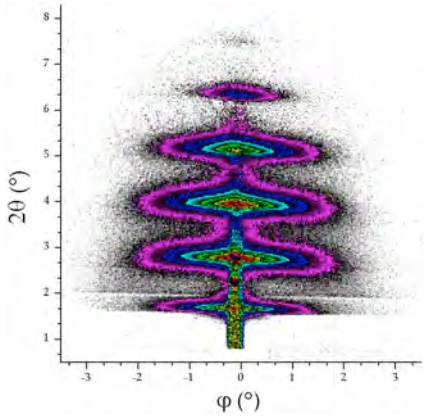

Figure 1. GISAXS intensity pattern for C/W multilayer sample with twenty C:W =6,0 : 1,0 nm bilayers.

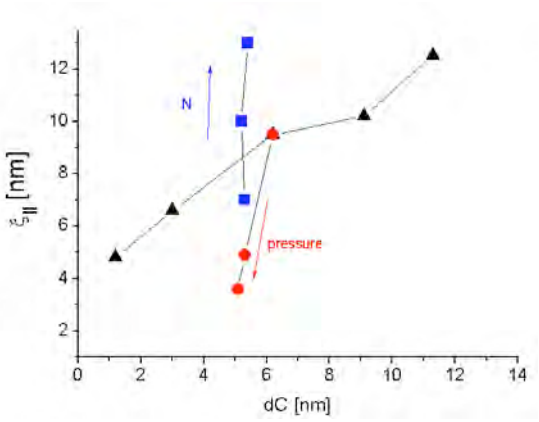

Figure 2. Lateral correlation length ξ of the C/W multilayers. The results are shown for different carbon layer thicknesses (▲),working gas pressure (2-10-20 mtorr) for tungsten deposition (●), and number (10-20-30) of bilayers (■).

The results of the analysis of the observed GISAXS patterns for a selected set is given in Figure 2., which shows a plot of the lateral correlation length ξ versus the C layer thickness dC, number of bilayers and Ar pressure, respectively. However, a single parameter which "measures" the bilayer regularity, smoothness and sharpness of all interfaces in a particular C/W multilayer is the reflectivity. For the sake of simplicity, we have determined the reflectivity at the angular position of the 1st Bragg maximum for all C/W multilayers considered above, and summarized them for a selected set of samples in Fig. 3. It is seen that the tungsten deposition parameters strongly affect the overall X-ray multilayer reflectivity, which proves the importance of the tungsten phase composition in that respect.

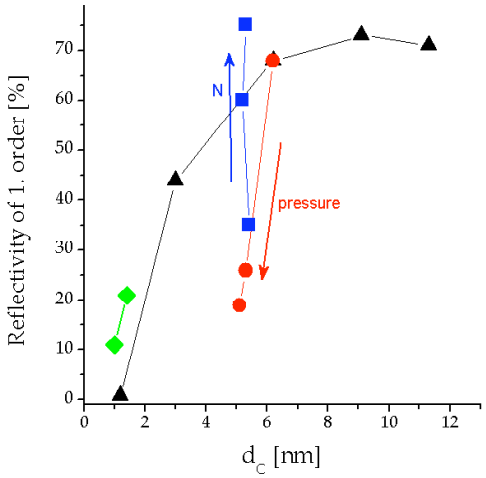

Figure 3. The C/W multilayers reflection coefficient for 0,154 nm X-ray radiation. The symbols are the same as in Fig. 2, except for two data points (◇) corresponding to the multilayers with tungsten layer deposited at higher deposition rate (2 nm/min at 40 W power).

References:

[1] T. Salditt, T.H.Metzger, Ch.Brandt, U.Klemradt, J.Peisl, Phys. Rev. B, 51, 5617, (1995)
[2] R. Paniago, R. Forrest, P. C. Chow, S. C. Moss, S. S. P. Parkin, D. Cookson, Phys. Rev. B 56, 13442, (1997)

TIME RESOLVED GISWAXS INVESTIGATIONS OF THE FORMATION OF POLYMER – COPPER INDIUM SULFIDE NANOCOMPOSITE LAYERS

T. Rath[1,2], M. Edler[1,2], J. Novak[1], A. Schenk[1,2], A. Fischereder[1,2], H. Amenitsch[3] and G. Trimmel[1,2]

1.) Institute for Chemistry and Technology of Materials, Graz University of Technology, Stremayrgasse 9, A-8010, Graz, Austria
2.) Christian Doppler Laboratory for Nanocomposite Solar Cells, Graz University of Technology and NanoTecCenter Weiz Forschungsgesellschaft mbH, Austria
3.) Institute of Biophysics and X-ray Structure Research, Austrian Academy of Sciences, Schmiedlstrasse 6, A-8042 Graz, Austria

Polymer – copper indium sulfide (CIS) nanocomposite layers can be used as active layers in nanocomposite solar cells. The fabrication and working principle of these solar cells is similar to polymer – fullerene solar cells, with the difference that the fullerenes are replaced by nanoparticles. For efficient nanocomposite solar cells the interface area between donor and acceptor material as well as a bicontinuous network of donor and acceptor materials are crucial parameters for charge generation and charge transport and thus have to be optimized [1,2]. A typical method for the preparation of the metal sulfide films is to apply precursor layers from a solution containing corresponding metal salts and a sulfur source for the formation of the metal sulfide layer on suitable substrates. To form the final semiconducting metal sulfide film, the precursor layer is thermally treated leading to decomposition of the sulfur source, hence, the release of sulfur species, which react with the metal ions to form the metal sulfides (see Figure 1).

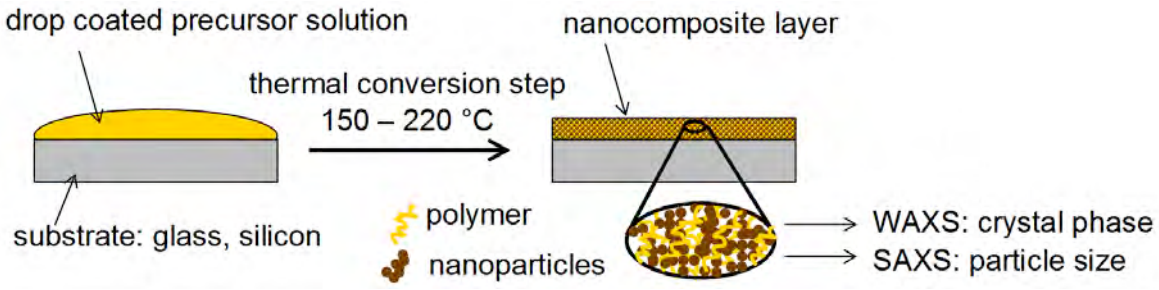

Figure 1. Scheme of the polymer – CIS nanocomposite-formation

With the experiments carried out at Elettra the thermal formation process of thin poly(3-(ethyl-4-butanoate)thiophene) (P3EBT) - CIS nanocomposite layers was simultaneously studied by time resolved GISAXS and GIWAXS measurements. This was done on a heating stage which allows simulating the annealing conditions used for the preparation of the nanocomposite layers for the solar cells. Parameters like internal surface area, porosity, correlation lengths of the nanostructure but also the thermal onset of the formation and the crystal phase of the metal sulfide were obtained.
As analyzed by in situ GIWAXS studies (see Figure 2A), nanocrystalline CIS is formed at temperatures above 160 °C. Figure 2A shows the temperature dependent evolution of the (112) reflection of CIS. Reflections of educts, dominating at the beginning, diminish in the course of heating, while the (112) reflection of CIS (~28° 2q) appears. Additionally two peaks stemming from ITO occur above 160°C. This is caused by the shrinkage and increasing porosity of the layer during heat treatment, for which we also have indication in the GISAXS data.

Complimentary to the GIWAXS analysis of the phase formation, the annealing process was studied by an in situ time resolved GISAXS experiment [3].

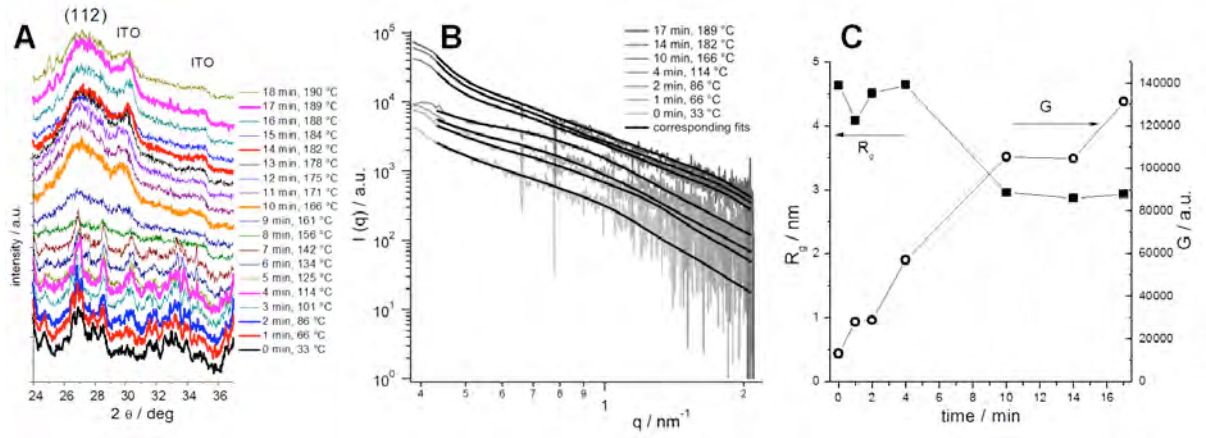

Figure 2. GIWAXS patterns of the polymer – CIS layer at temperatures between 33 and 190 °C (A), out of plane scattering at different temperatures (obtained by integration along the vertical cuts) with the corresponding fit results (B) and fit results of the vertical cuts showing the strong increase of the Guinier Prefactor G and the decrease of the Guinier Radius Rg of the particles (C).

The evolution of the GISAXS signal in vertical direction, shown in Figure 2 B, reveals that the scattering intensity increases during the annealing process. The data are analyzed using a generalized unified Guinier-exponential/power-law function [4-6] with polymeric constraint.

The main results demonstrate the compaction of the particles during the heating process. This is visible in the strong increase in the Guinier Prefactor (see Figure 2 C) and in the decreasing size of the particles (R_g). In the precursor layer the particles (containing metal salts and thiourea) have radii of about 5 nm. During the heating phase, thiourea decomposes, volatile decomposition products evolve out of the layer, CIS nanostructures are formed and therefore R_g decreases to about 3 nm, which corresponds well to the values obtained from TEM images (particle radii: 2-3 nm). The strong increase of the Guinier Prefactor during the heating process, i.e. the scattering intensity, corroborates the formation of an inorganic material in the polymer matrix which has higher density and thus increases scattering contrast.

References:

[1] B.R. Saunders, and M.L. Turner; Nanoparticle–polymer photovoltaic cells; **138**, 1-23 (2008)

[2] S. Guenes, N.S. Sariciftci; Hybrid solar cells; Inorg. Chim. Acta **361**, 581-588 (2008)

[3] E. Maier, T. Rath, W. Haas, O. Werzer, R. Saf, F. Hofer, D. Meissner, O. Volobujeva, S. Bereznev, E. Mellikov, H. Amenitsch, R. Resel, and G. Trimmel; $CuInS_2$ – Poly(3-(ethyl-4-butanoate)thiophene) Nanocomposite Solar Cells: Preparation by an In Situ Formation Route, Performance and Stability Issues; Sol. Energy Mater. Sol. Cells **95**, 1354-1361 (2011)

[4] G. Beaucage; Approximations Leading to a Unified Exponential/Power-Law Approach to Small-Angle Scattering; J. Appl. Crystallogr. **28**, 717–728 (1995)

[5] J.S. Pedersen; Analysis of small-angle scattering data from colloids and polymer solutions: modeling and least-squares fitting; Adv. Colloid Interface Sci. 70, 171 – 210 (1997)

[6] D.J. Kinning; E.L. Thomas; Hard-sphere interactions between spherical domains in diblock copolymers; Macromolecules 17, 1712-1718 (1984)

ARGON ADSORPTION ON CMK-5 CARBON MONITORED BY IN SITU LOW-ANGLE XRD

W. Schmidt[1], H. Amenitsch[2], A. Lu[3] and J. Nitz[1]

1.) Max-Planck-Institut für Kohlenforschung, Kaiser-Wilhelm-Platz 1, D-45470 Mülheim a.d. Ruhr, Germany
2.) IBN, Österreichische Akademie der Wissenschaften, A-8042 Graz, Austria
3.) School of Chemical Engineering, DUT, Dalian 116012, China

CMK-5 – type carbon with an ordered arrangement of tubular pores has been synthesized with mesoporous silica SBA-15 [1,2] as hard template by nanocasting of carbon [3-5]. Furfuryl alcohol as carbon precursor has been deposited and polymerized on the pore walls of the parent SBA-15 silica. Carbonization of the polymer resulted in a carbon coating on the pore walls. Dissolution of the parent silica in alkaline solution resulted in the mesoporous carbon material denoted as CMK-5. Such carbons possess very high surface areas up to 1600 m^2g^1 and consist of hexagonally ordered tubes, the walls of which consist of amorphous carbon. Small carbon bridges between the carbon tubes keep the tubes in the hexagonally ordered arrangement. Due to regular hexagonal ordering of the carbon nanotubes, diffraction patterns are observed in X-ray experiments. The reflections are observed in the low angle range because of unit cells with dimensions of about 10 nm. The diffraction patterns are superimposed to small angle scattering. The structure of CMK-5 can be described with hexagonal symmetry in two dimensions. Since no translational order exists along c, only (hk0) reflections are observed. Two independent types of mesopores exist in this material, one being the volume inside the carbon tubes, the other being the voids in between the tubes. These properties make CMK-5 materials interesting adsorbents. In a first study in 2009, adsorption of dichloromethane at room temperature had been investigated by monitoring the adsorption process by in-situ XRD measurements. These experiments showed that substantial contraction and expansion of the hexagonal array of carbon tubes occurred during the adsorption process. Adsorption at low relative pressures proceeded firstly in the interstitial pores between the carbon tubes. Once these pores are filled, further uptake occurred in the tubular pores.

Low angle XRD investigations on Argon adsorption at cryogenic temperature now have been performed at the SAXS beamline of the Austrian Academy of Sciences (IBN) at the synchrotron radiation source Elettra in Trieste, Italy. In situ XRD patterns have been recorded during the complete adsorption and desorption process. A CMK-5 sample was placed in a 2 mm quartz glass capillary which was attached to a dosing unit consisting of a manifold, pressure gauge, adsorptive reservoir, and a vacuum pump. After activation of the CMK-5 sample at 200°C under vacuum, it was cooled to cryogenic temperature by a nitrogen gas flow that was cooled down to temperatures of 77-80 K with liquid nitrogen. The temperature was maintained by an Oxford Cryostream system. Subsequently diffraction patterns were recorded prior to gas adsorption and successively during dosing Argon to the activated carbon material. Dosing of the argon proceeded stepwise by slowly increasing the dosing pressure in the manifold and then exposing the sample to the gas in the manifold. After equilibrium was achieved, XRD patterns have been measured at each pressure point. In that way, a full isotherm could be measured up to saturation pressure. From the saturation pressure of 290 mbar, the temperature at the sample was calculated to be 78 K. The measured XRD patterns showed up to 8 reflections which could be indexed assuming hexagonal symmetry.

From the integrated intensities of the individual reflections, structure factors (Fhk0) have been derived which have been used for calculation of electron density maps via inverse Fourier transformation, as illustrated in Figure 1. The respective phases have been calculated from structure models. From the electron density maps it could be seen that in the early stages of adsorption the interstitial pores between the carbon tubes are filled with the adsorbate,

similarly as for the adsorption with dichloromethane (DCM). However, a strong decrease followed by expansion of the lattice constant as for DCM adsorption at room temperature was not observed during argon adsorption at 78 K. Only a rather modest change of lattice constant during the whole adsorption process was observed. The tubular arrays are either less flexible at 78 K or the interaction of argon with the pore walls is less strong than with DCM. These results are of fundamental importance for the understanding of adsorption processes.

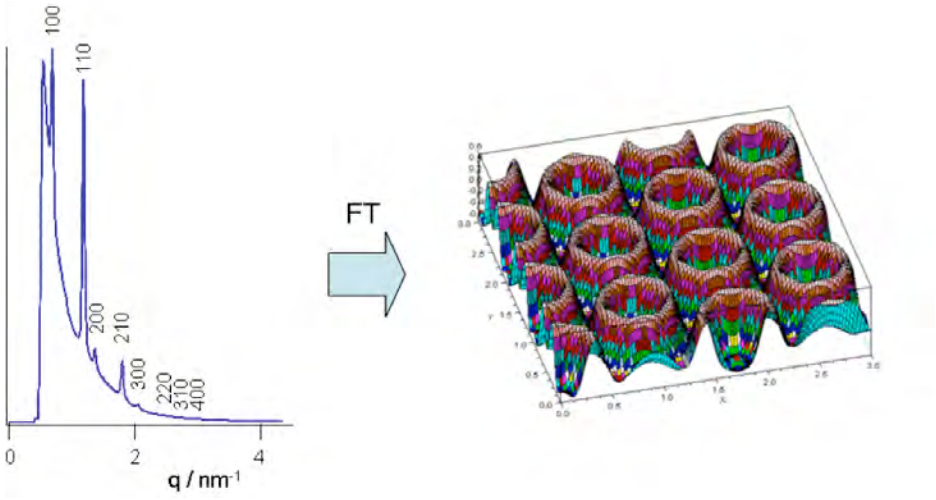

Figure 1. Low-angle XRD pattern of CMK-5 and electron density map calculated from structure factors that have been derived from integrated intensities of the individual reflections.

References:

[1] D. Zhao, J. Feng, Q. Huo, N. Melosh, G.H. Frederickson, B.F. Chmelka, G.D. Stucky, Science **279**, 548-552 (1998)

[2] D. Zhao, Q. Huo, J. Feng, B.F. Chmelka, G.D. Stucky, J. Am. Chem. Soc. **120**, 6024-6036, (1998).

[3] S. Jun, S.H. Joo, R. Ryoo, M. Kruk, M. Jaroniec, Z. Liu, T. Ohsuna, O. Terasaki, J. Am. Chem. Soc. 122, 10712-10713 (2000)

[4] S.H. Joo, S.J. Choi, I. Oh, J. Kwak, Z. Liu, O. Terasaki, R. Ryoo, Nature **412**, 169-172 (2001)

[5] S. Che, K. Lund, T. Tatsumi, S. Iijima, S.H. Joo, R. Ryoo, O. Terasaki, Angew. Chem. Int. Ed. **42**, 2182-2185 (2003)

SAXS/DSC/WAXD STUDY OF THE TEMPERATURE EVOLUTION IN NANOCOMPOSITE POLYMER ELECTROLYTES WITH DIFFERENT NANOFILLERS

A. Turković[1], P. Dubček[1], K. Juraić[1] and S. Bernstorff[2]

[1] Institute "Ruđer Bošković", P.O.Box 180, HR-10002 Zagreb, Croatia
[2] Sincrotrone Trieste, 34149 Basovizza /Trieste, Italy

Polymer electrolytes as nanostructured materials are very attractive components for batteries and opto-electronic devices. $(PEO)_8ZnCl_2$ polymer electrolytes were prepared from PEO and $ZnCl_2$. The nanocomposites $(PEO)_8ZnCl_2$ themselves contained TiO_2, Al_2O_3, MgO, ZnO and V_2O_5 nanograins. In this work, the influence of the ZnO and TiO_2 nanograins on the morphology and ionic conductivity of the nanocomposite was systematically studied by transmission small-angle X-ray scattering (SAXS) simultaneously recorded with wide-angle X-ray diffraction (WAXD) and differential scanning calorimetry (DSC). SAXS experiments are suitable to determine the structure of nanocomposite polymer electrolyte. Polymeric complexes of $(PEO)_n$ with $ZnCl_2$ have been used, due to their stability and very high conductivity [1,2].

The measurements yielded insight into the temperature-dependent changes of the grains of the electrolyte. The heating and cooling rates were 1°C/min, ½ °C/min and ¼ °C/min.

Our research was aimed to study the temperature behavior of the nanocomposite $(PEO)_8ZnCl_2$ electrolyte, and to optimize its properties [3-5] as these materials are attractive as electrolytes for second generation of polymer-based rechargeable batteries [6, 7]. This structural investigation provided informations about the behavior of the nanosizes through the superionic phase transition, which occurs at ~65 °C.

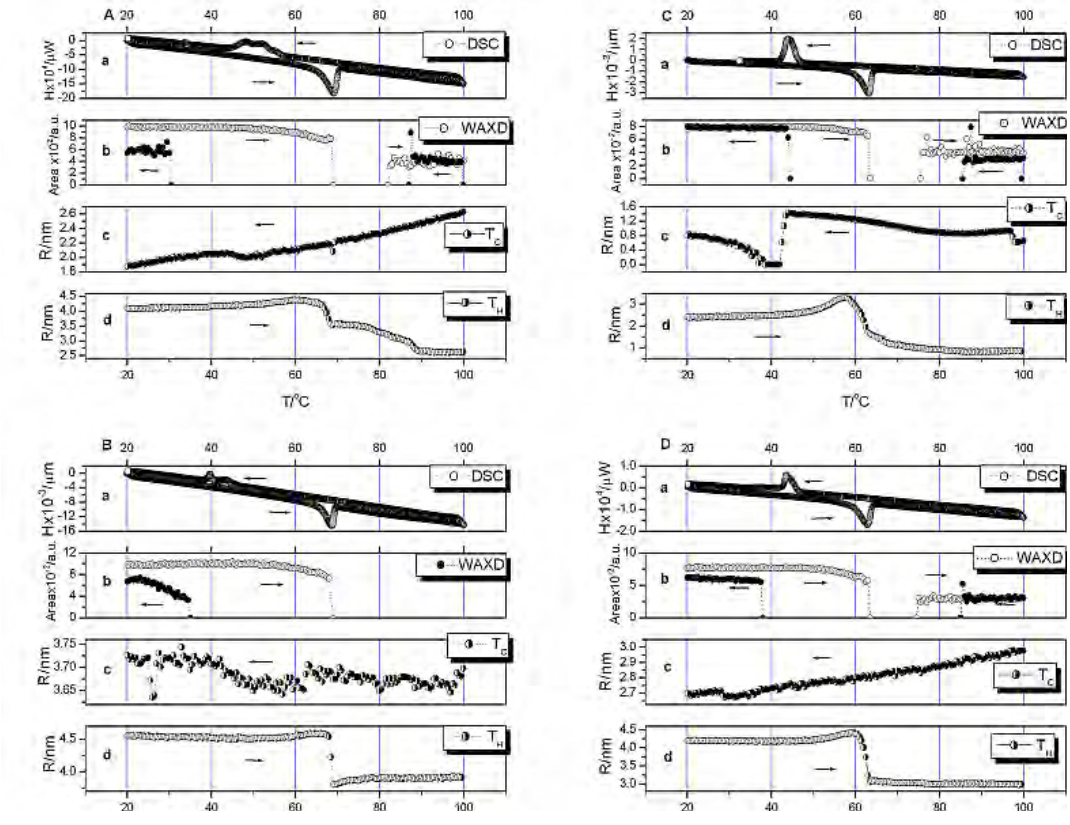

Figure 1. SAXS, DSC and WAXD results for samples A, B, C and D.

Figure 1 shows the results from the simultaneous SAXS, DSC and WAXD measurements in the temperature range from 20°C to 100°C to 20°C at rate of ½ C°/min on the polymer electrolytes: $(PEO)_8ZnCl_2$, $(PEO)_8ZnCl_2/TiO_2$, $(PEO)_8ZnCl_2$ irradiated with a dose of 309 KGy and $(PEO)_8ZnCl_2/TiO_2$ + 309 KGy (denoted as A, B, C and D respectively). In Fig. 1 graph A shows the results from the SAXS/WAXD/DSC measurements in the temperature range from 20°C -> 100°C -> 20°C at the rate of ½ C°/min performed on polymer electrolyte $(PEO)_8ZnCl_2$. The SAXS intensity close to I_s (for s~0) is falling at 68.3°C indicating the phase transition temperature in the heating cycle. The phase transition temperature in the cooling cycle is at 47.6°C due to hysteresis. The average grain radius varies from 4.0 nm to 4.4 nm in the region below the phase transition temperature and then from 3.5 nm to 2.6 nm in the highly conductive phase. The cooling cycle in the SAXS data shows a change of the grain sizes in the range from 2.6 nm to 1.9 nm. SAXS measurements for $(PEO)_8ZnCl_2/TiO_2$ (Fig. 1 B), result in changes of grain sizes from 4.6 to 3.7 nm, the third sample $(PEO)_8ZnCl_2$ irradiated with a dose of 309 KGy (Fig. 1 C), registers changes from 3.3 to 0.7 nm and during the fourth run on the sample $(PEO)_8ZnCl_2/ TiO_2$ + 309 KGy (Fig. 1 D), grain sizes change from 4.4 to 2.7 nm. From these we can generally conclude that the average grain sizes in all four samples remained in the same range from 0.7 to 4.6 nm. In a lamellar picture of PEO [8] these grain sizes would correspond to the lamellae LP2 with no integrally folded (NIF) chains [9] combined with salt and TiO_2.

Table 1. Changes of the average grain radius R (nm) as obtained by SAXS, R=D/2 as determined from WAXD and DSC-obtained phase transition temperatures t (in °C) in $(PEO)_8ZnCl_2/TiO_2$ nanocomposite polyelectrolyte during heating and cooling with a rate of ½ °C/min.

Sample	Heating				
	SAXS		WAXD		DSC
	t (°C)	*R (nm)*	*t (°C)*	*R (nm)*	*t (°C)*
A	68.3	4.0-4.4 3.5-2.6	68.9;82.2	34-45; 95-96	65.3
B	68.7	4.6-4.5 3.8-3.9	68.9	35-47	65.0
C	62.5	2.4-3.3 1.7-0.8	63.0; 75.5	45-51; 82-82	59.0
D	63.4	4.2-4.4 3.0-3.0	63.4; 74.7	45-58; 109-111	58.4
Sample	**Cooling**				
	SAXS		**WAXD**		**DSC**
	t (°C)	*R (nm)*	*t (°C)*	*R (nm)*	*t (°C)*
A	47.6	2.6-2.0 2.0-1.9	30.3; 87.0	57-61; 68-85	56.2
B	49.2	3.7-3.65 3.65-3.7	35.0	50-102	44.6
C	42.2	0.7-1.5 0.8-0.7	43.0; 85.6	45-45; 109-111	46.6
D	28.8	2.9-2.8 2.7-2.7	37.6; 85.1	54-62; 66-111	46.4

The SAXS, WAXD and DSC data show a hysteresis, i.e. the phase transition temperature in the cooling cycle is much lower than 65°C, which is the melting temperature of the PEO crystallites, i.e. the spherulites [10]. In the case of the nanocomposite polymer electrolyte, combined forms of PEO and ZnCl2, or both in combination with TiO2 crystallites, influence the melting temperature. The combined WAXD, SAXS and DCS results are summarized in the Table 1. Environment friendly galvanic cells as well as solar cells of the second generation are to be constructed with nanocomposite polymer as electrolyte.

References:

[1] T.M.A. Abrantes, LJ.Alcacer and C.A.C. Sequeira, Solid State Ionics 18/19, 315 (1986)
[2] M.J.C. Plancha, C.M. Rangel and C.A.C. Sequeira, Solid State Ionics 116, 293 (1999)
[3] A. Turković, P. Dubček, K. Juraić, A. Drašner and S. Bernstorff, Materials, 3/11, 4979 (2010)
[4] A. Turković, P. Dubček, K. Juraić, M. Rakić and S. Bernstorff, Journal of The Organic and Inorganic Polymers, 21, 1-5 (2011) DOI: 10.1007/s10904-011-9469-7, Online First
[5] A. Turković, P. Dubček, M. Rakić, M. Lončarić, B. Etlinger and S. Bernstorff, Vacuum, in press 2011
[6] S.J. Visco, M. Liu, L.C. Dejonge, Cell for making secondary batteries, Patent number 5162175, Nov.10, (1992)
[7] F. Brochu, M. Duval, Additives for extruding polymer electrolytes, Patent number: 5622792 Apr 22, (1997)
[8] J. Baldrian, M. Steinhart, A. Sikora, H. Amenitsch, S. Bernstorff, S. Fibres & Textiles in Eastern Europe, 13 (5), 35-40 (2005)
[9] J. Baldrian, M. Horky, A. Sikora, M. Steinhart, P. Vleek, H. Amenitsch, S. Bernstorff, Polymer, 40, 439-445(1999)
[10] I. Pucić, A. Turković, Solid State Ionics 176, 1797-1800 (2005)

STUDY OF POLYMER ELECTROLYTE FOR ZN RECHARGEABLE NANOSTRUCTURED GALVANIC CELLS VIA COMBINED IN SITU SAXS/DSC/WAXD MEASUREMENTS

A. Turković[1], P. Dubček[1], B. Etlinger[1] and S. Bernstorff[2]

[1] Institute "Ruđer Bošković", P.O.Box 180, HR-10002 Zagreb, Croatia
[2] Sincrotrone Trieste, 34149 Basovizza /Trieste, Italy

SAXS experiments are suitable to determine the microstructure of nanocomposite polymer electrolyte. Solid electrolyte poly(ethyleneoxide) (PEO) is one of the most extensively studied systems due to its relatively low melting point and glass transition temperature, Tg, its ability to play host to varied metal salt systems in a range of concentrations and to act as a binder for other phases. For these reasons PEO has been the basis of many investigations in the area based on composites of a polymer and an insulating ceramic. Polymeric complexes of $(PEO)_n$ with $ZnCl_2$ have been used, due to their stability and very high conductivity as compared to other complexes [1]. The mechanical properties of amorphous of PEO-based electrolytes are poor and attempts to improve these have included the addition of inert filler. Many kinds of ceramic fillers such as micron and nanosized TiO_2 or Al_2O_3 particles, as for instance these nano-particles with particle sizes of 5.8–13 nm in $(PEO)_8LiClO_4$ [2], were used. An increase in conductivity of three orders of magnitude was seen at temperatures up to the melting point of the PEO complex. Above the melting point of the complex, the effect of the filler on the conductivity was only moderate. We intend to improve the electrical conductivity of polymer electrolyte $(PEO)_8ZnCl_2$ by introducing nano-particles of TiO_2 and as a new project nano-particles of ZnO, Al_2O_3, MgO_2 and V_2O_5. An alternative approach is to bring about interchain linking by exposure of the polymer to high-energy radiation [3]. As polymer is a composite of an amorphous and a crystalline part and conductivity is occurring in the amorphous part, both treatments were directed towards inhibition of the crystalline phase in the polymer matrix [4-6].

The aims of the present investigation were to study the SAXS/DSC/WAXD temperature behaviour of $(PEO)_8ZnCl_2$ electrolyte, the same prepared as nanocomposite using 10 % of nano-sized Degussa P-25 TiO_2 and other different nano-fillers as ZnO, Al_2O_3, MgO_2 and V_2O_5, and that of cross linked $(PEO)_8ZnCl_2$ obtained by γ-radiation.

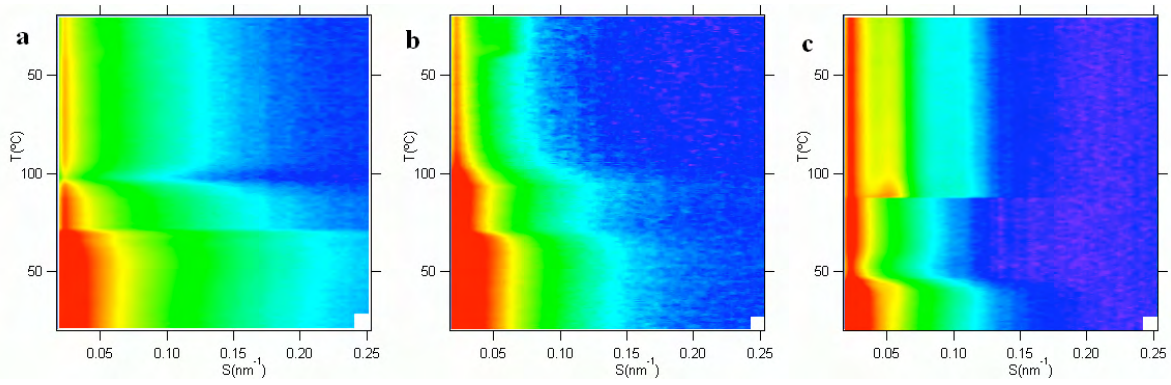

Figure 1. SAXS results for nanocomposite polyelectrolyte $(PEO)_8ZnCl_2$ in the temperature range from 20°C to 100°C, measured at a rate of ½°C/min, for a) $(PEO)_8ZnCl_2$ /Al_2O_3; b) $(PEO)_8ZnCl_2$ /MgO and c) $(PEO)_8ZnCl_2$ /V_2O_5.

Figure 1 shows the SAXS results on polymer electrolyte $(PEO)_8ZnCl_2$ nanocomposite with three nanofillers which were measured simultaneously with WAXD and DSC at the SAXS-beamline of ELETTRA. The evolution of the average radii of the grain sizes obtained

by applying the Guinier law is compared to the corresponding DSC and WAXD spectra behaviour. These results are presented in Table 1.

TABLE 1. Changes of the average grain radius <R>/nm determined by SAXS, and phase transition temperatures T (in °C) in $(PEO)_8ZnCl_2$ polyelectrolyte with different nanofillers (x) during heating and cooling as determined by simultaneous SAXS/WAXS/DSC measurements.

$(PEO)_8ZnCl_2$ + x	heating			
	SAXS		WAXS	DSC
x/nm	T (°C)	<R> (nm)	T (°C)	T (°C)
Al_2O_3 /5.1	66.9	8.6-6.1	70.1	66.8
MgO /13.3	66.4	11.7-9.8	71.2	65.3
V_2O_5 /9.1	45.4	10.1-9.9	48.0	64.1
$(PEO)_8ZnCl_2$ +x	cooling			
	SAXS		WAXS	DSC
x /nm	T (°C)	<R> (nm)	T (°C)	T (°C)
Al_2O_3/5.1	42.5	5.7	39.6	52.5
MgO/13.3	39.3	6.3	39.8	54.4; 48.9
V_2O_5 /9.1	40.6	6.2	40.4	49.9; 45.3; 44.1

The combined SAXS/WAXD/DSC measurements have shown that the nanostructure of the nanopolymer electrolyte $(PEO)_8ZnCl_2$ is changing during the crystalline-amorphous phase transition to a highly conductive superionic phase. In samples with nanofillers, the conductivity is higher and the phase transition temperature lower than for pure $(PEO)_8ZnCl_2$, which are desirable properties for applications in batteries. The significant role that the nanodimensions of the electrolyte material play in the Zn^{2+}-ion mobility was discussed. The combined SAXS/WAXD information about the evolution of the average grain sizes during the phase transition gave insight into the nanomorphology, which influences the ionic transport in a nanocomposite polymer electrolyte. Further optimizations of the electrolyte properties are in progress since these nanostructured materials are very attractive for batteries or other types of electronic devices.

References:

[1] T.M.A. Abrantes, LJ.Alcacer and C.A.C. Sequeira, Solid State Ionics 18/19, 315 (1986)
[2] F. Croce, G.B. Appetecchi, L. Persi and B. Scrosati, Nature 394, 456-458 (1998)
[3] I. Pucić, A. Turković, Solid State Ionics 176, 1797-1800 (2005)
[4] A. Turković, P. Dubček, K. Juraić, A. Drašner and S. Bernstorff, Materials, 3/11, 4979 (2010)
[5] A. Turković, P. Dubček, K. Juraić, M. Rakić and S. Bernstorff, Journal of The Organic and Inorganic Polymers, 21, 1-5 (2011) DOI: 10.1007/s10904-011-9469-7, Online First
[6] A. Turković, P. Dubček, M. Rakić, M. Lončarić, B. Etlinger and S. Bernstorff, Vacuum, in press 2011

Life Sciences

SAXS STUDIES OF NOVEL INTERNALLY STABILIZED LIPOSOMES

D. Belton[1], P. Laity[1], and M. Rappolt[2]

1.) University of Huddersfield, Queensgate, Huddersfield, HD1 3DH, UK
2.) Austrian Academy of Sciences, Institute of Biophysics and Nanosystems Research (IBN), c/o Sincrotrone Trieste, Strada Statale 14, km 163.5, 34149 Basovizza (Trieste), Italy

The use of SAXS for examining liposomes and phospholipid bilayers is well established [1, 2] and has been successfully used to study bilayer thickness, liposome size and structure, as well as lipid phase behaviour and dynamics. In the present work we use SAXS to study a novel composite nano-material; the "internally stabilized liposome" (ISL), which incorporates an internal support (a polymer nano-particle) enclosed by a liposome. The aim of the internal support is to help overcome liposome instabilities without compromising the bilayers ability to interact with living systems. Understanding ISLs could have a huge impact on many areas, including elucidating the origins of enveloped virus stability, developing improved drug and gene delivery systems, advancing liposome biophysics and creating synthetic biological components.

Here, we examine the structure of ISLs composed of 100nm amine-modified and sulphate-modified polystyrene nano-spheres coated with a DPPC bilayer. Using preformed polymer nano-particles ensures that reproducible ISLs with a low polydispersity are formed. The amine and sulphate groups provide two simple model systems for interacting with phospholipid head groups. The ISLs are formed by lipid film hydration in the presence of the nano-particles, followed by sonication and extrusion.

We have successfully used dynamic light scattering (DLS) and cryo-scanning electron microscopy (cryo-SEM) to study ISLs and to demonstrate that ISLs with the correct core-shell structure can be obtained. DLS results show that the ISLs have a larger hydrodynamic radius than the uncoated polymer nano-particles; larger by circa 5 nm, which equates to a single bilayer coat. Cyro-SEM results show that the outer lipid coat is spherical and patterned according to the internal polymer nano-particle. SAXS results from Elettra reveal further information about the lipid bilayer; Fig. 1 shows an example of the ISL SAXS data obtained. Preliminary data analysis indicates that the bilayer is located close to the polymer core and that increasing temperature changes bilayer thickness.

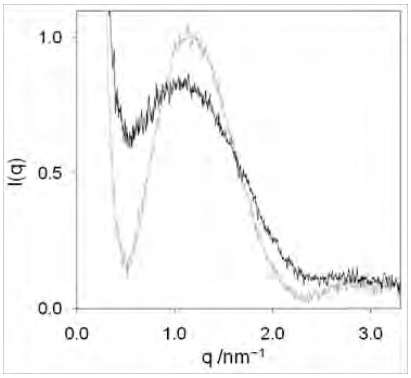

Figure 1: I(q) scattering profiles for ISL at 25°C (—) and 45°C (▬).

References:

[1] J. Katsaras, et al., Neutron and X-ray scattering from isotropic and aligned membranes, in Structure and dynamics of membranous interfaces, ed. K. Nag. 2008, Wiley
[2] Phospholipids Handbook, ed. G. Cevc. 1993, New York: Marcel Dekker

IN SITU STUDY OF SPHINGOMYELINASE ACTIVITY IN PLASMA-MEMBRANE MIMETICS

B. Boulgaropoulos, M. Rappolt, H. Amenitsch, and G. Pabst

Institute of Biophysics and Nanosystems Research, Austrian Academy of Sciences, Graz, Austria

The enzymatic hydrolysis of sphingomyelin (SM) by sphingomyelinase (SMase) was studied as a function of cholesterol (Chol) concentration in membranes mimicking mammalian plasma membranes. The enzymatic reaction was initiated by mixing liposomal dispersions of palmitoyl oleoyl phosphatidylcholine (POPC)/SM (molar ratio = 1/1) and POPC/SM/Chol (molar ratio = 9/9/2) rapidly with a buffer containing 10U of SMase. The samples were then rapidly injected into quartz capillaries and the evolution of the SWAXS signal was studied as a function of time at 37°C.

To obtain first insight on the SM turnover to ceramide (Cer) by the enzyme, we focused on the WAXS signal. In this regime, we observed the generation of a sharp acyl chain correlation peak, in agreement with the formation of a gel phase, rich in Cer reported in our previous studies [1, 2]. In particular, we compare the evolution of the normalized WAXS peak amplitude between the two mixtures. Fig. 1 clearly shows that the increase of the scattering amplitudes proceeds much faster for the cholesterol containing sample, i.e. the plateau value is reached after ~ 150 min, whereas it took ~ 400 min in the absence of ceramide.

At the same time, we performed osmotic pressure experiments of lipid mixtures mimicking the SM turnover to Cer, i.e. SM in POPC/SM/Chol mixtures was gradually replaced by C16:0 Cer. In a previous analogous study, performed in the absence of Chol, we found that Cer retracts SM from the fluid domains to the coexisting gel phase, which leads to a softening of the fluid phase [2]. Here, in the presence of 10 mol% Chol found that the mechanical properties of the fluid phase do not significantly. Thus, SM depletion of the fluid phase does not lead to a softening in the presence of Chol. This can be explained by an increase of Chol in the fluid phase due to its depletion from the gel phase. The higher Chol then accounts for the preservation of the mechanical rigidity of the fluid phase.

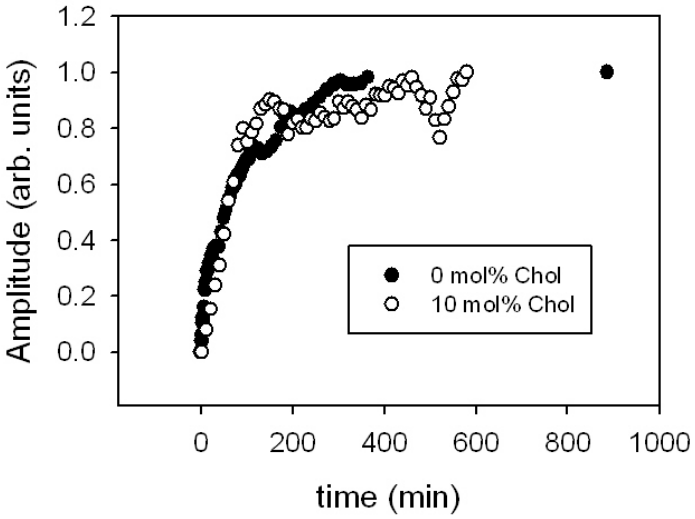

Figure 1. Normalized scatting amplitudes of the chain correlation peak as a function of time and cholesterol content.

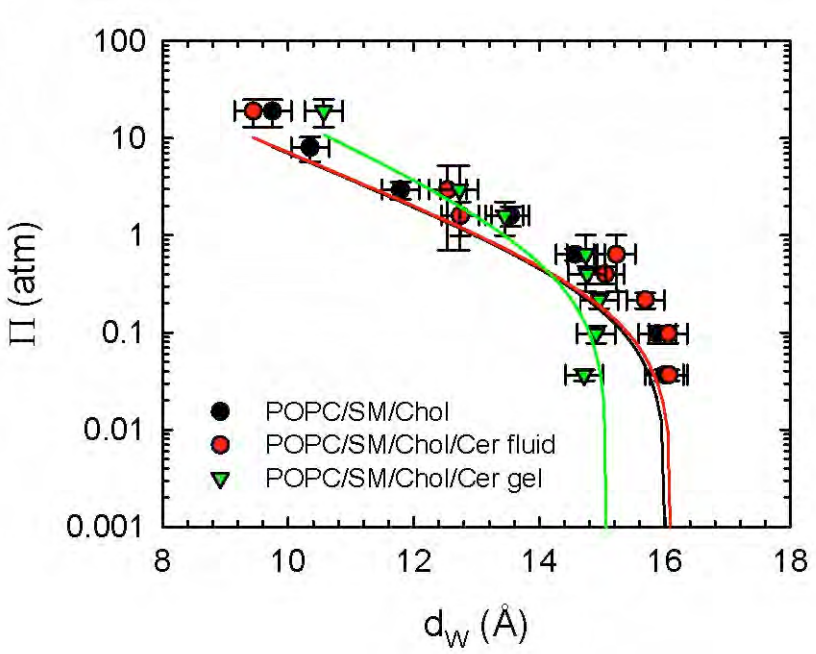

Figure 2. Experimental equation of state of POPC/SM/Chol/Cer mixtures. In the presence of Cer, we found a fluid-gel phase separation. The fluid phase shows an analogous osmotic pressure, Π, vs. water layer separation, d_w, behavior than POPC/SM/Chol.

References:

[1] B. Boulgaropoulos, H. Amenitsch, P. Laggner, and G. Pabst, Implication of sphingomyelin/ceramide molar ratio on the biological activity of sphingomyelinase. Biophys. J 99: 499 – 506 (2010)

[2] G. Pabst, B. Boulgaropoulos, E. Gander, B.R. Sarangi, H. Amenitsch, V.A. Raghunathan, and P. Laggner. Effect of ceramide on nonraft proteins. J. Membrane Biol. 231: 125 – 132 (2009)

CHARACTERIZATION OF STRUCTURES FORMED BY β-SITOSTEROL AND γ-ORIZANOL MIXTURES IN SUNFLOWER OIL

S. Calligaris[1], S. Da Pieve[1], L. Barba[2], G. Arrighetti[2], M.C. Nicoli[1], H. Amenitsch[3]

1.) Dipartimento di Scienze degli Alimenti, Università di Udine, 33100 Udine, Italy
2.) Istituto di Cristallografia, Consiglio Nazionale delle Ricerche, 34100 Trieste, Italy
3.) Institute of Biophysics and Nanosystems Research, Austrian Academy of Sciences, A-8042 Graz, Austria

In the industry sector there is a clear trend towards the development of new and healthier food products. As part of this development, new ways to achieve the reduction of the level of saturated fatty acids are massively investigated. This is linked to the evidences that the repeated consumption of high levels of saturated and trans-fats in the diet poses a chronic threat to human health by increasing, for instance, the risk of cardiovascular diseases and Type II diabetes.

A promising strategy consists in the possibility to structure oil phases using organogel systems. An organogel can be defined as an organic liquid entrapped within a thermo-reversible, three dimensional gel network (Rogers, 2009). Promising network-forming structurants appear to be mixtures of plant sterols, such as β-sitosterols and γ-oryzanol. The resulting organogel is a transparent system made by the self-assembly of β-sitosterols and γ-oryzanol in a three dimensional network of crystalline nanotubes. On the molecular scale, γ-oryzanol and β-sitosterol molecules are thought to stack very well, docking both sitosterol units on the top of each other and having the ferulic acid moiety of the γ-oryzanol stick out (Pernetti et al., 2007). Despite the interesting applications of these systems, still little information is available in the literature. The SAXS experiments aimed to investigate on one hand the microstructure of the building blocks in the β-sitosterols and γ-oryzanol organogels and on the other hand their self-/diss-assembly with time-resolved measurements. To this purpose, organogels were prepared by mixing increasing percentage (from 3 to 20 %) of the structuring agents in sunflower oil. Different ratios between β-sitosterols and γ-oryzanol were also considered. This research activity is part of a larger research work that is actually carried out at the Department of Food Science of the University of Udine on the development of new formulation strategies for the production of health-added value foods.

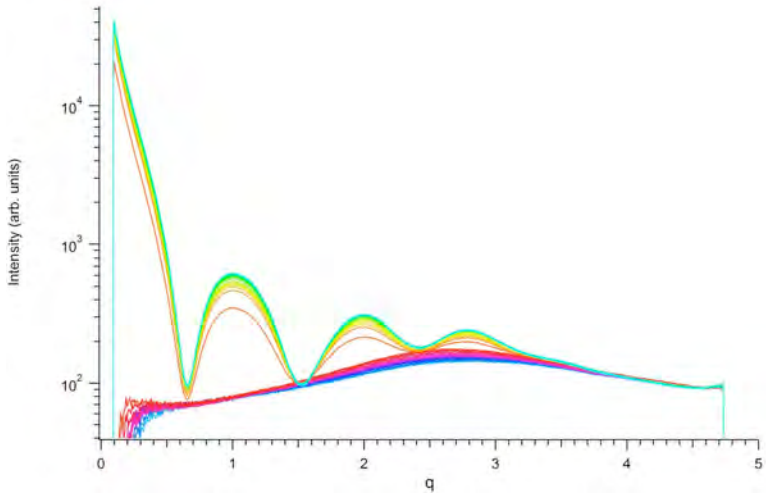

Figure 1. Time-resolved X-ray scattering pattern of 20 % organogel, containing β-sitosterols and γ-oryzanol in 40:60 ratio, recorded during cooling from 120 to 20 °C with 1°C/min.

A typical example is given in Figure 1, which shows the X-ray scattering pattern of just prepared 20 % organogel, containing β-sitosterols and γ-oryzanol in 40:60 ratio, recorded during cooling from 120 to 20 °C. Results seem to indicate that the β-sitosterols and γ-oryzanol organize to form tubes inside the sunflower oil. The correlation length of 20 November organogel, containing β-sitosterols and γ-oryzanol in 40:60 ratio, recorded during cooling and heating from 120 to 20 °C and *viceversa* is reported in Figure 2. The results reveal time/temperature course of the self- and diss-assembly process of the nanotubes.

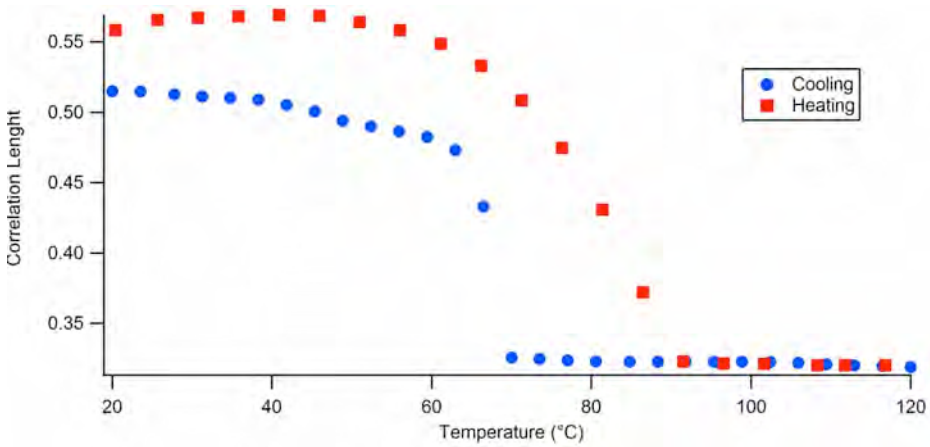

Figure 2. Correlation length of 20 November organogel, containing β-sitosterols and γ-oryzanol in 40:60 ratio, recorded during cooling (blue) and heating (red) from 120 to 20 °C (1°C/min) and *vice versa*.

References:

[1] M. A. Rogers, A. J. Wright, A. G. Marangoni, Oil organogels: the fat of the future? *Soft Matter* **5**, 1594-1596 (2009)

[2] M. Pernetti, K. F. van Malssen, E. Flöter, A. Bot. Structuring of edible oils by alternatives to crystalline fat. *Current Opinion in Colloid and Interface Science*, 12, 221-231 (2007)

EXISTENCE OF HYBRID STRUCTURES IN CATIONIC LIPOSOME/DNA COMPLEXES REVEALED BY THEIR INTERACTION WITH PLASMA PROTEINS

G. Caracciolo[1], D. Pozzi[1], H. Amenitsch[2]

1.) Department of Molecular Medicine, Sapienza University of Rome, Viale Regina Elena, 324, 00161, Rome, Italy
2.) Institute of Biophysics and Nanosystems Research, Austrian Academy of Sciences, Schmiedlstraße 6, A 8042 Graz, Austria

Research efforts are currently focused on studying diseases of genetic origin by introducing the defective gene(s) in malfunctioning target cells [1]. Initial efforts focused on viruses as these vectors exhibited high efficiency at delivering nucleic acids to numerous cell lines. Major drawbacks connected with viral vector systems, including toxicity, immunogenicity, and restrictions with respect to scale-up procedures, promoted the investigation of non-viral scaffolds [2-4]. Among these, cationic liposomes (CLs)/DNA complexes (lipoplexes), because of their least immunogenic nature, robust manufacture, ability to deliver large pieces of DNA and ease in handling and preparation techniques, are finding increasing applications in non-viral gene therapy. The improvement of lipoplex vectors necessitates a better understanding of their mechanism of transfection, and the chemical and physical parameters of lipoplexes influencing it. Thus, a large amount of work has been performed in order to understand the formation and structure of lipoplexes, and to identify correlations between the structures of the complexes and their transfection efficiency. However, many aspects of the compaction phenomena, mainly related to the structure and morphology of the complex, still remain unclear. In this study, the structure and morphology of lipoplexes made of the cationic lipid (3-[N-(N′,N′-dimethylaminoethane)-carbamoyl])-cholesterol (DC-Chol), the zwitterionic lipid dioleoylphosphatidylethanolamine (DOPE) and DNA were investigated. To this end, DLS, zeta potential, synchrotron SAXS, electrophoresis and one-dimensional polyacrylamide gel electrophoresis were performed. The latter technique is a powerful tool to investigate the 'protein corona' adsorbed at the lipoplex surface after interaction with human plasma (HP) proteins. Such a rich protein layer constitutes a major element of the biological identity of lipid nanoparticles in vivo. Since proteins binding to lipid membranes strongly depends on the particle surface characteristics, proteomics technique is expected to shed light on the surface properties of lipoplexes and to provide, in turn, new insights on their equilibrium structure [5]. Here we report synchrotron SAXS experiments performed at the Austrian SAXS station of the synchrotron light source ELETTRA (Trieste, Italy), aimed at revealing the structure of CLs and lipoplexes at the nanoscale. Figure 1, panel a, shows the SAXS profile of DC-Chol–DOPE CLs. The system exhibited only pure diffuse scattering, while quasi–Bragg peaks were not observed [6]. Such a diffraction pattern is typical of uncorrelated bilayers, e.g. small unilamellar vesicles (SUVs). The scattered intensity was fitted with a simple unilamellar vesicle model using the Gaussian-type representation of the electron density profile (EDP) as described in Refs. [6,7], where, according to [6], σ_H is the half width at half maximum of the Gaussian representing the polar region that can be assumed as a realistic estimate of the headgroup size, z_H is the distance of the headgroup to the bilayer center, σ_C is the standard deviation of the Gaussian at the centre of the bilayer accounting for the hydrocarbon chains and ρ is the ratio between the methyl terminus electron density amplitude and the headgroup. The resulting EDP is given in Figure 1, panel b. The more electron dense regions (i.e., the two maxima in the EDP) represent the headgroup region, and the pronounced central minimum at $z = 0$ corresponds to the terminal methyl groups of the opposing acyl chains. The full width at half maximum (FWHM) of the Gaussian representing the headgroup has been assumed as a realistic estimate of the headgroup size, d_H [6]. According to this definition, the bilayer thickness can be determined directly from the electron density profile by $d_B = 2z_H + 2\sigma_H$. From

the EDP of Figure 1, panel b, the bilayer thickness, d_B = 4.55 ± 0.02 nm, and the extension of the polar head group region d_H = 0.85 ± 0.03 nm, were determined. Figure 2, panel a, shows the SAXS pattern of DC-Chol–DOPE/DNA lipoplexes. The sharp periodically spaced peaks at q_{00l} are caused by alternating lipid bilayer–DNA–monolayer multilamellar structure with periodicity d=2q_{00l}=6.91 ± 0.01 nm. From the full width at half maximum (FWHM) of the first-order lamellar Bragg peaks, a domain lamellar size of about L_m =2/FWHM ~ 200 nm could be estimated. Given the lamellar d-spacing, d=6.91 nm, this finding suggests that multilamellar DC-Chol–DOPE/DNA lipoplexes are made of about thirty repeating lipid/DNA layers. Since an upper bound for L_m is given by the size of the globules, we can conclude that most DC-Chol–DOPE/DNA complexes consist of just one lamellar domain. The much broader peak marked by an arrow is the 'DNA peak' arising from the 1D in-plane lattice with repeat distance d_{DNA} = 2/q_{DNA} = 3.32 ± 0.03 nm. This peak is due to the in-plane DNA–DNA spatial correlation and shifts to lower q with increasing cationic lipid/DNA charge ratio. The EDP of DC-Chol–DOPE/DNA lipoplexes was calculated according to Refs. [8-11] and is reported in Figure 2, panel b. It shows the common lipid bilayer density plus high-density regions at the outer edges of the profile due to the DNA rod lattices intercalated between opposing bilayers. The bilayer thickness of lipoplexes (d_B=4.78±0.02 nm) was found to be ~0.2 nm larger than that of DC-Chol–DOPE CLs (d_B=4.55 nm). Such a difference could be almost completely associated to an expansion of the headgroup region, 2σ_H, that enlarged from 0.85±0.03 to about 1.08±0.02nm. Because the DC-Chol–DOPE bilayer thickness is d_B=4.78 nm, the water gap between bilayers d_W= d−d_B = 2.23 nm is just large enough to accommodate a hydrated monolayer of DNA.

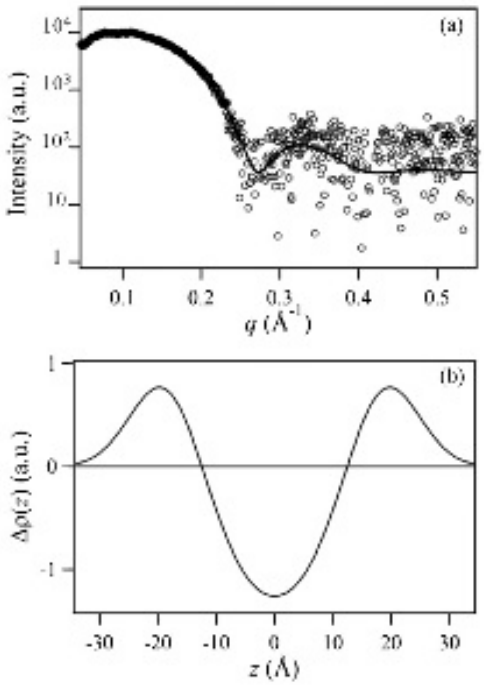

Figure 1. Panel a: SAXS pattern of DC-Chol–DOPE cationic liposomes. The pattern has been fitted using Eq. (1) (solid line). Panel b: electron density profile calculated from the SAXS pattern reported in panel a.

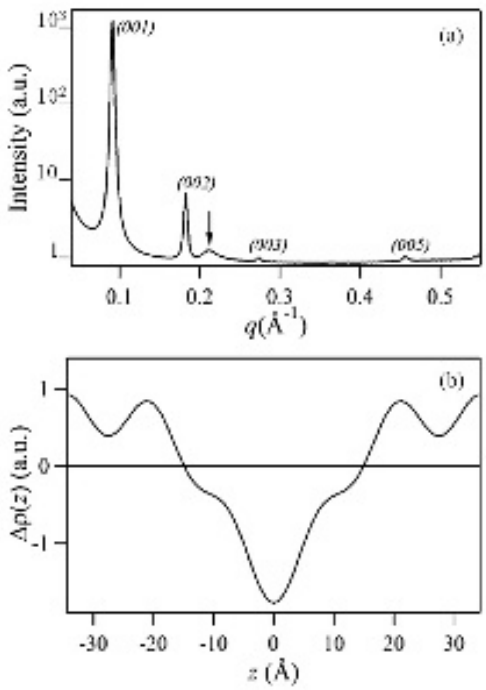

Figure 2. Panel a: SAXS pattern of DC-Chol–DOPE/DNA lipoplexes. Bragg peaks labeled as (*00l*) arise from the multilayered lipid membrane/DNA structure. Black arrow indicates the 'DNA peak' arising from the one-dimensional DNA–DNA in-plane correlation. Panel b: electron density profile calculated from the SAXS pattern reported in panel a: usual lipid bilayer density plus high-density regions at the outer edges of the profile due to the DNA rod lattices intercalated between opposing bilayers.

References:

[1] I. Niculescu-Duvaz, R. Spooner, R. Marais and C. J. Springer; Gene-directed enzyme prodrug therapy; Bioconjug. Chem. **9**, 4-22 (1998)

[2] M. Cavazzana-Calvo, S. Hacein-Bey, G. de Saint Basile, F. Gross, E. Yvon, P. Nus- baum, F. Selz, C. Hue, S. Certain, J.-L. Casanova, P. Bousso, F. Le Deist and A. Fischer; Gene therapy of human severe combined immunodeficiency (SCID)-X1 disease; Science **288**, 669-672 (2000)

[3] S. Hacein-Bey-Abina, C. von Kalle, M. Schmidt and F. Le Deist; A Serious Adverse Event after Successful Gene Therapy for X-Linked Severe Combined Immunodeficiency; N. Engl. J. Med. **348**, 255-256 (2003).

[4] E. Marshall; Gene therapy on trial; Science **288,** 951-952 (2002)

[5] H. Amenitsch, G. Caracciolo, P. Foglia, V. Fuscoletti, P. Giansanti, C. Marianecci, D. Pozzi, A. Laganà; Existence of hybrid structures in cationic liposome/DNA complexes revealed by their interaction with plasma proteins; Coll. Surf. B **82**, 141-146 (2011)

[6] G. Pabst, M. Rappolt, H. Amenitsch and P. Laggner; Structural information from multilamellar liposomes at full hydration: full q-range fitting with high-quality X-ray data; Phys. Rev. E **62**, 4000-4009 (2000).

[7] G. Pabst, R. Koschuch, B. Pozo-Navas, M. Rappolt, K. Lohner and P. Laggner; Structural analysis of weakly ordered membrane stacks; J. Appl. Cryst. **36**, 1378-1388 (2003)

[8] R. Zantl, L. Baicu, F. Artzner, I. Sprenger, G. Rapp and J. O. Rädler; Thermotropic Phase Behavior of Cationic Lipid-DNA Complexes compared to binary lipid mixtures; J. Phys. Chem. B **103**, 10300-10310 (1999)

[9] G. Caracciolo, D. Pozzi, H. Amenitsch and R. Caminiti; One-Dimensional Thermotropic Dilatation Area of Lipid Headgroups within Lamellar Lipid/DNA Complexes; Langmuir **22**, 4267-4273 (2006)

FACTORS DETERMINING THE SUPERIOR PERFORMANCE OF LIPID/DNA/PROTAMMINE NANOPARTICLES OVER LIPOPLEXES

G. Caracciolo[1], D. Pozzi[1], C. Marchini[2], M. Montani[2], A. Amici[2] and H. Amenitsch[3]

1.) Department of Molecular Medicine, SapienzaUniversity of Rome, Viale Regina Elena, 324, 00161, Rome, Italy
2.) Department of Bioscience and Biotechnology, University of Camerino, Via Gentile III da Varano, 62032 Camerino (MC), Italy
3.) Institute of Biophysics and Nanosystems Research, Austrian Academy of Sciences, Schmiedlstraße 6, A 8042 Graz, Austria

One of the most common nonviral gene delivery vectors are DNA-cationic lipid complexes (lipoplexes). On the basis of freeze-fracture electron micrographs and X-ray diffraction studies, it was suggested that lipoplexes are multilamellar onion-like systems with DNA sandwiched between opposing lipid bilayers [1,2]. Once inside the cell, such multilamellar structure offers protection from DNA degradation but do not often allow for an adequate DNA release from endosomal compartments. If gene payload is not released from endosomes, it is shuttled to the lysosomes, where it is degraded by the abundant nucleases and transfection may fail. To overcome this problem, lipid/DNA/polycation (LDP) complexes, in which plasmid DNA (pDNA) condensed with a polycation is encapsulated by a lipid envelope, have recently been developed [3]. Recent studies showed superiority of LPD-mediated gene transfer over conventional liposomes for delivering a gene to the liver [4]. Over the past few years several efforts to improve the delivery efficiency of LPD systems have been made [5,6]. The composition of the lipid envelope of LPD systems has been modified with novel chemical compounds, while the surface has been functionalized with several polymers and ligands. Because physicalchemical properties of gene vectors may determine their interaction with cells and tissues, a precise knowledge of these properties may be important for predicting their biological response both in vitro and in vivo. Comparative studies of pDNA-encapsulation type and lipoplex type gene vectors would therefore provide useful information to decipher the relationship between the physicalchemical properties of gene vectors and their mechanisms of interaction with the cell's components. This knowledge is expected to drive the rational design of highly efficient gene delivery systems.

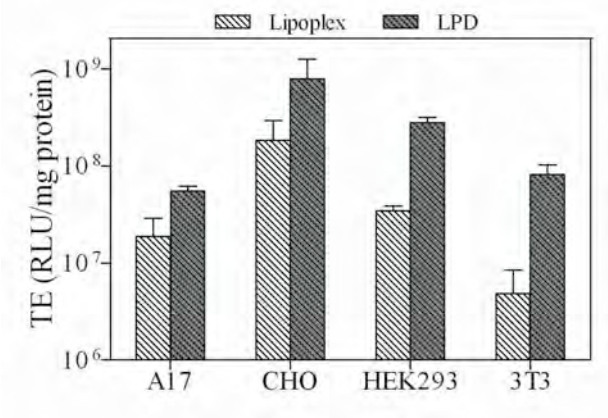

Figure 1. Transfection efficiency of LPD complexes and lipoplexes at the same lipid/DNA ratio (R_V = 2). Luciferase activity is expressed as relative light units/mg of protein in the cell lysate.

In the present study, we show that the transfection efficiency (TE) of protammine/DNA complexes coated with a lipid envelope made of cationic 1,2-dioleoyl-3-trimethylammonium propane (DOTAP) is from 3 to 20 times higher than that of DOTAP/DNA lipoplexes (Figure 1). We asked whether such remarkable difference in TE did correlate with particulate features of complexes. To answer this question, we investigated complex formation, DNA protection ability, surface properties, nanostructure, ability to release DNA upon interaction with cellular lipids, and intracellular trafficking. We present findings showing that the superior efficiency

of LPD complexes over lipoplexes does correlate with their distinctive physicalchemical properties. Here we report SAXS measurements performed at the Austrian SAXS station of the synchrotron light source ELETTRA (Trieste, Italy) with the aim of revealing differences in the nanostructure between DOTAP/DNA lipoplexes and LPD complexes.

Figure 2 (panel A) shows the synchrotron SAXS pattern of LPD complexes at a lipid/ DNA volume ratio, R_V=2. As evident, two broad Bragg peaks, corresponding to a periodicity dq_{001}=7.10 nm, were detected. The large peak width, which is characteristic of a system with a short scattering correlation length, is an indication that the bilayers are weakly bound. Further, the lamellar periodicity, d, is larger than that commonly observed in most DOTAP/DNA complexes (typically 5.56.2 nm). This suggests that the lipid membranes are in a highly swollen state due to electrostatic repulsion between adjacent charged DOTAP bilayers. From the full width at half-maximum (fwhm) of the first-order lamellar Bragg peaks, a domain lamellar size of L_m = 2. We next examined the nanostructure of DOTAP/DNA lipoplexes (R_V=2). Figure 2 (panel B) shows the SAXS pattern of DOTAP/DNA lipoplexes. The sharp periodically spaced peaks at q_{001} are caused by alternating lipid bilayerDNAmonolayer structure with periodicity dq_{001}= 6.01±0.01 nm. This result is in agreement with previous experimental evidence of the DNA- induced liposome restructuring upon lipoplex formation provided by different techniques such as X-ray diffraction and cryoelectron microscopy. The middle peak (marked by an arrow) results from one-dimensional (1D) ordering of the DNA sandwiched between the lipid bilayers. It is usually referred to as "DNA peak" and corresponds to a DNA interhelical spacing $d_{DNA}q_{DNA}$ = 4.01 nm. From the fwhm of the first-order lamellar Bragg peaks, a domain lamellar size of about L_m d-spacing, d=6.00 nm, this finding suggests that DOTAP/DNA lipoplexes are multilamellar onion-like structures made of more than 30 repeating lipid bilayer/DNA monolayer repeat units. The findings reported herein indicate that a LPD system is more efficient in transfecting cells if compared to the consolidated lipoplex strategy. Such a system has evident advantage in terms of endosomal escape and DNA release. Encapsulating pDNA in the lipid envelope would also be an ideal strategy to shield the mutual interactions between DNA and basic serum proteins for in vivo applications as well as to better investigate the interaction between nanocarriers and cellular compartments [7].

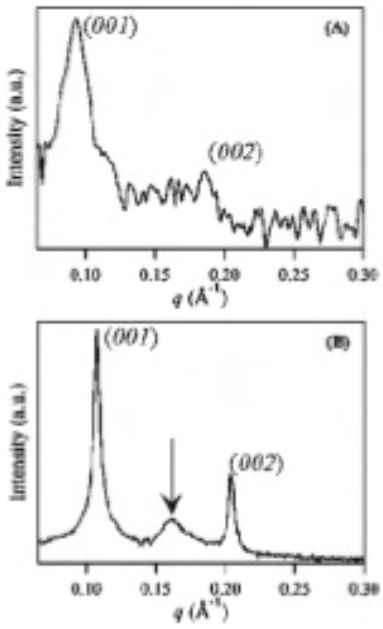

Figure 2. (A) Synchrotron SAXS pattern of LPD complexes at a lipid/ DNA volume ratio, R_V=2. Two broad Bragg peaks, corresponding to a periodicity dq_{001}= 7.10 nm, were detected and larger than those commonly observed in most DOTAP/DNA complexes (typically 5.56.2 nm). (B) Synchrotron SAXS pattern of DOTAP/DNA lipoplexes (R_V=2). The sharp periodically spaced peaks at q_{001} are caused by alternating lipid bilayer DNA monolayer structure with periodicity dq_{001}=6.01±0.01 nm. The middle peak (marked by an arrow) results from one-dimensional (1D) ordering of the DNA sandwiched between the lipid bilayers and corresponds to a DNA interhelical spacing $d_{DNA}q_{DNA}$ =4.01 nm.

References:

[1] T. Salditt, I. Koltover, J. O.Raëdler and C. R. Safinya; Two- dimensional smectic ordering of linear DNA chains in self-assembled DNAcationic liposome mixtures; Phys. Rev. Lett. **79**, 2582-2585 (1997)

[2] G. Caracciolo, R. Caminiti, F. Natali and A. Congiu Castellano; A new approach for the study of cationic lipidDNA complexes by energy dispersive X-ray diffraction; Chem. Phys. Lett. **366**, 200-204 (2002)

[3] K. Kogure, R. Moriguchi, K. Sasaki, M. Ueno, S. Futaki and H. Harashima; Development of efficient packaging method of oligo- deoxynucleotides by a condensed nano particle in lipid envelope structure; J. Controlled Release **98**, 317-323 (2004)

[4] J. Yamauchi, Y. Hayashi, K. Kajimoto, H. Akita and H. Harashima; Comparison between a multifunctional envelope-type nano device and lipoplex for delivery to the liver; Biol. Pharm. Bull. **33**, 926-929 (2010)

[5] Y. Chen, J. Sen, S. R. Bathula, Q. Yang, R. Fittipaldi and L. Huang; Novel cationic lipid that delivers siRNA and enhances therapeutic effect in lung cancer cells; Mol. Pharmaceutics **6**, 696-705 (2009)

[6] Y. Chen, S. R. Bathula, J. Li and L. Huang; Multifunctional nanoparticles delivering small interfering RNA and doxorubicin overcome drug resistance in cancer; J. Biol. Chem. **285**, 22639-22650 (2010)

[7] G. Caracciolo, D, Pozzi, A. Laura Capriotti, C. Marianecci, M. Carafa, C. Marchini, M. Montani, A. Amici, H. Amenitsch, M. A. Digman, E. Gratton, S. S. Sanchez and A. Laganà; Factors Determining the Superior Performance of Lipid/DNA/Protammine Nanoparticles over Lipoplexes; J. Med. Chem. **54**, 4160-4171 (2011)

STUDIES ON THE MECHANISM DELAYING THE POLYMORPHIC TRANSITION OF SOLID TRYGLYCERIDE DRUG CARRIER NANOPARTICLES

S. Joseph[1], M. Rappolt[2], and H. Bunjes[1]

1.) Technische Universität Braunschweig, Institut für Pharmazeutische Technologie, Mendelssohnstr. 1, D-38106 Braunschweig, Germany
2.) Austrian Academy of Sciences, Institute of Biophysics and Nanosystems Research (IBN), c/o Sincrotrone Trieste, Strada Statale 14, km 163.5, 34149 Basovizza (Trieste), Italy

Solid lipid nanoparticles are being investigated as delivery systems for poorly water soluble drugs. They consist of a core of comparatively non-polar lipids and can be stabilized with different emulsifiers. A common way of preparation is high-pressure melt-homogenization followed by a cooling step to crystallize the resulting nanodroplets. When prepared with a triglyceride matrix, solid lipid nanoparticles undergo polymorphic transitions after crystallization. In the case of triglycerides, the metastable α-form crystallizes from the melt which transforms monotropically into the stable β-modification, sometimes via a β'-modification. The type of crystal polymorph may have influence on the drug carrier properties of the nanoparticles, presumably because of the differences in particle shape and crystalline order between the different types of crystal modifications and due to the dynamic processes involved in the structural transformation. Also other pharmaceutically important properties like the viscosity or the colloidal stability of the dispersions may be affected by the type of crystal modification in the nanoparticles. The time-course of polymorphic transitions depends on the type of matrix triglyceride but also on the emulsifier and on the cooling conditions [1-4]. Stabilization of tristearin nanoparticles with poly(vinyl alcohol) (PVA), sodium glycocholate or a combination of sodium glycocholate with hydrogenated lecithin leads to a comparatively high stability of the metastable α-modification. In addition, for nanoparticles stabilized with PVA or sodium glycocholate, the occurrence of an uncommon form of the α-modification was observed that, upon cold storage, could be retained for a considerable period of time in PVA-stabilized nanoparticles. The particles in this uncommon modification exhibit a spherical shape and seem to be rather disordered, as they do not display a pronounced small angle X-ray reflection ("nonlamellar" α-modification).

To elucidate the mechanism of transformation in dependence on stabilization regime and crystallization conditions, tristearin nanoparticles stabilized with PVA, sodium glycocholate and hydrogenated lecithin/sodium glycocholate prepared by high-pressure melt-homogenization and crystallized into the α-form with different cooling rates (0.5 K/min and 70 K/s) were investigated. The samples were investigated shortly after crystallization and in addition after several weeks of storage by simultaneous small and wide angle X-ray diffraction coupled to DSC analysis at four heating rates (1 K/min, 2.5 K/min, 5 K/min and 10 K/min).

At the time point of the experiments, all dispersions displayed a wide angle X-ray diffraction pattern characteristic of the metastable α-modification. All rapidly cooled samples as well as the slowly cooled PVA dispersion did not display a pronounced small angle X-ray reflection, indicating the presence of the nonlamellar α-modification in dependence on the cooling conditions during crystallization. Upon heating, the nonlamellar α-modification transformed into the common, lamellar one observed on the forming as reflected in the formation of a pronounced small angle reflection and a sharper wide angle reflection (Fig. 1). In dependence on the heating rate during the measurements, the common metastable α-modification underwent polymorphic transition into the stable β-modification before the tristearin nanoparticles melted. This scenario, however, was only observed for heating rates lower than

10 K/min and PVA and sodium glycocholate stabilized solid lipid nanoparticles. For the hydrogenated lecithin/sodium glycocholate stabilization regime the polymorphic transition to the stable β-modification was observed independently of the heating rate. An influence of temperature during storage on the polymorphic state was observed as well. PVA stabilized solid lipid nanoparticles were unchanged after storage for 9 month at 5 °C whereas the formation of β-modification was observed on storage at 22 °C and with the other stabilization regimes. The kinetics of the transition of the non-lamellar to the lamellar α-modification and the one of the lamellar α-modification to the β-polymorph differ. The formation of the lamellar α-modification took more time than the formation of the β-modification, indicating that the uncommon structure of the α-modification may be responsible for the high stability of the metastable α-modification.

In conclusion, independent on their stabilization regime, triglyceride nanoparticles in an uncommon α-polymorph undergo polymorphic transition before they melt during heating. The presence of the non-lamellar α-modification depends on the stabilization regime, the cooling conditions during the preparation process and the storage conditions and seems to induce the high kinetic stability of the metastable α-modification. The particles in the uncommon modification seem to be rather disordered, but the detailed organization of the triglyceride molecules is not yet clear.

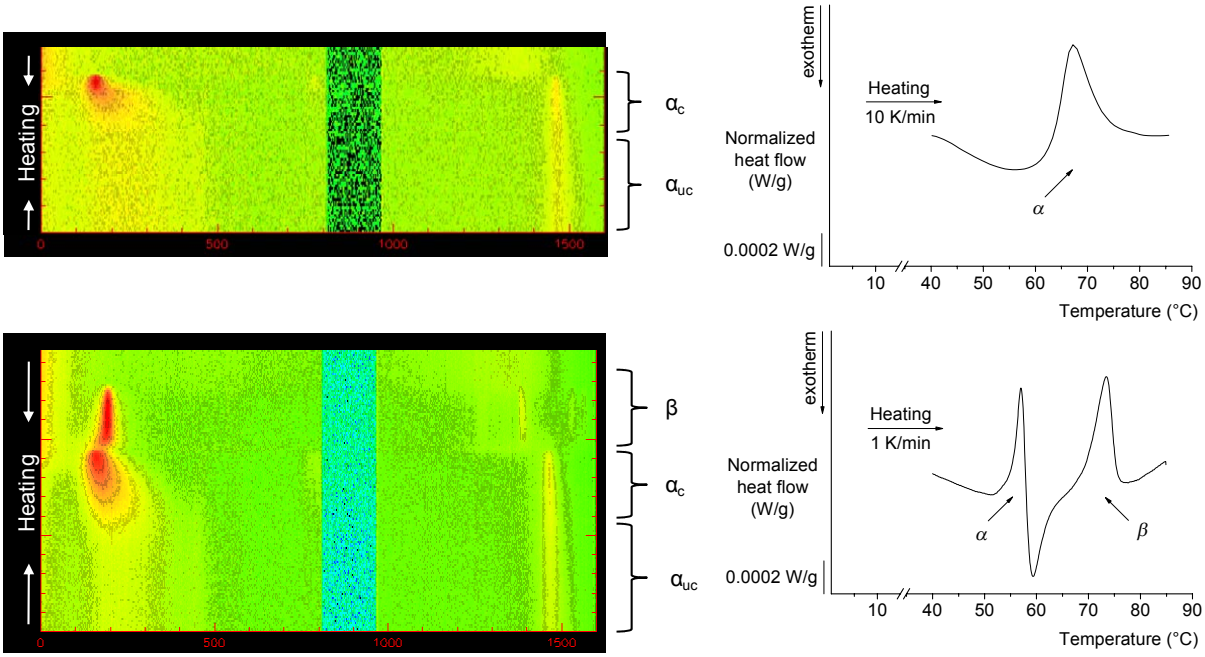

Figure 1. Images of simultaneous small and wide angle X-ray diffractograms and simultaneously recorded DSC curves of rapidly crystallized (70 K/s) PVA stabilized tristearin nanoparticles at two heating rates (10 K/min (top) and 1 K/min (bottom)) (α_c: common α-modification, α_{uc}: uncommon α-modification).

References:

[1] Bunjes, H., Koch, M.H.J., Westesen, K., J. Pharm. Sci. 92 (2003) 1509-1520.
[2] Bunjes, H., Koch, M.H.J., J. Control. Rel. 107 (2005) 229-243.
[3] Rosenblatt, K.M., Bunjes, H., Mol. Pharmaceutics 6 (2009) 105-120.
[4] Jasch, K., Barth, N., Fehr, S., Bunjes, H., Augustin, W., Scholl, S., Chem. Eng. Technol. 32 (2009) 1-10.

NANOASSEMBLIES OF NUCLEOSIDE ANALOGUES COUPLED TO SQUALENE: STRUCTURAL ANALYSIS

E. Lepeltier[1], J.J. Vachon[1], C. Bourgaux[1] and H. Amenitsch[2]

1) UMR CNRS 8612, Faculté de Pharmacie, Univ. Paris-Sud, 5 rue Jean-Baptiste Clément, Châtenay Malabry, France
2) Institute of Biophysics and Nanosystems Research, Austrian Academy of Sciences, Schmiedelstrasse 6, A-8042 Graz, Austria

The results presented below are part of a forecast long-time study on various prodrugs involving terpenoid moieties, within the framework of French or European (ERC) research contracts. Prodrugs are pharmacologically inactive compounds that yield therapeutically active metabolites upon exposure in the biological environment. We focus first on nucleosidic drugs coupled to squalene, an acyclic isoprenoid chain, precursor in the biosynthesis of sterols. Many molecules currently used in clinic against cancer or viral infections like AIDS are nucleoside analogues. Their main mechanism of action is a potent inhibition of DNA or RNA synthesis, which may lead to cell cycle blockage and eventually apoptosis. Squalenoyl prodrugs have been designed to overcome some drawbacks, like a poor stability in vivo and a limited passive intracellular diffusion due to their hydrophilicity, of these parent nucleosidic drugs.

It has been discovered that coupling squalene to nucleoside analogues leads to amphiphilic molecules that self-organize in water as nanoassemblies of 100-300 nm in diameter, irrespective of the nucleoside analogue used [1]. Furthermore, the squalenoyl prodrug of Gemcitabine, an anticancer nucleoside analogue, displays higher anticancer activity than gemcitabine against leukemia models.

When prodrugs self-organize in nanoparticles their supramolecular structure is expected to be an important parameter for the efficacy of the drug delivery system. Indeed, stability of nanoparticles in aqueous medium is sensitive to their structure and nanoassemblies size and shape can affect their ability to diffuse into tissues and to enter cells.

We had previously studied two nucleoside analogues derived from cytidine, Gemcitabine (Gem, dFdC) and Zalcitabine (dideoxycytidine, ddC), coupled to squalene. Small-angle X-ray experiments have evidenced the packing of Gem-SQ molecules in inverse hexagonal phase and of ddC-SQ molecules in inverse bicontinuous cubic phase [2,3]. We have recently investigated squalenoyl gemcitabine monophosphate (Gem-SQ-MP), synthesized with the aim to by-pass the primary phosphorylation step of gemcitabine within cells, necessary for gemcitabine being active.

SAXS investigations, further supported by cryo-TEM, revealed that triethylammonium Gem-SQ-MP self-organized in unilamellar liposomes. As shown in Fig1, the scattering curve corresponds to the form factor of a locally flat membrane. Indeed, in the range q= 0.02 – 0.06 $Å^{-1}$ the log I versus log q plot shows a linear variation with a slope close to -2. At higher q the scattering intensity is characterized by a broad bump followed by a small oscillation, arising from the bilayer thickness (~ 70 Å) [4]. These nanoassemblies were found more active than Gem and Gem-SQ on the resistant L1210 10K leukemia cell line.

Other examples, like that of dideoxyinosine-squalene (ddI-SQ), show that a diversity of structures can be observed, depending on slight modifications of the polar headgroup. The different supramolecular structures of these squalenoyl amphiphiles can be explained by their spontaneous monolayer curvature.

In parallel, we have confirmed that Gem-SQ could be transferred from nanoparticles to phospholipid bilayers and that the insertion of the prodrug within model membranes resulted in the formation of non-lamellar structures. Gem-SQ may induce the formation of an inverse bicontinuous cubic phase in fully hydrated DPPC at room temperature [5,6].

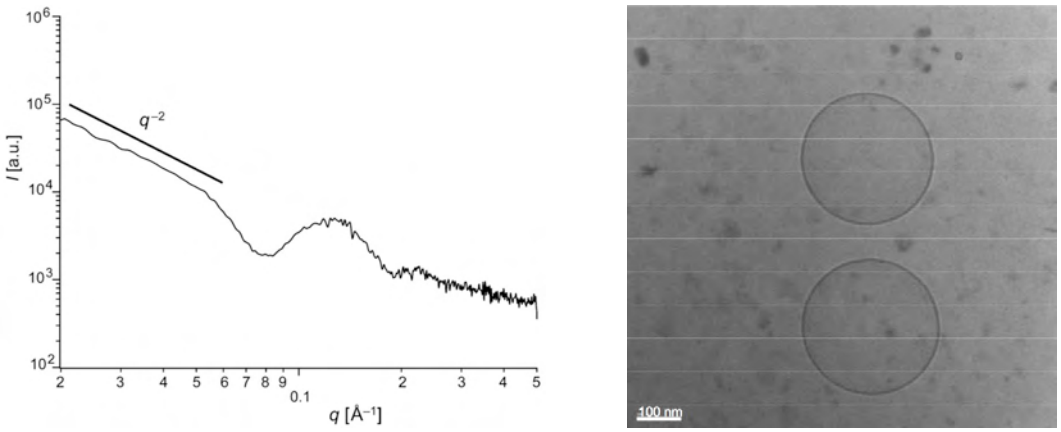

Figure 1. SAXS pattern and cryo-TEM image of unilamellar vesicles of Gem-SQ-MP

References

[1] P. Couvreur, B. Stella, H. Reddy, H. Hillaireau, C. Dubernet, D. Desmaele, S. Lepetre-Mouelhi, F. Rocco, N. Dereuddre-Bosquet, P. Clayette, V. Rosilio, V. Marsaud, J.M. Renoir, L. Cattel. Nanoletters. **6**, 2544-2548, (2006)

[2] P. Couvreur, LH Reddy, S. Mangenot, JH Poupaert, D. Desmaele, S. Lepetre-Mouelhi, B. Pili, C. Bourgaux, H. Amenitsch, M. Ollivon, Small, **4**, 247-253, (2008)

[3] F. Bekkara-Aounallah, R. Gref, M. Othman, L. H. Reddy, B. Pili, V. Allain, C. Bourgaux, H. Hillaireau, S. Lepêtre-Mouelhi, D. Desmaële, J. Nicolas, N. Chafi and P. Couvreur. Advanced Functional Materials, **18**, 3715-3725, (2008)

[4] J. Caron, E. Lepeltier, L.H. Reddy, S. Lepêtre-Mouelhi, S. Wack, C. Bourgaux, P. Couvreur and D. Desmaële, EJOC, **14**, 2615-2628, (2011)

[5] B. Pili, C. Bourgaux, H. Amenitsch, S. Lepêtre-Mouelhi, D. Desmaele, P. Couvreur and M. Ollivon, BBA Biomembrane, 98, 1, 19-28, (2010)

[6] L. Bildstein, B. Pili, V. Marsaud, S. Wack, F. Meneau, S. Lepêtre-Mouelhi, D. Desmaele, C. Bourgaux, P. Couvreur, C. Dubernet, *Accepted EJPB (2011)*

PRESSURE EFFECTS ON AMYLOID FIBRILS AND OLIGOMERS OF ALPHA-SYNUCLEIN: A SAXS INVESTIGATION ON THEIR DISSOCIATION AND REVERSIBLE NATURE

M. G. Ortore[1], F. Spinozzi[1], E. Jr. Baldassarri[1], M. Beltramini[2], I. Tessari[2], L. Bubacco[2], H. Amenitsch[3], M. Steinhart[4] and P. Mariani[1]

1.) Dipartimento di Scienze della Vita e dell'Ambiente, Università Politecnica delle Marche, Via brecce bianche, Ancona, Italy
2.) Dipartimento di Biologia, Università di Padova, Via Ugo Bassi 58b, Padova, Italy
3.) Institute of Biophysics and Nanosystems, Austrian Academy of Sciences, Schmiedlstrasse 6, Graz, Austria
4.) Institute of Macromolecular Chemistry, Heyrovskeho nam. 2, Prague, Czech Republic

It has been recently shown that high-pressure plays a specific role in driving both formation and dissolution of highly ordered aggregates referred to as amyloid fibrils, which are the hallmarks of several neurodegenerative diseases like Alzheimer, Parkinson and systemic amyloidosis [1]. In this context, it has been demonstrated that the fibrillation process can be reversed by hydrostatic pressure, for example by performing consecutive cycles of compression/decompression under aggregating conditions [2].

Because the pathological relevance to Parkinson, we peformed SAXS experiments at the ELETTRA 5.2 L beam-line to monitor the high hydrostatic pressure effects on stability and dissociation of α-synuclein fibrils and monomers, produced from the wild type protein and from two different mutants (A30P and A53T), which show a different fibril reaction pathway. Experiments were performed on 10 mg/ml mature fibril and monomers solutions, at ambient temperature and in a range of pressures between 1÷1500 bar to modify the amyloid fibril/monomer conformation [2]. In fact, for each sample condition, a series of compression-decompression-compression measurements have been performed.

The SAXS curves relative to the wild type and mutant monomers resulted to be not modified by the high pressure treatment. The SAXS curves of the three species of α-synuclein fibrils at ambient pressure were successfully analyzed considering simple cylindrical models for the fibrils. In agreement with AFM data, we observed that cylinders are very long, polydisperse in radii, and with electron densities indicating the presence of internal cavities. The higher pressures available at the SAXS beamline - about 1.5 kbar - slightly modify the fibrils' sizes and density features, without changing the average shape. In particular, high-pressure induces fibril compaction, as revealed both by the decrease of the average particle radius and by the corresponding increase of the electron density. It should be noticed that the increase of the fibrils' electron density induced by high-pressure treatment is larger than that expected from standard protein compressibility values. Such results, show in Table 1, seem to indicate the existence of packing defects in the fibril core, but also suggest that moderate pressures induce dehydration of amyloid fibrils. Indeed, synchrotron FTIR data, obtained by performing a few measurements on the SISSI beam-line at ELETTRA on the same samples, indicate that pressures higher than 3 kbar induce relevant transitions in the amount of fibril secondary structures, pointing out that higher pressures eventually available at the SAXS beamline would be very useful for the biophysicist community.

The whole experiments performed at the ELETTRA synchrotron then confirm that fibrillation can be tuned by compression. Noticeable is the fact that fibrils produced from the wild type α-synuclein were differently susceptible to pressure dissociation than the Parkinson's disease-linked variants, and that each species showed distinct reversibility. These findings suggest different dissociation mechanisms and intermediate states, hinting at the possibility that mutant fibrils would be more easily dissolved into small oligomers by the cellular machinery.

Because the most cytotoxic species are the small aggregates rather than the fibrils, our results gain physiological importance to the determination of therapies against amyloid diseases.

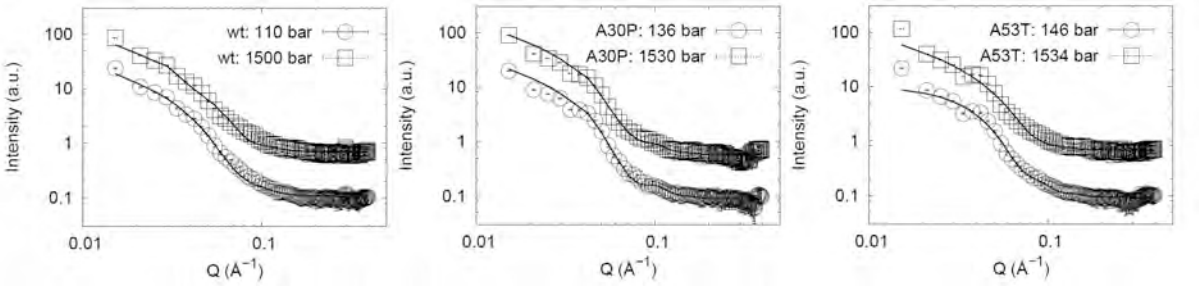

Figure 1. X-ray scattering patterns of wild type, mutants A30P and A53T fibrils at the pressures indicated in the legends. Curves at higher pressures are shifted for the sake of clearness.

Table 1. Parameters resulting from the theoretical curve fitting. Cylinders average radii and electron densities are reported for each fibril species at the lower and the higher pressures.

Sample	Pressure (bar)	Cylinder radius (Å)	ρ_e (e Å^{-3})
Wild type	110 ± 2	38.6 ± 0.3	0.400 ± 0.009
	1500 ± 2	37.0 ± 0.2	0.409 ± 0.005
Mutant A30P	136 ± 2	45.0 ± 0.7	0.404 ± 0.001
	1530 ± 2	41.7 ± 0.4	0.413 ± 0.005
Mutant A53T	146 ± 2	39.1 ± 0.4	0.404 ± 0.002
	1534 ± 2	35.6 ± 0.4	0.413 ± 0.005

References:

[1] D. Foguel, M. C. Suarez, O. D. Ferra-Gonzales, J. L. Silva et al.; Dissociation of amyloid fibrils of α-synuclein and transthyretin by pressure reveals their reversible nature and the formation of water-excluded cavities; PNAS 100, 9831-9836 (2003)

[2] D. Foguel and J. L. Silva; New Insights into the Mechanisms of Protein Misfolding and Aggregation in Amyloidogenic Diseases Derived from Pressure Studies; Biochemistry 43, 11361-11370 (2004)

SAXS CHARACTERIZATION OF INJECTABLE OCULAR DRUG DELIVERY SYSTEMS

M. Schmitt[1], K. Yamada[1], A. Yaghmur[2], M. Rappolt[3], and A. Urtti[1]

1.) Centre for Drug Research, Faculty of Pharmacy, University of Helsinki, Viikinkaari 5E, FIN-00790 Helsinki, Finland
2.) Department of Pharmaceutics and Analytical Chemistry, Faculty of Pharmaceutical Sciences, University of Copenhagen, Universitetsparken 2, DK-2100 Copenhagen, Denmark
3.) Institute of Biophysics and Nanosystems Research (IBN), Austrian Academy of Sciences, Graz, Austria

The main focus in ocular drug delivery studies has shifted from the anterior segment to the posterior segment. Drug delivery to the posterior eye is usually practiced either by intravitreal or by systemic drug administration. Adequate drug concentrations are easily achieved in the posterior segment with intravitreal drug delivery, but this is invasive and potentially dangerous way of drug administration [1]. Systemic drug administration is reasonable for safe antibiotics with wide safety margins, but it is not applicable for potent new drugs with systemic adverse effects [1, 2]. New improved technologies for ocular posterior segment drug delivery are focusing on implantable drug systems with sustained release properties: the drug is released within long period (few years). However, the surgical operation for the implantation of such systems is usually needed to be administered and therefore, it is considered a very big burden to the patients. Figure 1 shows the possible drug administration for ophthalmic treatment. Therefore, we are investigating the possibility of utilizing injectable lipid based systems with prolonged action for posterior segment drug delivery. In this respect, the formulation would be administered as freely flowing non-viscous solution as peri-ocular or subconjunctival injection. The change of temperature (body temperature) and the environmental conditions (e.g. body fluid, ionic strength, pH) upon administration should cause rapid phase change resulting in highly viscous self-assembled system (in situ formation of lipid-based liquid crystalline phase) that will release the drug over long period before the delivery system is biodegraded by the enzymes [3]. Thus, it is important to understand the effect of adding biological fluid, which is similar to that at the administration site, to the non-viscous lipid solution for gaining insight into the behavior of the lipid-based system under these conditions.

To solve these current issues for posterior eye diseases treatment, we are focusing on the possibility of utilizing low viscous injectable ternary mixtures of lipid/organic solvent/drug that self assemble in contact with the ocular biological fluid (e.g. vitreous humor, subconjunctival extract, and tear fluid) after administration to form in situ high viscous and well-ordered liquid crystalline phases [3-6]. For instance, the possible formation in situ of drug-loaded inverted type hexagonal (H_2) or bicontinuous cubic (V_2) liquid crystalline systems with sustained release properties. In Fig. 1, a typical SAX diffraction pattern of a well ordered liquid crystalline phase 7 days after the addition of biological aqueous medium is displayed.

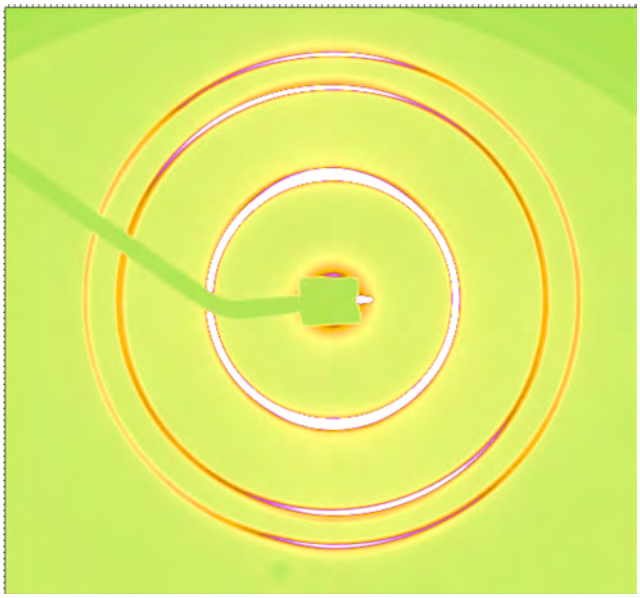

Figure 1. Image plate diffraction pattern of an inverse hexagonal phase (H_2) of an ocular drug delivery system 7 days after a simulated administration.

References:

[1] Urtti A. Adv Drug Deliv Rev. 2006, 58, 1131-1135
[2] Del Amo EM, Urtti A. Drug Discov Today. 2008, 13, 135-143
[3] Chang CM, Bodmeier R. Int J Pharm. 1998, 173, 51-60
[4] Clogston J, Cracium G, Hart DJ, Caffrey M. J Control Release . 2005, 102, 441-461
[5] Fong WK, Tracey Hanley, Ben J. Boyd. J Control Release. 2009, 135, 218-226
[6] Lee KW, Nguyen TH, Hanley T, Boyd BJ. Int J Pharm. 2009, 365, 190-199

SAPONINS MICELLAR BEHAVIOUR AND THEIR INTERACTION WITH LIPID BILAYERS

C.V.Teixeira[1,2], H. Amenitsch[3]

1.) Universitat Autonoma de Barcelona,Facultat de Medicina, Bellaterra, Barcelona, Spain
2.) Universidade Federal do Rio Grande do Sul, Instituto de Física, Av. Bento Gonçalves, 9500, Porto Alegre, 91501-970, RS, Brazil
3.) Institute of Biophysics and Nanosystems Research, Austrian Academy of Science, Schmiedlstrasse, 6, 8043, Graz, Austria

Saponins are natural surfactants, extracted from plants [1], and are normally formed by steroid rings bound to one or more sugar groups [2]. The distribution of sugar groups around the rings originates a huge variety of structures, which present several biological properties, as hypoglycemic, anti-fungal and immunoregulatory activities [3], inhibition of tumoral cells [4], prevention of metastasis and activity against cardiovascular diseases [5]. Saponins have also been shown to increase the intestinal permeability to drugs [6]. This work focuses on two particular saponins: Quillaja Saponin (QS), from the bark of a tree with the same name, and the Glycyrrhizic acid ammonium salt (GA), extracted from glycyrrhiza root (licorice), whose structures are represented in Figure 1. QS has been shown to have immunological activity and has been tested for the preparation of vaccines against influenza, Eschirichia Coli, HIV-1, measles, malaria, leishmaniasis and even for the treatment of melanoma [7]. It has also presented the property of interacting with cholesterol and reducing the plasma cholesterol in several mammalians [8]. However, QS, as well as other saponins, might present toxic or hemolytic effects. GA has been used for the treatment of stomach ulcers, bronchitis, sore throat and even viruses like hepatitis. QS has several sugar groups bound to two different sites of the triterpene ring, whereas the structure of GA is somewhat simpler, having only two sugar groups bound to only one end of the triterpene ring. Their toxic or immunoadjuvant behaviours are originated from their self-assembly properties and from their interaction with membranes.

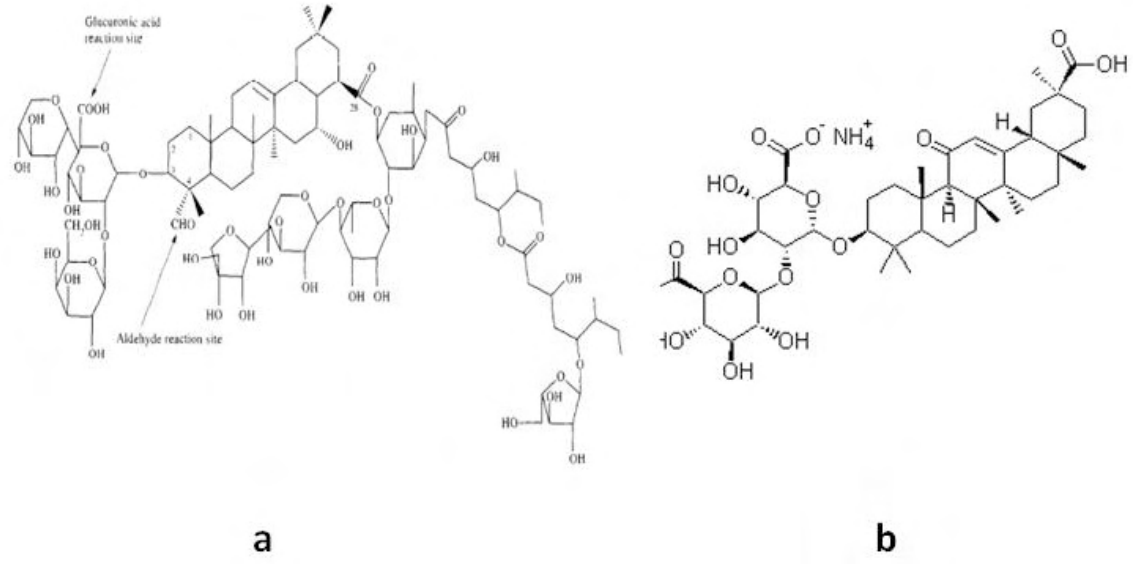

Figure 1. Structures of a. Quillaja Saponin and b. Glycyhrrizic Acid

To elucidate this behaviour, both saponins have been studied in aqueous solutions, as a function of concentration and temperature. In a second step, the influence of QS and GA, separately, on 1,2-Dipalmitoyl-*sn*-glycero-3-phosphocholine (DPPC) bilayers has also been

investigated. QS concentration varied from 3 to 12 wt% in water. From previous results, we know that elongated micelles are formed, whose sizes remain constant in the above concentration range, while the number of micelles in solution increases. Increasing temperature changes very slightly the micellar structure. However, GA is insoluble in water solution at room temperature, but at pH 10 it is able to form micelles even at room temperature. Increasing temperature produces the same effect as increasing pH. The initial big precipitates starts to form micelles at temperatures higher than 60 °C, which are disassembled when cooling down, forming long objects, which are different from the micelles and also from the big precipitates present at the beginning. Thus, the temperature effect seems to be irreversible, at least during the time of the experiment.

These different behaviours of both saponins are liable to reflect on their effects on lipid membranes. Films containing DPPC and QS or GA at different Saponin:DPPC molar ratios were prepared and hydrated with water solution. Both surfactants destroy the bilayers lamellar order (Figure 2). Only the bilayer form factor is present in the scattering curves. In the QS-DPPC films, at temperatures higher than the DPPC chain-melting temperature, the bilayer order is recovered. This is very similar to the system formed by the 16-12-Gemini surfactant and DPPC, in which the surfactant molecules can rearrange and mix inside the bilayers as the chains melt, being immiscible when they are crystalline at low temperature [9]. The higher the QS:DPPC molar ratio, the higher this transition temperature in which the ordered phase is recovered, in the same way as in the cited work. In the GA-DPPC samples, the bilayers are disordered at all temperatures. But the first minimum of the form factor is shifted towards lower q-values, showing the higher penetration of GA in the bilayers at high temperatures, which increases the bilayer thickness. At low temperatures, a high scattering is observed (not shown in the figures), at the same position of the form factor observed in the pure GA system at low temperature. Following the discussion presented by reference [9], we can infer that the immiscibility of the GA and QS (at low temperatures) might be associated to non- or less-toxicity in the lipids. The structural parameters of the bilayers in the different samples have to be characterized in detail to have the complete understanding of the effect of these two saponins in the membranes. . The pure saponin micelles have started to be analysed using the program GENFIT [10]. The first preliminary results show that the QS micelles are bicelles, with the main bicelle radius of the hydrophobic region of 15 Å, a rim radius of 19 Å and polar region thickness of 21 Å. The results also show that the electron density of the hydrophobic part is higher than the sugar groups, in accordance with the characterization of triterpene crystals [11].

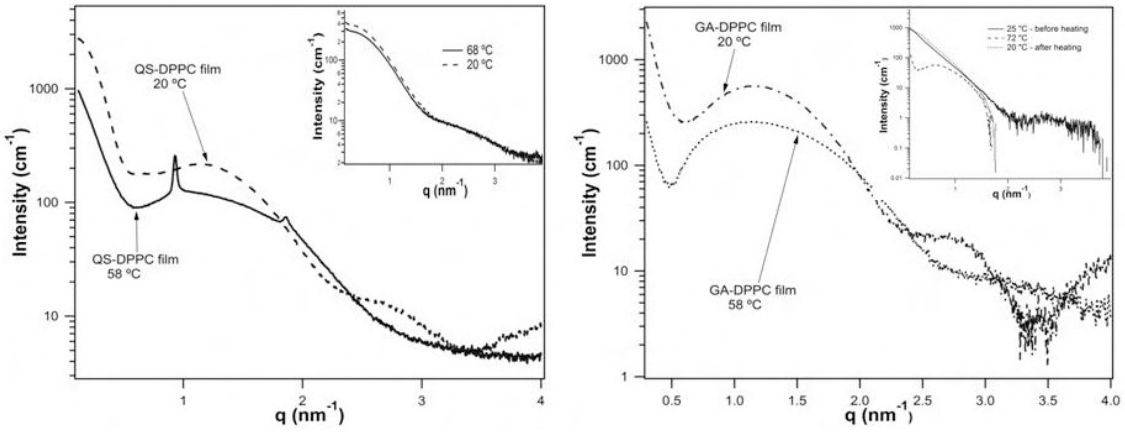

Figure 2. SAXS curves of a. DPPC bilayers with QS- Inset: SAXS curves of QS in water; b. SAXS curves of DPPC bilayers with GA; Inset: SAXS curves of GA in water

References:

[1] F.R.Vogel, International Journal of Immunopharmacology **17**,85-90 (1995)
[2] M.A.Lacaille-Dubois, in Studies in Natural Products Chemistry, Vol 32, Atta-ur-Rahman (Ed) Elsevier, B.V., 209 (2005)
[3] C.R.Kensil, Crit. Rev. Ther. Drug. Carrier, **13**, 1.(1996)
[4] Y.Kikuchi, H.Sasa, T.Kita, J.Hirata, T.Tode., I.Nagata, Anti-cancer drugs, , 2, 63 (1991)
[5] M.Sugano, S. Goto, Y. Yamada, K. Yoshido,Y.Hsshimoto,,T. Matsuo, M. Kimoto,.J. Nutr., 120, 977 (1990)
[6] A.C.Chao, J.V.Nguyen, M.Broughall, J.Recchia, C.R. Kensil, P.E.Daddona,J.A Fix, J.Pharm.Sci, , 87, 1395 (1998)
[7] K.A.Foon, J.Lutzky, A.N.Baral, J.R.Yannelli, L.Hutchins, A.Teitelbaum;O.I Kashala,R.Das, J. Garrison. R.A.Reisfeld,M.Bhattacharya-Chatterjee , *J. Clinical Oncology*, 18, 376-384 (2000)
[8] D.Oakenfull, G.S.Sidhu, in Toxicants of Plant Origin, Volume II.Glycosides, Cheecke,P.R., Ed.; CRC Press, Inc.: Boca Raton, FL.,pp 97-141 (1989)
[9] C.V.Teixeira, M.Blanzat, J. Koetz, I.Rico-Lattes, G.Brezesinski, BBActa **1758**, 1797-1808 (2006)
[10] F.Spinozzi, P.Mariani, L.Saturni, F.Carsughi, S.Bernstorff, S.Cinelli, G.Onori, J.Phys.Chem.B., 111, 3822-3830 (2007)
[11] A.B.Cota, Y.P.Mascarenhas, G.D.F.Silva, J.R.Souza,Acta Cryst. C46, 326-327,1990

THE ROLE OF CALCIUM IN MEMBRANE CONDENSATION AND SPONTANEOUS CURVATURE VARIATIONS IN MODEL LIPIDIC SYSTEMS

A. Yaghmur[1], B. Sartori[2], and M. Rappolt[1]

1.) Department of Pharmaceutics and Analytical Chemistry, Faculty of Pharmaceutical Sciences, University of Copenhagen, Universitetsparken 2, DK-2100 Copenhagen, Denmark
2.) Institute of Biophysics and Nanosystems Research (IBN), Austrian Academy of Sciences, Graz, Austria

In this report, the dynamics of the electrostatic interactions of Ca^{2+} ions with a series of aqueous dispersions containing different DOPG/MO ratios was investigated in milliseconds to seconds range by the combination of synchrotron SAXS with stopped-flow apparatus [1]. The study described here is the continuation of our recent work on the combination of rapid mixing and time-resolved synchrotron SAXS for the *in-situ* investigations of structural transitions of diluted DOPG/MO vesicles into well-ordered nanostructures by the addition of low Ca^{2+} concentrations [2]. Figure 1 schematically illustrates the applied set-up and one representative example on dynamics of Ca^{2+}-induced structural transitions. The present structural analysis is performed on experiments done on the effect of rapidly mixing Ca^{2+} with DOPG/MO-based aqueous dispersions at three different DOPG/MO molar ratios of 15/85 (sample A), 50/50 (sample B), and 70/30 (sample C), respectively. The obtained results are compared with those previously reported on vesicles with a DOPG/MO molar ratio of 30/70 (sample D) [2]. In absence of Ca^{2+} ions, how the lipid composition can significantly affect the structure of the DOPG/MO-based aqueous dispersions is also discussed in this work.

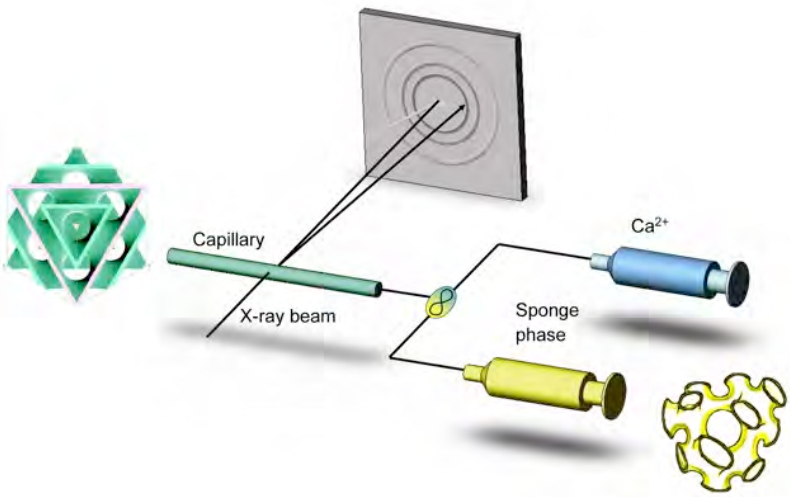

Figure 1. Schematic illustration of the set-up combining synchrotron SAXS with a stopped-flow apparatus. In the stopped-flow apparatus, one syringe contains a buffer with Ca^{2+} ions, whereas the other contains DOPG/MO-based aqueous dispersion. The rapid mixing was conducted within 10 ms. The presented example shows the *in situ* formation of the inverted type bicontinuous cubic (V_2) phase of the symmetry Pn3m.

Under static conditions and in the absence of Ca^{2+} ions, the evaluation of SAXS data for the DOPG/MO aqueous dispersions prepared indicates the formation of either a sponge-like L_3 phase or uncorrelated bilayers [1]. Clearly, the lipid composition plays a vital role in modulating the structural behavior of these aqueous dispersions in the absence and also in the presence of Ca^{2+} ions. The rapid-mixing experiments reveal that the fast and the strong interactions of Ca^{2+} ions with the negatively charged DOPG/MO membranes trigger the transformation from the L_3 phase or the uncorrelated bilayers to well-ordered dehydrated L_α phase or non-bilayers (inverted type bicontinuous cubic phases, V_2, with either a symmetry of Pn3m or Im3m). A representative example on the *in situ* monitoring of direct and fast highly swollen L_3 to V_2 transition is illustrated in Figure 2. Additionally, we recently reported [2]

that low concentrations of Ca^{2+} ions trigger the formation of the inverted type hexagonal (H_2) phase in DOPG/MO aqueous dispersions with a molar DOPG/MO ratio of 30/70. These are also temperature-sensitive structural transitions.

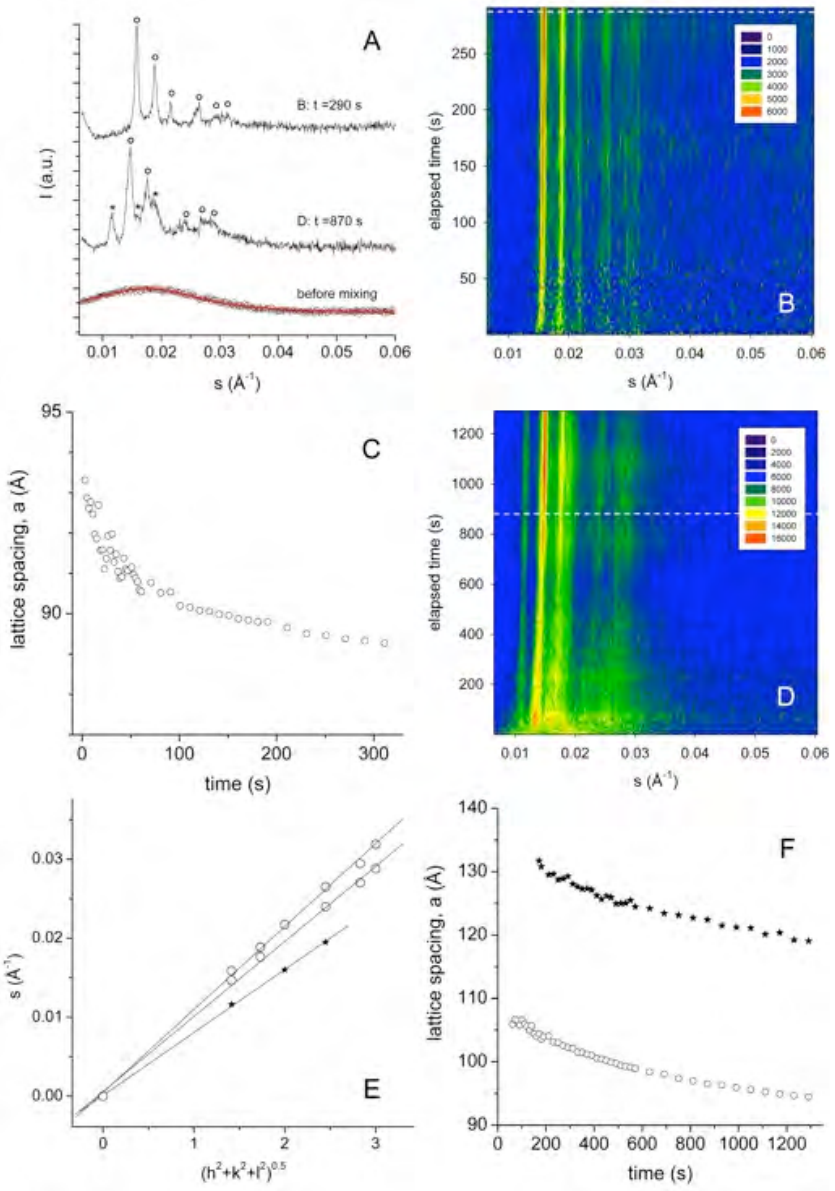

Figure 2. The rapid calcium-triggered V_2 phase formation at 50 °C for sample A. Panel (A) shows selected SAXS scattering patterns for three investigations: sample A in the absence of Ca^{2+} ions (background subtracted scattering pattern of the proposed L_3 phase), and two examples on the *in situ* formation of V_2 phases. In panel (B), the contour plot clearly displays the characteristic reflections of the Pn3m phase (final Ca^{2+} concentration of 34.0 mM). Panel (C) presents the time dependence of the unit cell parameter of the rapidly formed Pn3m phase referring to the experiment given in panel (B). In panel (D), the contour plot clearly displays the *in situ* formation of a biphasic system: coexistence of Im3m with Pn3m (final Ca^{2+} concentration of 6.8 mM). In both rapid-mixing experiments there is no indication for the formation of an intermediate phase. Panel (E) illustrates the indexing of the cubic phases: the Pn3m (○) and the Im3m (★) phases. In panel (F), the plot shows the time dependence of the unit cell parameter of the rapidly formed Pn3m and Im3m phases referring to the experiment given in panel (D). For further details refer to [1].

The *in situ* investigations of the calcium triggered phase transitions reveal a very fast re-organization of the lipid molecules in the aqueous media to form a variety of nanostructures. Figure 3 shows a schematic illustration of the various intriguing and fast structural transitions observed in the present study, which also includes the fast L_α-H_2 transitions that was monitored in our recent report[1]. One of the most striking features in these investigations is the

occurrence of disordered-ordered transitions within milliseconds to seconds range. While the binding steps of Ca^{2+} ions to the negatively charged DOPG/MO membrane are not detectable in this time window, the rapid condensation of bilayers due to the screened electrostatic repulsion forces and the subsequent formation of one-, two- or three-dimensional nanostructures are well documented.

In general, the obtained results expand our knowledge both regarding the strong impact of Ca^{2+} ions on the negatively charged membranes as shown in this study in the DOPG/MO-based vesicular and sponge-like systems, especially regarding the very fast re-ordering of the lipids in the self-assembled structures. Clearly, the lipid composition and the applied experimental conditions including the temperature and the investigated Ca^{2+} ion concentration are important factors in the modulation of the calcium-induced structures.

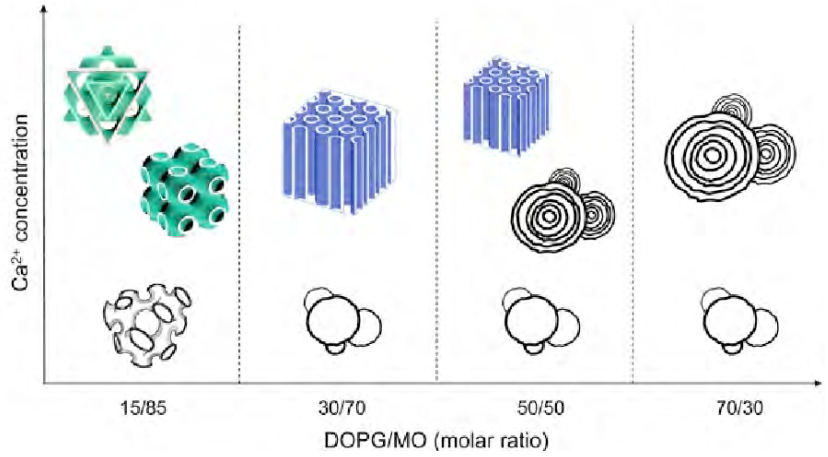

Figure 3. Schematic illustration of the lipid composition dependence of the rapid calcium-triggered nanostructures in DOPG/MO-based aqueous dispersions. Four different examples for fast disordered-ordered structural transitions are given. The *in situ* formation of the well-ordered nanostructures: the two V_2 phases of the symmetries Pn3m and Im3m, the H_2 phase, and the L_α phase.

References:

[1] A. Yaghmur, P. Laggner, B. Sartori and M. Rappolt; Calcium Triggered L_α-H_2 Phase Transition Monitored by Combined Rapid Mixing and Time-Resolved Synchrotron SAXS; PLoS ONE **3**, e2072Journal **25**, 236-266 (2000)

[2] A. Yaghmur, B. Sartori and M. Rappolt; The Role of Calcium in Membrane Condensation and Spontaneous Curvature Variations in Model Lipidic Systems; Phys. Chem. Chem. Phys. **13**, 3115-3125 (2011)

Chemistry

IN-SITU STUDIES OF THE FORMATION OF LAYERED MICROSPHERICAL ZINC HYDROXIDE CARBONATE

M. Bitenc[1,2], P. Podbrščček[1], P. Dubček[3], S. Bernstorff[4], G. Dražić[5], B. Orel[6], Z. Crnjak Orel[1,2]

1.) National Institute of Chemistry Slovenia, Hajdrihova 19, SI-1001 Ljubljana, Slovenia
2.) Center of Excellence for Polymer Materials and Technologies, Tehnološki Park 24, 1000 Ljubljana, Slovenia
3.) Ruđer Bošković Institute, P.O. Box 180, 10002, Zagreb Croatia
4.) Sincrotrone Trieste, S.C.p.A., I-34149 Basovizza (TS), Italy
5.) Jožef Stefan Institute, Jamova 39, SI-1000, Ljubljana, Slovenia
6.) University of Ljubljana, Aškerčeva 5, SI-1000, Ljubljana, Slovenia

Layered zinc hydroxide carbonate (ZnHC) compounds have attracted an increasing attention since they could be used as precursor in the preparation of layered zinc oxide (LZnO) particles by their thermal decomposition. As-prepared LZnO has a specific structure and potential applications in many areas, such as chemical sensors, photocatalysts, phosphors and dye-sensitive solar cells [1].

LZnHC is commonly prepared by a solution method. The hydrothermal precipitation of LZnHC from zinc nitrate with urea was already presented in our previous paper, where the influence of the different additives on the final morphology of the particles was studied in a closed reactor system [2]. The precipitated ZnHC decomposed in only one relatively sharp step. The decomposition activation energy of the ZnHC into ZnO was calculated on the basis of isothermal decomposition studies [2, 3].

In order to follow the particle growth of LZnHC, to the best of our knowledge only ex-situ characterization methods such as TEM and SEM have been used [4]. An ex-situ observation essentially involves large time steps and a statistical uncertainty in the sampling and sample preparation. Additionally, an ex-situ observation in a rigorous microscope environment can considerably alter the information about the products.

For this reason we performed an in-situ measurement with small-angle-X-ray scattering (SAXS), since with this method a direct look at the growth of the nanoparticles of ZnHC was possible. In-situ SAXS measurements and the growth kinetics of ZnO nanocrystals were already presented in a series of papers. However, we found no reports, to the best of our knowledge, of in-situ SAXS measurements of ZnHC growth.

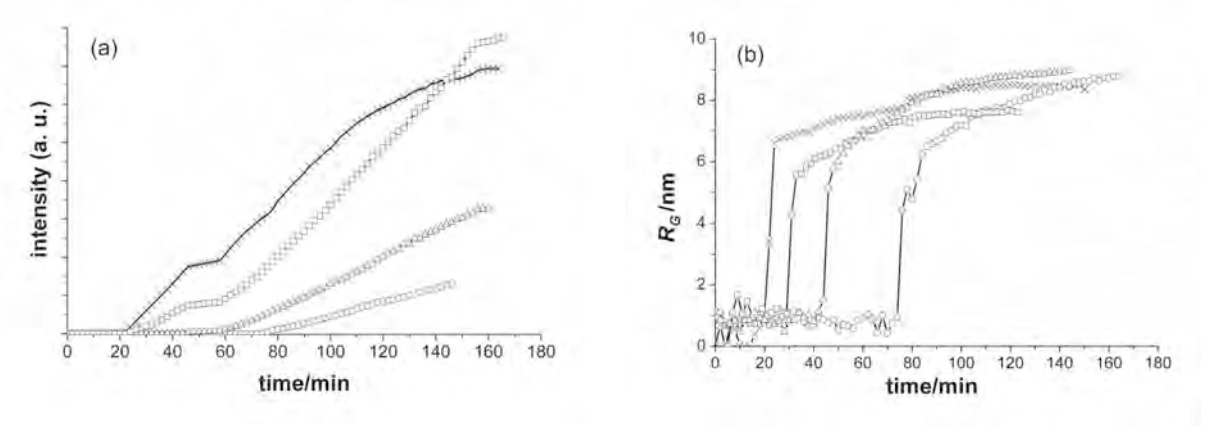

Figure 1. (a) – Integral scattering intensity vs. reaction time and (b) – radius R_G vs. reaction time for synthesis in: water medium (×) and 3/1 vol. ratio of water/PEG400 with different concentration of initial reagents (○ – lowest, △ – medium and □ – highest).

The SAXS data are presented as the time evolution of the integral intensity (Figure 1a) and the radius R_G of the nanoparticles (Figure 1b) for the synthesis in water medium and in

water/PEG400 mixture with volume ratios 3/1. The SAXS scattering was followed in-situ from the beginning of the synthesis, in order to study the full range of particle formation. The intensity integration was made over 120 s in order to obtain an adequate signal-to-noise ratio, and this represents the time resolution of the experiment. In the beginning of the reaction the sample scattering is equal to the solvent scattering, and this is taken as a reference. Only when the particles start to form the SAXS intensity begins to change. In the first 20 minutes of the reaction the formation of the particles was not expected, since the thermal decomposition of the urea was slow at the beginning of the synthesis and subsequently the appropriate formation of the zinc complexes needed for the nucleation were not possible.
The particles' formation, in the water and water/PEG mixture, was found to be very rapid and is schematically presented in Figure 2. We supposed that the nanoparticles' building units were stable, as an individual, only in the reaction solution. The nanoparticles' building units were further self-assembling into leaves of ZnHC with a thickness of around 20 nm. The leaves were agglomerated into porous, microsphere-like particles with sizes from 1 to 4 μm. The size of the nanoparticles remained nearly constant during the synthesis. The formation and growth mechanism follows the particle-mediated growth, which is part of the "non-classical crystallization" concept [5].

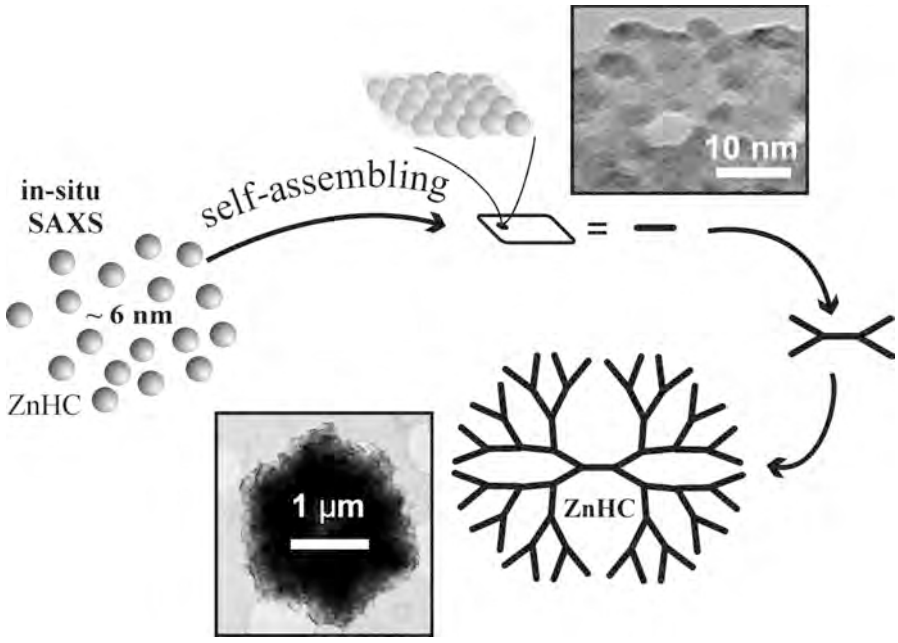

Figure 2. Schematic description of the growth mechanism of the hydrozincite (ZnHC) and (HR)TEM micrographs.

References:

[1] E. Hosono, S. Fujihara, I. Honna and H. S. Zhou; The fabrication of an upright-standing zinc oxide nanosheet for use in dye-sensitized solar cells; *Adv. Mater.* **17,** 2091-2094 (2005)
[2] M. Bitenc, M. Marinšek and Z. C. Orel; Preparation and characterization of zinc hydroxide carbonate and porous zinc oxide particles; *J. Eur. Ceram. Soc.* 28**,** 2915-2921 (2008)
[3] M. Bitenc, P. Podbrščček, P. Dubček, S. Bernstorff, G. Drazić, B. Orel, S. Pejovnik and Z. C. Orel; In and Ex Situ Studies of the Formation of Layered Microspherical Hydrozincite as Precursor for ZnO; *Chem.–Eur. J.* **16,** 11481-11488 (2010)
[4] X. F. Zhou, D. Y. Zhang, Y. Zhu, Y. Q. Shen, X. F. Guo, W. P. Ding and Y. Chen; Mechanistic investigations of PEG-directed assembly of one-dimensional ZnO nanostructures; *J. Phys. Chem. B* **110,** 25734-25739 (2006)
[5] F. C. Meldrum and H. Colfen; Controlling Mineral Morphologies and Structures in Biological and Synthetic Systems; *Chem. Rev.* 108**,** 4332-4432 (2008)

SPATIAL CORRELATIONS IN DYNAMIC POLYMERIC NETWORKS AFFECT THE MORPHOLOGY OF SILVER NANOSTRUCTURES

G. Campi[1], A. Mari[2], A. Pifferi[1] and L. Suber[2]

1.) CNR- Istituto di Cristallografia, Via Salaria, Km 29.300, Monterotondo (RM), I-00015, Italy
2.) CNR- Istituto di Struttura della Materia, Via Salaria, Km 29.300, Monterotondo (RM), I-00015, Italy

Capping molecular agents such as organic surfactants and polymers are widely used to tailor the size and shape of forming nano-composited architectures in wet chemical reactions [1]. We recently exploited a silver nanoparticle synthesis utilizing silver nitrate as salt, nitric acid to set acidic condition, ascorbic acid as reducing agent and polynaphtalene sulphonate polymer, termed Daxad 19, as stabilizer in aqueous phase. In this system, we have found that different silver-polymer morphologies can be selectively grown, through the control of the reaction temperature, while all other experimental parameters such as pH, concentrations of all species in solution and the addition rate of reducing ascorbic acid, are kept fixed [2]. This emerged simplicity led us to investigate their formation mechanism simply by tuning the temperature in the chemical reaction; in particular, we report the syntheses carried out at 20, 40 and 60 °C at which rods-like, hexagonal-like and chain-like polymer-Ag composites are obtained respectively.

Aqueous solution of $AgNO_3$ and Daxad was prepared before the addition of ascorbic acid at $t=t_o=10s$. Time evolution of SAXS intensity at different time intervals is shown in Fig. 1 (a, b, c) for the three investigated temperatures. For each temperature, the SAXS profiles present the following main features: *i)* the scattered intensity gradually increases in the low q region indicating the nucleation and growth of Ag-polymer particles; *ii)* a power law profile in the high q region; *iii)* the development of interference oscillations particularly evident at T=40 °C. In order to describe and quantify these peculiar aspects of our experimental data we assume a theoretical model consisting of two components. The first component, $I_B(q)$, takes into account the power law behaviour with exponent P_E predominating at high q and is ascribed to like-fractal polymeric clusters in the solution; the second one, $I_P(q)$, describes highly dispersed particles interacting via hard-sphere potential. Thus the model $I(q)$ can be written as

$$I(q) = I_B(q) + I_P(q) \tag{1}$$

where the first power law term

$$I_B(q) = P_C q^{P_E} \tag{2}$$

is due to the polymer and $AgNO_3$ salt background in the solution, while the second term

$$I_P(q) = CNS(q, R_{HS}, \eta) \int_0^\infty P(R)\left[V(R)(q,R)\right]^2 dR \tag{3}$$

takes into account the formation of N spherical primary particles with radius R; C is a constant independent of q and R; $V(R)$ and $\Phi(q,R)$ are the volume and the form factor of the single spherical particle, respectively. In order to account for the polydispersivity of the particles, the intensity has been integrated over a *log-normal* distribution of R, $P(R)$. Finally, the scattering oscillations have been modelled in the monodisperse approximation of hard spheres with radius R_{HS} and volume fraction η calculated with the Percus-Yevick equation. The trust-region-reflective algorithm has been used to fit the data and to get the time dependence of parameters [3].

After the nucleation and growth takes place, diffraction peaks arise, indicating spatial correlations on different volume fractions and distances as a function of both the temperature and the time. In Fig. 1 g), h), i), we show the interference oscillations obtained from the structure factor $S(q, R_{HS}, \eta)$ in eq. 3. These oscillations are stronger at 40 °C (Fig. 1h) where

the ordering turns on after an incubation time of about 10s and covers all the available volume fraction of 0.3 in about 30 seconds. This behavior is consistent with a nucleation regime (I) typical of cooperative phenomena, followed by an ordering regime (II) characterized by a nearly linear shifting of the correlation length. Temperature changes leads to weaker correlations, as shown in Fig. 1g) and 1i) [4]. The arising and development of these correlations during the reduction proces, come out from the polymer network arrangement. This arrangement is found to be "dynamic", changing during the aggregation process as described by the time evolution of the Ag-polymer background matrix in the solution, $I_B(q)$, in Eq. 1. At the beginning of the Ag^+ reduction ($t>t_0$), P_E assume low values, less than 2; as the reaction goes on P_E increases and reaches its steady value of about 2.1 at T=20 °C (Fig. 1j) and 2.5 at T=60 °C (Fig. 1l). On the other hand, at T=40 °C P_E reaches values around 3.2 (Fig. 1k); since P_E values from 1 to 3 indicate *mass fractal* dimension, at T=20 °C and 60 °C we have mass fractal Ag^0-polymer clusters in the colloid; as P_E exceeds 3 the system undergoes a mass-surface fractal transition, indicating the formation of more compact objects only at T=40 °C [4].

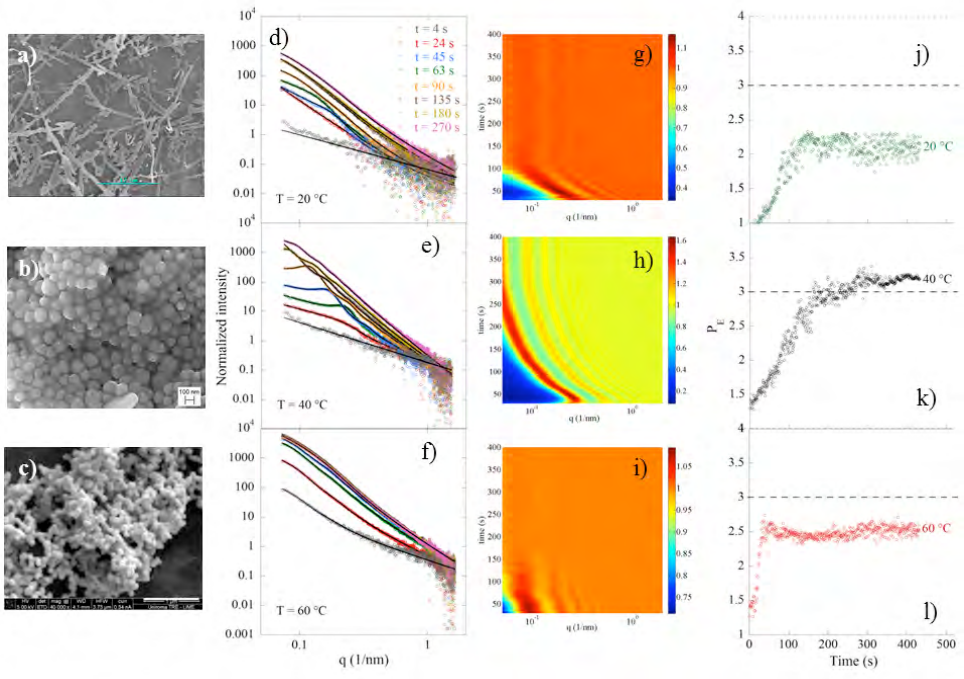

Figure 1. SEM images of nanoparticles obtained at a) T=20 °C, b) T=40 °C, c) T=60 °C; SAXS normalized profiles (open circles) along best fit curves (solid lines) collected at the time intervals indicated and at d) T=20 °C, e) T=40 °C, f) T=60 °C ; Percus-Yevick structure factor at g) T=20 °C, h) T=40 °C, i) T=60 °C; P_E as a function of time at j) T=20 °C, k) T=40 °C, l) T=60 °C.

In conclusion, our time resolved SAXS measurements show that the extent of spatial correlations in variable fractal geometries, during nanoparticle formation, constitutes a key point for understanding the different morphologies of the emerging patterns.

References:

[1] J.H. Fendler, Self-Assembled Nanostructured Materials, *Chem.Mater*. **8**, 1616-1624 (1996)

[2] L. Suber, I. Sondi, E. Matijević and Dan V. Goia, Preparation and the mechanism of formation of silver particles of different morphologies in homogeneous solutions, *J. Colloid Interface Sci.*, **288**, 489-495 (2005)

[3] G. Campi, A. Mari, H. Amenitsch, A. Pifferi, C. Cannas and L. Suber, Monitoring early stages of silver particle formation in a polymer solution by in situ and time resolved Small Angle X ray Scattering, *Nanoscale*, **2(11)**, 2447–2455 (2010)

[4] G. Campi, A. Mari, A. Pifferi, H. Amenitsch, M. Fratini and L. Suber, Control of silver-polymer aggregation mechanism by primary particle spatial correlations in dynamic fractal-like geometry, *Nanoscale*, in press

SIMULTANEOUS IN SITU AND TIME-RESOLVED SAXS-WAXS ANALYSIS ON HIERARCHICAL POROUS SILICA FILMS

D. Marongiu[1], L. Malfatti[1], P. Falcaro[2], S. Costacurta[3], H. Amenitsch[4], and P. Innocenzi[1]

1.) Laboratorio di Scienza dei Materiali e Nanotecnologie, CR-INSTM, D.A.D.U., Università di Sassari, Palazzo Pou Salid, Piazza Duomo 6, 07041 Alghero (SS), Italy
2.) Division of Materials Science and Engineering, Commonwealth Scientific and Industrial Research Organisation (CSIRO), Private Bag 33, Clayton South MDC, Victoria 3169, Australia
3.) Associazione CIVEN, Via delle Industrie 5, 30175 Venezia, Italy
4.) Institute of Biophysics and Nanosystems Research, Austrian Academy of Sciences, Schmiedlstrasse 6, 8042 Graz, Austria

In previous experiments, thin films made of hierarchical meso-macro porous hybrid silica have been obtained by self-assembly from a liquid phase using a surfactant and an inorganic crystal template [1]. In this experiment an in-situ, time-resolved measurement has been performed on in-situ prepared samples using synchrotron radiation. Silica films have been deposited on silicon substrates by dip-coating from a precursor solution in a solvent containing the surfactant Pluronic F127 and dissolved sodium chloride. The surfactant is able to self organize during solvent evaporation giving rise to ordered micelles, while sodium chloride nucleates and forms nano-crystals within the film. The micelles can be removed by thermal treatment which does not affect the salt crystals, on the other side, nanocubes can be removed by a simple water washing thus leaving empty cubic pores. The final material is a hierarchical meso-macro porous hybrid silica film. The two processes have been studied by time-resolved simultaneous experiments using synchrotron radiation to get a better insight into the phenomenon.

The experiments have been realized in the SAXS beamline by using a dip-coater mounted in the sample stage in order to record the signals during film deposition. SAXS and WAXS signals have been recorded simultaneously by using an incident wavelength of 1.54 Å (8 KeV) [2]. SAXS signal is generated by the electronic contrast between the micelles and the silica pore walls and it gives information on the ordered mesopores. WAXS was recorded around the most intense Bragg diffraction peak of fcc NaCl and it gives information on the nanocrystals formation. The dimensions of the two structures fall in two different ranges, in particular mesopores coming from micelles are around 6 nm while salt crystals are in the 100-280 nm range; the two processes are time dependent and can be monitored with a time resolution of seconds.

Figure 1a and 1b show the 3D representation of SAXS signal intensity as a function of time (in seconds) and scattering vector, S_z, (nm^{-1}). The intensity variation of the scattered signal is shown in false color scale. The initial evaporation of solvent lasts few tens of seconds and no signal is detected during this stage. As soon as the micelles start to form and organize, the SAXS signal appears and it reaches the maximum intensity after 80 seconds from the beginning of EISA. The WAXS signal appears later and suddenly and it increases in intensity with time.

Figure 2 shows the comparison between the SAXS and the WAXS integrated intensity at 0.077 nm^{-1} and 31.8° respectively, as a function of time. It is interesting to notice that the SAXS intensity decreases with time after 80 seconds while the WAXS signal increases in intensity starting from 150th second and it keeps growing indicating the formation of NaCl crystals. The decrease of SAXS intensity, once it reaches a maximum, is due to the interaction of Na^+ and Cl^- ions with the micelles which affects the dimension and organization at the mesoscale.

We have then treated the films at 350°C for 30 minutes and we have analyzed the final structure of the films by 2D GISAXS (not reported). The GISAXS pattern showed a typical body-centered cubic porous organized structure. The re-organization after a thermal treatment

has been attributed to the migration of Na^+ and Cl^- ions towards the salt crystals during dehydration of the micelles.

The analysis has shown that the formation of the two templating agents is an evaporation-triggered phenomenon, which is time-dependent. The technique represents a simple and flexible tool to produce hierarchical silica film with well defined pore shapes and dimensions.

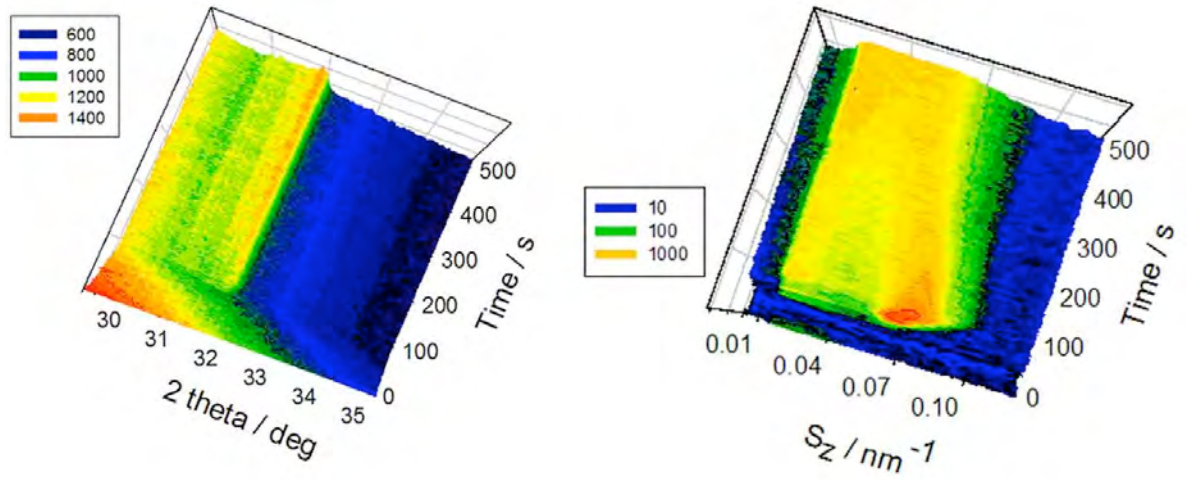

Figure 1. 3D representation of time-resolved SAXS (a) and WAXS (b) measurements on hierarchical porous films as a function of time and scattering vector, S_z. The intensity variation of the peaks is reported in false color scale.

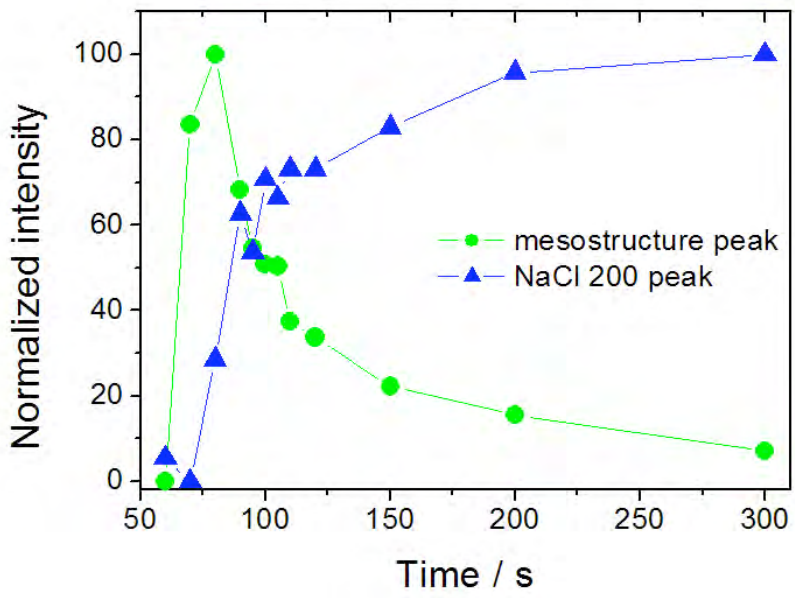

Figure 2. Integrated intensity of the SAXS and WAXS signals at 0.077 nm^{-1} and 31.8° as a function of time during simultaneous and time-resolved in situ measurements on hierarchical porous films.

References:

[1] L. Malfatti, P. Falcaro, D. Marongiu, M.F. Casula, H. Amenitsch, P. Innocenzi; Self-Assembly of Shape Controlled Hierarchical Porous Thin Films: Mesopores and Nanoboxes; Chem. Mater. **21**, 4846–4850 (2009)

[2] L. Malfatti, D. Marongiu, H. Amenitsch, Plinio Innocenzi; Simultaneous in situ and Time Resolved Study of Hierarchical Porous Films Templated by Salt Nanocrystals and Self-Assembled Micelles; J. Phys. Chem. C **115**, 12702-12707 (2011)

GISAXS STUDY OF THE SELF ORGANISATION OF POLYSTYRENE-B-POLYLACTIDE IN THIN FILMS UPON SOLVENT EXPOSURE

M. Vayer[1], D. Grosso[2], H. Amenitsch[3] and C. Sinturel[1]

[1] Centre de Recherche sur la Matière Divisée, 1b rue de la Férollerie, 45 071 Orléans, France
[2] Laboratoire Chimie de la Matière Condensée de Paris, UMR UPMC-CNRS 7574, Université Pierre et Marie Curie, Collège de France, 11 place Marcelin Berthelot, 75231, Paris, France
[3] Institute of Biophysics and Nanosystems Research, Austrian Academy of Sciences, Schmiedlstr. 6, 8042 Graz, Austria

The motivation of this project was to understand the reorganization mechanisms of thin films of polylactide (PLA) based block copolymer (BCP) induced by exposure to vapors of solvents. The goal of the study was to perform accurate *in situ* GISAXS characterizations of the films upon exposure in order to examine the characteristics of the system in the swollen state (disordered/ordered, perpendicular/parallel cylinders). Figure 1 presents the 2D GISAXS diffraction patterns (bottom) of PS-*b*-PLA films with the three types of organizations depicted on the AFM images top). In figure 1a, the off plane radial scattering is consistent with disorganized PLA domains with a faint diffraction signal in the evanescence. The off plane diffusion is however attributed to randomly oriented PLA domains in the depth profile of the film, characteristic of a poorly ordered system. In figure 1b, the GISAXS pattern presents a series of sharp in-plane Bragg peaks, accompanied by diffraction rods in the qz direction (vertical streaks) which are characteristics of a 2D hexagonal organization of PLA domains (space group : P6mm) with d(100) = 49 nm. Figure 1c presents an ellipsoidal diffraction ring with in plane periodicity equal to 52 nm (qx=0.12 nm^{-1}) and off-plane periodicity of 36 nm (qz = 0.18 nm^{-1}) corresponding to hexagonally packed bunches of cylindrical PLA domains with their c axis parallel to the surface and with their a axis randomly oriented with respect to the surface. The off-plane elongation of the diffraction ring is typical of a unidirectional contraction (35%) of the hexagonal domains normal to the surface.

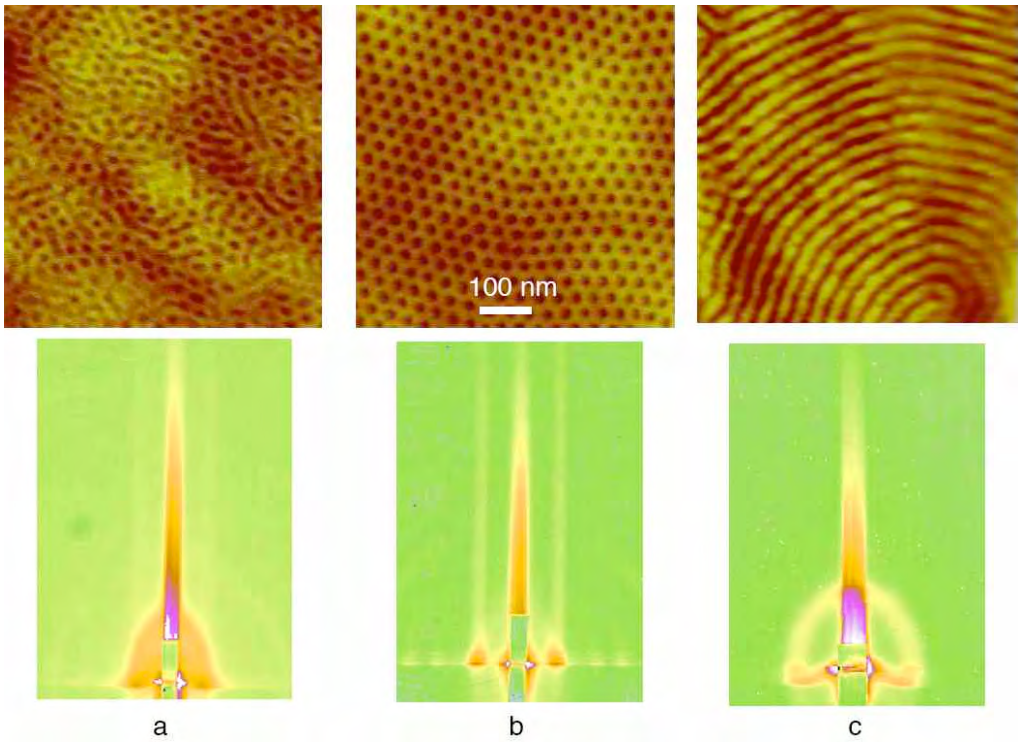

Figure 1. a. disorganized (as spun), b. perpendicular (4 hours in THF), c. parallel (6 hours in THF)

For *in situ* experiments, samples were exposed to saturated vapors of THF in dynamic mode (continuous flux of nitrogen with THF at the saturation vapor pressure). First *in situ* measurements were carried out on an initially disorganized sample. GISAXS patterns have been recorded during the whole solvent vapor exposure (Figure 2). After an annealing time sufficient to ensure a global reorganization of the substrate, solvent vapors were removed and a final GISAXS pattern was recorded. AFM images of the resulting organization have been taken afterwards. Figure 2a displays the scattering patterns recorded during the experiment and AFM images of the initial and final state. It can be seen that the intensity of the initial scattering peak of the SAXS pattern decreases and that the position of the maxima is shifted towards lover values. After evaporation, the maximum is shifted to higher value, close to the initial value. It is clear that no scattering pattern of a perpendicular state has been recorded (during the solvent annealing or the evaporation) indicating that in the annealing conditions used for the study, the perpendicular state is not reached. This result is consistent with the *ex situ* AFM images taken after the total evaporation of the solvent where a disorganized state, similar of a film after spin coating, is observed.

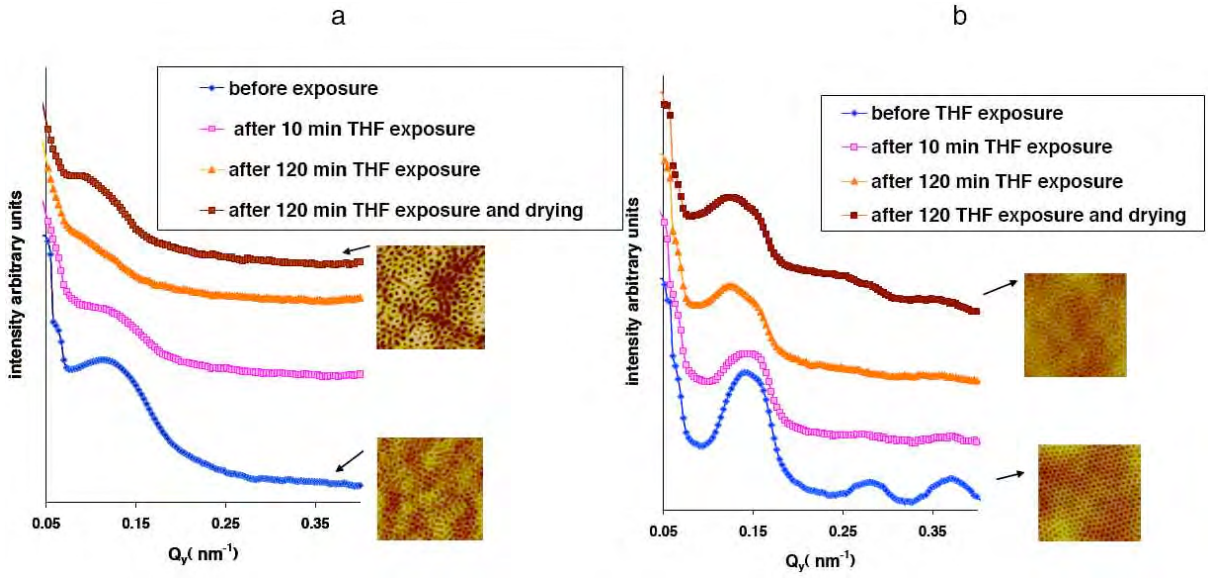

Figure 2. In situ GISAXS upon solvent annealing

In order to observe the transition perpendicular/parallel observed in our conventional annealing procedure, *in situ* GISAXS measurements have been recorded from an initially perpendicular sample. In Figure 2b it can be clearly seen on the GISAXS pattern that the harmonic of the principal reflection are lost indicating that the perpendicular orientation of the PLA cylinders is lost within the film. After an annealing time sufficient to ensure the perpendicular/parallel transition in our conventional static annealing set-up, the flux is stopped and solvent vapors are removed from the chamber. Corresponding AFM and GISAXS measurements on the obtained sample show a disorganized morphology. This unexpected result suggests that the annealing conditions play a major role in the re-organization mechanisms. This is under careful examination.

References:

[1] M. Vayer, M. A. Hillmyer, M. Dirany, G. Thevenin, R. Erre, C. Sinturel, Perpendicular orientation of cylindrical domains upon solvent annealing thin films of poly(styrene)-b-poly(lactide); Thin Solid Film, 518, 3710-3715 (2010)

Publications

Publications in Journals and Reviewed Proceedings 2010

B. Alonso, F. Fayon, D. Massiot, H. Amenitsch, L. Malfatti, T. Kidchob, S. Costacurta and P. Innocenzi
Hybrid Organic-Inorganic Mesostructured Membranes: Interfaces and Organization at Different Length Scales
The Journal of Physical-Chemistry C **114**, 11730–11740, (2010)

L.R.S. Barbosa, M.G. Ortore, F. Spinozzi, P. Mariani, S. Bernstorff and R. Itri
The Importance of Protein-Protein Interactions on the pH-Induced Conformational Changes of Bovine Serum Albumin: A Small-Angle X-Ray Scattering Study
Biophysical Journal, Volume 98 (1), pp. 147-157 (2010)

M. Bitenc, P. Podbrščček, P. Dubček, S. Bernstorff, G. Dražić, B. Orel, S. Pejovnik, Z. Crnjak Orel
In and Ex situ studies of the formation of layered microspherical hydrozincite as precursor for ZnO
Chem. Eur. J. 16 (37), pp.11481-11488 (2010)

B. Boulgaropoulos, H. Amenitsch, P. Laggner, and G. Pabst
Implication of Sphingomyelin/Ceramide Molar Ratio on the Biological Activity of Sphingomyelinase
Biophysical Journal Volume 99, 499–506 (2010)

K. Brandenburg, J. Howe, S. Sánchez-Gómez, P. Garidel, M. Roessle, J Andrä, R. Jerala, D., Zweytick, K. Lohner, M. Rappolt, S. Blondelle, I. Moriyon, G.M. De Tejada
Effective antimicrobial and anti-endotoxin activity of cationic peptides based on lactoferricin: A biophysical and microbiological study
Anti-Infective Agents in Medicinal Chemistry 9 (1), pp. 9-22 (2010)

M. Buljan, J. Grenzer, V. Holy, N. Radić, T. Mišic-Radić, S. Levichev, S. Bernstorff, B. Pivac and I. Capan
Structural and charge trapping properties of two bi-layer ($Ge+SiO_2$)/SiO_2 films deposited on rippled substrate
Applied Physics Letters 97 (16), 163117 (2010)

M. Buljan, J. Grenzer, A. Keller, N. Radic, V. Vales, S. Bernstorff, T. Cornelius, H.T. Metzger and V. Holy
Growth of spatially ordered Ge nanoclusters in an amorphous matrix on rippled substrates
Physical Review B 82, 125316 (2010)

M. Buljan, S.R.C. Pinto, A. G. Rolo, M. J. M. Gomes, J. Grenzer, A. Muecklich, S. Bernstorff, and V. Holy
Self-assembling of Ge quantum dots in alumina matrix
Physical Review B82, 235407 (2010)

Campi, G., Mari, A., Amenitsch, H., Pifferi, A., Cannas, C., Suber, L.
Monitoring early stages of silver particle formation in a polymer solution by in situ and time resolved small angle X-ray scattering
Nanoscale 2 (11), pp. 2447-2455 (2010)

G. Caracciolo, D. Pozzi, A. Amici, H. Amenitsch
Universality of DNA Adsorption Behavior on the Cationic Membranes of Nanolipoplexes
Journal of Physical Chemistry B 114 (5), pp. 2028-2032 (2010)

Dan Cojoc, Heinz Amenitsch, Enrico Ferrari, Silvia C. Santucci, Barbara Sartori, Michael Rappolt, Benedetta Marmiroli, Manfred Burghammer, and Christian Riekel
Local x-ray structure analysis of optically manipulated biological micro-objects
Applied Physics Letters 97 (24), art. no. 244101 (2010)

S. Costacurta, L. Malfatti, A. Patelli, P. Falcaro, H. Amenitsch, B. Marmiroli, G. Grenci, M. Picinini and P. Innocenzi
Deep X-ray Lithography for Direct Patterning of PECVD Films
Plasma Processes and Polymers 7, 459–465, (2010)

Y.-D. Dong, A.J. Tilley, I. Larson, M.J. Lawrence, H. Amenitsch, M. Rappolt, T. Hanley, B.J. Boyd
Non-equilibrium effects in self assembled mesophase materials - unexpected supercooling effects for cubosomes and hexosomes
Langmuir 26, 9000-9010 (2010)

Faustini, M., Vayer, M., Marmiroli, B., Hillmyer, M., Amenitsch, H., Sinturel, C., Grosso, D.
Bottom-up approach toward titanosilicate mesoporous pillared planar nanochannels for nanofluidic applications
Chemistry of Materials 22 (20), pp. 5687-5694 (2010)

A. Fischereder, T. Rath, W. Haas, H. Amenitsch, J. Albering, D. Meischler, S. Larissegger, M. Edler, R. Saf, F. Hofer, G. Trimmel
Investigation of Cu2ZnSnS4 formation from metal salts and thioacetamide
Chemistry of Materials 22 (11), pp. 3399-3406 (2010)

C. Fotakis , S. Gega , E. Siapi , C. Potamitis , K. Viras , P. Moutevelis-Minakakis , C.G. Kokotos, S. Durdagi, S. Golic Grdadolnik, B. Sartori, M. Rappolt, T. Mavromoustakos
Interactions at the bilayer interface and receptor site induced by the novel synthetic pyrrolidinone analog MMK3
Biochimica et Biophysica Acta - Biomembranes 1798 (3), pp. 422-432 (2010)

Innocenzi, P., Kidchob, T., Costacurta, S., Falcaro, P., Marmiroli, B., Cacho-Nerin, F., Amenitsch, H.
Patterning block copolymer thin films by deep X-ray lithography
Soft Matter 6 (14), pp. 3172-3176 (2010)

H. Jerabek, G. Pabst, M. Rappolt and T. Stockner
Membrane-mediated effect on ion channels induced by the anesthetic drug ketamine
J. Am. Chem. Soc. 132 (23), 7990-7997 (2010)

K. Juraić, D. Gracin, B. Šantić, D. Meljanac, N. Zorić, A. Gajović, P. Dubček, S. Bernstorff, M. Čeh
GISAXS and GIWAXS analysis of amorphous–nanocrystalline silicon thin films
Nuclear Instruments and Methods B 268, 259-262 (2010)

A. Khodorov, S. Levichev, A. Chahboun, A.G. Rolo, S. Bernstorff, N. P. Barradas, E. Alves, M.J.M. Gomes
Growth and characterization of Mn- doped ZnO/TiO2 multilayered nanostructures grown by pulsed laser deposition
Physica Status Solidi (C) 7 (11-12), pp. 2724-2726 (2010)

S. Lepoutre, B. Julián-López, C. Sanchez, H. Amenitsch, M. Linden, and D. Grosso
Nanocasted mesoporous nanocrystalline ZnO thin films
Journal of Materials Chemistry 20 (3), pp. 537-542 (2010)

M. Loncaric, J. Sancho-Parramon, M. Pavlovic, H. Zorc, P. Dubcek, A. Turkovic, S. Bernstorff, G. Jakopic, A. Haase
Optical and structural characterization of silver islands films on glass substrates
Vacuum 84 (2010) 188–192

L. Malfatti, D. Marongiu, S. Costacurta, P. Falcaro, H. Amenitsch, B. Marmiroli, G. Grenci, M.F. Casula, P. Innocenzi
Writing Self-Assembled Mesostructured Films with In situ Formation of Gold Nanoparticles
Chemistry of Materials 22 (6), pp. 2132-2137 (2010)

Marchini, C., Pozzi, D., Montani, M., Alfonsi, C., Amici, A., Amenitsch, H., De Sanctis, S.C., Caracciolo, G.
Tailoring lipoplex composition to the lipid composition of plasma membrane: A trojan horse for cell entry?
Langmuir 26 (17), pp. 13867-13873 (2010)

P. Mariani, F. Spinozzi, F. Federiconi, M.G. Ortore, H. Amenitsch, L. Spindler, I. Drevensek-Olenik
Guanosine Quadruplexes in Solution: A Small-Angle X-Ray Scattering Analysis of Temperature Effects on Self-Assembling of Deoxyguanosine Monophosphate
Journal of Nucleic Acids. Volume 2010, Article ID 472478, 10 pages (2010)

B. Marmiroli, G. Grenci, F. Cacho-Nerin, B. Sartori, P. Laggner, L. Businaro and H. Amenitsch
Experimental set-up for time resolved small angle x-ray scattering studies of nanoparticles formation using a free -jet micromixer
Nucl. Instrum. & Meth. B 268 (3-4), pp. 329-333 (2010)

J.M. O'Callaghan, N. Petkov, M.P. Copley, D.C. Arnold, M.A. Morris, H. Amenitsch, J.D. Holmes
Time-resolved SAXS studies of periodic mesoporous organosilicas in anodic alumina membranes
Microporous and Mesoporous Materials 130 (1-3), pp. 203-207 (2010)

M. G. Ortore, F. Spinozzi, P. Mariani, A. Paciaroni, L. R. S. Barbosa, H. Amenitsch, M. Steinhart, J. Ollivier, D. Russo
High-pressure simultaneously modifies structural and dynamical properties of lysozyme hydration shell
Scientific Highlights in ILL Annual Report 2009, pp. 60-61 (2010)

L. Paasonen, T. Sipilä, A. Subrizi, P. Laurinmäki, S.J. Butcher, M. Rappolt, A. Yaghmur, A. Urtti, M. Yliperttula
Gold-embedded photosensitive liposomes for drug delivery: Triggering mechanism and intracellular release
Journal of Controlled Release 147 (1), pp. 136-143 (2010)

B. Pili, C. Bourgaux, H. Amenitsch, G. Keller, S. Lepêtre-Mouelhi, D. Desmaële, P. Couvreur, M. Ollivon
Interaction of a new anticancer prodrug, gemcitabine-squalene, with a model membrane. Coupled DSC and XRD study
Biochimica et Biophysica Acta - Biomembranes 1798 (8), pp. 1522-1532 (2010)

S.R.C. Pinto, R.J. Kashtiban, A.G. Rolo, M. Buljan, A. Chahboun, U. Bangert, N.P. Barradas, E. Alves, M.J.M. Gomes
Structural study of $Si_{1-x}Ge_x$ nanocrystals embedded in SiO_2 films
Thin Solid Films 518 (2010) 2569-2572

S.R.C. Pinto, A.G. Rolo, A. Chahboun, M. Buljan, A. Khodorov, R.J. Kashtiban, U. Bangert, N.P. Barradas, E. Alves, S. Bernstorff and M.J.M. Gomes,
Multilayers of Ge nanocrystals embedded in Al_2O_3 matrix: Structural and electrical studies
Microelectronic Engineering 87, 2508-2512 (2010)

S. R. C. Pinto, A. G. Rolo, M. J. M. Gomes, M. Ivanda, I. Bogdanović-Radović, J. Grenzer, A. Mücklich, D. J. Barber, S. Bernstorff, and M. Buljan
Formation of void lattice after annealing of Ge quantum dot lattice in alumina matrix
Applied Physics Letters 97, 173113 2010 (3 pages)

D. Pozzi, H. Amenitsch, C. Marchini, G. Caracciolo
Phase diagram of 3β -[N-(N,N -dimethylaminoethane)-carbamoyl]- cholesterol-dioleoylphosphatidylethanolamine/DNA complexes suggests strategies for efficient lipoplex transfection
Applied Physics Letters 96 (18), art. no. 183703 (2010)

Pozzi D, Caminiti R, Marianecci C, Carafa M, Santucci E, De Sanctis SC, Caracciolo G.
Effect of cholesterol on the formation and hydration behavior of solid-supported niosomal membranes
Langmuir. 26(4), 2268-73 (2010)

M. Rappolt
Bilayer thickness estimations with "poor" diffraction data
Journal of Applied Physics 107 (8), art. no. 084701 (2010)

A.A. Rempel and A. Magerl
Non-periodicity in nanoparticles with closed-packed structures
Acta Cryst. A66, 479-483 (2010)

J. Sancho-Parramon, V. Janicki, P. Dubček, M. Karlušić, D. Gracin, M. Jakšić, S. Bernstorff, D. Meljanac, K. Juraić
Optical and structural properties of silver nanoparticles in glass matrix formed by thermal annealing of field assisted film dissolution
Optical Materials 32, 510–514 (2010)

E. Schafler
Effects of releasing the hydrostatic pressure on the nanostructure after severe plastic deformation of Cu
Scripta Mater, Vol. 62 - 6, pp. 423-4 (2010)

W. Schmidt, P. Bussian, M. Lindén, H. Amenitsch, P. Agren, M. Tiemann, F. Schüth
Accessing ultrashort reaction times in particle formation with SAXS experiments: ZnS precipitation on the microsecond time scale
Journal of the American Chemical Society 132 (19), pp. 6822-6826 (2010)

F. Spieckermann, H. Wilhelma, M. Kerber, E. Schafler, G. Polt, S. Bernstorff, F. Addiego, M. Zehetbauer
Determination of lamella thickness distributions in isotactic polypropylene by X-ray line profile analysis
Polymer 51 (2010) 4195-4199

F. Spieckermann, H. Wilhelm, E.Schafler, M. Kerber, S. Bernstorff and M.J. Zehetbauer
Plasticity and X-ray Line Profile Analysis of the Semicrystalline Polymer Poly(3-hydroxybutyrate)
Journal of Physics: Conference Series 240 (2010) 012146

F. Spinozzi, L. Paccamiccio, P. Mariani, L. Q. Amaral
Melting regime of the anionic phospholipid DMPG: new Lamellar phase and porous bilayer model
Langmuir 26, 6484-6493 (2010)

C. V. Teixeira, H. Amenitsch, T. Fukushima, J. P. Hill, W. Jin, T. Aida, M. Hotokka and M. Lindén
Form factor of an N-layered helical tape and its application to nanotube formation of hexa-peri-hexabenzocoronene-based molecules
J. Appl. Cryst. 43, 850-857 (2010)

F.M. Toma, A. Sartorel, M. Iurlo, M. Carraro, P. Parisse, C. Maccato, S. Rapino, B.R. Gonzalez, H. Amenitsch, T. Da Ros, L. Casalis, A. Goldoni, M. Marcaccio, G. Scorrano, G. Scoles, F. Paolucci, M. Prato & M. Bonchio
Efficient water oxidation at carbon nanotube–polyoxometalate electrocatalytic interfaces
Nature Chemistry 2, pp. 826–831 (2010)

A. Turković, P. Dubcek, K. Juraic, A. Drašner and S. Bernstorff
SAXS Studies of TiO_2 Nanoparticles in Polymer Electrolytes and in Nanostructured Films
Materials 3 (11), 4979-4993 (2010)

R. Viswanatha, H. Amenitsch, S. Santra, S. Sapra, S.S. Datar, Y. Zhou, S.K. Nayak, S. Kumar, D.D. Sarma
Growth mechanism of cadmium sulfide nanocrystals
Journal of Physical Chemistry Letters 1 (1), pp. 304-308 (2010)

A. Yaghmur, M. Kriechbaum, H. Amenitsch, M. Steinhart, P. Laggner, M. Rappolt
Effects of pressure and temperature on the self-assembled fully hydrated nanostructures of monoolein-oil systems
Langmuir 26 (2), pp. 1177-1185 (2010)

A. Yaghmur, L. Paasonen, M. Yliperttula, A. Urtti, M. Rappolt
Structural elucidation of light activated vesicles
Journal of Physical Chemistry Letters 1 (6), pp. 962-966 (2010)

Publications January to July 2011

Amenitsch, H., Bombelli, C., Borocci, S., Caminiti, R., Ceccacci, F., Concilio, S., La Mesa, C., Mancini, G., Piotto, S., Rappolt, M.
Segregation into domains observed in liquid crystal phases: Comparison of experimental and theoretical data
Soft Matter 7 (7), pp. 3392-3403 (2011)

Amenitsch, H., Caracciolo, G., Foglia, P., Fuscoletti, V., Giansanti, P., Marianecci, C., Pozzi, D., Laganà, A.
Existence of hybrid structures in cationic liposome/DNA complexes revealed by their interaction with plasma proteins
Colloids and Surfaces B: Biointerfaces 82 (1), pp. 141-146 (2011)

J. Caron, E. Lepeltier, L.H. Reddy, S. Lepêtre-Mouelhi, S. Wack, C. Bourgaux, P. Couvreur and D. Desmaële
Squalenoyl gemcitabine monophosphate: synthesis, characterisation of nanoassemblies and biological evaluation
Eur.J. Org. Chem., 14, 2615-2628 (2011)

G. Campi, A. Pifferi, A. Mari, H. Amenitsch, C. Cannas and L. Suber
Dynamic templating role of polynaphtalene sulphonate in the formation of silver nanocrystals in aqueous solution
Journal of Nanoparticle Research 13 (8), 3107-3112 (2011)

I. Capan , J. Bak-Misiuk, B. Pivac, P. Dubček, A. Misiuk, S. Bernstorff, P. Romanowski
Defects in silicon introduced by helium implantation and subsequent annealing
Radiation Physics and Chemistry 80 (2011) 1099–1103

G. Caracciolo, D. Pozzi, A.L. Capriotti, C. Marianecci, M. Carafa, C. Marchini, M. Montani, A. Amici, H. Amenitsch, M.A. Digman, E. Gratton, SS. Sanchez, A. Laganà
Factors Determining the Superior Performance of Lipid/DNA/Protammine Nanoparticles over Lipoplexes
J. Med. Chem., 2011, 54 (12), pp 4160–4171

G. Ciasca, M. Chiarpotto, G. Campi, B. Bocca, M. Rodio, A. Pino, A. Ricci, N. Poccia, C. Rossi, A. Alimonti, H. Amenitsch, P. De Sole and A. Bianconi
Reconstitution of aluminium and iron core in horse spleen apoferritin
Journal of Nanoparticle Research, available online (2011)
DOI: 10.1007/s11051-011-0294-2

S. Costacurta, P. Falcaro, L. Malfatti, D. Marongiu, B. Marmiroli, F. Cacho-Nerin, H. Amenitsch, N. Kirkby and P. Innocenzi
Shaping mesoporous films using dewetting on X-ray pre-patterned hydrophilic/hydrophobic layers and pinning effects at the pattern edge
Langmuir 27 (7), pp. 3898-3905 (2011)

P. Dubček, B. Pivac, S. Milošević, N. Krstulović, Z. Kregar, S. Bernstorff
Pulsed laser ablation of GaAs using nano pulse length
Applied Surface Science 257 (2011) 5358–5361

Falcaro, P., Costacurta, S., Malfatti, L., Buso, D., Patelli, A., Schiavuta, P., Piccinini, M., Grenci, G., Marmiroli, B., Amenitsch, H., Innocenzi, P.
Chemical tailoring of hybrid sol-gel thick coatings as hosting matrix for functional patterned microstructures.
ACS applied materials & interfaces 3 (2), pp. 245-251 (2011)

J. Falta, Th. Schmidt, S. Gangopadhyay, T. Clausen, O. Brunke, J. I. Flege, S. Heun
S. Bernstorff, L. Gregoratti and M. Kiskinova
Ultra-thin high-quality silicon nitride films on Si(111)
EPL, 94 (2011) 16003

M. Faustini, B. Marmiroli, L. Malfatti, B. Louis, N. Krins, P. Falcaro, G. Grenci, C. Laberty-Robert, H. Amenitsch, P. Innocenzi and D. Grosso
Direct nano-in-micropatterning of TiO2 thin layers and TiO 2/Pt nanoelectrode arrays by deep X-ray lithography
Journal of Materials Chemistry 21 (11), pp. 3597-3603 (2011)

V. Holy, M. Buljan, R. Lechner
X-ray characterization of semiconductor nanostructures
Semiconductor Science and Technology 26 (2011), 6; 064002

P. Innocenzi, L. Malfatti, T. Kidchob, S. Costacurta, P. Falcaro, B. Marmiroli, F. Cacho-Nerin, H. Amenitsch
Densification of sol-gel silica thin films induced by hard X-rays generated by synchrotron radiation
Journal of Synchrotron Radiation 18 (2), pp. 280-286 (2011)

K. Jungnikl; M. Rappolt; I. Shyjumon; B. Sartori; P. Laggner; H. Amenitsch
Aerosol Flow Reactor with Controlled Temperature Gradient for In Situ Gas-Phase X-Ray Experiments—Measurements of Evaporation-Induced Self-Assembly (EISA) in Aerosols
Aerosol Science and Technology, Volume 45, Issue 7, 2011, Pages 805 – 810

M.B. Kerber, M.J. Zehetbauer, E. Schafler, F.C. Spieckermann, S. Bernstorff and T. Ungar
X-ray Line Profile Analysis – An Ideal Tool to Quantify Structural Parameters of Nanomaterials
JOM Vol. 63 No. 7, pp. 61-69 (July 2011) www.tms.org/jom.html

N. Krins, J.D. Bass, B. Julián-López, P. Evrar, C. Boissière, L. Nicole, C. Sanchez, H. Amenitsch and D. Grosso
Mesoporous SiO2 thin films containing photoluminescent ZnO nanoparticles and simultaneous SAXS/WAXS/ellipsometry experiments
Journal of Materials Chemistry 21 (4), pp. 1139-1146 (2011)

M. Lučić Lavčević, A. Turković, P. Dubček, Z. Crnjak Orel, B. Orel and S. Bernstorff
GISAXS View of Induced Morphological Changes in Nanostructured CeVO4 Thin Films
Journal of Nanomaterials, Volume 2011, Article 303808 (2011)

E. Maier, T. Rath, W. Haas, O. Werzer, R. Saf, F. Hofer, D. Meissner, O. Volobujeva, S. Bereznev, E. Mellikov, H. Amenitsch, R. Resel, G. Trimmel
$CuInS_2$-Poly(3-(ethyl-4-butanoate)thiophene) nanocomposite solar cells: Preparation by an in situ formation route, performance and stability issues
Solar Energy Materials and Solar Cells 95 (5), pp. 1354-1361 (2011)

C. Marchini, D. Pozzi, M. Montani, C. Alfonsi, A. Amici, S. Candeloro De Sanctis, M.A. Digman, S. Sanchez, E. Gratton, H. Amenitsch, A. Fabbretti, C.O. Gualerzi and G. Caracciolo
Role of temperature-independent lipoplex-cell membrane interactions in the efficiency boost of multicomponent lipoplexes
Cancer Gene Therapy 18, 543-552 (August 2011) doi:10.1038/cgt.2011.12

A. Pein, M. Baghbanzadeh, T. Rath, W. Haas, E. Maier, H. Amenitsch, F. Hofer, C.O. Kappe, G.Trimmel
Investigation of the formation of CuInS2 nanoparticles by the oleylamine route: Comparison of microwave-assisted and conventional syntheses
Inorganic Chemistry 50 (1), pp. 193-200 (2011)

Š. Perutková, M. Daniel, M. Rappolt, G. Pabst, G. Dolinar, V. Kralj-Iglič, and A. Iglič
Elastic deformations in hexagonal phases studied by small-angle X-ray diffraction and simulations
Physical Chemistry Chemical Physics 13,3100-3107 (2011)

S.R.C. Pinto, A. G Rolo, M. Buljan, A. Chahboun, S. Bernstorff, N.P. Barradas, E. Alves, R.J. Kashtiban, U. Bangert and M.J.M. Gomes
Low-temperature fabrication of layered self-organized Ge clusters by RF-sputtering
Nanoscale Research Letters 2011, 6:341

C. Potamitis, P. Chatzigeorgiou, E. Siapi, K. Viras, T. Mavromoustakos, A. Hodzic, G. Pabst, F. Cacho-Nerin, P. Laggner and M. Rappolt
Interactions of the AT1 antagonist valsartan with dipalmitoyl-phosphatidylcholine bilayers
Biochimica et Biophysica Acta - Biomembranes 1808 (6), pp. 1753-1763 (2011)

J. Sancho-Parramon, V. Janicki, M. Lončarić, H. Zorc, P. Dubček and S. Bernstorff
Optical and structural properties of Au-Ag islands films for plasmonic applications
Applied Physics A: Materials Science & Processing, Volume 103, Number 3, 745-748 (2011)
DOI: 10.1007/s00339-010-6231-x

Shyjumon, I., Rappolt, M., Sartori, B., Cacho-Nerin, F., Grenci, G., Laggner, P., Amenitsch, H.
Mesostructured silica aerosol particles: Comparison of gas-phase and powder deposit X-ray diffraction data
Langmuir 27 (9), pp. 5542-5548 (2011)

Teixeira, C.V., Amenitsch, H., Linton, P., Lindén, M., Alfredsson, V.
The role played by salts in the formation of SBA-15, an in situ small-angle X-ray scattering/diffraction study
Langmuir 27 (11), pp. 7121-7131 (2011)

A. Tilley, Y.-D. Dong, H. Amenitsch, M. Rappolt and B.J. Boyd
Transfer of lipid and phase reorganisation in self-assembled liquid crystal nanostructured particles based on phytantriol
Physical Chemistry Chemical Physics 13, 3026-3032 (2011)

E.M.F. Vieira, S.R.C. Pinto, S. Levichev, A.G. Rolo, A. Chahboun, M. Buljan, N.P. Barradas ,E. Alves, S. Bernstorff, O. Conde, M.J.M. Gomes
Influence of the deposition parameters on the growth of SiGe nanocrystals embedded in Al_2O_3 matrix
Microelectronic Engineering 88 (2011) 509–513

Anan Yaghmur, Barbara Sartori, and Michael Rappolt
The role of calcium in membrane condensation and spontaneous curvature variations in model lipidic systems
Physical Chemistry Chemical Physics 13, 3115-3125 (2011)

International Conferences and Workshops in 2010

Z. Arsov, B. Boulgaropoulos, P. Laggner, G. Pabst
Effect of ceramide on model membrane lipid phase properties studied by ATR-FTIR spectroscopy
Regional Biophysics Conference 2010, Primosten, Croatia, 17.9.2010 (poster)

B. Boulgaropoulos, H. Amenitsch, P. Laggner, G. Pabst
Structure and dynamics of an apoptotic model membrane
54th Annual Biophysical Society Meeting, San Francisco, USA, 22.2.2010 (poster)

M. Buljan, P. Dubček, N. Radić, I. Capan, U.V. Desnica, S. Bernstorff, V. Holý, B. Pivac
A comparative study of self ordering growth of silicon and germanium quantum dots in amorphous matrix
E-MRS Spring Meeting, Strasbourg, France, 7-11.6.2010 (Oral contribution)

M. Buljan, U.V. Desnica, N. Radić, G. Dražić, S. Bernstorff, T. Cornelius, H. Metzger, V. Holý
Production and design of regularly ordered quantum dot lattices in amorphous matrices
13th Joint Vacuum Conference Štrbske Pleso, Slovakia 21-24.06.2010 (invited talk)

M. Buljan, I. Bogdanović-Radović, U.V. Desnica, N. Radić, G. Dražić, M. Karlušić, S. Bernstorff, V. Holý
Production of spatially correlated nanoparticles by ion beam irradiation
Vakuumska znanost i tehnika, Tuheljske Toplice, Croatia, 01.06.2010 (Oral contribution)

M. Buljan, U.V. Desnica, N. Radić, G. Dražić, S. Bernstorff, V. Holy
Application of Monte-Carlo method on simulations of the growth of Ge quantum dot lattices in amorphous matrices
Workshop on designing and applying computational tools for reliable prediction of metal oxides properties, Zagreb, Croatia, 20-22.05.2010 (invited talk)

M. Buljan, I. Bogdanović-Radović,G. Dražić, N. Radić, S. Bernstorff and V. Holy *Formation of quantum dot lattices by ion beam irradiation-GISAXS study*
10th Biennial Conference on High Resolution X-ray Diffraction and Imaging-*XTOP*, 2010, Warwick United Kingdom, 20-23. October 2010 (poster)

M. Buljan, U.V. Desnica, N. Radić, I. Bogdanović-Radović, M. Ivanda, G. Dražić, M. Karlušić, P. Dubček, K. Salamon, S. Bernstorff, J. Grenzer, V. Holý
Structural Properties of semiconductor quantum dots
17 znanstveni sastanak Vakuumska znanost i tehnika, Tuheljske toplice, Hrvatska, 1. July2010 (invited lecture)

Gaetano Campi
In situ Small Angle X ray Scattering study of silver nanocrystals formation in a template of polynaphthalene polymer aqueous solutions
X International Conference, NANO2010, Rome, Italy, 13-17 September, 2010 (oral)

G. Caracciolo, L. Callipo, S. Candeloro De Sanctis, C. Cavaliere, D. Pozzi, G. Caruso, M.A. Digman, S.A. Sanchez, E. Gratton
Surface adsorption of protein corona controls the cell internalization mechanism of multicomponent lipoplexes in serum
In: Biophys J. San Francisco, California, USA, February 20-24, 2010., p. 3752-Pos.

G. Caracciolo, D. Pozzi, C. Marianecci, M. Carafa, C. Marchini, M. Montani, A. Amici
Programmed Packaging of Multicomponent Envelope-type Nanoparticle System (MENS)
11th European Symposium on controlled drug delivery, Netherlands, 7-9 April 2010

P. Dubček, B. Pivac, S. Milošević, N. Krstulović, Z. Kregar, S. Bernstorff
Pulsed laser ablation of GaAs using nano pulse length
EMRS Spring Meeting, Strasbourg, France, 7-11.6.2010 (poster)

A. Fischereder, W. Haas, T. Rath, H. Amenitsch, J. Albering, D. Meischler, S. Larissegger, M. Edler, R. Saf, F. Hofer, G. Trimmel
Investigation of Cu_2ZnSnS_4 formation from metals salts and thioacetamide
2010 MRS Spring Meeting. San Francisco USA, April 2, 2010 (talk)

D. Gracin, K. Juraić, N.Zorić, A. Gajović, P. Dubček, S. Bernstorff, M. Čeh
Structural and optical properties of amorphous-nanocrystalline silicon thin films
E-MRS Spring Meeting, Strasbourg, France, 7-11.6.2010 (poster)

D. Gracin, K. Juraić, J. Sancho-Parramon, P. Dubček, S. Bernstorff, M. Čeh
Amorphous-nano-crystalline silicon thin films in next generation of solar cells
IVC-18, August 23-27, 2010, Beijing, China (talk)

A. Hodzic, T. Mavromoustakos, P. Zoumpoulakis, M. Rappolt, P. Laggner & G. Pabst
Chemical structure role of cell-membrane hydrocarbon chain in interactions with antihypertensive drugs (sartans)
8th Central European Symposium on Pharmaceutical Technology, Graz, 16.-18. September 2010 (Poster)

P. Innocenzi
New applications of micro– and meso-porous materials
Summer School (related to the International Zeolite Conference joint with the 7th Internazional Mesostructured Materials Symposium, IZC-IMMS 2010), 2-3.7.2010, Sorrento, Italy

P. Innocenzi, C. Figus, M. Takahashi
Nanocrystalline Organosilicates through Self-Organization in Organic-Inorganic Hybrid Materials
III International Congress on Ceramics (ICC3), Osaka (Japan), 14-17. 11.2010

P. Innocenzi
Hierarchical Films with Multiscale and Multi-shape Pores: Nanoboxes, Nanospheres and Mesopores
III International Congress on Ceramics (ICC3) Osaka (Japan) 14-17. 11.2010

P. Innocenzi
Mesoporous films: mastering the complexity by self-assembly
International Conference on Nanoscience and Nanotechnology (ICONN 2010), 22-26th February 2010, Sydney, Australia

A. Keilbach, J. Schuster, Y. Li, M. Döblinger, T. Bein
Periodic Mesoporous Organosilicas and Carbons in Confined Spaces
16th International Zeolite Conference, Sorrento, Italy, 04.-07.07.2010

A. Khodorov, S. Levichev, A. Chahboun, A.G. Rolo, N. P. Barradas, E. Alves, M.J.M. Gomes
Growth and characterization of Mn- doped ZnO/TiO2 multilayered nanostructures grown by pulsed laser deposition
International Conference Trends in NanoTechnology (TNT2010), Braga, Portugal, September 6-10, 2010 (Poster)

E. Lepeltier, C. Bourgaux, J. Caron, E. Sliwinski, D. Desmaele, P. Couvreur
Nanoassemblies of nucleoside analogues coupled to squalene: structural analysis
GTRV, Toulouse, France, 6 - 8 décembre 2010 (poster)

S. Levichev, E. M. F. Vieira, C. J. Dias, R. Igreja, A.G. Rolo, A. Chahboun, M. Buljan, S. Bernstorff, and M. J. M. Gomes
Correlation between structural and electrical properties of SiGe nanocrystals embedded in SiO2 matrix
E-MRS 2010 Fall Meeting, Symposium E, Warsaw, Poland, September 13 - 17, 2010

L. Malfatti
Ordered Functional Porous Thin Films
III FORUM Nazionale dei Giovani Ricercatori di Scienza e Tecnologia dei Materiali, Padova (Italy), 22-24 March 2010

L. Malfatti
Pattering Self-assembled Mesostructured Films with In-Situ Formation of Gold Nanoparticles
VII Workshop Italiano Sol-Gel, Napoli (Italy) 17-18, June, 2010

L. Malfatti
Litografia di Materiali Mesostrutturati Autoassemblati con Formazione In-Situ di Nanoparticelle di Oro
X Convegno Nazionale AIMAT, Capo Vaticano (VV) 5-8, September, 2010

L. Malfatti
Self-assembled Materials Studied by Time-Resolved Analytical Techniques
I Bilateral Italian/Chinese Workshop Shanghai (Cina) 11, November, 2010

L. Malfatti
A Combined Bottom-Up and Top-Down Approach Towards the Design of Thin Films on Multiple Length Scales
III International Congress on Ceramics (ICC3) Osaka (Japan) 14-17, November, 2010

C. Marianecci, D. Pozzi, S. Candeloro De Sanctis, G. Caracciolo, L. Di Marzio, F. Rinaldi, M. Carafa
Niosomal vesicles: characterization by X-ray diffraction and cell-interaction studies
In: 7th World Meeting on Parmaceutics, Biopharmaceutics and Pharmaceutical technology, Valletta, Malta, 8-11 March 2010

P. Mariani
SAXS and SANS analysis of biomolecular systems in solution
International Workshop on Spectroscopy in Biology, Maresias, Brazil,18 - 22 October 2010

B. Marmiroli, F. Cacho-Nerin, B. Sartori, G. Grenci, J. Perez, P. Laggner and H. Amenitsch
Sub 100 μs studies of fast chemical and biological reactions using a free-jet micromixer
60th Annual Meeting of the Austrian Physical Society, Salzburg, Austria, September 6 – 10, 2010

B. Marmiroli, F. Cacho-Nerin, B. Sartori, G. Grenci, J. Perez, P. Laggner
and H. Amenitsch
Free jet micromixer: a versatile tool for sub 100 μs studies of fast chemical and biological reactions.
NANO ROME conference, september 2010

D. Meischler, T. Rath, A. Fischereder, K. Bartl, H. Amenitsch, G. Trimmel, F. Stelzer, R. Saf
Investigation of the formation of $CuInS_2$ layers prepared at moderate temperatures
MRS Spring Meeting 2010, San Francisco, USA, April 5, 2010 (poster)

G. Pabst
Biomembrane Physics Matters?
Lipotox - Seminar, Center for Moleculare Bio-sciences, Karl-Franzens-University Graz, Austria, 9.4.2010 (talk)

G. Pabst
Apoptosis: A Physicists View on Programmed Cell Death
Seminar of the Physics Department (Aalto University School of Science and Technology), Helsinki, Finland, 3.6.2010 (talk)

G. Pabst
Membrane Mediated Effects of General Anesthetics on Ion Channels
Softmatter Group Meeting (Aalto University School of Science and Technology), Helsinki, Finland, 4.6.2010 (talk)

G. Pabst, H. Jerebek, M. Rappolt & T. Stockner
Membrane-mediated effects of general anaesthetics on ion channels
8th Central European Symposium on Pharmaceutical Technology, Graz, 16.-18.9.2010 (Poster)

G. Pabst
Membrane-Mediated Effects of General Anesthetics on Ion Channels
OeGMBT Jahrestagung (Boku), Wien, Austria, 28.9.2010 (talk)

G. Pabst
Effect of Domain Formation on the Membrane Activity of Enzymes in the Context of Apoptosis
467th Wilhelm and Else Heraeus Seminar: Biophysics of Membrane Transformations, Bad Honnef, Germany, 28.10.2010 (talk)

G. Pabst
Label-Free Determination of Compositional Fluctuations and Macroscopic Phase Separation in a Ternary Lipid Mixture
5th Biophysics Christmas Workshop, Ptuj, Slovenia, 11.12.2010 (talk)

S. Perutkova, A. Iglic, M. Daniel, V. Kralj-Iglic and M. Rappolt
Modelling of inverted hexagonal phospholipids phase including lipid anisotropy
9th International Symposium of Computer Methods in Biomechanics and Biomedical Engineering, Valencia, Spain, 24-27.02.2010 (lecture)

S. R. C. Pinto, R. J. Kashtiban, M. Buljan, A. G. Rolo, A. Chahboun, U. Bangert, and M. J. M. Gomes
Production and structural characterisation of Ge nanocrystals embedded in alumina
E-MRS 2010 Spring Meeting, Symposium H, Strasbourg, France, June 7-11, 2010

S. R. C. Pinto, A. G. Rolo, M. Buljan, A. Chahboun, A. Chahboun, R. J. Kashtiban, U. Bangert, N. P. Barradas, E. Alves, S.Bernstorff, and M. J. M. Gomes
Structural study of multilayers of $Si_{1-x}Ge_x$ Nanocrystals embedded in SiO_2 matrix
International Conference on "Trends in NanoTechnology" (TNT2010), Braga, Portugal, September 6-10, 2010 (Poster)

P. Pivette, V. Faivre, G. Daste, M. Ollivon, S. Lesieur
Formulation of lipid microspheres by a prilling process: theoretical and experimental aspects
7th World Meeting on Pharmaceutics, Biopharmaceutics and Pharmaceutical Technology, Valetta, Malta, 8-11 Mars 2010 (Oral communication)

P. Pivette, V. Faivre, G. Daste, M. Ollivon, S. Lesieur
Sustained release lipid microspheres obtained by a prilling process: formulation and drug release
Workshop "Novel structures & delivery systems", AgroParisTech-Centre de Massy, France, 28-29 Octobre 2010 (Oral communication)

P. Pivette, V. Faivre, G. Daste, M. Ollivon, S. Lesieur
Incorporation of water-soluble API in lipid-based microspheres obtained by prilling: from the process to the controlled release mechanisms
GPEN, Chapel Hill, USA, 10-12 Novembre 2010 (Oral communication)

P. Pivette, V. Faivre, G. Daste, M. Ollivon, S. Lesieur
Incorporation of water-soluble API in lipid-based microspheres obtained by prilling: from the process to the controlled release mechanisms
AAPS Pharmaceutical Sciences World Congress, New Orleans, USA, 15-18 Novembre 2010 (Oral communication)

G. Polt, F. Spieckermann, H. Wilhelm, M. Kerber, E. Schafler, M.J. Zehetbauer
Mechanisms of Plasticity in γ-Polypropylene
4th ICPB-IUPAC - International Conference on Polymer Behavior, Lodz, Poland, September 2010

D. Pozzi, G. Caracciolo, C. Marchini, M. Montani, A. Amici, L. Callipo, AL Capriotti, C. Cavaliere, A. Lagana
Surface Adsorption of protein corona controls the cell uptake mechanism in efficient cationic liposome/DNA complexes in serum
11th European Symposium on "Controlled drug delivery", The Netherlands, 7-9 April 2010

N.Radić, M. Jerčinović, P. Dubček, K. Salamon, O. Milat, G. Dražić, S. Bernstorff
Ultra-tanki viseslojni filmovi ugljika i volframa
17th International Meeting "Vacuum Science & Technique"

N. Radić, M. Jerčinović, K. Salamon, P. Dubček, S.Bernstorff
W/C Multilayers growth - experiment and modelling
JVC 13 Joint Vacuum Conference, High Tatras, Slovakia, June 20-25, 2010

N. Radic, M. Jercinovic, P. Dubcek, M. Ivanda, K. Salomon and S. Bernstorff
C/W nanolaminates - alternating various C & W phases
EMRS Spring Meeting, Strasbourg, France, 7-11.6.2010 (Talk Tuesday 8.6.10, 08:30-9:00 Symposium L)

M. Rappolt
Talking interfaces: from model membranes to drug delivery
XMAS Workshop at Elettra, Basovizza, Italy, 14.12.2010 (Invited lecture)

M. Rappolt
"Talking" interfaces: from model membranes to drug delivery
5th Christmas Biophysics Workshop, Ptuj, Sovenia, 11.12.2010 (Invited lecture)

M. Rappolt
Structure and dynamics of the inverse hexagonal phase: from nature to application
"Membrane Biophysics Course" at the University of Ljubljana, 14.09.2010

M. Rappolt
Bilayer thickness estimations with "poor" diffraction data
Workshop "Glycolipids, Structures, Function and Interactions" organized by Klaus Brandenburg (Forschungszentrum Borstel) at the University of Hamburg, 04.06.2010 (Invited lecture)

M. Rappolt
My first electron density map: a beginners guide to SAXD.
Applications of Synchrotron Radiation in Life Science, Student Courses at ELETTRA, Trieste, Italy, 26.05.2010 (Invited lecture)

M. Rappolt
Lamellar to Inverted Hexagonal Phase Transition as „Seen" by X-rays
"Membrane Biophysics Course" at the University of Ljubljana, 12.03.2010

M. Rappolt
Structure and dynamics of the inverse hexagonal phase: from nature to application
IBN in-house SEMINAR, Graz, 05.05.2010

M. Rappolt, B. Sartori, A. Hodzic, G. Pabst & T. Mavromoustakos
Interactions of different sartans with the bilayer interface studied by SAXS
8th Central European Symposium on Pharmaceutical Technology, Graz, 16.09.-18.09.2010 (poster)

T. Rath, G. Trimmel
New Synthesis Methods for Nanocomposite Solar Cells
11. Symposium Energieinnovation, Graz, Austria, 10 – 12 February, 2010 (talk)

T. Rath
Das Christian Doppler Labor für Nanokomposit-Solarzellen
8. Österreichische Photovoltaik Tagung, Wien, October 28, 2010 (talk)

T. Rath, E. Maier, M. Edler, W. Haas, A. Santis Alvarez, H. Amenitsch, F. Hofer, G. Trimmel
Application of Nanocomposite Layers Consisting of Electroactive Polymers and Copper Indium Disulfide Nanoparticles in Hybrid Photovoltaics
ISOS 3 International Summit on OPV Stability 2010. Roskilde, Denmark, October 21, 2010 (poster)

T. Rath, A. Fischereder, W. Haas, H. Amenitsch, E. Maier, J. Albering, D. Meischler, M. Edler, R. Saf, F. Hofer, G. Trimmel
Preparation of Copper Zinc Tin Sulfide Layers for Photovoltaic Applications
25th European Solar Energy Conference and Exhibition. Valencia, Spain, September 6, 2010 (poster)

A.A. Rempel and A. Magerl
Non-periodicity in cadmium sulfide nanopartciles
XVIII International Synchrotron Radiation Conference, Budker Institute of Nuclear Physics, Novosibirsk, Russia, 19-22 July 2010 (invited talk)

J. Sancho-Parramon, V. Janicki, M. Lončarić, H. Zorc, P. Dubček and S. Bernstorff
Optical and structural properties of Au-Ag islands films for plasmonic applications
META'10, 2. International Conference on Metamaterials, Photonic crystals and Plasmonics, Cairo, Egypt, February 22- 25, 2010

M. Sauerbrey, A. Zargham, Th. Schmidt, J. I. Flege, and J. Falta.
Determining the internal structure and morphology of nanoparticle films using element-specific xray techniques
DPG-Fruehjahrstagung 2010, Regensburg (Germany), March 21–26, 2010 (oral)

E. Schafler
Defect Losses in nanomaterials during SPD processing as investigated by in-situ synchrotron Bragg profile analysis
Seminar Uni Vienna, Austria, 27.1.2010

W. Schmidt, H. Amenitsch, A. Lu, J. Nitz
Vapor adsorption on CMK-5 as traced by in situ XRD experiments
16th Internernational Zeolite Conference, Sorrento, Italy, 4-9 Mar 2010 (Poster)

J. Schuster, R. Köhn, A. Keilbach, M. Döblinger, H. Amenitsch, T. Bein
Thermally-Induced Mesostructure Formation of Polymer Resin-Surfactant Composites in Confined Environments: An In-Situ GISAXS Study
MRS Spring Meeting, San Francisco, USA, 05.-09.04.2010

F. Spieckermann, H. Wilhelm, M. Kerber, E. Schafler, G. Polt, S. Bernstorff, F. Addiego, M. Zehetbauer
Determination of Lamella Thickness Distributions in Isotactic Polypropylene by Multiple X-ray Line Profile Analysis
4th ICPB-IUPAC - International Conference on Polymer Behavior, Lodz, Poland, September 2010

F. Spinozzi
Proteins in solution investigated by small-angle scattering: a global fit strategy
Regional Biophysics Conference, Primosten, Croatia, 15 - 18 September 2010

F. Spinozzi
Proteins in Solutions: An Analysis of preferential hydration, structural properties and stability by neutron and X-ray scattering techniques
International Workshop on Spectroscopy in Biology, Maresias, Brazil, 18 - 22 October 2010

F. M. Toma, A. Sartorel, M. Iurlo, M. Carraro, T. Da Ros, G. Scoles, F. Paolucci, M. Prato and M. Bonchio
Efficient Water Oxidation at Carbon Nanotube/Polyoxometalate Electrocatalytic Interfaces
Summer School on Preparative Strategies in Solid State and Material Chemistry, UCSB, Santa Barbara (California, USA) 8-21 August 2010 (poster)

F. M. Toma
Functionalization of carbon nanostructures for efficient water oxidation
Energy materials: electro- and photho-Chemical Interfaces and devices" at Chemistry Department of University College of London, organized by The Tomas Young Center, London Centre for Theory and Simulation of Materials, London (UK) 7-9 September 2010 (invited talk)

G. Trimmel
Organic-inorganic hybrid solar cells
Winterschool on "Organic Electronics, Fundamental Properties of Devices – Sensors, Transistors and Solar Cells", Planneralm, Austria, March 6-12, 2010 (talk)

G. Trimmel, T. Rath, A. Fischereder, E. Maier, J. Albering, W. Haas, F. Hofer, G. Mauthner, E. List, D. Meissner
Organic-Inorganic Hybrid Solar Cells Based on Metal Sulfides and Electroactive Polymers 25th European Solar Energy Conference and Exhibition. Valencia, Spain, September 6, 2010 (poster)

A. Turković, P.Dubček, M. Rakić, M. Lončarić and S. Bernstorff
SAXS studies of TiO_2 nanoparticles in polymer electrolytes and nanophased films
JVC 13 Joint Vacuum Conference, High Tatras, Slovakia, June 20-25, 2010

A. Turković
SAXS/DSC/WAXD Study of γ-irradiated Polymer Electrolyte for Zn Rechargeable Nanostructured Galvanic Cells
17. Medunarodni sastanak Vakuumska znanost i tehnika, Zbornik sažetaka / Pivac, Branko, editor(s) Zagreb : Hrvatsko Vakuumsko društvo, 2010. 5-5 (poster)

A. Turković
(Antun Drašner, Krunoslav Juraić, Pavo Dubček, Aleksandra Turković *, Sigrid Bernstorff)
SAXS Studies of TiO2 Nanoparticles in Polymer Electrolytes
Second Regional Symposium on Electrochemistry, South-East Europe Sava Center, Belgrade, Srbia, June 6 to 10, 2010

T. Ungár
Single-Grain Microstructure from Polycrystalline Specimens
2010 TMS Annual Meeting & Exhibition, Seattle, WA, USA, February 14-18, 2010 (Invited Talk)

E.M.F. Vieira, S. R. C. Pinto, S. Levichev, A. G. Rolo, A. Chahboun, M. Buljan, S. Bernstorff, O. Conde and M. J. M. Gomes
Influence of the deposition parameters on the growth of SiGe nanocrystals embedded in Al2O3 matrix
EMRS Spring Meeting 2010, Strasbourg, France, June 7-11, 2010

E. M. F. Vieira, S.R.C. Pinto, A.G. Rolo, A. Chahboun, S. Levichev, M. Buljan, S.Bernstorff, O. Conde and M. J. M. Gomes
Study of the size, shape and spatial homogeneity of SiGe nanocrystals in alumina and silica matrix
11th International Symposium on Multiscale, Multifunctional and Functionally Graded Materials, Guimarães, Portugal, 26-29 September 2010 (poster)

E. M. F. Vieira, S.R.C. Pinto, A.G. Rolo, A. Chahboun, S. Levichev, M. Buljan, S.Bernstorff, O. Conde and M. J. M. Gomes
Structural and electrical characterization of $Si_{1-x}Ge_x$ nanocrystals embedded in Al_2O_3 matrix
International Conference Trends in NanoTechnology (TNT2010), Braga, Portugal, September 6-10, 2010 (Poster)

E.M.F. Vieira, S.R.C. Pinto, A.G. Rolo, A. Chahboun, M. Buljan, S. Levichev, S. Bernstorff, and M.J.M. Gomes
Structural investigation of SiGe nanocrystals embedded in dielectric matrix grown by magnetron sputtering deposition
European Conference on X-ray spectrometry, Coimbra, Portugal, June 20-25, 2010

E. M. F. Vieira, S. R. C. Pinto, A. G. Rolo, A. Chahboun, M. Buljan, S. Levichev, S. Bernstorff, O. Conde and M. J. M. Gomes
Structural and electrical characterization of $Si_{1-x}Ge_x$ nanocrystals embedded in Al_2O_3 and SiO_2 matrices
18th International Vacuum Congress (IVC-18), Beijing, China, August 23-27, 2010 (poster)

E. M. F. Vieira, S.R.C. Pinto, A.G. Rolo, A. Chahboun, S. Levichev, M. Buljan, O. Conde and M. J. M. Gomes
$Si_{1-x}Ge_x$ nanocrystals embedded in dielectric matrices grown by RF- magnetron sputtering
Scientific First Meeting COST Action MP0901 HZB, Berlin, Germany, March 18-19, 2010

A. Yaghmur, P. Laggner, M. Almgren, B. Sartori, L. Paasonen, M. Yliperttula, Arto Urtti, and M. Rappolt
Structural Transitions in lipidic aqueous dispersions
24th Conference European Colloid and Interface Society (ECIS 2010), Prague, Czech Republic, September 5-10, 2010 (poster)

A. Yaghmur
Characterization of lipidic aqueous dispersions
Otto Glatter Special Workshop, 24th Conference European Colloid and Interface Society (ECIS 2010), Prague, Czech Republic, September 5-10, 2010 (talk)

A. Yaghmur
Lamellar-nonlamellar structural transition
Nano Science Center, University of Copenhagen, Copenhagen, Denmark, April 28, 2010 (invited talk)

A. Yaghmur, P. Laggner, M. Almgren and Michael Rappolt
Characterization of lipidic aqueous dispersions
Seventh Nordic Workshop on Scattering from Soft Matter, at the Department of Physics, University of Helsinki, Helsinki, Finland, 27-28th January 2010 (talk)

A. Zargham
Revealing the internal structure and ordering of Pt-containing colloidal bimetallic nanoparticles by synchrotron based X-ray techniques
7th International Conference on Synchrotron Radiation in Materials Science – SRMS 2010,
Oxford (U.K.), July 11–14, 2010 (oral)

M. Zehetbauer, E. Schafler, M. Kerber, S. Bernstorff and T. Ungar
X-ray Line Profile Analysis – An Ideal Tool to Quantify Structural Parameters of Nanomaterials
TMS 2010 Annual Meeting & Exhibition, Symposium "Neutron and X-Ray Studies of Advanced Materials″, Seattle, WA, USA, February 14-18, 2010
(2:00 PM Keynote Talk)

ELETTRA Highlights 2009-2010

P. Falcaro, L. Malfatti, S. Costacurta, B. Marmiroli, G. Grenci, L.Vaccari, H. Amenitsch, P. Innocenzi
Fabrication of advanced functional devices combining Sol-Gel with X-ray lithography
Elettra Research Highlight, pp. 16-17 (2010)

F.M. Toma, P. Parisse, M. Carraro, A. Sartorel, T. Da Ros, L. Casalis, A. Goldoni, H. Amenitsch, F. Bondino, G. Scoles, M. Prato, M. Bonchio
Bio-inspired water oxidation electrodes integrating carbon nanotubes and olyoxometalates
Elettra Research Highlight, pp. 22-23 (2010)

PhD Thesis / Doktorarbeiten 2010

Marko Bitenc
Vpliv reakcijskih poti na morfologijo, rast in lastnosti delcev ZnO
University of Ljubljana, Slovenia

Aurelia W Dong
The Characterisation of Self-assembled Amphiphiles using Positron Annihilation Lifetime Spectroscopy (PALS)
Monash University, Australia

Lijing Ke
Mechanism of anti-influenza virus activity of the Maillard reaction products derived from Radix isatidis extract
University of Edinburgh, United Kingdom

Andreas Keilbach
Oriented Nanochannels for Nanowire Synthesis
Ludwig-Maximilians-University Munich, Germany

Daniela Marongiu
Top-down and bottom-up approach to self-assemble multifunctional porous films
Università di Milano-Bicocca, Italy

Serena Mazzoni
Polymorphism, structural properties and stability of monoolein cubic phases in the presence of cytochrome
Università Politecnica delle Marche, Ancona

B. Pili
Nanoparticules de gemcitabine-squalène : interaction avec des membranes modèles et activité anticancéreuse de la prodrogue sous forme de liposomes
University of Châtenay-Malabry, France

Sara Pinto
Estudo estrutural de Nanocristais de Si1-xGex embebidos em matrizes dieléctricas
Universidade do Minho, Braga, Portugal

Florian Spieckermann
Investigation of Deformation Induced Changes of the Microstructure of Semicrystalline Polymers and their Impact on Mechanical Properties
University of Vienna, Austria

Ardalan Zargham,
Synchrotron Radiation Based Multi-Scale Structural Characterization of CoPt3 Colloidal Nanoparticles
University of Bremen, Germany

Master Theses (Tesi di Laurea, Diplomarbeit) 2010

Danilo Burattini
Stabilita' di quadrieliche di guanosina: effetto della carica e dei controioni
Università Politecnica delle Marche, Ancona, Italy

Enrico Jr. Baldassarri
Effetto dei contro ioni sul processo di auto assemblaggio e sulla stabilità di quadri eliche di guanosina
Università Politecnica delle Marche, Ancona, Italy

M.M. Suchanova
Fluorescence properties of glass with 2.0 wt.% of CdS
Ural Federal University, Ekaterinburg, Russia

M. Battiston
Films of semiconductor nanocrystals: a SAXS characterization
University of Trieste, Italy

Authors Index

IBN
Institute of Biophysics and Nanosystems Research
Austrian Academy of Sciences
Schmiedlstraße 6, 8042 Graz, Austria
Tel.: +43 316 41 20-302
Fax: +43 316 41 20-390
E-mail: ibn.office@oeaw.ac.at
Web: www.ibn.oeaw.ac.at

ELETTRA
Sincrotrone Trieste
Strada Statale 14, km 163,5
34012 Basovizza (TS), Italy
Tel.: +39 040 375 8572
Fax: +39 040 93 809 02
E-mail: bernstorff@elettra.trieste.it
Web: www.elettra.trieste.it

Cover-picturetaken from S. Joseph et al. (see pages 96-97).
The pure fractal image is a modified version of Randall C. Page's translucent spiral.